



HAL
open science

De l'estimation et du contrôle non linéaire à l'avionique de systèmes de drones plus sûrs et robustes

Jean-Philippe Condomines

► To cite this version:

Jean-Philippe Condomines. De l'estimation et du contrôle non linéaire à l'avionique de systèmes de drones plus sûrs et robustes. Sciences de l'ingénieur [physics]. Université Toulouse 3 - Paul Sabatier, 2022. tel-04718678

HAL Id: tel-04718678

<https://enac.hal.science/tel-04718678v1>

Submitted on 2 Oct 2024

HAL is a multi-disciplinary open access archive for the deposit and dissemination of scientific research documents, whether they are published or not. The documents may come from teaching and research institutions in France or abroad, or from public or private research centers.

L'archive ouverte pluridisciplinaire **HAL**, est destinée au dépôt et à la diffusion de documents scientifiques de niveau recherche, publiés ou non, émanant des établissements d'enseignement et de recherche français ou étrangers, des laboratoires publics ou privés.



Distributed under a Creative Commons Attribution 4.0 International License

HABILITATION A DIRIGER DES RECHERCHES

De l'estimation et du contrôle non linéaire à
l'avionique de systèmes de drones plus sûrs et
robustes.

- Synthèse des travaux de recherche -

JEAN-PHILIPPE CONDOMINES
ENAC

7 Av. Marc Pélegrin
31400 Toulouse

Université : Paul Sabatier
Spécialité : Automatique

Parrain de Recherche : DANIEL ALAZARD

HDR soutenue le 9 mai 2022 devant le jury :

GUIDO DE CROON (Delft University of Technology, Rapporteur)

FRANCK CAZAURANG (Institut evering Bordeaux, Rapporteur)

PASCAL MORIN (Institut Systèmes Intelligents et de Robotique, Rapporteur)

ISABELLE FANTONI (Laboratoire des Sciences du Numérique de Nantes, Examinatrice)

FRÉDÉRIC GOUAISBAUT (LAAS/CNRS, Examineur)

DANIEL ALAZARD (ISAE-SUPAERO, Examineur)

Table des matières

1	Curriculum Vitae	1
2	Activités d'enseignement	5
2.1	Cours & Travaux Pratiques	5
2.2	Travaux Dirigés	6
3	Mémoires et diplômes dirigés	7
3.1	Master et projet d'initiation à la recherche (PIR)	9
4	Travaux et publications	11
4.1	Ouvrages collectifs	11
4.2	Supports de cours (polycopiés) et de travaux pratiques (TP)	11
4.3	Revue internationale avec comité de lecture	11
4.4	Congrès	12
4.5	Brevets, séminaire et rapport de recherche	14
5	Synthèse des travaux	15
5.1	Introduction	15
5.2	Vers des systèmes avioniques plus sûrs et robustes	17
5.2.1	Les différents systèmes de drones étudiés	17
5.2.1.1	Les commandes de vol de drones dotés de structures complexes	17
5.2.1.2	La reprise d'un drone à ailes rigides en situation de décrochage	20
5.2.1.3	Détection d'une cyber-intrusion dans un réseau de communi- cation	22
5.2.2	Estimation, filtrage invariant pour la navigation inertielle	25
5.3	Apports méthodologiques et techniques en estimation	26
5.3.1	Sur l'estimation d'état des systèmes nonlinéaires invariants	26
5.3.1.1	La construction d'un estimateur invariant	27
5.3.1.2	La formulation invariante du filtre de Kalman Unscented : l'IUKF	28
5.3.2	Sur l'estimation des régions de stabilités des systèmes nonlinéaire	34

5.3.2.1	Région d'attraction & systèmes définis par des polynômes par morceaux	36
5.3.2.2	Les Sum-of-Squares pour prouver la stabilité du Contrôle Prédictif	40
5.3.3	Etude de l'approche algébrique pour la commande « sans modèle »	42
5.3.4	Etude de l'approche multifractale pour la détection d'une cyber-intrusion	47
5.4	Conclusion & perspectives	49
6	Copie de 5 articles	59

Table des figures

5.1	Le drone à corps basculant « Darko » pour des missions de longue endurance. . .	19
5.2	Le drone à ailes flexibles destinée à la récupération d'énergie.	19
5.3	Description des vulnérabilités des communications dans une flotte de drones. . .	24
5.4	La dynamique de l'inclinomètre est invariante sous l'action du groupe $SO(2)$. . .	31
5.5	Variation temporelle de tous les gains de correction, de chaque variation de θ . . .	33
5.6	Comparaison des gains UKF et IUKF.	33
5.7	Modèle par morceaux des coefficients aérodynamiques.	39
5.8	Ensemble stable du modèle longitudinal par morceaux comparé à (Chakraborty et al. [2011]).	39
5.9	Essai en vol de transition à l'intérieur, face à la soufflerie <i>WindShape</i> de l'ENAC. . .	44
5.10	Résultats du vol de transition à l'intérieur, face à la soufflerie <i>WindShape</i>	45
5.11	Influence des paramètres de réglages de la commande sans modèle.	46
5.12	Résultats de l'analyse multifractale lors d'une attaque par usurpation d'identité. . .	48
5.13	Formulation de l'UKF dans un cadre invariant.	50
5.14	Résultats sur l'identification d'un modèle à ailes rigides au décrochage.	53

ACTIVITES DE RECHERCHES

Co-conception d'avioniques robustes et sûres par construction

- Problématiques multi-domaines (aérodynamique, réseau informatique, automatique);
- Développement de méthodes en estimation et d'études en traitement du signal;
- Méthodologie d'utilisation de lois de commande avancées;
- Implémentation, programmation sur STM32 et validation en embarqué sur mini-drone;
- Essais expérimentaux (VDTO¹, WindShape²);

Estimation/filtrage

- Estimation par approche géométrique, algébrique et analyse des régions de stabilité;
- Conception et intégration de capteurs logiciels (AHRS, INS, estimateur de vent);
- Influence des bruits de mesures sur la performance des filtres géométriques;
- Conception et dimensionnement de supports expérimentaux;

ACTIVITES D'ENSEIGNEMENT

En lien étroit avec mes activités de recherche, je mène une activité d'enseignement de 118h Eq. TD/an et d'ingénierie pédagogique de 30h Eq. TD/an à l'ENAC en cycle ingénieur pour les promotions IENAC (Ingénieur ENAC) et ISESA (Ingénieur des Systèmes Electroniques de la Sécurité Aérienne). Ces liens sont volontairement entretenus pour garantir un enseignement en constante adaptation aux évolutions de la robotique aérienne. La liste présentée ci-dessous résume mon activité d'enseignements de cours, TD et BE qui sera présentée dans le chapitre 2.

- Rappel de classe préparatoire : TD (2h)
- Mineure drone (commande et estimation d'état) : cours, TD, TP et projet (12h)
- Introduction aux commandes automatiques du vol : projet (8h)
- Commandes des systèmes linéaires : TD (20h)
- Projet de synthèse avion 1ère et 2ème année : cours, projet (20h)
- Représentation des systèmes dynamiques : TD (8h)
- Systèmes linéaires : TD (16h)
- Commandes linéaires des systèmes mono-entrées mono-sorties : TD (8h)
- Soutenance de projets (10h)

1. Volière Drone Toulouse Occitanie

2. Soufflerie à veine ouverte : <https://www.windshape.ch>

ACTIVITES D'ENCADREMENT

La liste présentée ci-dessous résume mes activités d'encadrement qui seront reprises avec plus de détails dans le chapitre 3.

- 6 co-encadrements de thèse dont 3 thèses soutenues entre 2018 et 2022 ;
- 1 thèse en fin de montage pour un démarrage courant 2022 ;
- 8 co-encadrements de stage dont 5 en stage de fin d'études (niveau M2) ;
- Participation au co-encadrement de projets étudiants (PIR,...).

COORDINATION, ANIMATION, RAYONNEMENT SCIENTIFIQUE,...

- Participation au montage de plusieurs appels à projets internationaux : contributions sur les spécifications du système avionique et la coordination des différentes tâches à réaliser dans le projet MISTRALÉ³ qui porte sur l'utilisation de drones pour évaluer le stress hydrique des sols (application en agriculture). Le projet Aerosafe-5D⁴ qui vise à développer des concepts d'opérations pour une meilleure insertion des drones dans les espaces aériens.
- Participation au montage de plusieurs appels à projets nationaux en lien avec ma thématique de recherche (CONVEX, MODIfyME, MOBIUS, ICASC).
- Collaboration avec le Professeur Laurent Burlion de l'Université de Rutgers aux USA : co-encadrement international d'un étudiant en thèse sur de la commande de système sur-actionné.
- Collaboration avec le Professeur Silvère Bonnabel de MinesParisTech : co-encadrement d'un stage de fin d'étude sur le développement de filtre de Kalman pour estimer le vent. Réalisation d'un article de conférence AIAA GNC.
- Collaboration avec le Professeur Michel Fliess de l'Ecole Polytechnique et avec Cédric Join du CRAN de Nancy. Dépôt d'un brevet.
- Organisation de séminaires scientifiques : 1) sur les filtres de Kalman invariants ; 2) sur l'application de la commande sans modèle.
- Participation active au comité de pilotage de la recherche ENAC en tant que représentant du programme transverse drone.
- Représentant ENAC au sein de la fédération de recherche ISAE/ENAC/ONERA pour l'équipe PGNC (Pilotage, Guidage, Navigation et Contrôle) : élaboration de feuille de route, relecture et évaluation de sujets de recherches, etc.
- Activité de relecture de publications et d'articles soumis à des congrès (conférence IFAC, American Control Conference, Conference on Decision and Control,...).

3. www.mistrale.eu

4. <https://cordis.europa.eu/project/id/861635/fr>

- Contribution au projet Open-Source Paparazzi (<https://blog.paparazziuav.org>) avec l'intégration d'algorithmes d'estimation pour améliorer la navigation et la reconstruction du vecteur vent.

COLLABORATIONS

- Instituts académiques français (ISAE-SUPAERO, ONERA, MineParisTech, CRAN Nancy, Ecole Polytechnique, Université Rennes 3).
- Industriel : montage en cours d'un projet de collaboration avec le CNES.
- Instituts internationaux : Université de Rutgers (US).

CINQ PUBLICATIONS LES PLUS SIGNIFICATIVES

- **Conf 9** : J.P. Condomines, C. Seren, G. Hattenberger. « Invariant Unscented Kalman Filter with Application to Attitude Estimation », *56th IEEE Conference on Decision and Control (CDC)*, MELB., Australia, 2017.
- **Revue 3** : T. Cunis, J.P. Condomines, L. Burlion. « Dynamical Stability Analysis of Aircraft Flight in Deep-Stall », *AIAA Journal of Aircraft*, 2019.
- **Conf 21** : V. Guibert, J.P. Condomines, M. Brunot, M. Bronz. « Piecewise Polynomial Model Identification using Constrained Least Squares for UAS Stall », *SYSID, System Identification*, 2021.
- **Revue 1** : J.M.O. Barth, J.P. Condomines, M. Bronz, J.M. Moschetta, C. Join, M. Fliess. « Model-Free Control Algorithms For Micro Air Vehicles With Transitioning Flight Capabilities », *International Journal of Micro Air Vehicles*, 2020.
- **Revue 7** : R. Zhang, J.P. Condomines, E.Lochin. « A Multifractal Analysis and Machine Learning based Intrusion Detection System with Application in a UAS/RADAR system », *Drones*, MDPI, 2022.

Activités d'enseignement

2.1 Cours & Travaux Pratiques

- **Navigation, Command and state Estimation** : ce cours est une introduction aux techniques d'estimation d'état linéaire et non linéaire à base de modèle. Il présente un état de l'art du domaine de l'estimation et détaille plus particulièrement la construction d'observateurs et de filtres de Kalman. Ces techniques sont appliquées aux mini-drones. On détaille donc différents modèles cinématiques communément exploités pour la navigation des systèmes dynamiques. Les notions classiques de covariance et d'observabilité sont également discutées.
Support de cours : [Poly 1] : J.P. Condomines. *Introduction au filtre de Kalman et à la théorie des estimateurs invariants : Application aux traitements multi-information pour la navigation*. Notes de cours ENAC ; [TP 1] : J.P. Condomines. *Le filtre de Kalman : Application aux traitements multi-information pour la navigation*, sessions Matlab (Disponible à partir de l'adresse : <http://recherche.enac.fr/~jean-philippe.condomines>)
- **Introduction to quadrirotor modeling and control** : l'objectif de ce cours est de présenter un panorama de la robotique aérienne et des architectures de contrôle d'un système de drone. Il présente donc les outils mathématiques pour la modélisation des mini-drones et les outils mathématiques pour l'analyse et la conception d'un pilote automatique sous la forme de *boîtes à outils mathématiques*. **Support de cours** : [Note 1] : J.P. Condomines. *Introduction à la modélisation des drones quadrirotor*. Notes de cours ENAC (Disponible à partir de l'adresse : <http://recherche.enac.fr/~jean-philippe.condomines>)
- **Projet de synthèse avion 1ère et 2ème année** : En première année, le but de ce cours/projet est d'analyser la dynamique latérale et longitudinale d'un avion de transport à partir des équations de la mécanique du vol codées en langage Python. En deuxième année, nous reprenons le modèle de la dynamique longitudinale d'un avion de transport commercial. L'objectif est de concevoir les différentes lois du pilote automatique via Matlab / Simulink (point d'équilibre, linéarisation, commande classique : synthèse de la boucle de tenue d'assiette, commande optimale : synthèse de la boucle de tenue de la vitesse indiquée, commande modale : synthèse MIMO pour la tenue de la vitesse indiquée et de l'altitude) **Support de cours** : [TP 1] : T. Miquel, J. Sharples, J.P. Condomines, A. Drouin. *Commande linéaire des systèmes dynamiques : Projet de synthèse*. Sujet de TP ENAC pour les majeures et mineures AVI. (Disponible à partir de l'adresse : <http://recherche.enac.fr/~jean-philippe.condomines>)
- **Introduction aux commandes automatiques du vol** : L'objectif de ce cours/projet est de concevoir et de tester à l'aide du logiciel Matlab/Simulink quelques modes supérieurs du pilote automatique à partir d'un modèle simple d'avion issu de la mécanique du point.

Ces quatre modules d'enseignement (Responsable : THIERRY MIQUEL) sont dispensés aux élèves ingénieurs en seconde et dernière année de l'ENAC ayant choisi la majeure ou mineure *Systemes Avioniques*.

2.2 Travaux Dirigés

Dans les travaux dirigés ci-dessous, les principales techniques de modélisation sont abordées et la technique de linéarisation qui permet de manipuler des équations différentielles linéaires à coefficients constants est illustrée dans le contexte aéronautique. Les propriétés des systèmes linéaires et invariants sont présentées, ainsi que la notion de fonction de transfert et les propriétés des systèmes bouclés.

- **Représentation des systèmes dynamiques ;**
- **Système linéaires ;**
- **Commande linéaire des systèmes mono-entrées/mono-sorties ;**
- **Commande des systèmes linéaires.**

Mémoires et diplômes dirigés

JACSON MIGUEL OLSZANECKI BARTH

« *Algorithmes de contrôle sans modèle pour les micro drones de type tail-sitter* » : participation à l'encadrement à 50% avec JEAN-MARC MOSCHETTA ; thèse soutenue le 28 mai 2020 (thèse ENAC/ISAE).

Publications :

- **Revue 1** : J.M.O. Barth, J.P. Condomines, M. Bronz, J.M. Moschetta, C. Join, M. Fliess. « Model-Free Control Algorithms For Micro Air Vehicles With Transitioning Flight Capabilities », *International Journal of Micro Air Vehicles*, 2020.
- **Conf 1** : J.M.O. Barth, J.P. Condomines, M. Bronz, J.M. Moschetta, G. Hattenberger, C. Join, M. Fliess. « Towards a Unified Model-Free Control Architecture for Tail Sitter Micro Air Vehicles : Flight Simulation Analysis and Experimental Flights », *AIAA SciTech Forum : Guidance, Nav., and Control*, Orlando, 2020.
- **Conf 2** : J.M.O. Barth, J.P. Condomines, J.M. Moschetta, A. Cabarbaye, C. Join, M. Fliess. « Full Model-Free Control Architecture for Hybrid UAVs », *American Control Conference (ACC)*, Philadelphia, 2019.
- **Conf 6** : J.M.O. Barth, J.P. Condomines, M. Bronz, L.R. Lustosa, J.M. Moschetta, C. Join, M. Fliess. « Fixed-wind UAV with transitioning flight capabilities; Model-Based or Model-Free Control approach? A preliminary study », *International Conference on Unmanned Aircraft Systems (ICUAS)*, 2018.
- **Conf 7** : J.M.O. Barth, J.P. Condomines, J.M. Moschetta, C. Join, M. Fliess. « Model-Free Control Approach for Fixed-Wing UAVs with Uncertain Parameters Analysis ». *International Conference on Methods and Models in Automation and Robotics (MMAR)*, Poland, 2018.
- **Conf 8** : L.R. Lustosa, J.M.O. Barth, J.P. Condomines, F. Defay, J.M. Moschetta. « Team MAVion entry in the IMAV'17 outdoor challenge—A tail-sitting trajectory-tracking Micro UAV », *Inter. Micro-Air Vehicle (IMAV)*, Toulouse, 2017.

Devenir du candidat : ingénieur en recherche et développement sur les lois de contrôle, ALTRAN

TORBJØRN CUNIS

« *Modélisation, analyse et commande pour la récupération d'un aéronef en situation de décrochage : de la théorie des systèmes au pilote automatique* » : participation à l'encadrement à 50% avec LAURENT BURLION ; thèse soutenue le 27 septembre 2019 (thèse ONERA/ENAC).

Publications :

- **Revue 2** : T. Cunis, J.P. Condomines, L. Burlion. « Local Stability Analysis For Large Polynomial Spline Systems », *Automatica*, 2019.
- **Revue 3** : T. Cunis, J.P. Condomines, L. Burlion. « Dynamical Stability Analysis of Aircraft Flight in Deep-Stall », *AIAA Journal of Aircraft*, 2019.
- **Revue 4** : T. Cunis, J.P. Condomines, L. Burlion. « Piecewise Polynomial Modeling for Control and Analysis of Aircraft Dynamics beyond Stall », *AIAA Journal in Guidance, Control and Dynamics*, 2018.
- **Conf 12** : T. Cunis, L. Burlion, J.P. Condomines. « Nonlinear Analysis and Control Proposal for in-flight Loss-of-control », *20th World Congress of the Inter. Federation of Automatic Control (IFAC)*, 2017.
- **Conf 3** : T. Cunis, J.P. Condomines, L. Burlion. « Full-Envelope, six-degrees-of-freedom tim analysis of unmanned aerial systems based on picewise polynomial aerodynamic coefficients », *Research, Education and Development of Unmanned Aerial Systems (RED-UAS)*, Sweden, 2018.
- **Conf 4** : T. Cunis, J.P. Condomines, L. Burlion. « Piece-Wise identification and analysis of the aerodynamic coefficients, tim conditions, and safe sets of the generic transport model », *AIAA Guidance Navigaion & Control*, Florida, 2018.
- **Conf 20** : Cunis, Torbjørn and Liao-McPherson, Dominic and Condomines, Jean-Philippe and Burlion, Laurent and Kolmanovsky, Ilya. « Economic Model-Predictive Control Strategies for Aircraft Deep-stall Recovery with Stability Guarantees », *58th IEEE Conference on Decision and Control*, 2019.

Devenir du candidat : Enseignant-chercheur à l'université du Stuttgart

RUOHAO ZHANG

« *Modélisation, reconstruction et détection de cyber-intrusion malveillante dans un essaim de drones* » : participation à 50% à l'encadrement avec NICOLAS LARRIEU ; thèse soutenue le 18 janvier 2022 (thèse ENAC).

Publications :

- **Revue 5** : J.P. Condomines, R. Zhang, N. Larrieu. « Network Intrusion Detection System For UAV Ad-Hoc Communication : From Methodology Design To Real Test Validation », *Ad Hoc Network Journal*, Elsevier, 2018.

- **Revue 7** : J.P. Condomines, R. Zhang, E.Lochin. « Multifractal Analysis and Machine Learning based IntrusionDetection Systemwith Application in a UAS/RADAR system », *Drones communication Journal*, MDPI, 2022.

VINCENT GUIBERT

« *Identification et contrôle d'un uAV dans les conditions de post-stall* » : participation à 50% à l'encadrement avec MATHIEU BRUNO ; 3ème année de thèse (thèse ONERA/ENAC).

Publications :

- **Conf 19** : V. Guibert, M. Brunot, M. Bronz, J.P Condomines. « Semi-parametric Regression based on Machine Learning Methods for UAS Stall Identification », SYSID, System Identification, 2021
- **Conf 21** : V. Guibert, J.P Condomines, M. Brunot, M. Bronz. « Piecewise Polynomial Model Identification using Constrained Least Squares for UAS Stall », SYSID, System Identification, 2021

ROMAIN JAN

« *Loi de commandes d'un drone flexible pour l'extraction d'énergie* » : participation à 50% à l'encadrement avec JEAN-MARC MOSCHETTA ; 3ème année de thèse (thèse ISAE/ENAC).

Publications :

- **Conf 22** : R. Jan, J.P Condomines, J.M. Moschetta. « Fast simulation model for control law design and benchmark of high aspect ratio flexible UAVs »,IMAV, International Micro Air Vehicule conference, 2021.

JUAN LÓPEZ MURO

« *Loi de commandes d'un drone flexible sur-actionné* » : participation à 50% à un encadrement international avec LAURENT BURLION ; 2ème année de thèse (thèse Rutgers University/ENAC). Publications :

- **Conf 23** : Juan López Muro, Xianping Du, Jean-Philippe Condomines, Onur Bilgen and Laurent Burlion. « Wind Turbine Tower Thickness and Blade Pitch Control Co-Design Optimization »,IMAV, AIAA 2022-1150. AIAA SCITECH 2022 Forum. January 2022.

3.1 Master et projet d'initiation à la recherche (PIR)

- **2015 M. HUI**
Caractérisation et implémentation d'une solution DGPS pour mini-drone 2015. Projet de fin d'études UPSSITECH.

- **2016** J.F. ERDELYI
Développement d'un planeur microdrone autonome pour la recherche d'ascendances thermiques. Projet de fin d'études UPSSITECH, 2016.
- **2016** I. BOUKILI
Conception et mise en oeuvre d'une méthode de détection d'intrusion dans une flotte de drones 2016. Projet de fin d'études ENAC.
- **2017** M. BROSSARD
Filtre de Kalman sans parfum invariant et estimation du vent pour un drone. Projet de fin d'études Mines-Paris Tech.
- **2017** R. CHEMALI
Mise en oeuvre d'une méthode de détection d'intrusion dans une flotte de drones. Projet de fin d'études UPS.
- **2018** D. BEREZIAT
L'estimation/filtrage pour améliorer la navigation autonome d'un drone. PIR ENAC.
- **2018** A. CISOWSKI
Applications of signatures to classification of air traffic density. PIR ENAC.
- **2019** N. HABBAKI
New design of Intrusion Prevention System (IPS) for drone network communications. Projet de fin d'études ENAC.

Travaux et publications

Les versions HTML des documents ci-dessous sont disponibles à partir de ma page personnelle (voir chapitre 1).

4.1 Ouvrages collectifs

- **Ouv 1** : T. Miquel, J.P. Condomines, Y. Brière, J. Bordeneuve-Guibé. Rédaction d'un Chapitre. « Introduction au contrôle des mini-drones : de la conception à la mise en œuvre - Modélisation, identification et synthèse des lois de commande ». *Formations & Techniques*, Ellipses Edition, 2020.
- **Ouv 2** : C. Seren, J.P. Condomines, G. Hattenberger. Chapitre 22 : « Optimal invariant observer theory for nonlinear state estimation ». *Multisensor Attitude Estimation - Fundamental Concepts and Applications -*, CRC Press, Taylor & Francis Group, 2015.

4.2 Supports de cours (polycopiés) et de travaux pratiques (TP)

- **Poly 1** : J.P. Condomines. *Introduction au filtre de Kalman et à la théorie des estimateurs invariants : Application aux traitements multi-information pour la navigation*. Notes de cours ENAC, Octobre 2016.
- **Poly 2** : J.P. Condomines. *Le filtre de Kalman : Application aux traitements multi-information pour la navigation*. Notes de cours ENAC et sessions Matlab.
- **TP 1** : T. Miquel, J. Sharples, J.P. Condomines, A. Drouin. *Commande linéaire des systèmes dynamiques : Projet de synthèse*. Sujet de TP ENAC pour les majeures et mineures AVI.
- **TP 2** : J.P. Condomines, T. Miquel. *DC Motor : position control*, Sujet de TP pour les élèves ingénieurs ENAC 1ère année.

4.3 Revues internationales avec comité de lecture

- **Revue 1** : J.M.O. Barth, J.P. Condomines, M. Bronz, J.M. Moschetta, C. Join, M. Fliess. « Model-Free Control Algorithms For Micro Air Vehicles With Transitioning Flight Capabilities », *International Journal of Micro Air Vehicles*, 2020.

- **Revue 2** : T. Cunis, J.P. Condomines, L. Burlion. « Local Stability Analysis For Large Polynomial Spline Systems », *Automatica*, 2019.
- **Revue 3** : T. Cunis, J.P. Condomines, L. Burlion. « Dynamical Stability Analysis of Aircraft Flight in Deep-Stall », *AIAA Journal of Aircraft*, 2019.
- **Revue 4** : T. Cunis, J.P. Condomines, L. Burlion. « Piecewise Polynomial Modeling for Control and Analysis of Aircraft Dynamics beyond Stall », *AIAA Journal in Guidance, Control and Dynamics*, 2018.
- **Revue 5** : J.P. Condomines, R. Zhang, N. Larrieu. « Network Intrusion Detection System For UAV Ad-Hoc Communication : From Methodology Design To Real Test Validation », *Ad Hoc Network Journal*, Elsevier, 2018.
- **Revue 6** : J.P. Condomines. « A Study of Non Linear State Estimation Based On Invariant Observers », *International Journal of Control*, Open-Science, ISTE Edition, 2017.
- **Revue 7** : J.P. Condomines, R. Zhang, E.Lochin. « Multifractal Analysis and Machine Learning based IntrusionDetection Systemwith Application in a UAS/RADAR system », *Drones communication*, MDPI, 2022.

4.4 Congrès

Tous les congrès mentionnés dans la bibliographie ci-dessous sont à comité de lecture.

- **Conf 1** : J.M.O. Barth, J.P. Condomines, M. Bronz, J.M. Moschetta, G. Hattenberger, C. Join, M. Fliess. « Towards a Unified Model-Free Control Architecture for Tail Sitter Micro Air Vehicles : Flight Simulation Analysis and Experimental Flights », *AIAA SciTech Forum : Guidance, Navigation, and Control*, Orlando, Florida, 2020.
- **Conf 2** : J.M.O. Barth, J.P. Condomines, J.M. Moschetta, A. Cabarbaye, C. Join, M. Fliess. « Full Model-Free Control Architecture for Hybrid UAVs », *American Control Conference (ACC)*, Philadelphia, 2019.
- **Conf 3** : T. Cunis, J.P. Condomines, L. Burlion. « Full-Envelope, six-degrees-of-freedom tim analysis of unmanned aerial systems based on pice-wise polynomial aerodynamic coefficients », *Research, Education and Development of Unmanned Aerial Systems (RED-UAS)*, Sweden, 2018.
- **Conf 4** : T. Cunis, J.P. Condomines, L. Burlion. « Piece-Wise identification and analysis of the aerodynamic coefficients, tim conditions, and safe sets of the generic transport model », *AIAA Guidance Navigaion & Control*, Florida, 2018.
- **Conf 5** : M. Brossard, J.P. Condomines, S. Bonnabel. « Tightly Coupled Navigation And Wind Estimation For Mini-UAVs », *AIAA Guidance Navigaion & Control*, Florida, 2018.

- **Conf 6** : J.M.O. Barth, J.P. Condomines, M. Bronz, L.R. Lustosa, J.M Moschetta, C. Join, M. Fliess. « Fixed-wind UAV with transitioning flight capabilities; Model-Based or Model-Free Control approach? A preliminary study », *International Conference on Unmanned Aircraft Systems (ICUAS)*, 2018.
- **Conf 7** : J.M.O. Barth, J.P. Condomines, J.M. Moschetta, C. Join, M. Fliess. « Model-Free Control Approach for Fixed-Wing UAVs with Uncertain Parameters Analysis ». *International Conference on Methods and Models in Automation and Robotics (MMAR)*, Poland, 2018.
- **Conf 8** : L.R. Lustosa, J.M.O. Barth, J.P. Condomines, F. Defay, J.M. Moschetta. « Team MAVion entry in the IMAV'17 outdoor challenge—A tail-sitting trajectory-tracking Micro UAV », *Inter. Micro-Air Vehicle (IMAV)*, Toulouse, 2017.
- **Conf 9** : J.P. Condomines, C. Seren, G. Hattenberger. « Invariant Unscented Kalman Filter with Application to Attitude Estimation », *56th IEEE Conference on Decision and Control (CDC)*, MELB., Australia, 2017.
- **Conf 10** : M. Brossard, S. Bonnabel, J.P. Condomines. « Unscented Kalman Filtering on Lie Groups », *IEEE/RSJ Int. Conference on Intelligent Robots and Systems, Vanc., (IROS)*, 2017.
- **Conf 11** : T. Miquel, J.P. Condomines, R. Chemali, N. Larrieu. « Design of Robust Controller/Observer for TCP/AQM Network : First Application to intrusion detection systems for drone fleet », *IEEE/RSJ Int. Conference on Intelligent Robots and Systems, Vanc., (IROS)*, 2017.
- **Conf 12** : T. Cunis, L. Burlion, J.P. Condomines. « Nonlinear Analysis and Control Proposal for in-flight Loss-of-control », *20th World Congress of the Inter. Federation of Automatic Control (IFAC)*, 2017.
- **Conf 13** : J.P. Condomines, C. Seren, G. Hattenberger. « Pi-invariant unscented Kalman filter for sensor fusion », *IEEE Conference on Decision and Control (CDC)*, Los Angeles, 2014.
- **Conf 14** : J.P. Condomines, C. Seren, G. Hattenberger. « Nonlinear State Estimation Using an Invariant Unscented Kalman Filter », *AIAA Guidance Navigation & Control*, Boston, 2013.
- **Conf 15** : J.P. Condomines, C. Seren, G. Hattenberger. « Experimental Wind Field Estimation And Aircraft Identification », *Inter. Micro-Air Vehicle (IMAV)*, Delft, 2013.
- **Conf 16** : M. Bronz, J.P. Condomines, G. Hattenberger. « Development of An 18cm Micro Air Vehicle : Quark ». *Inter. Micro-Air Vehicle (IMAV)*, Delft, 2013.
- **Conf 17** : J.P. Condomines, F. Defay, D. Alazard. « Robust Impedance Active Control of Flight Control Devices ». *World Congress of the Inter. Federation of Automatic Control (IFAC)*, Cape Town, 2013.

- **Conf 18** : R. Zhang, J.P. Condomines, E. Lochin. « Spectral Analysis and Machine Learning based IDS for UAS Location Reporting System », ICRA 2021, International Conference on Robotics and Automation, en cours de relecture.
- **Conf 19** : V. Guibert, M. Brunot, M. Bronz, J.P Condomines. « Semi-parametric Regression based on Machine Learning Methods for UAS Stall Identification », SYSID, System Identification, 2021.
- **Conf 20** : Cunis, Torbjørn and Liao-McPherson, Dominic and Condomines, Jean-Philippe and Burlion, Laurent and Kolmanovsky, Ilya. « Economic Model-Predictive Control Strategies for Aircraft Deep-stall Recovery with Stability Guarantees », *58th IEEE Conference on Decision and Control*, 2019.
- **Conf 21** : V. Guibert, J.P Condomines, M. Brunot, M. Bronz. « Piecewise Polynomial Model Identification using Constrained Least Squares for UAS Stall », SYSID, System Identification, 2021.
- **Conf 22** : R. Jan, J.P Condomines, J.M. Moschetta. simulation model for control law design and benchmark of high aspect ratio flexible UAVs », IMAV, International Micro Air Vehicle conference, 2021.
- **Conf 23** : Juan López Muro, Xianping Du, Jean-Philippe Condomines, Onur Bilgen and Laurent Burlion. « Wind Turbine Tower Thickness and Blade Pitch Control Co-Design Optimization », IMAV, AIAA 2022-1150. AIAA SCITECH 2022 Forum. January 2022.

4.5 Brevets, séminaire et rapport de recherche

- **Brevet 1** : R. Zhang, J.P. Condomines, N. Larrieu, C. Moy. (en cours de dépôt) « Système de détection et de prévention d'intrusion pour une flotte de drones », 2020.
- **Brevet 2** : J.M.O. Barth, J.P. Condomines, J.M. Moschetta, C. Join, M. Fliess. (WO/2019/238375) « Système et procédé de contrôle de vol d'un drone convertible à voilure fixe permettant une transition continue stabilisée entre un vol stationnaire vertical et un vol de croisière à l'horizontal », 2019.
- **Sem 1** : J.P. Condomines. séminaire du laboratoire ENAC « Signature invariante & équivariances : Théorie et application pour l'aviation civile » (contact : Prof. Stéphane Puechmorel, 2016).
- **Rapport 1** : J.P. Condomines. « Estimation non linéaire basée sur la théorie des observateurs invariants ». Référence HAL ENAC : RR-2017-001, 2017.

Synthèse des travaux

Ce chapitre présente une synthèse de mes travaux de recherche structurés autour de deux axes principaux, l'élaboration de systèmes avioniques de drones plus sûrs et robustes par construction ainsi que l'apport de nouvelles méthodes en estimation pour la commande des systèmes étudiés. Tout au long de ce document, nous essayerons de montrer la complémentarité entre ces deux axes et notamment en quoi les méthodes d'estimation classiquement utilisées dans la littérature doivent être adaptées pour répondre aux objectifs de sécurisation des différents systèmes avioniques de drones que nous avons étudiés. Pour étayer ces propos, nous avons choisi 5 articles, repérés par le symbole (*) et présentés dans le chapitre 6 dans lesquels le lecteur trouvera plus de détails sur certaines techniques qui n'ont pas été systématiquement abordées dans ce manuscrit par soucis de clarté et de cohérence d'ensemble. Au terme de cette démarche, l'objectif visé est le développement d'une collection de briques algorithmiques répondant aux besoins d'une avionique plus sûre et robuste par construction pour l'insertion des drones dans les espaces aériens civils. Si aujourd'hui cet objectif est déjà partiellement atteint, nous verrons qu'une longue distance reste encore à parcourir avant qu'il ne le soit complètement.

5.1 Introduction

Alors que les drones aériens n'ont eu de cesse d'alimenter la recherche en automatique durant ces dix dernières années pour réaliser des missions toujours plus complexes, de nouvelles problématiques en estimation et en commande émergent tout juste pour intégrer ces engins de manière sûre et robuste dans les espaces aériens civils. Autrefois considérés comme une technologie exclusivement militaire, les drones aériens ont réussi aujourd'hui à perforer la sphère de l'aviation civile avec de nombreux projets de recherche, certains financés par la Commission européenne, permettant d'étudier des idées d'application potentielle notamment pour le transport aérien. Parmi tant d'autres, citons leurs exploitations futures pour répondre aux problèmes du trafic routier et des interventions d'urgence avec la livraison de poches de sang, d'organes ou d'échantillons entre hôpitaux ; ou encore l'utilisation de plusieurs mini-drones en flotte coordonnée lors de catastrophes naturelles ou accidentelles pour lesquelles les premiers secours doivent intervenir le plus rapidement possible sur des zones multiples, là où celles-ci sont dévastées ou instables et donc dangereuses pour les sauveteurs. Grâce aux nouvelles techniques de robotique inspirées des progrès de l'Intelligence Artificielle (IA), les mini-drones sont

désormais capables de percevoir, de décider et de s'adapter localement à l'environnement pour mener à bien des missions de façon plus ou moins autonome. Pour cela, le drone dispose d'un système avionique dont l'optimisation confère à l'engin un degré d'autonomie et des qualités de vol en boucle fermée en adéquation avec la ou les missions qu'il doit remplir. De façon très concrète, il se compose d'une partie matérielle (comprenant un ordinateur embarqué, des capteurs, un ensemble d'actionneurs et un module de communication sol/bord) et d'une partie logicielle qui regroupe un certain nombre de fonctionnalités algorithmiques :

- ▶ des algorithmes de traitement du signal qui assurent des fonctions aussi diverses que le débruitage des sorties des capteurs ou la reconstruction des états du drone ou d'autres paramètres de vol, à partir d'une fusion des données mesurées disponibles à bord ;
- ▶ des algorithmes de contrôle « bas-niveau », synthétisés à partir d'une connaissance de la dynamique de l'engin, pour le pilotage et le guidage de l'appareil en boucle fermée de sorte que celui-ci soit commandé en consigne à atteindre ;
- ▶ et enfin, des algorithmes de contrôle « haut-niveau » pour la communication, la navigation, la re-planification ou l'aide à la décision en l'absence d'un opérateur humain.

Les algorithmes d'estimation, d'état ou de paramètres, et de contrôle apparaissent donc primordiaux dans le développement de tout drone aérien. L'estimation permet de fusionner, en temps réel, les informations imparfaites provenant des différents capteurs et de fournir une estimée, par exemple de l'état du drone (orientation, vitesse, position), la masse au décollage ou l'environnement de vol (vent, obstacles, etc.), au calculateur embarqué où sont implémentés les algorithmes de commande de l'engin. Ce contrôle de l'appareil doit garantir sa stabilité en boucle fermée quel que soit l'ordre de consigne fourni directement par l'opérateur ou par tout système automatique de gestion du vol et, assurer que celle-ci soit correctement recopiée. Estimation et commande participent donc grandement au succès de toute mission. Le contexte des systèmes de transports aériens vise désormais à mettre l'accent sur une plus grande sécurisation des vols de mini-drones afin que ces engins puissent de manière sûre s'insérer et partager les espaces aériens civils. Nous pensons ici notamment aux problématiques liées aux mini-drones à voilure fixe pour lesquels des conditions aérologiques difficiles peuvent faire sortir l'engin de son enveloppe de vol nominale ou bien à de potentielles pannes structurelles et/ou algorithmiques, issues de circonstances accidentelles ou malveillantes. Pour répondre à cet enjeu, les travaux de recherche actuels sur le développement des futurs systèmes de drones se fondent sur un triple constat : comme mentionné précédemment, il est possible aujourd'hui de doter un drone de fonctionnalités suffisamment performantes pour qu'il réalise des missions extrêmement complexes (vol en zone urbaine, en flotte de drones coordonnées, etc.) ; de telles fonctions d'autonomie sont intrinsèquement liées à un gain d'efficacité dans la mission et une amélioration de la sécurité et de la sûreté de fonctionnement ; pour concevoir ces fonctions d'autonomie, on a besoin d'outils permettant de garantir la sûreté et la sécurité de fonctionnement de l'engin dans tous les cas d'application. Ce dernier point ainsi que le précédent, motivent l'ensemble de nos recherches en estimation qui doivent conduire *in fine*, aux développements de systèmes avioniques plus sûrs et robustes dès leurs conceptions.

5.2 Vers des systèmes avioniques plus sûrs et robustes

L'approche de développement des systèmes avioniques plus sûrs et robustes par construction consiste à élaborer pour chaque application visée, un système avionique spécifique dont l'optimisation confèrera à l'engin un degré d'autonomie au regard des aspects liés à la conception, la performance et la sécurité du vol. La conception du drone devra être adaptée à sa mission dans des conditions d'emploi nominales et dégradées ; en matière de performance, les différentes algorithmiques du système avionique devront être en mesure de garantir des exigences sur le contrôle de l'appareil soumis à des perturbations aérologiques et des aléas issus de circonstance accidentelle ou malveillante. Ainsi, au plan de la sécurité, le drone devra rester dans une enveloppe de sécurité garantie pour un retour au sol sans danger pour autrui. Les travaux présentés dans ce manuscrit s'inscrivent dans cette démarche et ont contribué au développement de systèmes avioniques de drones à ailes rigides, flexibles et convertibles plus sûrs et/ou robustes dès leur conception. En particulier, les **fonctionnalités d'estimation et d'analyse** ont progressé et ce, pour fournir une **reconstruction fidèle des paramètres de vol, de l'état et des régions de stabilité du drone** afin d'élaborer différentes lois de commande performantes pour en assurer le contrôle en toute situation.

5.2.1 Les différents systèmes de drones étudiés

5.2.1.1 Les commandes de vol de drones dotés de structures complexes

Contrôle d'un drone à corps basculant : Cette structure de drone propose la possibilité d'atterrir et de décoller verticalement mais aussi de faire une transition vers un vol de longue durée, à très haute vitesse, ce qu'aucune configuration standard de drone, qu'elle soit à voilure fixe ou quadrirotor, ne permet de faire à l'heure actuelle. Les drones convertibles de type « corps basculant » (tilt-body) offrent l'avantage de ne pas recourir à des parties articulées à bord, sources de poids et de fragilité. Par rapport à des concepts de type « quadplane » combinant une configuration avion et un quadrirotor, le drone à corps basculant est une formule beaucoup plus pure sur le plan aérodynamique, capable de s'adapter naturellement aux conditions de fort vent en réduisant la prise au vent. La conception optimale de drones convertibles, pose toutefois deux difficultés majeures. La première est celle des performances aérodynamique de l'engin qui résultent d'un compromis entre deux phases de vol très différentes : les phases stationnaire et d'avancement. On doit soigneusement dimensionner le drone pour trouver le meilleur compromis entre ces deux phases. Le second défi est d'assurer une transition sûre et maîtrisée entre les deux phases de vol (Figure 5.1(a)). Ce dernier point nécessite d'étudier de très près les réalités aérodynamiques du vol de transition et les qualités de robustesse et de précision des lois de pilotage. Sur le plan aérodynamique, on a à faire à une physique relativement complexe, marquée par l'interaction entre le souffle des hélices et le vent relatif autour du drone. Il ne suffit pas de passer d'un mode vertical au mode horizontal comme on franchit un ruisseau, le plus vite possible. Il faut être en mesure de rester en équilibre

stable dans les phases intermédiaires en raison du fait que le drone doit pouvoir voler en conditions de vent latéral (Figure 5.1(b)). C'est le concept de « transition équilibrée » qui n'est possible que grâce à l'association de performances aérodynamiques parfaitement maîtrisées et l'utilisation de lois de commande sophistiquées : les forces aérodynamiques et propulsives doivent se compenser et les lois de commande doivent être suffisamment robustes pour pallier aux phénomènes aérodynamiques non modélisés.

Une solution de commande originale apportée dans le cadre de la thèse de JACSON BARTH [Conf 1],[Conf 2],[Conf 7] consiste à élaborer une architecture de contrôle de vol basé sur une méthode dite « sans modèle » dans laquelle **l'estimation de la dynamique d'état** du système est nécessaire pour compenser les différents **phénomènes aérodynamiques et perturbations extérieures** (efficacité des actionneurs, flux d'interactions entre les ailes et les hélices, vent latéral,...). A partir de cette estimée, la loi de commande souhaitée par l'ingénieur (PID par exemple) est réglée à travers un seul gain fixe de sorte qu'elle stabilise l'attitude du drone ainsi que sa vitesse et sa position dans toutes ses phases de vol. La méthode « sans modèle » est fortement dépendante de la qualité de l'estimateur et des mesures mais elle contourne le besoin de régler la loi de commande à partir d'une connaissance forte *a priori* de la dynamique du système dont l'obtention est longue et coûteuse. Un ensemble complet de résultats caractérisant les performances de l'architecture de la commande sans modèle pour drone à corps basculant, testé en simulation et implémenté sur un drone nommé Darko, a été présenté dans [Revue 1]*. Ce type d'engin construit en impression 3D permet d'être utilisé dans différentes configurations matérielles (changement de charge utile, modification de la structure ou des parties propulsives). A la différence d'une stratégie de commande classique qui utiliserait plusieurs dizaines de gains tabulés pour couvrir toute l'enveloppe de vol (LQR par exemple), l'architecture de commande sans modèle permet de faire basculer le corps du drone de manière stable et continue à partir de quelques gains fixes compensée par une estimation de l'état du système. Les résultats présentés dans [Revue 1]* permettent de conclure quant au bien-fondé de la méthode du sans modèle, de l'architecture proposée et de son apport pour les drones convertibles vis-à-vis de la robustesse paramétrique.

Contrôle d'un drone à voilure souple destiné à la récupération d'énergie : Pour les mini-drones à voilure fixe fonctionnant à basse altitude et à basse vitesse, de nombreuses études ont montré que le survol des perturbations atmosphériques représentent une source d'énergie importante pour augmenter l'endurance. Cet effet est aussi exploité dans la nature par un certain nombre d'oiseaux. Jusqu'à présent, le travail s'est concentré sur des drones à voilure rigides dont les performances en terme d'apport énergétique vont uniquement de pair avec l'augmentation de la dimension de la cellule. Ainsi, dans la continuité des travaux initiés dans (Allen et al. [2007], Bonnin [2015] et Nikola [2018]) l'approche présentée dans les travaux de thèse en cours de ROMAIN JAN consiste à introduire une certaine flexibilité dans la structure pour maximiser l'énergie extraite pendant le vol tout comme le ferait un oiseau, par la déformation de l'aile en torsion et en flexion (Figure 5.2) .

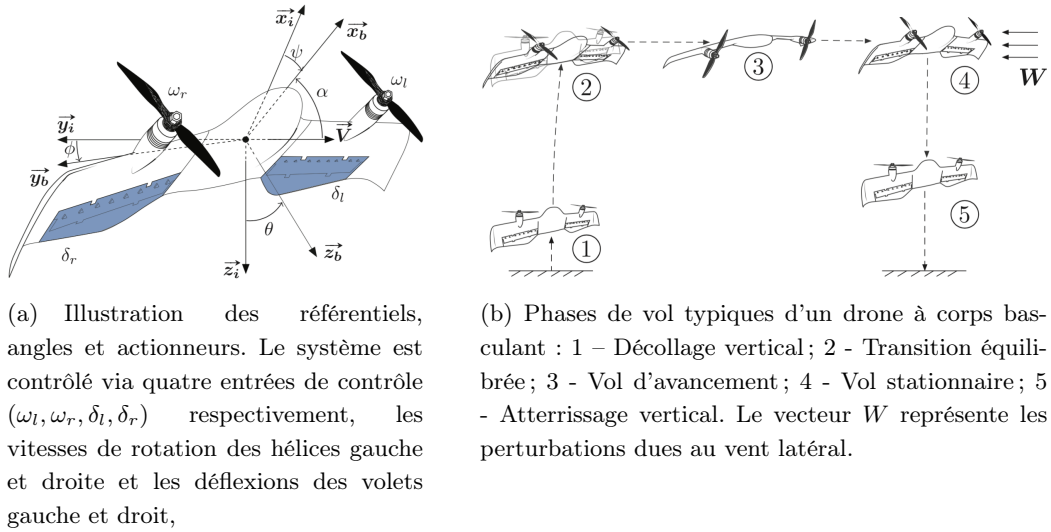


FIGURE 5.1 – Le drone à corps basculant « Darko » pour des missions de longue endurance.

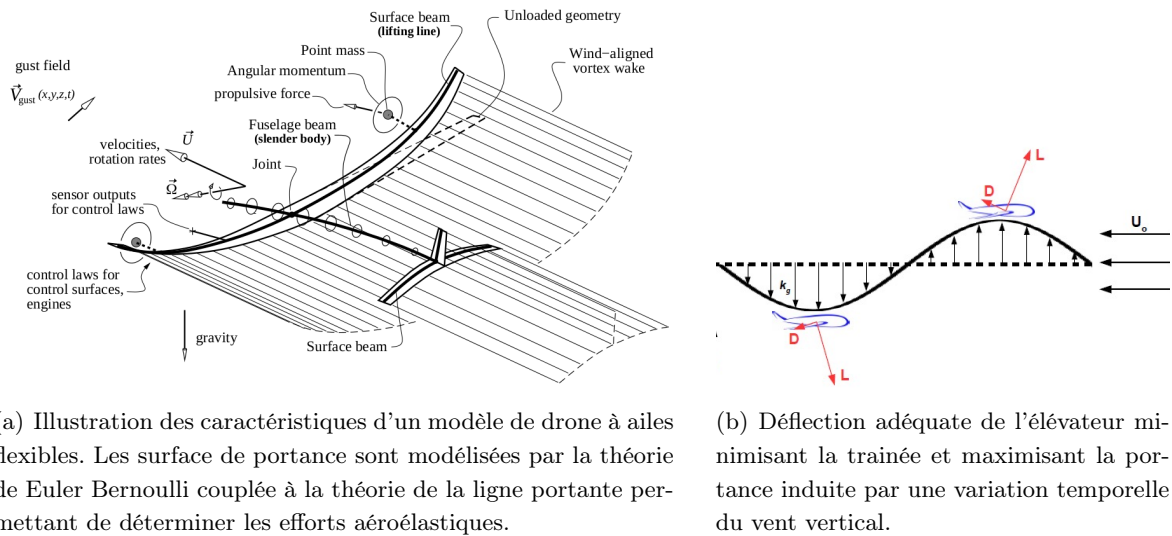


FIGURE 5.2 – Le drone à ailes flexibles destinée à la récupération d'énergie.

En effet, à la lecture des précédents travaux, nous pouvons statuer que certains paramètres géométriques ainsi que la flexibilité de la voilure peuvent augmenter les performances d'extraction d'énergie dans le cadre d'une réponse à une rafale de type sinusoïdale. Nous pouvons rappeler quelques résultats intéressants. 1) la flexibilité de la voilure peut apporter jusqu'à 5% de performance supplémentaire ; 2) le coefficient d'amortissement de la structure a un impact important sur les performances ; 3) la position du centre d'élasticité n'a pas d'impact sur les performances mais celle-ci doit être bornée par des bonnes limites évitant l'instabilité mécanique. De ce fait, le problème de la récupération d'énergie peut être appréhendé en le décomposant en deux étapes. La première étape consiste à faire une **estimation des paramètres** d'un **modèle aéroélastique** d'une aile flexible qui s'appuie conjointement sur des études menées en soufflerie et sur des méthodes numériques dédiées aux **structures flexibles**. Ce faisant, il sera possible d'étudier l'extraction de l'énergie de manière active ou passive dans le domaine fréquentiel. En effet, en calculant la réponse fréquentielle en boucle ouverte (réponse passive) de l'altitude sur une perturbation en vitesse verticale, nous pouvons déterminer les fréquences pour lesquelles le phénomène est maximal et déterminer l'impact de chaque mode propre de la structure sur les performances d'extraction d'énergie. À l'issue de ces résultats nous pourrions déterminer la bande passante des perturbations atmosphériques susceptibles d'être exploitée passivement par des mini UAVs ainsi que les paramètres géométriques et structurels dominants permettant de favoriser naturellement le processus d'extraction d'énergie. Suite à cette étude, la seconde partie des travaux s'appuie sur le développement d'un **outil de co-conception** intégrant les aspects aéroélastiques et commandes dans un même programme afin d'en optimiser le système avionique pour qu'il soit performant et robuste face aux perturbations. Ce travail a d'ores-et-déjà été commencé dans [Conf 22] avec la modification du logiciel **ASWING**¹.

5.2.1.2 La reprise d'un drone à ailes rigides en situation de décrochage

La conception de nouvelles structures de mini-drones telles que les convertibles ou les voilures souples à fort allongement intègrent des lois de commandes toujours plus performantes qui peuvent rapidement amener l'avion aux limites de son enveloppe de vol et le faire basculer dans une situation de décrochage. L'aéronef devient alors trop difficile à contrôler et le pilote automatique n'ayant pas été prévu pour fonctionner dans un domaine d'emploi non linéaire n'a plus d'autorité. Sur le plan aérodynamique, le décrochage se définit comme la réduction de la portance subie par l'aéronef lorsque son angle d'attaque augmente et ce, du fait du décollement du flux d'air sur la surface supérieure de l'aile. On appelle cela le décrochage statique. Dans le cas d'un écoulement non régulier, lorsque le profil aérodynamique change rapidement d'angle d'attaque par exemple, l'écoulement reste attaché au profil aérodynamique à un angle d'attaque plus élevé que ce qui était le cas en conditions stationnaires. Le décrochage semble retardé et on parle alors de décrochage dynamique. Ce même phénomène est présent au retour lorsque l'aéronef pique en piqué, où le flux se rattache à un angle d'attaque plus faible qu'en régime permanent, formant une boucle d'hystérésis. Les solutions de lois de commande

1. <https://web.mit.edu/drela/Public/web/aswing/>

intégrées à bord des drones, qu'ils soient à voilure fixe ou à voilure tournant, ont pour la plupart été synthétisés à partir de modèles dit cinématiques, dans lesquels le principe fondamental de la dynamique est appliqué à un corps en mouvement sans se préoccuper de la cause de celui-ci. Bien que cette catégorie de modélisation ait largement contribué à l'impressionnant essor de la robotique aérienne ces 10-15 dernières années, elle n'apparaît bien adaptée qu'aux drones à voilure tournante ou à ailes fixes pour de faibles angles d'attaque mais pas ou peu aux situations de **décrochages statiques** et **dynamiques** pour lesquelles les phénomènes aérodynamiques doivent être représentés de façon plus détaillée. La construction et l'analyse d'un modèle aérodynamique spécifique le plus représentatif possible de la réalité sont donc centrales dans l'élaboration des fonctionnalités de reprise au décrochage d'un drone. Nous nous concentrerons dans cette partie sur l'étude d'un modèle d'avion à ailes rigides. Ce modèle sera par la suite exploité pour être analysé tant d'un point de vue de sa stabilité en boucle ouverte que dans l'élaboration de n'importe quel type de synthèse de loi de commande avancée dédié à la reprise au décrochage.

Une solution d'identification plutôt intuitive proposée dans le cadre de la thèse de TORBJOERN CUNIS consiste à utiliser des **fonctions polynomiales par morceaux** pour représenter avec précision les parties pré et post-décrochage du modèle aérodynamique de vol. Les polynômes sont déterminés à partir d'une régression obtenue par minimisation d'un critère de type moindre carré autour de k données de référence ; le modèle complet est ensuite obtenu en mettant bout à bout les polynômes à travers une fonction logistique qui assure la continuité de l'ensemble. L'avantage d'utiliser cette technique de modélisation par polynôme est double : d'une part, le partitionnement des fonctions polynomiales est effectué grâce à une ou plusieurs valeurs de coupures qui ont un sens physique, ici l'angle d'incidence au décrochage ; et d'autre part, il est possible d'appliquer différentes techniques numériques dédiées aux représentations par polynômes telles que la **programmation semi-définie** (technique des **Sum of Squares** (SoS)) ou bien l'analyse des bifurcations pour en déduire différentes **régions de stabilités** et origines des phénomènes. Les travaux publiés dans [Conf 3] et [Conf 4] fournissent un ensemble complet de résultats sur les performances de la méthode d'identification par polynômes et l'analyse des stabilités appliquée à un modèle générique d'avion de transport (GTM) et un modèle longitudinal de mini-drone obtenu par simulations numériques (CFD). A travers ces deux exemples, résumés dans [Revue 3]* et [Revue 4], nous avons montré la possibilité de transposer les méthodes d'analyse par SoS et bifurcations à un ensemble de polynômes par morceaux et d'en déduire des domaines de stabilité bien moins conservatifs que si l'analyse avait été faite à travers la construction d'un seul polynôme. Ce résultat majeur étend donc le domaine d'application des méthodes par SoS et bifurcations à une classe de système dit « hybride ». De ce premier galop d'essais visant à valider les outils méthodologiques, nous nous sommes focalisés sur la synthèse d'un correcteur permettant à l'engin de sortir d'un décrochage de manière sûre et robuste. Pour ce faire, l'état de l'art du domaine nous apprend que les techniques par Sum of Square permettent non seulement d'analyser la stabilité *a priori* des systèmes nonlinéaires mais qu'elles peuvent également être intégrées dans n'importe quelle

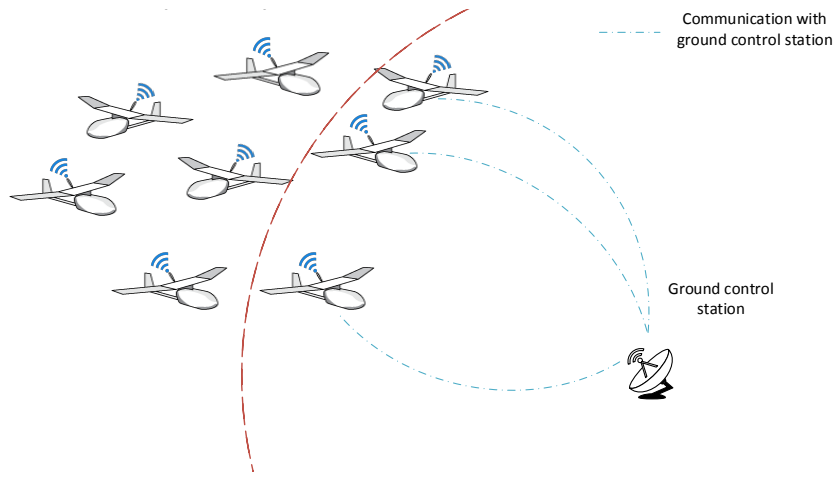
synthèse de loi de commande dans le but de trouver un contrôleur stabilisant le système sur la plus grande plage de variation de paramètres de vol, y compris ceux liés aux conditions de décrochage. Ainsi, en adaptant cette technique dans [Conf 20] aux modèles polynomiaux par morceaux représentatifs d'un mini-drone à ailes fixes, différentes lois de commande linéaires (LQR), polynomiales et prédictives (MPC, NMPC et e-MPC) ont été comparées en terme de performances et de temps de calcul pour un décrochage dit profond (en anglais Deep-Stall). De ces trois approches, la commande prédictive s'est avérée être la plus performante notamment en terme de temps de calcul pour synthétiser le correcteur mais aussi dans le cas d'une dynamique fortement non linéaire et qui plus est soumise à des contraintes d'état (perte d'altitudes, vitesse des gouvernes de profondeurs) indispensables à la reprise au décrochage. Ce faisant, nous avons reformulé dans [Conf 20] une synthèse de loi de commande prédictive qui minimise la perte d'altitude avec l'ajout d'une étape d'estimation de la région d'attraction afin de garantir que les gains calculés assurent la stabilité du système vers l'état final. D'autres résultats sont présentés notamment pour la reprise d'un décrochage en spirale (Steep spiral). Jusqu'à présent, l'ensemble des résultats ont permis d'adresser la problématique du décrochage pour des modèles aérodynamiques identifiés en régime statique. Pour traiter proprement le cas des phénomènes **dynamiques du décrochage**, la structure du modèle doit évoluer pour prendre en compte la **boucle hystérésis**. Celle-ci doit être identifiée par des tests menés en soufflerie sur une maquette de l'engin. Dériver un tel modèle n'est pas une chose aisée, d'autant plus lorsque celui-ci se doit de représenter des effets instationnaires au-delà de l'enveloppe de vol nominale. De premières études en soufflerie ont été menées tout récemment dans le cadre de la thèse de VINCENT GUIBERT pour identifier le plus précisément possible les coefficients aérodynamiques d'une aile fixe. De ce fait, il a donc été nécessaire de retravailler la structure du modèle dans [Conf 21], notamment en ajoutant des jonctions dans la technique des moindres carrés sous contraintes, afin que celui-ci soit le plus représentatif possible des phénomènes observés. Bien évidemment, tous les outils développés en première étape pourront être appliqués à ces récents travaux dans le but d'obtenir des lois de commandes les plus performantes et robustes possible.

5.2.1.3 Détection d'une cyber-intrusion dans un réseau de communication

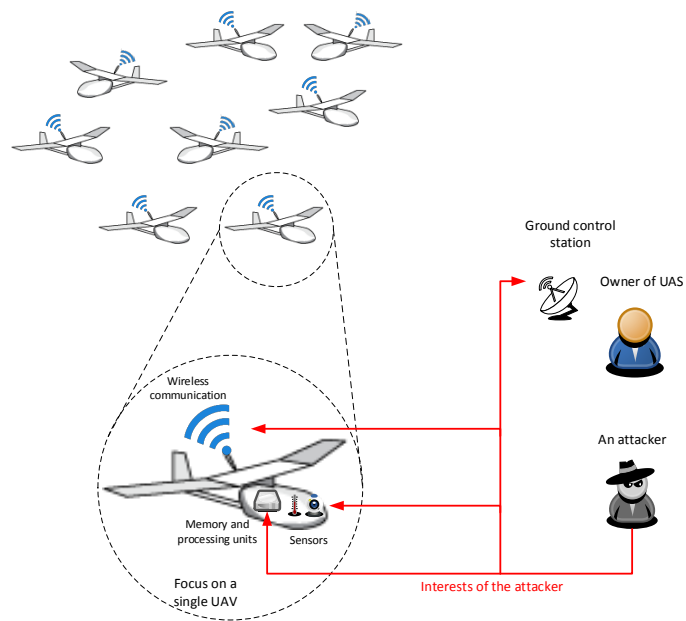
L'élaboration de ce dernier système plus sûr et robuste par construction nous a permis d'adapter des techniques d'estimation et de traitement du signal pour répondre à la problématique de la sécurisation des flux de communications entre drones. Grâce à l'utilisation de drones dotés de capacités de communication suffisantes, des scénarios d'intervention ont pu être complètement repensés en utilisant une flotte coordonnée de drones basée sur une architecture de communication complexe dite « Ad hoc ». Dans cette architecture, chaque drone est vu comme un maillon actif d'un réseau de communication, soit émetteur, routeur ou destinataire d'une information cruciale pour la mission (coordonnées GPS, vidéo,...). Déployer une telle architecture au sein d'une flotte de drone présente de nombreux intérêts : couvrir une zone géographique large, utiliser la flotte en milieu urbain ou encore garantir la redondance

des informations. A l'inverse, l'utilisation d'une flotte de drone présente de nombreux points d'entrées pour d'éventuelles intrusions malveillantes : les liens de communication sol/bord, les charges utiles du drone ou encore la station sol de contrôle (Figure 5.3). La manière traditionnelle de gérer l'intrusion dans un réseau de communication qu'il soit fixe ou mobile, consiste à utiliser des systèmes de détection d'intrusion (IDS). Cet outil logiciel permet d'écouter le trafic de façon non-intrusive dans un réseau de communication dans le but de détecter des activités anormales qui pourraient être assimilées à des cyber-attaques. Malgré de nombreuses technologies disponibles sur le marché, la plupart d'entre elles sont peu ou pas adaptées aux structures de communication entre drones dans lesquels les attaques peuvent se propager facilement. Nous pensons ici à des attaques par injection de fausse information dans la trajectoire des drones (en anglais spoofing) ou bien à des attaques par dénis de service (DoS) qui visent à saturer les données du réseau de communication, rendant ainsi inopérant le contrôle de la flotte (en anglais flooding). Une solution originale de détection/reconstruction d'attaques utilisant à la fois des techniques issues de l'automatique et du traitement du signal a été proposée pour la première fois dans le cadre de la thèse de RUOHAO ZHANG [Conf 11]. Ce travail s'est tout d'abord concentré sur l'élaboration d'un **contrôleur-observateur** permettant de reconstituer les paquets d'une attaque de type DoS à travers la modélisation d'un réseau de communication TCP (Transmission Control Protocol). Le principe consiste à exploiter le modèle dynamique du réseau de communication TPC, notamment celui de la file d'attente des paquets, pour reconstruire tous les flux d'informations qui circulent dans le réseau, y compris les flux entrants qui peuvent être perçus comme malveillants. La robustesse de l'observateur par rapport aux différents retards inhérents au système a été prouvée grâce à l'utilisation de fonctionnelle dite de LYAPUNOV KRASOVKII. Par la suite, cette solution a été complétée avec une technique de **détection** de l'anomalie par **analyse multifractale** afin de déclencher la reconstruction du signal au moment où apparaît l'attaque. L'analyse multifractale par ondelette² fournit un **spectre temporel** des **moments d'un signal aléatoire** qui peut être considéré comme la signature unique d'un signal. En comparant le spectre d'un signal normal et d'un signal infecté, il est donc possible de détecter la présence d'une intrusion malveillante. Cette information a été utilisée pour la première fois dans [Conf 11] afin d'identifier des anomalies provoquées par une attaque DoS. Un ensemble complet de résultats caractérisant les performances de la détection et de la reconstruction a ensuite été présenté dans [Revue 5]. Suite à cela, nous nous sommes focalisés sur des attaques plus élaborées comme de l'usurpation d'identité (en anglais Man in the Middle (MITM)). L'intrus peut infliger des messages malveillants au sein du réseau, usurper le contrôle du réseau ou un noeud individuel et dévier les trajectoires des drones. En hybridant l'analyse multifractale par ondelette avec des techniques d'intelligence artificielle, nous avons proposé dans [Revue 7]* une nouvelle méthode de détection d'intrusion efficace contre des attaques sur les coordonnées géographiques de drones.

2. l'algorithme WLM (Wavelet Leader Multifractal) voir : <https://hal-ens-lyon.archives-ouvertes.fr/ensl-00195088/document>



(a) Topologie d'une flotte de drones.



(b) Les différents points d'entrées pour une intrusion malveillante.

FIGURE 5.3 – Description des vulnérabilités des communications dans une flotte de drones.

5.2.2 Estimation, filtrage invariant pour la navigation inertielle

Le développement de systèmes avioniques plus sûrs et robustes par construction dans le domaine de la robotique aérienne a favorisé l'essor de nouvelles techniques d'estimation dites « invariantes » sur lesquelles nous avons largement contribué sur le plan méthodologique pour améliorer la navigation inertielle d'un drone [Conf 9]*,[Conf 10],[Conf 13],[Conf 14],[Conf 15],[Revue 6]. De nombreux travaux de recherche sur les observateurs invariants non linéaires ont été menés durant ces dix dernières années notamment par P. Rouchon, S. Bonnabel et E. Salaun dont les résultats ont permis d'élaborer une méthode constructive utilisant conjointement la géométrie différentielle et la théorie des groupes pour synthétiser des filtres non linéaires dédiés aux problèmes d'estimation non linéaire de l'état d'un système. La conception d'un tel filtre est caractérisée principalement par une redéfinition classique de l'erreur d'estimation d'état utilisée traditionnellement dans les méthodes de conception d'observateur ou filtre non linéaire. Ainsi, les nombreux résultats obtenus par Bonnabel (Bonnabel [2007], Bonnabel et al. [2008], Bonnabel et al. [2009], Bonnabel et al. [2009]) ont permis de proposer une théorie des observateurs et **filtres invariants** pour une classe importante de **systèmes qui présentent des symétries** (par exemple des transformations galiléennes). En particulier, l'erreur invariante d'estimation est utilisée dans le schéma récursif du filtre de Kalman étendu (EKF) pour élargir *a priori* son domaine de convergence : *Désormais, la linéarisation ne se fera plus autour d'un point d'équilibre mais autour de l'élément neutre d'un groupe, ce qui permet d'élargir le domaine de convergence de l'estimation et d'avoir une forme simplifiée de la dynamique de l'erreur d'estimation sur l'état.*

A l'instar des travaux menés autour de l'IEKF (Invariant Extended Kalman Filter), les gains de correction de cet estimateur, construit pour être invariant, peuvent être obtenus en suivant les étapes de calcul propres au **filtrage de type UKF** (Uncented Kalman Filter). Toutefois, l'intégration à la théorie des observateurs d'une procédure de calcul des gains de correction qui suit un schéma algorithmique emprunté au filtrage de Kalman dit *unscented*, nécessite un certain nombre de développements méthodologiques. Ces travaux de recherche ont conduit *in fine* à la mise au point de deux variantes algorithmiques de l'UKF baptisées π -IUKF (Invariant Unscented Kalman Filter) publié dans [Conf 13] , utilisant une condition de compatibilité π et **IUKF** publié dans [Conf 9]* , sans condition de compatibilité. Tout comme pour l'IEKF, l'IUKF a cherché à conférer à l'estimateur les mêmes propriétés d'invariance que celles qui peuvent caractériser le système observé. De tous les résultats accumulés jusqu'à présent, il ressort que le filtrage de Kalman invariant que nous avons introduit, à l'instar des observateurs invariants déjà existants dans la littérature, l'IUKF et le π -IUKF permettent de caractériser avec précision l'incertitude sur l'état estimé pour certaine trajectoire dite permanente. La relative constance de celle-ci en fait une information potentiellement très utile à exploiter dans le cadre d'autres problématiques (commande robuste, FDIR, etc.).

5.3 Apports méthodologiques et techniques en estimation

Comme nous avons pu le voir apparaître en filigrane des différents systèmes étudiés, la conception d'une chaîne avionique de contrôle du mini-drone performante ne nécessite pas seulement de disposer de lois de commande qui le sont elles-mêmes mais également d'algorithmes d'estimation qui pré-traitent efficacement les données issues directement des capteurs, voire même qui essaient de reconstruire des paramètres inconnus ou bien qui fournissent des informations diverses et variées sur la dynamique du système étudié. Cela nous a naturellement conduit vers des apports méthodologiques et techniques originaux en estimation pour améliorer la performance et la robustesse du contrôle des systèmes étudiés dans ce manuscrit. Dans ce qui suit, nous allons donc présenter **deux apports méthodologiques** sur l'estimation d'état dite « invariante » et sur l'estimation, au sens analyse, des régions de stabilité des systèmes hybrides ainsi que **deux études techniques** menées sur l'estimation de paramètres pour la commande dite « sans modèle » et la détection de cyber-intrusions par analyse multifractale. Les conclusions et prospectives de ces contributions seront présentées dans la dernière section de ce manuscrit.

5.3.1 Sur l'estimation d'état des systèmes nonlinéaires invariants

Nous présentons ici le fil conducteur des principaux travaux de recherche que nous avons menés autour de la synthèse du filtre de Kalman Unscented Invariant : l'IUKF.

Considérons la représentation d'état non linéaire suivante définie par :

$$\dot{\mathbf{x}} = f(\mathbf{x}, \mathbf{u}), \quad \mathbf{y} = h(\mathbf{x}, \mathbf{u}) \quad (5.1)$$

Dans l'équation (5.1) \mathbf{x} désigne l'état du système, \mathbf{y} ses sorties, supposées mesurables, et \mathbf{u} un ensemble d'entrées connues. le vecteur d'état \mathbf{x} (resp. d'entrée \mathbf{u}) (resp. de sortie \mathbf{y}) appartient à un ensemble ouvert $\mathcal{X} \in \mathbb{R}^n$ (resp. $\mathcal{U} \in \mathbb{R}^m$) (resp. $\mathcal{Y} \in \mathbb{R}^p, p \leq n$). Etant donné cette représentation d'état non linéaire, nous pouvons définir de manière très générale un estimateur de (5.1) qui produit à tout instant t une estimation $\hat{\mathbf{x}}(t)$ qui tend vers $\mathbf{x}(t)$ à partir des signaux connus $\{\mathbf{y}(\tau), \mathbf{u}(\tau); 0 \leq \tau \leq t\}$, à savoir un système dynamique de la forme :

$$\dot{\hat{\mathbf{x}}} = f(\hat{\mathbf{x}}, \mathbf{u}) + g(\hat{\mathbf{x}}, \mathbf{u}, \mathbf{y}, \mathbf{P}) \quad (5.2)$$

$$\dot{\mathbf{P}} = G(\hat{\mathbf{x}}, \mathbf{u}, \mathbf{y}, \mathbf{P}) \quad (5.3)$$

où $g(\hat{\mathbf{x}}, \mathbf{u}, h(\hat{\mathbf{x}}, \mathbf{u}), \mathbf{P}) = 0$ pour tout $\hat{\mathbf{x}}, \mathbf{u}, \mathbf{P}$ (pas de correction si l'erreur de sortie $\mathbf{y} - h(\hat{\mathbf{x}}, \mathbf{u}) = 0$) et $\hat{\mathbf{x}} \rightarrow \mathbf{x}$ quand $t \rightarrow +\infty$ (observateur asymptotique). Un estimateur apparaît ainsi comme la copie du système dynamique de (5.1) modifié par le terme correctif $g(\hat{\mathbf{x}}, \mathbf{u}, \mathbf{y}, \mathbf{P})$ qui dépend d'un vecteur de paramètres \mathbf{P} . On dira que l'estimateur est à gains constants quand \mathbf{P} est constant ($\dot{\mathbf{P}} = 0$). Ainsi, un estimateur peut-être vu comme un « filtre » linéaire ou non-linéaire dans le sens où l'estimation fournie est le résultat d'une intégration, ce qui a pour effet bénéfique de lisser les bruits qui entachent inévitablement les signaux réels.

D'un point de vue mathématique, le problème de la convergence d'un observateur (ou estimateur) est largement ouvert : étant donné un système quelconque (5.1), on ne sait de manière générale pas construire d'observateur globalement convergent, ni même seulement localement convergent autour de toute trajectoire tel que $\hat{\mathbf{x}}(t) \rightarrow \mathbf{x}(t)$ pour toute condition initiale $(\mathbf{x}_0, \mathbf{u}_0, \hat{\mathbf{x}}_0 \approx \mathbf{x}_0, \mathbf{P}_0)$. On sait par contre toujours construire un observateur qui converge localement autour de tout point d'équilibre tel que $\hat{\mathbf{x}}(t) \rightarrow \mathbf{x}(t)$ pour toute condition initiale $(\mathbf{x}_0, \mathbf{u}_0, \hat{\mathbf{x}}_0, \mathbf{P}_0) \approx (\bar{\mathbf{x}}, \bar{\mathbf{u}}, \bar{\mathbf{x}}, \bar{\mathbf{P}})$ où $(\bar{\mathbf{x}}, \bar{\mathbf{u}}, \bar{\mathbf{P}})$ vérifie $f(\bar{\mathbf{x}}, \bar{\mathbf{u}}) = 0$ et $G(\bar{\mathbf{x}}, \bar{\mathbf{u}}, h(\bar{\mathbf{x}}, \bar{\mathbf{u}}), \bar{\mathbf{P}}) = 0$; ainsi on se ramène par approximation au cas linéaire pour lequel le problème est facilement résolu.

5.3.1.1 La construction d'un estimateur invariant

Afin d'obtenir de meilleures garanties de performances et de convergence de l'estimation de l'état nonlinéaire, nous nous sommes focalisés dans [Conf 9] sur une approche d'estimation géométrique dédiée à une certaine classe de systèmes possédant des symétries. Plutôt que d'utiliser des erreurs linéaires de sortie notée $y - h(\hat{\mathbf{x}}, \mathbf{u})$ et d'état notée $\hat{\mathbf{x}} - \mathbf{x}$, il s'agit ici d'utiliser l'invariance du système vis-à-vis de certaines transformations géométriques (rotations, translations, etc.) pour construire un estimateur dit invariant de la forme suivante.

$$\dot{\hat{\mathbf{x}}} = f(\hat{\mathbf{x}}, \mathbf{u}) + \sum_{i=1}^n \mathbf{K}_i(I(\hat{\mathbf{x}}, \mathbf{u}), \mathbf{E}) \cdot w_i(\hat{\mathbf{x}}) \quad (5.4)$$

où le gain matriciel \mathbf{K}_i dépend de la trajectoire du système seulement au travers de l'ensemble complet d'invariant connu $I(\hat{\mathbf{x}}, \mathbf{u})$ et $\mathbf{E}(\mathbf{y}, \hat{\mathbf{x}}, \hat{\mathbf{y}}) = \rho_{\hat{\mathbf{x}}^{-1}}(\hat{\mathbf{y}}) - \rho_{\hat{\mathbf{x}}^{-1}}(\mathbf{y})$ est une erreur invariante de sortie de dimension p . $w_i(\hat{\mathbf{x}})$ est un vecteur invariant qui projette l'ensemble des termes de correction invariants sur chaque composante de l'équation d'évolution $f(\hat{\mathbf{x}}, \mathbf{u})$, c'est-à-dire l'espace tangent. Les propriétés de convergence de l'équation (5.4) dépendent des gains \mathbf{K}_i et de la façon dont l'erreur d'estimation sur l'état est définie. En effet, la théorie des observateurs invariants définit une erreur d'estimation invariante sur l'état du système notée $\eta(\mathbf{x}, \hat{\mathbf{x}}) = \mathbf{x}^{-1}\hat{\mathbf{x}}$. Ainsi, le principal résultat à retenir de (Bonnabel et al. [2008]) est que si l'on sait trouver un groupe de transformation sur l'état, l'entrée et la sortie tels que $(\varphi_g(\mathbf{x}), \psi_g(\mathbf{u}), \rho_g(\mathbf{y})) = (\mathbf{X}, \mathbf{U}, \mathbf{Y})$ où $(\varphi_g, \psi_g, \rho_g)$ sont trois difféomorphismes paramétrisés par $g \in G^3$, qui laissent l'entière dynamique du système inchangée, c'est à dire $\dot{\mathbf{X}} = f(\mathbf{X}, \mathbf{U})$ et $\mathbf{Y} = h(\mathbf{X}, \mathbf{U})$, alors la convergence asymptotique de $\hat{\mathbf{x}}$ vers \mathbf{x} est équivalente à la stabilité de la dynamique de l'erreur d'état invariante qui est régie par l'équation très générale suivante :

$$\dot{\eta} = \Upsilon(\eta, I(\hat{\mathbf{x}}, \mathbf{u})) \quad (5.5)$$

où Υ est une fonction lisse (de classe \mathcal{C}^∞). Dans (5.5), il apparaît que η dépend de la trajectoire du système seulement au travers des invariants connus $I(\hat{\mathbf{x}}, \mathbf{u})$. *Cette dynamique dépend des*

3. G est un groupe de Lie qui vérifie $\dim(G) = \dim(\mathcal{X}) = n$, nous identifions G à l'espace d'état $\mathcal{X} = \mathbb{R}^n$ de sorte que la transformation locale φ_g puisse être assimilée à une multiplication à gauche telle que $\varphi_g(\mathbf{x}) = g \cdot \mathbf{x}$. Ainsi, nous considérerons dans la suite le cas particulier $\varphi_g(\mathbf{x}) = g \cdot \mathbf{x} = e$, où e désigne l'élément neutre du groupe G et $g = \mathbf{x}^{-1} = \gamma(\mathbf{x})$ qui est déduit de la méthode du repère mobile de Cartan.

trajectoires estimées par le système uniquement au travers de la non-linéarité I.

Il s'agit là d'une grande différence par rapport à la plupart des algorithmes d'estimation non linéaires conventionnels tels que l'EKF ou l'UKF pour lesquels la dynamique de l'erreur d'estimation dépend directement de la trajectoire suivie par l'engin. Ceci étend donc le domaine de convergence des observateurs invariants et en fait des estimateurs plus robustes. Ainsi, pour un système dynamique qui suit une trajectoire de référence quasi-permanente, i.e. tels que les invariants fondamentaux $I(\hat{\mathbf{x}}, \mathbf{u})$ ne dépendent pas du temps, $I(\hat{\mathbf{x}}, \mathbf{u}) = c$, il peut être démontré que les matrices de gain $\bar{\mathbf{K}}$ convergent vers des valeurs fixes pour toutes trajectoires \mathbf{x}' telles que $I(\mathbf{x}', \mathbf{u}) = c$. Par la suite, il peut être démontré que, pour certain système comme le système de l'AHRS (Attitude and Heading Reference System), et sous certaines conditions de découplage de l'estimation des composantes du vecteur d'état \mathbf{x} , la dynamique de l'erreur d'estimation sur l'état invariante $\eta(\mathbf{x}, \hat{\mathbf{x}})$ obéit à une équation dite *autonome* c'est-à-dire de la forme : $\dot{\eta} = \Upsilon(\eta, c)$. Un tel filtre sera caractérisé par un large domaine de convergence pour différents réglages des valeurs des gains.

Pour pallier à la difficulté de régler les gains de correction manuellement, l'état de l'art du domaine rapporte qu'un algorithme de type EKF, généralisé, a été développé dans (Barrau et al. [2015]) pour obtenir ces derniers. Un exemple de mise en oeuvre a été introduit dans (Barczyk et al. [2015]). Celui-ci repose sur une linéarisation de la dynamique de l'erreur d'estimation sur l'état invariante qui permet d'identifier des matrices d'évolution ($\mathbf{A}(\hat{I})$) et d'observation ($\mathbf{C}(\hat{I})$) dépendantes des invariants du problème d'estimation. Par la suite, les équations du filtrage de Kalman étendu peuvent être appliquées au système des erreurs invariantes linéarisées de sorte que la résolution de l'équation de Riccati soit menée avec le couple ($\mathbf{A}(\hat{I}), \mathbf{C}(\hat{I})$). La démarche suivie dans l'IEKF revient à formuler mathématiquement un EKF classique mais pour une erreur d'estimation sur l'état invariante. L'IEKF fournit une approximation, au 2nd ordre, de l'erreur d'estimation sur l'état invariante. Malgré ses nombreux avantages, cette technique peut être relativement complexe à exploiter du fait de la linéarisation qu'elle nécessite pour identifier les matrices $\mathbf{A}(\hat{I})$ et $\mathbf{C}(\hat{I})$.

Afin de s'affranchir de ce point difficile, nos recherches ont conduit au développement d'une méthode différente pour l'estimation de l'état des systèmes dynamiques dans un cadre non linéaire. Tout comme pour l'IEKF, l'IUKF a cherché à conférer à l'estimateur les mêmes propriétés d'invariance que celles qui peuvent caractériser le système observé.

5.3.1.2 La formulation invariante du filtre de Kalman Unscented : l'IUKF

Nous proposons donc une modification de l'UKF classique (Julier [2002]), pour des systèmes dynamiques possédant des symétries. Le filtrage de type UKF présente l'avantage de calculer une solution approchée au problème d'estimation non linéaire optimal de l'état d'un système dynamique, en temps discret, sans recourir à une quelconque linéarisation d'équations différentielles. La technique dénommée « approche par sigma point » (en anglais, Sigma Point Approach - SPA) est habituellement utilisée pour déterminer l'approximation du processus

aléatoire gaussien $\mathbf{x}_{k|k}$, au cours du temps, sur lequel sont appliquées des transformations non linéaires telles que :

$$\begin{cases} \mathbf{x}_k \sim \mathcal{N}(\hat{\mathbf{x}}_{k|k}, \mathbf{P}_{k|k}) & \text{tel que : } \mathbf{x}_{k+1} = f(\mathbf{x}_k, k) + \mathbf{w}_k \\ \mathbf{y}_k = h(\mathbf{x}_k, k) + \mathbf{v}_k \end{cases} \quad (5.6)$$

où $\mathbf{x} \in \mathbb{R}^n$, $\mathbf{y} \in \mathbb{R}^p$ et \mathbf{w} , \mathbf{v} sont des bruits blancs gaussiens. Rappelons que le but de la technique SPA est de définir, au cours du temps, un nombre fini de sigma points $\mathcal{X}_{k|k}$ qui capturent la vraie moyenne $\hat{\mathbf{x}}_{k|k}$ et la vraie covariance $\mathbf{P}_{k|k}$ de la distribution de probabilité caractérisant $\mathbf{x}_{k|k}$. Dans le cas gaussien, cet ensemble de points doit représenter précisément les deux premiers moments de la variable aléatoire. Ces sigma points sont ensuite propagés à travers les fonctions non linéaires f et h , apparaissant dans l'équation (5.6). Cette propagation fournit un nuage de points modifiés par rapport à la répartition initiale des sigma points. La moyenne $\hat{\mathbf{x}}_{k+1|k}$ et la covariance $\mathbf{P}_{k+1|k}$ estimées associées aux points transformés sont ensuite calculées par rapport à la statistique de ce nouvel ensemble de points. L'UKF peut être considéré comme une simple extension de la technique SPA qui permet donc de calculer les approximations du problème d'estimation dans le cas où :

$$\mathbf{x}_{k+1} = f(\mathbf{x}_k, \mathbf{u}_k) + \mathbf{w}_k \quad (5.7)$$

$$\mathbf{y}_k = h(\mathbf{x}_k, \mathbf{u}_k) + \mathbf{v}_k \quad (5.8)$$

Comme cela est présenté dans (Barrau et al. [2015]), nous considérerons que les bruits d'évolution et d'observation (\mathbf{w} et \mathbf{v}) entrent dans le système de façon invariante. Ces bruits peuvent être considérés comme des entrées exogènes qui ne remettent pas en cause l'existence même de symétries propres au système. Afin donc de préserver celles-ci, leur insertion respective dans les équations d'évolution et d'observation du système se fait au travers de termes G -invariant/équivalent.

Lorsque la dynamique du système observé présente des propriétés d'invariance par symétries, les équations de base du SRUKF ne permettent pas de synthétiser un estimateur de l'état du système disposant de propriétés analogues. Pourtant, du point de vue de la convergence, il peut être très intéressant de chercher à conférer à tout filtre estimateur candidat les propriétés d'invariance du système, à l'instar de ce qui est fait pour les observateurs invariants et l'IEKF. Ainsi, nous avons modifié l'algorithme SRUKF afin que cela soit le cas également. A partir des principes mis en œuvre et des multiples étapes de calcul qui fondent l'algorithme du SRUKF, une réécriture naturelle des équations, visant à adapter la méthode à un cadre invariant pour l'estimation, peut être obtenue simplement en redéfinissant les termes d'erreur utilisés dans la version standard présentée au cours de la section précédente. En effet, les termes d'erreur linéaires $\hat{\mathbf{x}} - \mathbf{x}$ et $\mathbf{y} - \hat{\mathbf{y}}$, classiquement rencontrés en filtrage de Kalman, ne préservent en rien les symétries et les invariances du système.

Ainsi, nous considérerons les erreurs d'état et de sortie invariantes suivantes :

$$\begin{cases} \eta(\mathbf{x}, \hat{\mathbf{x}}) = \varphi_{\mathbf{x}^{-1}}(\mathbf{x}) - \varphi_{\mathbf{x}^{-1}}(\hat{\mathbf{x}}) = \mathbf{x}^{-1} \cdot \hat{\mathbf{x}} \\ \mathbf{E}(\mathbf{y}, \hat{\mathbf{x}}, \hat{\mathbf{y}}) = \rho_{\hat{\mathbf{x}}^{-1}}(\hat{\mathbf{y}}) - \rho_{\hat{\mathbf{x}}^{-1}}(\mathbf{y}) \end{cases} \quad (5.9)$$

Dès lors, la notion de matrice de covariance des erreurs d'estimation utilisée jusqu'à maintenant en continu, dont le calcul dans l'algorithme du SRUKF peut être approché à partir de la donnée des $(2n + 1)$ sigma points $\mathcal{X}_{k|k}^{(i)}$, $i \in \llbracket 1; (2n + 1) \rrbracket$, construits à chaque pas de temps $k \in \mathbb{Z}^*$, se trouve désormais modifiée pour être associée aux erreurs définies par l'équation (5.9). Nous parlerons alors de matrice de covariance des erreurs d'estimation invariantes. L'étape de décomposition de la matrice de covariance associée à l'erreur d'estimation sur l'état fait donc apparaître un ensemble de $(2n + 1)$ erreurs invariantes calculées entre chaque sigma point et l'état prédit. La notion de covariance porte donc désormais sur l'erreur d'état invariante et non plus sur un terme d'erreur linéaire. Il s'agit de la principale nuance introduite avec le filtrage de Kalman *unscented* classique. Hormis cette modification majeure, l'étape de prédiction n'est que peu modifiée par rapport à sa version originale.

Pour ce qui est de l'étape de correction, nous voyons que les modifications apportées à la version standard du SRUKF sont plus nombreuses. En effet, la redéfinition de la notion de matrice de covariance, associant celle-ci à des erreurs d'estimation désormais invariantes, modifie :

- ① le calcul de la covariance prédite relative à la sortie \mathbf{y} tel que :

$$\mathbf{P}_{\mathbf{y}, k+1|k} \propto \mathbf{E}(\hat{\mathbf{y}}_{k+1|k}, \mathcal{X}_{k+1|k}, \hat{\mathbf{Y}}_{k+1|k})$$

- ② et le calcul de la covariance croisée prédite entre les erreurs d'estimation portant sur l'état \mathbf{x} et la sortie \mathbf{y} tel que :

$$\mathbf{P}_{\mathbf{xy}, k+1|k} \propto \eta(\mathcal{X}_{k+1|k}, \hat{\mathbf{x}}_{k+1|k}), \mathbf{E}(\hat{\mathbf{y}}_{k+1|k}, \mathcal{X}_{k+1|k}, \hat{\mathbf{Y}}_{k+1|k})$$

Il s'ensuit naturellement que le gain de correction calculé pour l'estimation de l'état par une technique de type UKF dépendra, par transitivité, d'invariants fondamentaux pour le système considéré ($\psi_{\mathbf{x}^{-1}}(u)$) et d'erreurs de sortie invariantes ($\mathbf{E}(\hat{\mathbf{y}}, \mathbf{x}, \cdot)$). Le cadre invariant défini pour le système considéré entraîne également une réécriture des équations de correction de l'état prédit. En effet, il apparaît que le terme de correction additif repose dorénavant sur : un gain qui dépend des invariants du problème d'estimation ; une innovation invariante. De plus, ce terme correctif se retrouve projeté dans le repère invariant, de sorte que, la correction de l'état prédit soit réalisée, composante par composante, i.e. selon les directions des n vecteurs de la base canonique de \mathbb{R}^n formée par le champ de vecteurs invariants $\mathcal{B}(\hat{\mathbf{x}}_{k+1|k}) = \{\omega_i(\hat{\mathbf{x}}_{k+1|k})\}_{i \in \llbracket 1; n \rrbracket}$.

Exemple révélateur de l'erreur de sortie invariante Le concept d'erreur de sortie invariante est une idée clé dans la construction de tout filtre invariant. Nous mettrons donc en avant cette propriété en comparant l'UKF et l'IUKF sur un système appelé inclinomètre ou en

anglais tilt sensor system. Ce système, comme son nom l'indique, permet de mesurer l'inclinaison de tout objet disposant d'un capteur mesurant l'accélération de celui-ci. D'autres systèmes sur lesquels nous avons contribué dans **[Conf 2]***, plus complexes, comme un AHRS (Attitude and Heading Reference System), seraient en mesure de réaliser la même opération mais ne nous permettraient pas de mettre en exergue les différentes propriétés intrinsèques de l'IUKF. Par ailleurs, le modèle d'observation de l'inclinomètre mérite que l'on s'y attache puisqu'il est communément utilisé dans de nombreux domaines : communication, radars, optométrie, etc. Enfin, cet exemple nous permettra d'étudier la non linéarité du modèle uniquement sur l'équation d'observation. Comme nous le verrons par la suite, l'erreur de sortie usuelle (i.e. linéaire), calculée à partir de cette équation, ne préserve pas la géométrie du système.

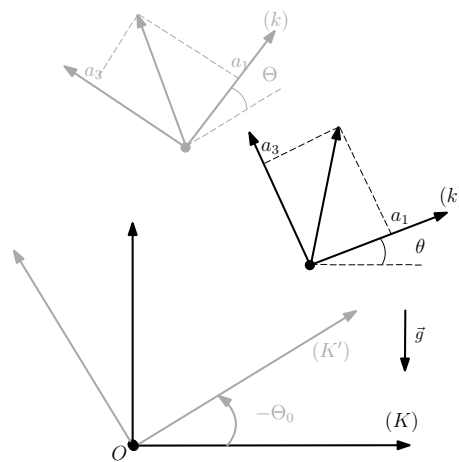


FIGURE 5.4 – La dynamique de l'inclinomètre est invariante sous l'action du groupe $SO(2)$.

Ainsi, pour estimer l'angle d'attitude d'un objet, il nous sera nécessaire de disposer de trois accéléromètres donnant une mesure de l'accélération spécifique de l'objet notée $a_m = (a_1, a_2, a_3)$. Nous considérons ici plus particulièrement l'estimation de l'angle θ , qui décrit la rotation de l'objet dans le plan vertical comme le montre la Figure 5.4. En suivant la méthode de construction des filtres invariants décrite dans (Bonnabel et al. [2009]), l'équation du filtre invariant s'écrira :

$$\dot{\hat{\theta}} = 0 + \bar{\mathbf{K}} \begin{pmatrix} \cos \hat{\theta} & \sin \hat{\theta} \\ -\sin \hat{\theta} & \cos \hat{\theta} \end{pmatrix} \begin{pmatrix} \hat{y}_{a_1} - y_{a_1} \\ \hat{y}_{a_3} - y_{a_3} \end{pmatrix} \quad (5.10)$$

où $\bar{\mathbf{K}}$ est une matrice de gains 1×2 . Comme tout modèle utilisé par l'algorithme IUKF, celui-ci doit être exprimé en temps discret, soit à l'aide d'un schéma d'intégration numérique de type Runge-Kutta ou bien à partir de l'exponentielle matricielle des équations du modèle dynamique. Par ailleurs, afin d'obtenir un résultat le plus réaliste possible, nous supposons que les accéléromètres dont nous disposons pour la conception d'un inclinomètre ont des performances limitées et présentent donc des imperfections. Nous représentons donc les mesures fournies par les accéléromètres comme la somme d'un signal déterministe et d'un bruit blanc Gaussien de covariance \mathbf{R}_v . Enfin, un bruit d'état de covariance \mathbf{Q}_u est introduit dans l'équation d'évolution afin d'être capable d'estimer une variation éventuelle de l'angle.

Nous pouvons donc re-écrire les équations de l'inclinomètre de façon suivante :

$$\begin{cases} \theta_k = \theta_{k-1} + u_k \\ \begin{pmatrix} y_k^{a1} \\ y_k^{a3} \end{pmatrix} = \begin{pmatrix} -\sin(\theta_k) \\ \cos(\theta_k) \end{pmatrix} + \begin{pmatrix} v_k^{a1} \\ v_k^{a3} \end{pmatrix} \end{cases} \quad (5.11)$$

Les principes de l'algorithme UKF reposent sur une utilisation implicite d'une technique connue sous le nom de régression linéaire statistique pondérée (Weighted Statistical Linear Regression, en anglais WSLR). Cette technique propage les sigmas points représentatifs de la moyenne $\mathbf{x}^{(0)} = \hat{\mathbf{x}}$ et des bornes $\mathbf{x}^{(1)} = \hat{\mathbf{x}} - \sigma_{\mathbf{x}}$ et $\mathbf{x}^{(2)} = \hat{\mathbf{x}} + \sigma_{\mathbf{x}}$ où $\sigma_{\mathbf{x}}$ constitue l'écart-type de la distribution associée à \mathbf{x} . La propagation de ces points permet d'obtenir les sigma-points images (ou *a posteriori*). Dès lors, il est possible de calculer l'erreur commise entre le sigma point prédit par l'état et l'état prédit par le modèle d'évolution d'une part et d'autre part l'erreur commise entre le sigma point prédit par la sortie et la sortie prédite par le modèle d'observation. Ainsi, la Figure 5.6 fournit à chaque pas de temps les erreurs calculées respectivement par l'UKF et l'IUKF à partir des sigmas points $\mathbf{x}^{(0)}$ (0, 0), $\mathbf{x}^{(1)}$ ($\text{Exm} < 0$), $\mathbf{x}^{(2)}$ ($\text{Exm} > 0$) et de la première sortie de notre système (i.e., $y_k^{a1} = -\sin(\theta_k)$). De plus, sont représentées différentes dynamiques d'erreur, pour deux angles particuliers $\theta = 0$ ou 80 degrés à estimer. En effet, deux cas nous intéressent : soit nous disposons d'un modèle de sortie linéaire à $\theta = 0$ degré, moyennant un bruit relativement faible, soit d'un modèle de sortie fortement non linéaire, à $\theta = 80$ degrés. La simulation s'est donc faite avec un bruit Gaussien de matrice de covariance $\mathbf{Q}_u = 1e-2$ et $\mathbf{R}_v = 0.5 \text{ rad}$. Ce faisant, nous pouvons observer sur la Figure 5.6 que les algorithmes UKF et IUKF génèrent des erreurs, fonction de l'angle d'attitude à estimer, ne convergeant pas de la même manière. Les résultats permettent de mettre en évidence les principes théoriques discutés précédemment puisqu'il apparaît ici clairement que la convergence des erreurs calculée par l'IUKF est la même quelque soit l'angle d'attitude estimé alors que la convergence des erreurs calculée par l'UKF est différente suivant l'angle estimé par l'algorithme. De ce fait, les sigmas points de l'IUKF convergent systématiquement comme si l'on se trouvait constamment dans la partie linéaire du système d'observation, c'est à dire pour $\theta = 0$ degré. Ce résultat illustre les propriétés d'invariance de l'IUKF puisque son comportement vis-à-vis des erreurs d'estimation est le même quelque soit l'angle d'attitude à estimer. Pour chacune des trajectoires générées à partir des différents angles d'attitude, l'erreur de sortie classique est projetée dans un repère de Frenet, qui préserve les symétries du système. La Figure 5.5 dessine les variations temporelles de tous les gains de correction, de chaque variation d'angle d'attitude, pour l'UKF et l'IUKF. Les différentes échelles en ordonnée sont identiques entre les deux cas ce qui facilite la lecture des résultats. Une nouvelle fois, la relative constance des gains de Kalman caractérisant l'IUKF apparaît comme remarquable. Elle est l'illustration du cadre invariant introduit pour l'estimation de l'état du système. Les nombreuses et fréquentes fluctuations des gains de l'UKF pour chacun des angles sont annulées lorsque l'on passe à la version invariante du filtrage et le seul gain calculé par l'IUKF est le même que celui calculé par l'UKF à $\theta = 0$ degrés.

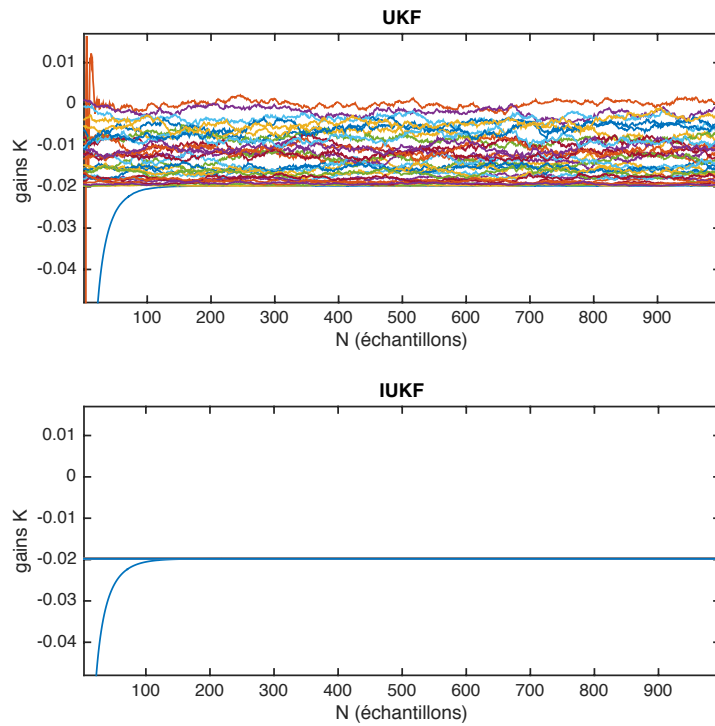


FIGURE 5.5 – Variation temporelle de tous les gains de correction, de chaque variantion de θ .

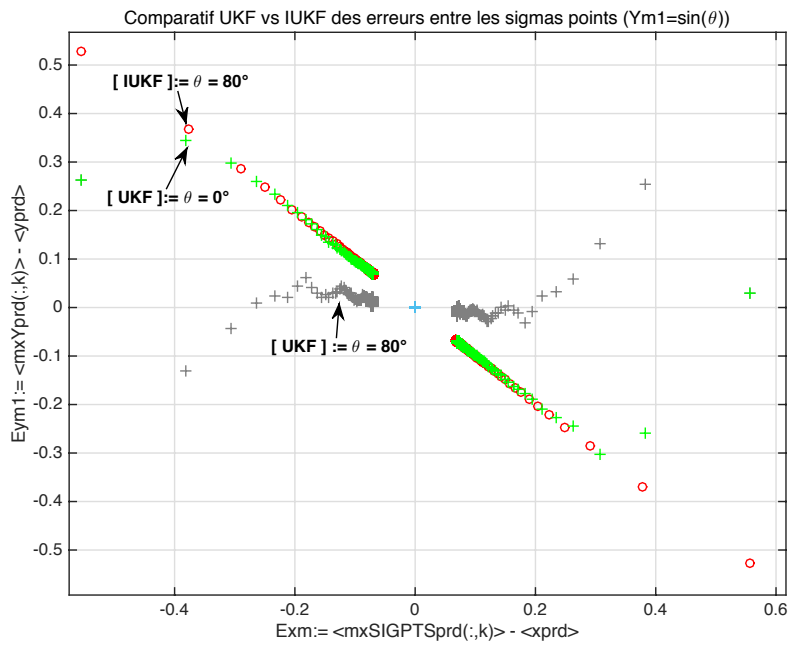


FIGURE 5.6 – Comparaison des gains UKF et IUKF.

5.3.2 Sur l'estimation des régions de stabilités des systèmes nonlinéaire

La problématique du décrochage d'un drone à ailes fixes décrite à la section 2.2.1 nous a conduit vers la définition d'une nouvelle représentation des coefficients aérodynamiques du vol basée sur une technique de régression polynomiale dite « par morceaux ». Couplée aux équations différentielles de la dynamique du vol, cette modélisation nous a permis de montrer qu'il a été possible d'étendre l'analyse de la stabilité des systèmes nonlinéaires basés sur la programmation par Sum-of-Square (SoS) (Motzkin et al. [1967]) à une classe de système hybride pour une future utilisation dans la conception de lois de commande dédiées à la reprise au décrochage. La dernière partie de cette section sera donc consacrée à la présentation d'une technique de commande optimale nommée MPC (Model Predictif Control) que nous avons modifiée pour obtenir une preuve intrinsèque de la stabilité du système par la résolution d'un problème de SoS. Nous présentons ici le fil conducteur des principaux travaux de recherche menés autour de ces développements. Tout d'abord rappelons quelques définitions utiles pour la compréhension des étapes de calculs qui suivent.

Définition 5.1

Un matrice symétrique $\mathbf{M} \in \mathbb{R}^{n \times n}$ est semi-définie positive ($\mathbf{M} \succeq 0$) si et seulement si $\mathbf{x}^T \mathbf{M} \mathbf{x} \geq 0$ pour tout $\mathbf{x} \in \mathbb{R}^n$ ou, par équivalence, si toutes les valeurs propres de \mathbf{M} sont non négative.

Lemme 5.1 (Choi et al. [1995], p. 106–108)

Un polynome $f \in \mathbb{R}[\mathbf{x}]$ de degré $2k$ est de la forme « somme de carrés » (SoS), c'est à dire $f = \sum_{i=1}^l f_i^2$ tel que $f \in \Sigma[\mathbf{x}]$, si et seulement si il existe une matrice \mathbf{Q} de taille l et un vecteur \mathbf{z} de monomes en \mathbf{x} de degré k ou inférieur tel que $f = \mathbf{z}^T \mathbf{Q} \mathbf{z}$. \triangleleft

Définition 5.2 (Monotonie globale)

Soit une fonction de Lyapunov candidate \mathcal{V} de forme polynomiale et un système f de variables d'état \mathbf{x} . Nous pouvons vérifier les conditions de stabilité globale du théorème de Lyapunov (Slotine et al. [1991]) à travers une décomposition du polynôme en SoS (Parillo et al. [2003]); tel que la dérivée est strictement monotone autour de l'équilibre⁴. Pour pouvoir résoudre le problème par la programmation en SoS, nous devons restreindre notre étude à une condition semi-définie négative telle que :

$$\nabla \mathcal{V} \cdot f(\mathbf{x}) + \epsilon \|\mathbf{x}\|_2^2 \leq 0 \quad (5.12)$$

avec $\epsilon > 0$ petit. Si \mathcal{V} est inconnu mais de degré borné, alors nous pouvons chercher une fonction de Lyapunov tel que celle-ci est décomposable en SoS soit $\mathcal{V} - \epsilon \|\mathbf{x}\|_2^2 \leq 0$. Par la suite, nous noterons l'ensemble $\mathcal{X}_{\mathcal{V}, f, \epsilon}$ pour tout $\mathbf{x} \in \mathbb{R}^n$ telle que la condition de (5.12) soit vérifiée pour $\mathcal{V} \in \mathbb{R}[\mathbf{x}]$, $f \in \mathbb{R}[\mathbf{x}]^n$, et $\epsilon > 0$.

4. assumé ici, sans perte de généralité, comme étant l'origine

Définition 5.3 (Monotonie locale)

La recherche d'une fonction de Lyapunov candidate localement monotone négative peut être effectué en évaluant des ensembles d'inclusion semi algébrique tel que :

$$\Phi \subseteq_{\Sigma} \mathcal{X}_{\mathcal{V},f,\epsilon}, \quad (5.13)$$

où Φ est un ensemble obtenu par inégalités polynomiales (d'intersection de polynômes) tel qu'il existe une fonction de Lyapunov dont la forme est décomposable en somme des carrée. Cette définition sera particulièrement utile pour l'analyse de la stabilité locale, sans a priori sur la région d'attraction, d'un système représenté par des polynômes ou de l'analyse de la stabilité globale des systèmes hybrides (*Papachristodoulou et al. [2009]*). Ainsi, l'ensemble le plus large possible pour une fonction de Lyapunov invariante donnée, peut être obtenu en reformulant l'équation (5.13) en un problème quasi-convexe tel que :

$$\max \lambda \quad \mathcal{X}_{\mathcal{V} \leq \lambda} \subseteq_{\Sigma} \mathcal{X}_{\mathcal{V},f,\epsilon}. \quad (5.14)$$

Sur la base de ces définitions, nous avons donc cherché à répondre à la problématique du décrochage par l'utilisation d'une représentation polynomiale par morceaux des coefficients aérodynamiques. La régression par polynôme est une technique qui recherche basiquement à déterminer une relation de cause à effet paramétrique (une régression) qui exprime au mieux les observations (ou données bruitées) disponibles d'un système physique. Cette relation peut-être linéaire ou non linéaire. Elle est généralement obtenue par minimisation d'un critère de type moindre carré construit autour de k données de référence tel que :

$$\Gamma_{\text{opt}} = \arg \min_{\Gamma} \sum_{i=0}^k w_i |\Gamma(\alpha_i) - C_{\odot,i}|^2, \quad (5.15)$$

où Γ est un polynôme de degrés finis, $C_{\odot,i}$ sont les mesures obtenues à une valeur α_i et $w_i > 0$ est une variable qui pondère chaque terme d'écart quadratique pour éviter le sur-apprentissage dans certaine phase de la fonction à identifier. Toutefois, dans le cas d'une relation fortement nonlinéaire à identifier, un unique polynôme obtenu à partir de (5.15), même de degré élevé, n'est pas en mesure de représenter avec suffisamment de précision toutes les variations des données du système comme dans (*Chakraborty et al. [2011]*, *Kwatny et al. [2013]*) qui s'intéressent à la représentation de coefficients aérodynamiques. Il est alors nécessaire d'utiliser une modélisation via des polynômes dit par morceaux (*McGee [1970]*, *Robison [1964]*), mis bout à bout à travers une fonction logistique qui assure la continuité entre les morceaux. L'optimisation est ensuite menée simultanément sur les n polynômes à identifier avec comme variable de décision les paramètres de chaque régression. En reprenant les mêmes notations que dans l'équation (5.15), pour $n = 2$, cela nous donne la minimisation suivante :

$$\left(\Gamma_{\text{opt}}^{\text{pre}}, \Gamma_{\text{opt}}^{\text{post}} \right) = \arg \min_{\Gamma_{1,2}} \sum_{i \in \mathcal{I}_1} w_i |\Gamma_1(\alpha_i) - C_{\odot,i}|^2 + \sum_{i \in \mathcal{I}_2} w_i |\Gamma_2(\alpha_i) - C_{\odot,i}|^2, \quad (5.16)$$

où $\mathcal{I}_{1,2}$ sont les intervalles choisis *a priori*. Le modèle par morceaux résultant est donné par

$$\Gamma_{\text{pw}}(\alpha, \dots) = \begin{cases} \Gamma_{\text{opt}}^{\text{pre}}(\alpha, \dots) & \text{si } \alpha \leq \alpha_0; \\ \Gamma_{\text{opt}}^{\text{post}}(\alpha, \dots) & \text{sinon;} \end{cases} \quad (5.17)$$

avec $\Gamma_{\text{opt}}^{\text{pre}}(\alpha_0, \cdot) \equiv \Gamma_{\text{opt}}^{\text{post}}(\alpha_0, \cdot)$ et α_0 est trouvé comme la jonction entre les deux fonctions à identifier de $C_{\odot,i}$. Cette technique nous a permis de représenter les coefficients aérodynamiques d'un aéronef sous la forme de polynômes par morceaux pour la première fois dans [Revue 4]. De la sorte, de nouveaux développements ont été menés dans [Revue 3] sur la stabilité des systèmes nonlinéaires exploitant conjointement la représentation polynomiale par morceaux et la programmation par Sum-of-Square (SoS).

5.3.2.1 Région d'attraction & systèmes définis par des polynômes par morceaux

L'estimation des régions de stabilité d'un système nonlinéaire consiste à trouver par itération successive une fonction de Lyapunov candidate représentant l'ensemble invariant stable le plus large possible⁵. De la sorte, la recherche d'un tel ensemble se traduit en la formulation d'un problème d'optimisation quasi-convexe dont la solution est obtenue en évaluant des inégalités polynomiales à l'aide de la programmation par SoS. Bien que l'estimation des régions d'attraction ait été largement appliquée à des systèmes nonlinéaires représentés par un seul polynôme (Bulka et al. [2017]), aucune formulation du problème n'avait été à notre connaissance adaptée pour des polynômes par morceaux. Nous présentons donc les étapes de calcul nécessaires pour arriver à cette nouvelle formulation avec le cas particulier d'un polynôme à deux morceaux ($n = 2$) décrit précédemment par l'équation (5.17). Le lecteur trouvera dans [Revue 2] une formulation générale de la méthode. Considérons un système dynamique représenté par un polynôme à deux morceaux :

$$\dot{\mathbf{x}} = f(\mathbf{x}, \mathbf{u}) = \begin{cases} f^{\text{pre}}(\mathbf{x}, \mathbf{u}) & \text{if } \alpha \leq \alpha_0; \\ f^{\text{post}}(\mathbf{x}, \mathbf{u}) & \text{else;} \end{cases} \quad (5.18)$$

Soit $\mathcal{P}(\mathbf{x})$ une fonction quadratique telle que $\mathcal{P}(\mathbf{x}) = \mathbf{x}^T \Sigma \mathbf{x}$ avec Σ une matrice diagonale. Soit \mathcal{V} une fonction de Lyapunov candidate telle que $\mathcal{V}(\mathbf{x}) > 0$ pour tout $\mathbf{x} \neq \mathbf{0}$, et \mathbf{x}^* un point d'équilibre. L'ensemble définit par :

$$\mathcal{X}_\rho = \{\mathbf{x} \in \mathcal{X} \mid \mathcal{P}(\mathbf{x}) \leq \rho\} \quad (5.19)$$

avec $\rho > 0$ est stable si et seulement si (Théorème de La Salle) :

$$\dot{\mathcal{V}}(\mathbf{x}) = \nabla \mathcal{V} f(\mathbf{x}) < 0 \quad (5.20)$$

5. c'est à dire le plus grand ensemble de conditions initiales de l'état d'un système noté $\mathbf{x}_0 \in \mathcal{X}^{\text{stable}}$ tel que l'état du système converge en un temps fini vers une condition d'équilibre notée \mathbf{x}^*

pour tout $\mathbf{x} \in \mathcal{X}_\rho - \{\mathbf{x}^*\}$. L'équation (5.20) est vérifiée s'il existe un polynôme semi-défini positif $h \in \mathbb{R}[\mathbf{x}]$ tel que

$$\nabla \mathcal{V}f(\mathbf{x}) + h(\mathbf{x}) (\rho - \mathcal{P}(\mathbf{x})) \leq -\epsilon \|\mathbf{x}\|_2^2, \quad (5.21)$$

pour $\epsilon > 0$. A ce stade, il est nécessaire d'utiliser la théorie des fonctions de Lyapunov commune démontrée dans (Johansson et al. [2003]) pour adapter l'équation (5.21) à un système défini par des polynômes par morceaux. Ce résultat a amené l'énoncé du théorème qui suit :

Théorème 5.1

Soit $(f_i)_{i \in I}$ défini sur des ensembles disjointes deux-à-deux $(\mathcal{X}_i)_{i \in I}$ et $\mathcal{V}(\mathbf{x}) > 0$ pour tout $\mathbf{x} \neq \mathbf{0}$; le voisinage \mathcal{X}_ρ est stable si pour tout $i \in I$ et $\mathbf{x} \in \mathcal{X}_\rho \cap \mathcal{X}_i - \{\mathbf{0}\}$

$$\dot{\mathcal{V}}(\mathbf{x}) = \nabla \mathcal{V}f_i(\mathbf{x}) < 0. \quad (5.22)$$

◁

L'application de ce théorème revient à ajouter à l'équation (5.21) une opération similaire à $h(\mathbf{x}) (\rho - \mathcal{V}(\cdot))$ pour compenser les dérivées non négatives en dehors de l'ensemble stable. Soit g_1, g_2 deux fonctions semi-définies positives avec :

$$g_1(\mathbf{x}) (\alpha_0 - \alpha) \geq 0 \iff \alpha \leq \alpha_0 \quad (5.23)$$

$$g_2(\mathbf{x}) (\alpha - \alpha_0) > 0 \iff \alpha > \alpha_0 \quad (5.24)$$

Ainsi nous obtenons les conditions suivantes pour les phases f^{pre} et f^{post}

$$\begin{cases} \nabla \mathcal{V}f^{pre}(\mathbf{x}) + h_1(\mathbf{x}) (\rho - \mathcal{P}(\mathbf{x})) + g_1(\mathbf{x}) (\alpha_0 - \alpha) \leq -\epsilon \|\mathbf{x}\|_2^2, \\ \nabla \mathcal{V}f^{post}(\mathbf{x}) + h_2(\mathbf{x}) (\rho - \mathcal{P}(\mathbf{x})) + g_2(\mathbf{x}) (\alpha - \alpha_0) \leq -\epsilon \|\mathbf{x}\|_2^2 \end{cases} \quad (5.25)$$

Avec $\epsilon > 0$. L'équation (5.25) nous permet donc de vérifier si l'ensemble \mathcal{X}_ρ est stable pour le système défini par l'équation (5.18). Reste maintenant à trouver une fonction de Lyapunov candidate dont la taille ρ est la plus grande possible pour un facteur d'échelle Σ donné. Pour cela, nous utilisons une procédure nommée V-s itération (Chakraborty et al. [2011]) dont les étapes sont les suivantes :

1. trouver $\lambda^\diamond = \max \lambda$ tel que $h'(\cdot)$ est semi-défini positif avec

$$\nabla \mathcal{V}f(\mathbf{x}) + h'(\mathbf{x}) (\lambda - \mathcal{V}(\mathbf{x})) \leq -\epsilon \|\mathbf{x}\|_2^2;$$

2. trouver $\rho^\diamond = \max \rho$ tel que $h_0(\cdot)$ est semi-défini positif avec

$$(\mathcal{V}(\mathbf{x}) - \lambda^\diamond) + h_0(\mathbf{x}) (\rho - \mathcal{P}(\mathbf{x})) \leq 0$$

pour λ^\diamond constant ;

3. trouver $\mathcal{V}(\cdot)$ tel que

$$\begin{cases} \mathcal{V}(\mathbf{x}) \geq \epsilon \|\mathbf{x}\|_2^2, \\ \nabla \mathcal{V}f(\mathbf{x}) + h'(\mathbf{x})(\lambda^\diamond - \mathcal{V}(\mathbf{x})) \leq -\epsilon \|\mathbf{x}\|_2^2, \\ (\mathcal{V}(\mathbf{x}) - \lambda^\diamond) + h_0(\mathbf{x})(\rho^\diamond - \mathcal{P}(\mathbf{x})) \leq 0, \end{cases}$$

avec $\lambda^\diamond, \rho^\diamond$ ainsi que $h'(\cdot)$ et $h_0(\cdot)$ issus des étapes précédentes.

Une première estimation de la région de stabilité plutôt « conservative » peut-être obtenue à partir d'une fonction de Lyapunov $\mathcal{V}(\cdot)$ déterminée pour le système linéarisé autour de \mathbf{x}^* . Pour pallier à la difficulté de trouver simultanément une fonction de Lyapunov candidate et sa région de stabilité associée dans laquelle sa dérivée temporelle est strictement négative (région de dissipation), la V-s itération utilise trois étapes distinctes de calcul dans lesquelles une optimisation par SOS est effectuée : 1) la première étape consiste à déterminer une région de dissipation de $\mathcal{V}(\cdot)$ telle que pour la ligne de niveau $\mathcal{V}(\mathbf{x}) = \lambda$, la dérivée de la fonction est strictement négative ; 2) l'ellipsoïde représenté par $\mathcal{P}(\mathbf{x}) = \rho$ associé à l'ensemble stable \mathcal{X}_ρ est ajusté dans cette ligne de niveaux ; 3) à partir des optimisations précédentes, on cherche une nouvelle fonction de Lyapunov vérifiant si celle-ci représente la plus grande région de stabilité.

Illustration sur un exemple de modèle longitudinal d'aéronef À titre d'exemple, étudions la stabilité du mode d'oscillation d'incidence d'un aéronef représenté par le système suivant :

$$\begin{bmatrix} \dot{\alpha} \\ \dot{q} \end{bmatrix} = \begin{cases} f_{sp}^{pre}(\alpha, q, \eta = \eta^*) & \text{if } \alpha \leq \alpha_0; \\ f_{sp}^{post}(\alpha, q, \eta = \eta^*) & \text{else;} \end{cases} \quad (5.26)$$

Nous reconnaissons l'expression d'un système nonlinéaire que nous avons représenté par une modélisation polynomiale par morceaux (voir figure 5.7) avec les conditions d'équilibre suivantes : $V^* = 45.7 \text{ m s}^{-1}$, $\gamma^* = 0$, $\alpha^* = 3.75^\circ$, $\eta^* = 1.49^\circ$, $F^* = 21.44 \text{ N}$. La forme initiale de l'ellipse $\mathcal{P}(\mathbf{x})$ est définie par $\Sigma = \text{diag}(20^\circ, 50^\circ \text{ s}^{-1})^{-2}$. Après 94 itérations, nous obtenons l'ensemble stable avec $\mathcal{X}_{\rho_0} = \{\mathbf{x} \mid \mathcal{P}(\mathbf{x}) \leq \rho_0\}$ tel que $\rho_0 = 1.4404$ et la région de dissipation $\{\mathbf{x} \mid \mathcal{V}_0(\mathbf{x}) \leq \lambda_0\} \subseteq \{\mathbf{x} \mid \dot{\mathcal{V}}_0(\mathbf{x}) < 0\}$ de la fonction de Lyapunov quadratique $\mathcal{V}_0(\cdot)$ tel que $\lambda_0 = 0.3265$. De ce fait, les fonctions de Lyapunov obtenues sont les suivantes :

$$\begin{aligned} \mathcal{V}_0 &= 6.5\alpha^4 + 0.37\alpha^3q + 0.19\alpha^2q^2 + 0.023\alpha q^3 + 0.0027q^4 - 0.080\alpha^3 \\ &+ 0.00044\alpha^2q + 0.012\alpha q^2 - 0.0067q^3 + 0.69\alpha^2 - 0.016\alpha q + 0.020q^2 \end{aligned} \quad (5.27)$$

et

$$\begin{aligned} \mathcal{V}_{\text{Pol}} &= 20\alpha^4 - 2.8\alpha^3q + 1.6\alpha^2q^2 - 0.21\alpha q^3 + 0.029q^4 + 0.0033\alpha^3 + 0.00088\alpha^2q \\ &+ 0.00013\alpha q^2 - 2.5 \times 10^{-6}q^3 + 2.6 \times 10^{-5}\alpha^2 + 3.2 \times 10^{-7}\alpha q + 1.4 \times 10^{-6}q^2 \end{aligned}$$

Les résultats de la V-s itération sont présentés sur la figure 5.8. L'ensemble stable est noté \mathcal{X}_{ρ_0} et la région de dissipation de la fonction de Lyapunov commune calculée est notée \mathcal{V}_0 . Pour comparer ces résultats avec une optimisation menée sur un modèle polynomial continu, nous avons superposé l'ensemble stable $\mathcal{X}_{\rho_{Pol}}$ et la fonction quartique de Lyapunov \mathcal{V}_{Pol} issue de (Chakraborty et al. [2011]) pour $\rho_{Pol} = 1.7$ et $\lambda_{Pol} = 0.85$ respectivement. Ainsi, ce résultat met d'une part en évidence qu'il est possible de trouver une fonction de Lyapunov représentant l'ensemble stable commun entre les polynômes définis par morceaux en utilisant la programmation par SoS et d'autre part montre que cette région englobe un plus large ensemble stable de valeurs.

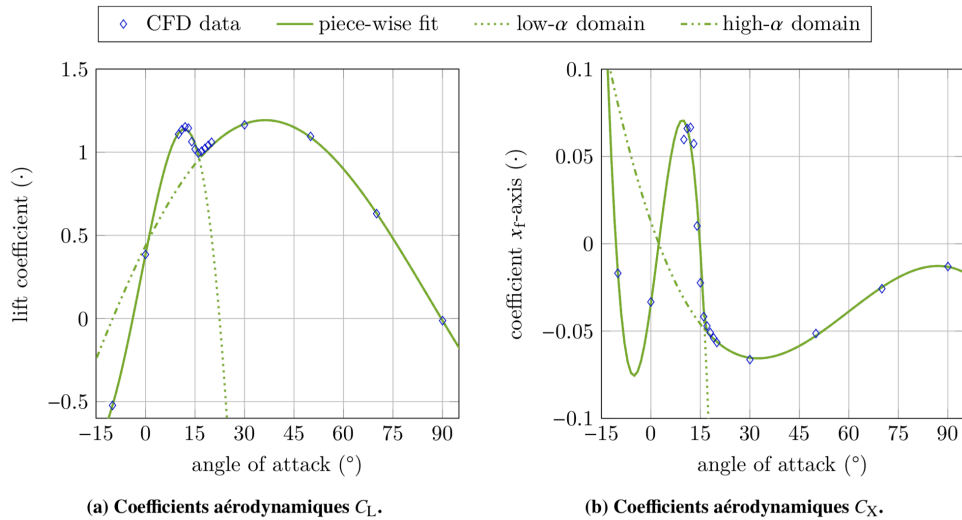


FIGURE 5.7 – Modèle par morceaux des coefficients aérodynamiques.

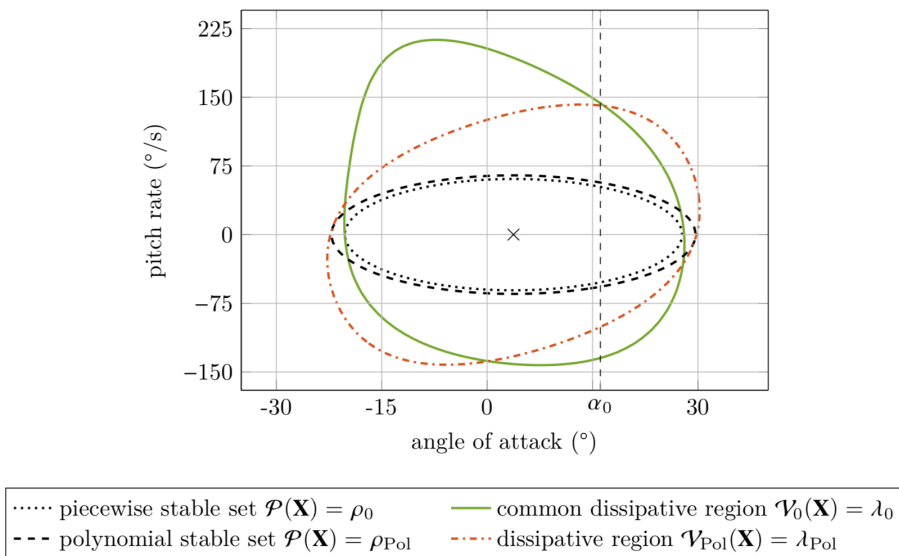


FIGURE 5.8 – Ensemble stable du modèle longitudinal par morceaux comparé à (Chakraborty et al. [2011]).

5.3.2.2 Les Sum-of-Squares pour prouver la stabilité du Contrôle Prédicatif

Les progrès significatifs des capacités de calcul permettent aujourd’hui d’envisager la commande prédictive ou MPC (Engelbrecht et al. [2016], Schuet et al. [2017]) (Model Predictive Control) comme une approche extrêmement intéressante pour les systèmes embarqués dont la dynamique à contrôler est soumise à des contraintes d’état. L’estimation de l’état et de la commande, solution du problème, est construite de manière itérative et minimise un critère de coût des erreurs qui doit être dans le cas classique défini négatif. Dans le cas contraire, pour garantir la robustesse du système à contrôler d’un point de vue de sa convergence, il faut se tourner vers des algorithmes plus récents, comme le Economic MPC (EMPC)⁶ (Ellis et al. [2017]) qui intègre des conditions algébriques pour que la dynamique du système soit dite « dissipative ». Pour autant, ces conditions sont souvent difficiles à obtenir dans le cas général. C’est précisément cette recherche de preuve de stabilité qui nous a conduit dans [Conf 20] à intégrer dans le EMPC une étape de calcul des régions d’attraction et de pondération des erreurs quadratiques de la fonction de coût par programmation semi-définie. Dans ce qui suit, nous allons développer cette contribution pour le cas d’application d’un drone à ailes fixes en situation de décrochage.

Commençons par rappeler un peu de théorie. Considérons un système non linéaire représenté par l’équation (5.28) tel que :

$$\dot{x} = f(x, u), \quad (5.28)$$

ce système est soumis à des contraintes d’état noté $x \in \mathcal{X} \subseteq \mathbb{R}^n$ et de commande notée $u \in \mathcal{U} \subseteq \mathbb{R}^m$. Dans le reste du document, nous travaillerons avec une représentation à temps discret tel que :

$$x^+ = f^+(x, u) = x + \tau f(x, u) \quad (5.29)$$

avec $\tau > 0$ la période d’échantillonnage. Les propriétés de convergence de la commande prédictive dépendent de la manière dont la fonction de coût est définie. Nous présentons donc les hypothèses nécessaires qui prouvent la stabilité du EMPC en boucle fermée. Ces résultats sont énoncés dans le théorème (Parillo et al. [2003]) qui suit.

Définition 5.4

Le système $x^+ = f^+(x, u)$ est dit « strictement dissipatif » par rapport une fonction $\varsigma: \mathcal{Z} \rightarrow \mathbb{R}$ si et seulement si il existe une fonction dite de stockage $\Lambda: \mathcal{X} \rightarrow \mathbb{R}$ tel que :

$$\Lambda(x^+) - \Lambda(x) \leq -\rho(x - x_f) + \varsigma(x, u) \quad (5.30)$$

pour un ensemble $\rho: \mathcal{X} \rightarrow \mathbb{R}_{\geq 0}$ défini positif⁷ et pour tout $(x, u) \in \mathcal{Z}$.

6. En raison de sa première utilisation en économie.

7. Une fonction continue ϕ est dite défini positive si $\phi(\cdot) > 0$ partout excepté à l’origine $\phi(0) = 0$.

Théorème 5.2

Soit $(x_f, u_f) \in \mathcal{Z}^{\text{trim}}$ tel que :⁸

1. f^+ est strictement dissipative par rapport à la fonction ς_ℓ tel que $\varsigma_\ell : (x, u) \mapsto \ell(x, u) - \ell(x_f, u_f)$;
2. $\ell(x_f, u_f) \leq \ell(x, u)$ pour tout $(x, u) \in \mathcal{Z}^{\text{trim}}$;

Alors x_f est un état d'équilibre de $x^+ = f^+(x, u)$ asymptotiquement stable.

La commande prédictive est définie comme la solution d'un problème de contrôle optimal. Etant donné un état mesuré $x_0 \in \mathcal{X}$, un état final et une commande finale notée $(x_f, u_f) \in \mathcal{Z}^{\text{trim}}$; nous devons résoudre un problème nonlinéaire sous contrainte tel que celui-ci minimise une fonction de coût, notée $\ell : \mathcal{Z} \rightarrow \mathbb{R}$, soit l'expression suivante :

$$\min_{\mathbf{x}, \mathbf{u}} \sum_{i=1}^{N-1} \ell(x_i, u_i), \quad (5.31a)$$

$$x_{i+1} = f^+(x_i, u_i), \quad i = 0, \dots, N-1, \quad (5.31b)$$

$$x_N = x_f, \quad \mathbf{x} \in \mathcal{X}^N, \quad \mathbf{u} \in \mathcal{U}^N \quad (5.31c)$$

La loi de commande du MPC sera de la forme suivante :

$$u(t) = \hat{\mathbf{u}}[1](x(t)) \quad (5.32)$$

où $(\hat{\mathbf{x}}, \hat{\mathbf{u}})$ minimise l'équation (5.31) avec $x_0 = x(t)$. L'ensemble des solutions admissibles pour la récupération au décrochage est défini tel que :

$$\mathcal{Z}_N = \left\{ (x_0, \mathbf{u}) \in \mathcal{X} \times \mathcal{U}^N \mid f^N(x_0, \mathbf{u}) = x_f \text{ et } \forall k \leq N. f^k(x_0, \mathbf{u}^k) \in \mathcal{X} \right\}, \quad (5.33)$$

Dans le cas d'un drone à ailes fixes en situation de décrochage, il est tout à fait souhaitable d'avoir une perte d'altitude (LOA) minimale $\Delta z_g = z_{gN} - z_{g0}$ qui s'exprime avec une fonction de coût de la manière suivante (Sparks et al. [2002], Bunge et al. [2018]) :

$$\ell_\Delta(x) = z_g^+ - z_g = -\tau V \sin \gamma. \quad (5.34)$$

Sans effort propulsif, l'avion descend avec un transfert d'énergie potentielle et cinétique tel que la perte d'altitude en régime permanent (altitude finale) $\ell_\Delta^* = \ell_\Delta(x_f, u_f) \leq \ell_\Delta(x, u)$ est positive pour tout $(x, u) \in \mathcal{Z}^{\text{trim}}$. Cependant, l'équation (5.34) montre que la fonction de coût n'est pas définie positive (l'avion descend quelque soit l'angle d'inclinaison γ) sur \mathcal{Z} , ce qui nécessite d'ajouter un terme quadratique pour vérifier la première condition du Théorème 2.2 tel que :

$$\ell_R(x, u) = \ell_\Delta(x) + \frac{1}{2} \|x - x_f\|_{Q_x}^2 + \frac{1}{2} \|u - u_f\|_{Q_u}^2, \quad (5.35)$$

ou $Q_x \in \mathbb{R}^{n \times n}$, $Q_u \in \mathbb{R}^{m \times m}$ sont des matrices diagonales positives.

8. Si f^+ est localement contrôlable sur un ouvert de x_f .

De précédents travaux dans (Jäschke et al. [2014]) montrent que la dynamique du système est dissipative si les gains $Q = \text{diag}(Q_x, Q_u)$ sont choisis suffisamment large par rapport à la fonction de coût. Cependant, cette technique de réglage est très conservative. Une autre manière de garantir la stabilité du système en boucle fermée est d’obtenir une fonction de stockage candidate qui vérifie l’équation (5.30). Bien qu’une fonction de stockage polynomiale *prouvant la dissipation* peut être synthétisée en résolvant un problème de programmation semi-définie, on ignore souvent *a priori* le degré du polynôme. Pour résoudre cette ambiguïté, nous avons proposé dans [Conf 20] d’appliquer la programmation par SoS pour trouver simultanément une fonction polynomiale candidate de stockage notée \mathfrak{L} tout en minimisant la trace de la matrice de pondération Q qui prouve que la dynamique du système est dissipative. En reprenant les mêmes notations que dans l’exemple du modèle longitudinale d’un aéronef à la section 2.3.2.1, nous devons donc résoudre le problème suivant :

$$\min_{\substack{Q \succeq 0 \\ \mathfrak{L} \in \mathbb{R}[x]}} \text{tr}(Q) \quad \text{s.t.} \quad \begin{cases} \mathcal{Z} \cap \mathcal{X}_{\alpha \leq \alpha_0} \subseteq_{\Sigma} \mathcal{X}_{\mathfrak{L}, Q}^{pre} \\ \mathcal{Z} \cap \mathcal{X}_{\alpha \geq \alpha_0} \subseteq_{\Sigma} \mathcal{X}_{\mathfrak{L}, Q}^{post} \end{cases} \quad (5.36)$$

Où l’ensemble stable est noté $\Omega_{\mathfrak{L}, Q}^{(\cdot)}$ pour tout $z \in \mathbb{R}^{m+n}$ tel que :

$$\mathfrak{L} \circ f^{(\cdot)}(z) - \mathfrak{L}(z) - \mathfrak{S}_{\ell}(z) \leq \frac{1}{2} \|z - z_f\|_Q^2 - \epsilon \|\bar{x}\|_2^2 \quad (5.37)$$

pour $\epsilon > 0$, $x^+ = f^{(\cdot)} \in \{f^{pre}, f^{post}\}$ et \mathfrak{S}_{ℓ} la fonction de dissipation. Cette approche permet d’obtenir un polynôme \mathfrak{L} de degré arbitraire tout en garantissant que $Q \rightarrow 0$ si le système est considéré comme dissipatif.

5.3.3 Etude de l’approche algébrique pour la commande « sans modèle »

L’amélioration constante des moyens d’expérimentation permet aujourd’hui, de bâtir des modèles prévisionnels de plus en plus fiables et précis, en témoigne les travaux de la section précédente. Cependant, disposer de ces modèles précis représente un investissement (temps, euros) important qu’il convient de mesurer avant de mettre en place une telle démarche de modélisation. Dès lors, si nous disposons, comme c’est notamment le cas pour les drones convertibles, uniquement d’un modèle de faible précision de l’engin dans lequel les phénomènes aérodynamiques sont difficiles à identifier, alors il peut être plus avantageux pour effectuer un premier vol, de se tourner vers des techniques d’estimation et de commande dite « sans modèle ». Nous nous sommes donc focalisés sur une solution de commande sans modèle nommée Model-Free Control (MFC) (Fliess et al. [2009], Fliess et al. [2013]) qui consiste à faire une estimation entrée/sortie de la dynamique du système observé pour compenser en temps réel l’erreur qui serait générée par la commande en boucle fermée du fait des incertitudes paramétriques. Bien que cette approche ait donné de très bons résultats dans le cadre de la thèse de JACSON BARTH, sur la commande du drone convertible nommé « Darko » (voir section 2.2.1), il nous semble utile dans ce manuscrit d’exposer clairement les limites et les contraintes de réglage de la commande MFC pour discuter en prospective des problématiques que nous allons adresser dans nos futurs travaux de recherche.

Quelques éléments sur la théorie de la commande dite « sans modèle » Nous commençons donc par rappeler quelques résultats théoriques sur la MFC. Le modèle d'un système non linéaire peut être approché par une équation dite *Ultra-local* telle que :

$$y^{(v)}(t) = F(t) + \lambda \cdot u(t) \quad (5.38)$$

Dans (5.38), v est l'ordre de la dérivée de la sortie $y(t)$, $u(t)$ est l'entrée du système, $\lambda \in \mathbb{R}$ est un paramètre constant non physique utilisé pour obtenir le même ordre de grandeur entre les trois termes dans (5.38) et $F(t)$ représente la dynamique la connue du système ainsi que les différentes perturbations qui pourraient dégrader les performances de l'architecture de commande. A partir de l'estimation de $F(t)$, notée $\hat{F}(t)$ et pour $v = 2$, il est alors possible de concevoir une architecture de commande, robuste aux variations paramétriques et aux perturbations extérieures avec la commande suivante :

$$u(t) = \underbrace{-\frac{\hat{F}(t)}{\lambda}}_{\text{Estimation}} + \underbrace{\frac{\ddot{y}_{sp}(t) + u_{\mathcal{K}}(t)}{\lambda}}_{\text{Suivi en boucle fermée}} \quad (5.39)$$

où $u_{\mathcal{K}}(t)$ est la commande en boucle fermée produite par le correcteur $\mathcal{K}(\xi(t))$ qui peut être classiquement défini comme un gain proportionnel dérivée ou proportionnel intégral dérivée avec $\xi(t) = y(t) - y_{sp}(t)$ qui représente l'erreur du suivi de la trajectoire de référence notée $y_{sp}(t)$ ou en d'autres termes l'erreur de poursuite. Nous reconnaissons dans (5.39) l'expression classique d'une boucle d'asservissement dans laquelle la dynamique non linéaire estimée par $\hat{F}(t)$ est ajoutée à la dynamique de poursuite en boucle fermée. On obtient alors une « bonne » poursuite si l'estimée $\hat{F}(t)$ est « bonne », c'est à dire si $\xi_F = F(t) - \hat{F}(t) \approx 0$.

Les performances de l'estimation joue un rôle crucial dans la dynamique de l'erreur de poursuite et *a fortiori* dans la robustesse de la commande. L'expression de $\hat{F}(t)$ pour la dynamique du premier ordre peut être obtenu dans (Fliess et al. [2013]) suite au calcul de différente transformée de Laplace de l'équation $\dot{y}(t) = F(t) + \lambda \cdot u(t)$ puis exprimée dans le domaine temporel en utilisant la *Transformée de Laplace Inverse* et le *Théorème de Cauchy* afin de réduire les intégrales multiples en une simple intégrale tel que :

$$\hat{F}(t) = \frac{-6}{T^3} \int_{t-T}^t \left[(T - 2\sigma)y(\sigma) - \lambda\sigma(T - \sigma)u(\sigma) \right] d\sigma \quad (5.40)$$

L'équation (5.40) estime la dynamique d'un système du premier ordre à partir des mesures d'un signal bruité $y(t)$. Le résultat est un paramètre constant $\hat{F}(t)$ qui est valable dans l'intervalle $[t - T, t]$. Néanmoins, en pratique, il peut s'avérer nécessaire d'identifier l'estimateur à un comportement du second ordre avec de faibles coefficients de friction. Ainsi, de manière similaire, nous pouvons développer les calculs pour une dynamique du second ordre ($v = 2$), ce qui conduit à l'expression suivante :

$$\hat{F}(t) = \frac{5!}{2T^5} \int_{t-T}^t \left[\left[(T - \sigma)^2 - 4\sigma(T - \sigma) + \sigma^2 \right] y(\sigma) - \left[\frac{\lambda}{2} \sigma^2 (T - \sigma)^2 u(\sigma) \right] \right] d\sigma \quad (5.41)$$

Application sur un drone convertible nommé Darko L'architecture de commande sans modèle a été adaptée dans [Revue 1]* pour être appliquée au contrôle d'un drone convertible nommé Darko. L'étude de ses performances en terme de précision se sont avérées comparables ou légèrement meilleures que d'autres algorithmes de commande du même type comme par exemple l'INDI (Incremental Nonlinear Dynamic Inversion) (Smeur [2018]), mais nous avons observé des propriétés de robustesse intéressantes à travers des essais en intérieur. Les vols intérieurs ont été effectués dans une arène de vol qui présente un volume de 10x10x10 mètres ainsi qu'un ensemble de caméras permettant de retourner l'orientation et la position de l'engin. L'attitude est calculée à bord à une fréquence de 500hz. Les essais en vol révèlent que l'architecture permet de stabiliser le drone dans les phases stationnaires et de transition avec une adaptation de la loi de commande extrêmement réactive aux variations paramétriques.



FIGURE 5.9 – Essai en vol de transition à l'intérieur, face à la soufflerie *WindShape* de l'ENAC.

En effet, nous avons réalisé des vols de transitions rapides qui induisent des variations significatives des forces et des moments aérodynamiques, qui sont correctement estimées et stabilisées par les propriétés adaptatives de l'approche sans modèle. C'est une caractéristique particulièrement puissante de cette approche de contrôle qui adapte sa commande pour suivre la dynamique souhaitée, même si le système contrôlé présente des variations de ses paramètres internes comme dans notre cas des variations des coefficients aérodynamiques. Pour étudier la robustesse de la loi de commande face à des perturbations aérologiques, nous avons réalisé un vol en phase de transition face à une soufflerie à veine ouverte nommée *WindShape* (voir figure 5.9). Les résultats obtenus sont présentés sur la figure 5.10. L'étude démarre en vol stationnaire face à la soufflerie. Le point de consigne de l'angle de tangage a été imposé afin que le drone effectue la transition du vol stationnaire vers le vol en croisière, suite à une augmentation de la vitesse du vent de zéro à 9 m/s . Les vitesses de vent générées par la soufflerie créent des conditions de vol turbulentes autour de l'engin, ce qui affecte directement

sa dynamique d'attitude. La zone ombrée met en évidence la phase de vol où l'angle de tangage diminue à l'approche du vol en croisière, ainsi que la phase de vol où le vent augmente.

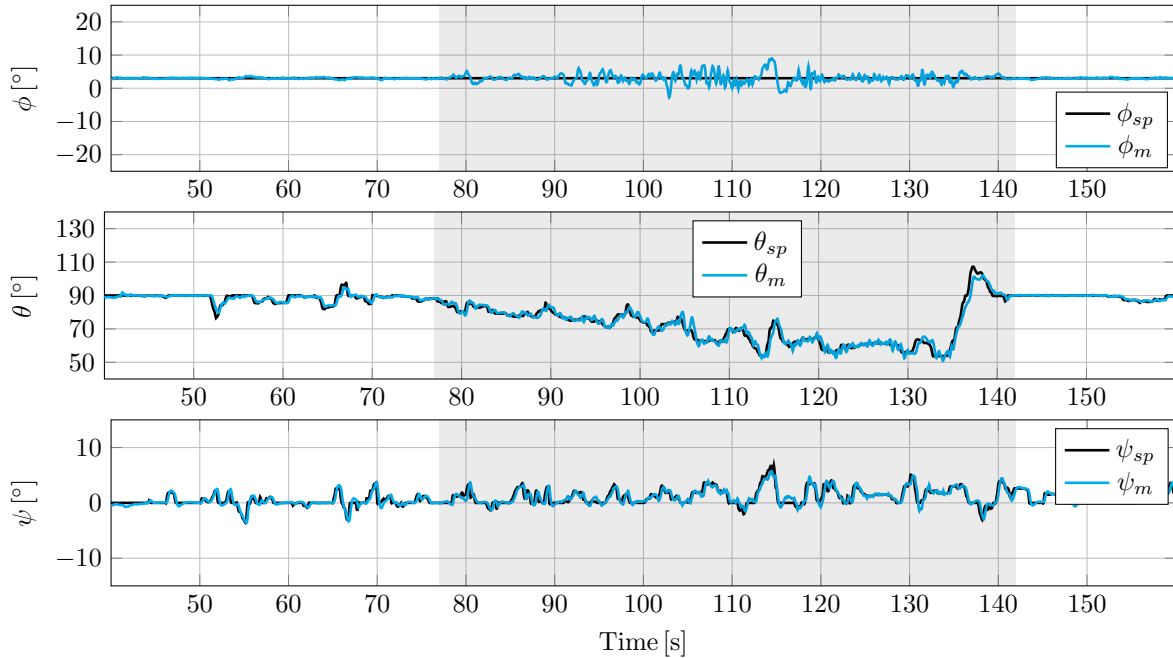
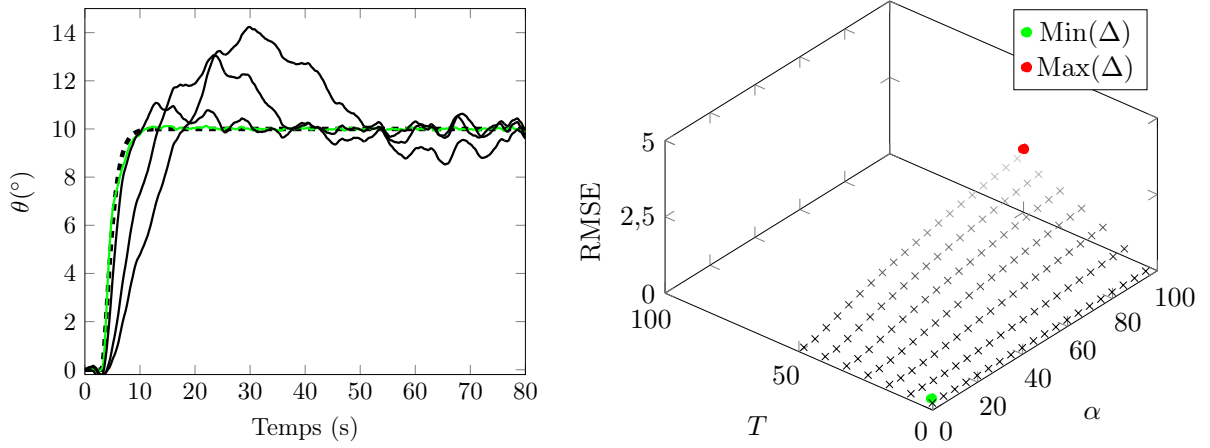


FIGURE 5.10 – Résultats du vol de transition à l'intérieur, face à la soufflerie *WindShape*.

Malgré ces perturbations, le drone reste stable ce qui montre un bon rejet des perturbations. A noter que des oscillations de roulis peuvent être observées à 100 secondes de vol avec une amplitude maximale de 8° . Ce comportement de roulis se produit dans un domaine de vol où les perturbations sont intenses. Les performances de l'engin, en particulier sa dynamique de roulis, pourraient être optimisées en réduisant la fenêtre d'intégration de l'estimateur qui fournira une plus grande réactivité au système. Toutefois, le compromis entre des estimations rapides avec une réactivité rapide en boucle fermée et une atténuation efficace du bruit semble approprié dans des conditions de vol calme sans vent, comme observé lors du précédent essai en vol.

Analyse critique Il ne s'agit pas ici de critiquer la commande sans modèle mais plutôt le discours qui aurait pu laisser croire que cette technique comme son nom l'indique ne nécessitait aucune connaissance sur le système à contrôler pour produire ce que l'on appelle plus communément un asservissement. La fenêtre d'intégration (T) doit être définie avec des informations préalables sur le bruit présent dans le signal mesuré $y(t)$. Le choix de la fenêtre d'intégration implique une certaine expertise avec un compromis entre la rapidité de l'estimation et une atténuation suffisante du bruit pour qu'il ne rejaillisse pas sur la boucle de commande. Ainsi, une grande fenêtre d'intégration fournira une forte atténuation du bruit mais ralentira l'estimation avec un impact direct sur la réactivité du contrôle en boucle fermée. A l'inverse, une

petite fenêtre d'intégration permettra une estimation rapide mais sous contrainte d'éventuels bruits haute fréquence sur la commande connue sous le nom de *chattering*. Dans les équations (5.40) et (5.41), la constante λ est utilisée pour mettre à l'échelle l'amplitude entre la commande $u(t)$ et la dynamique de $\ddot{y}(t)$ (pour un second ordre). Ce paramètre peut-être vu comme l'efficacité des actionneurs du système et nécessite une étape d'identification préalable à toute implémentation de la commande. Un avantage majeur par rapport à d'autre commande sans modèle telle que la commande Nonlinéaire Dynamique Inverse Incrémentale (INDI) est que si ce paramètre est mal défini ou si l'efficacité des actionneurs du système change, l'estimateur $\hat{F}(t)$ sera en mesure dans la limite du possible et sous réserve qu'il soit bien réglé, de compenser l'erreur tout en assurant la stabilité en boucle fermée. Un réglage nominal de λ peut être obtenu en calculant le rapport entre la commande et la valeur maximale autorisée de $\ddot{y}(t)$.



(a) Réponse de l'angle de tangage pour différentes combinaisons de α et T . (b) Etude comparative de l'erreur quadratique moyenne (RMSE) pour différents α et différents intervalles d'intégration T .

FIGURE 5.11 – Influence des paramètres de réglages de la commande sans modèle.

Exemple illustratif A titre d'exemple, nous considérons la dynamique de l'assiette d'un modèle longitudinal d'avion représentée par la fonction de transfert suivante [Conf 6] :

$$\frac{\theta(s)}{\delta_e(s)} = \frac{1.151s + 0.1774}{s^3 + 0.739s^2 + 0.921s} \quad (5.42)$$

On désire asservir la sortie $\theta(s)$ sur la consigne d'une déflexion de la gouverne de profondeur $\delta_e(s)$. Nous ne rajoutons pas de bruit sur la sortie car le problème n'est pas d'analyser ici les performances de l'algorithme mais plutôt de mettre en avant l'influence du réglage sur l'asservissement. Nous choisissons un modèle *Ultra-Local* du second ordre tel que :

$$\ddot{\theta}_m = F_\theta + \lambda \cdot \delta_e \quad (5.43)$$

L'expression de la commande est déterminée grâce à l'équation (5.39) tel que :

$$\delta_e = \frac{-\hat{F}_\theta + \ddot{\theta}_d + \mathcal{K} \xi_\theta}{\lambda} \quad (5.44)$$

La dynamique du système en boucle fermée, sous hypothèse que $\xi_F \approx 0$ peut être approchée par un double intégrateur dont les pôles seront choisis pour satisfaire le polynôme caractéristique suivant :

$$(s + s_d)^2 = s^2 + 2s_d s + s_d^2 \quad (5.45)$$

Cela nous conduira à choisir un correcteur de type proportionnel dérivé dont les deux gains k_p et k_d seront obtenus par identification avec une dynamique d'erreur du second ordre tel que :

$$\frac{U_{\mathcal{K}}(s)}{\xi_y(s)} = s^2 - k_d s - k_p \quad \text{avec} \quad \begin{cases} k_p = -s_d^2 & \text{avec } s_d > 0, \\ k_d = -2s_d & \text{avec } s_d > 0 \end{cases} \quad (5.46)$$

A ce stade nous pouvons régler facilement les gains k_p et k_d pour obtenir en boucle fermée un système suffisamment rapide pour une « bonne » poursuite, soit $(k_p, k_d) = (-1.5, -2.5)$. Par contre, il n'est pas du tout évident de trouver *a priori* le bon couple de paramètres (T, λ) ! Indépendamment de la présence d'un bruit sur la mesure, on peut constater sur la réponse à un suivi de trajectoire (figure 5.11(a)) que ces paramètres influencent fortement la dynamique du contrôle en boucle fermée. Une augmentation du paramètre λ introduit une dynamique rapide peu amortie et une augmentation du paramètre T rend progressivement le système instable en boucle fermée (pour $T > 50s$). Pour espérer obtenir une « bonne » poursuite de l'architecture sans modèle, une solution proposée dans [Conf 6] consiste à introduire un critère noté Δ qui minimise l'erreur (ξ_F) au sens des moindres carrés (voir figure 5.11(b)). Néanmoins, cette technique nécessite de nombreuses simulations sur la base d'un modèle du système, ce qui nous éloigne un peu de la philosophie de la commande sans modèle. Une manière de surmonter partiellement le problème du réglage du filtre sera discuté dans les prospectives.

5.3.4 Etude de l'approche multifractale pour la détection d'une cyber-intrusion

Les nombreux travaux de recherche sur la caractérisation du trafic internet ont permis de montrer que les flux échangés dans un réseau de communication pouvaient être identifiés à un processus à dépendance longue (en anglais, long range dependance) dont la densité spectrale de puissance moyenne se comporte en loi puissance pour de petite échelle de temps. Cette propriété appelée aussi auto-similarité signifie qu'il est possible d'analyser le trafic de communication indépendamment d'une dilatation temporelle ou fréquentielle, ce qui a justifié notre approche multifractale pour la détection d'une cyber-intrusion dans la thèse de RUOHAO ZHANG. L'analyse multifractale est un outil qui permet d'effectuer des zooms sur des structures du signal bien localisées en jouant sur un paramètre d'échelle pour en extraire des singularités ou des irrégularités. Elle repose basiquement sur l'estimation d'un spectre fréquentiel calculé

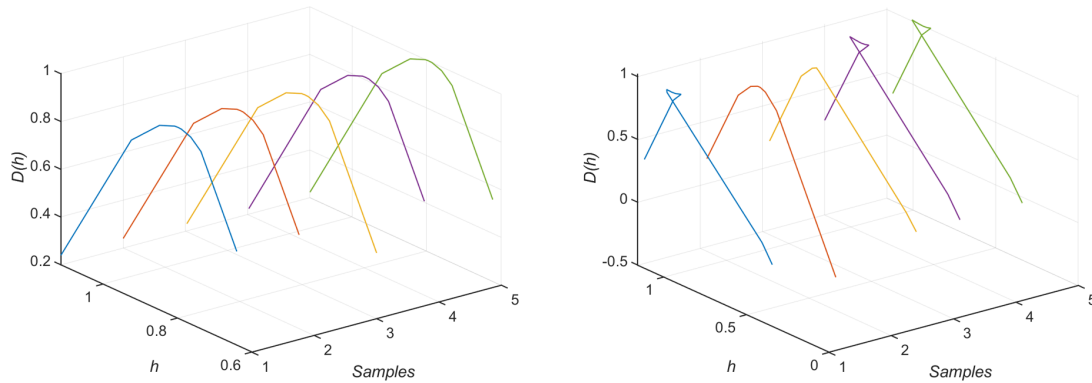
à partir de la transformation discrète du signal en coefficient d'ondelettes $T_x(\tau, k)^q$, qui sont fonction d'une analyse à différentes échelles de temps τ et des moments statistiques du signal q . Lorsque le signal à analyser présente une propriété d'auto-similarité, et donc que le spectre fréquentiel issu de l'analyse multifractale s'apparente à une loi puissance, il est possible de détecter des irrégularités du signal à travers un facteur d'échelle nommé $\zeta(q)$. De la sorte, le spectre du signal à analyser peut-être explicité tel que :

$$S(\tau, q) = \frac{1}{n_\tau} \sum_{k=1}^n T_x(\tau, k)^q \quad (5.47)$$

Pour de petites échelles ($\tau = 2^j \rightarrow 0$) il a été montré dans (Stéphane et al. [2006]) que les fonctions $S(2^j, q)$ présentent un comportement en loi de puissance tel que :

$$S(2^j, q) \approx C_q 2^{j\zeta(q)} \quad \text{avec} \quad \zeta(q) = \liminf_{2^j \rightarrow 0} \frac{\ln(S(2^j, q))}{\ln(2^j)} \quad (5.48)$$

A partir des équations précédentes, l'étude menée dans la [Revue 7]* montre qu'il est possible de détecter une anomalie à travers un algorithme d'analyse multifractale en ondelette nommé WML (Wavelet Multifractal Leader). Nous présentons donc ici les principaux résultats. Tout d'abord, un prétraitement des données provenant soit du segment « sol » (station sol, traces radars), soit du segment « air » (drone(s), avion(s), aéronef(s), ou plus généralement des agents) est effectué pour convertir la position des agents $(x(t), y(t))$ ou $(\rho(t), \theta(t))$ en un vecteur de différentiel de position entre agents $\Delta(x(t), y(t))$ ou $\Delta(\rho(t), \theta(t))$ afin d'accroître la sensibilité de l'algorithme WLM.



(a) Résultats de l'analyse multifractale sans attaque sur la position $\Delta(\rho(t), \theta(t))$. (b) Résultats de l'analyse multifractale avec attaque sur la position $\Delta(\rho(t), \theta(t))$.

FIGURE 5.12 – Résultats de l'analyse multifractale lors d'une attaque par usurpation d'identité.

Ce faisant, l'algorithme WLM fournit des caractéristiques (appelées signatures) dont les notations sont légèrement différentes que dans les équations précédentes. La signature est composée du spectre multifractal $D(h)$ défini par les moments du signal q et le facteur d'échelle

$\zeta(q)$ tel que $D(h) = \inf(1 + qh - \zeta(q))$ en fonction de h (l'exposant d'Hölder) et de la fenêtre des échantillons. La figure 5.12 présente un exemple de détection d'intrusion sur une attaque par usurpation d'identité. A partir de ces signatures, nous avons développé deux méthodes pour détecter l'anomalie. La première consiste à utiliser des seuils d'intrusion par comparer la forme de la signature pour un trafic normal et la forme de la signature lors d'une attaque. Cette comparaison est basée sur l'utilisation d'un algorithme de comparaison (en anglais, curve matching) qui calcule à chaque pas de temps t la distance (par exemple : la distance euclidienne) entre la signature fournie par l'algorithme WLM à l'instant t et la signature fournie par l'algorithme WLM à l'instant $t-1$. Enfin, lorsqu'une intrusion apparaît via l'algorithme de comparaison, nous pouvons la détecter grâce à un seuil qui permet de déclencher une alerte. La deuxième méthode consiste à utiliser un algorithme de classification (LSTM, Long Short-Term Memory ou SVM, Support Vector Machine) pour une comparaison plus précise permettant de détailler le type d'attaque en fonction du niveau de déformation de la signature. Une fois l'attaque apprise elle sera enregistrée dans une banque de signature. L'article [Revue 7]* joint à ce document présente un ensemble de résultat qui détaille la partie classification.

5.4 Conclusion & prospectives

Portés par le développement de systèmes avioniques de drones plus sûrs et robustes par construction, nos travaux de recherche au cours de ces cinq dernières années à l'ENAC se sont focalisés sur l'apport de solutions algorithmiques en estimation qui soient les mieux adaptées possible pour répondre aux problématiques de chacun des systèmes étudiés dans ce manuscrit. C'est en initiant ces travaux sur la nécessité de fournir des preuves de convergence pour les systèmes non linéaires que nous nous sommes tout d'abord orientés vers des méthodes d'estimation et d'analyse à base de modèle. Les développements sur le filtrage de Kalman et l'analyse par Sum-of-Square (SoS) ont permis d'apporter des solutions algorithmiques extrêmement intéressantes aux problèmes rencontrés en navigation inertielle et à l'étude de la dynamique du vol d'un drone au décrochage. Cependant, la recherche d'un modèle le plus complet possible et suffisant qui soit capable notamment de représenter au mieux toutes les dynamiques du système peut s'avérer complexe car il est généralement obtenu au moyen d'expérimentation en conditions réelles. Cela a notamment été le cas pour les systèmes de drones à corps basculant et la détection d'une cyber-intrusion d'un réseau de communication. C'est pourquoi, nous nous sommes tournés vers l'étude de méthodes plus proches du traitement du signal comme l'estimation algébrique ou bien l'analyse multifractale, qui apporte des solutions pour un prototypage rapide et robuste mais *a contrario* sans aucune prédiction possible sur la connaissance de l'état de l'aéronef. Du fait que ces deux types d'approche soient utiles dans le développement de systèmes avioniques plus sûrs et robustes par construction, il devient difficile de rattacher nos travaux actuels à une approche en particulier. Ce constat nous amène à décrire différentes pistes de recherche qui mériteraient d'être approfondies.

Sur l'estimation invariante et la commande des systèmes non linéaires

Le travail d'adaptation de la version standard de l'UKF présentée à la section 2.3.1 constitue l'approche la plus naturelle (voir figure 5.13) pour dériver un estimateur invariant dont les termes de correction sont d'une part, calculés selon un schéma de type UKF adapté au cadre invariant du problème d'estimation posé; et d'autre part, respectent les symétries propres au système du fait qu'ils sont construits à partir d'une innovation invariante et de gains dépendant des invariants fondamentaux et de l'erreur de sortie invariante. Comparativement à d'autres formulations de l'IUKF (Brossard et al. [2020]), l'approche proposée ici apparaît comme étant plus facilement applicable à n'importe quel type de modélisation dynamique du fait qu'elle repose uniquement sur la donnée de la transformation de groupe composite en définissant successivement chaque inverse de sigma point comme paramètre à considérer pour l'application composite $\phi_g = (\varphi_g, \psi_g, \rho_g)$.

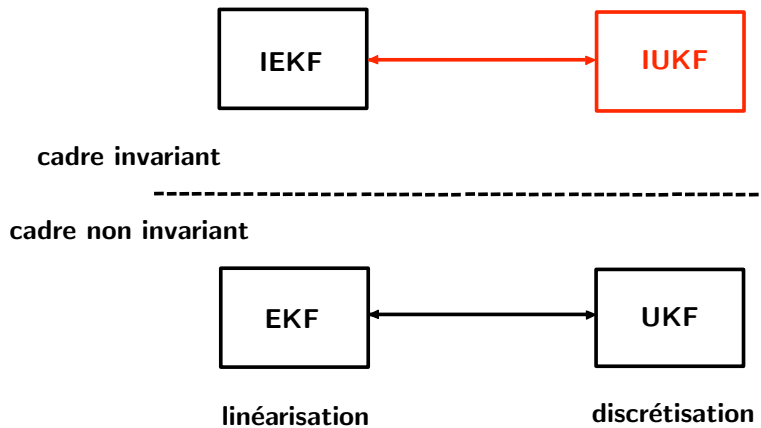


FIGURE 5.13 – Formulation de l'UKF dans un cadre invariant.

Une première piste de recherche consiste à appliquer l'IUKF à des modèles de mini-drones décrits sous forme de coefficient aérodynamique comme ceux décrits à la section 2.3.2. Ainsi une application immédiate serait de travailler au développement d'un schéma d'hybridation entre un modèle cinématique et un modèle aérodynamique dans un cadre invariant pour rendre robuste la navigation à d'éventuelles pannes capteurs (panne sur le tube de pitot par exemple). La connaissance des modèles sera complétée par des méthodes d'apprentissage utilisant des techniques de géométrie de l'information. Ainsi, les données récoltées en expérimentation seront immergées dans le groupe de transformations des rotations et translations, $SU(3)$, afin d'apporter de la connaissance sur la structure de la donnée et améliorer la performance des algorithmes d'apprentissage. Cette piste de recherche pourra être travaillée dans le cadre d'un appel à projet avec l'EASA⁹ dont l'ENAC est partenaire. Pour l'heure, elle fait déjà l'objet d'un futur projet de thèse en co-encadrement avec Gustav Olman Lundin de l'ONERA

9. <https://www.easa.europa.eu/research-projects/flight-control-laws-and-air-data-monitors>

(Office National des Etudes et de Recherches Aérospatiales) à travers un financement de la fédération de recherche ISAE/ONERA/ENAC¹⁰. Dans la même veine, nous pouvons utiliser l'erreur d'état invariante dans la synthèse d'un correcteur/estimateur afin d'améliorer les performances de la reprise autonome d'un drone en situation de décrochage. Ce point repose sur une idée qui suit une démarche similaire à ce qui a été proposé dans (Diemer et al. [2015]) avec le développement d'un contrôleur ILQG (Invariant Linear Quadratic Gaussian) appliqué à un robot mobile. Dans cet exemple, les auteurs expriment les équations du modèle linéarisées dans un repère de FRESNET dont la matrice de commande est constante et la matrice dynamique dépend uniquement des entrées. Dans le prolongement de ces travaux, il serait donc possible d'exploiter la linéarisation des équations aérodynamiques du vol autour de l'élément neutre du groupe pour étendre le domaine de convergence du système en boucle fermée et faciliter le réglage de loi de commande. Notons tout de même que des recherches complémentaires devront être menées afin de trouver le groupe de transformations adéquat qui laisse l'entière dynamique du modèle aérodynamique inchangée. Au vu de la complexité du système, cela pourra aussi nous amener à réfléchir à une méthode plus systématique de recherche de groupe de transformation, en gardant en tête que l'action du groupe doit être transitive de rang plein tel que $\dim(g) = \dim(\mathbf{x})$ pour pouvoir appliquer le théorème d'inversion locale.

Une deuxième piste de recherche consiste à trouver une manière plus précise de représenter des bruits gaussiens entrant dans les équations du filtre IUKF. Pour traiter proprement le problème de la représentation des bruits invariants dans le filtre IUKF, il est nécessaire de particulariser le groupe de transformation avec un groupe de Lie. Ainsi, dès lors que nous considérons des espaces non euclidiens, les choses deviennent plus complexes pour trouver un modèle correct de bruit Gaussien car toutes les propriétés caractéristiques de la densité normale ne sont plus détenues par une seule distribution. A titre d'exemple, la distribution de VON MISES-FISHER sur le cercle maximise l'entropie lorsque le premier moment est imposé. Dans le prolongement de récents travaux réalisés sur l'IUKF (Brossard et al. [2020]), nous envisageons d'optimiser les transformations par sigma-points grâce à une approche par quantification optimale. Une revue est en cours de rédaction avec Stéphane Puechmorel et Gautier Hattenberger.

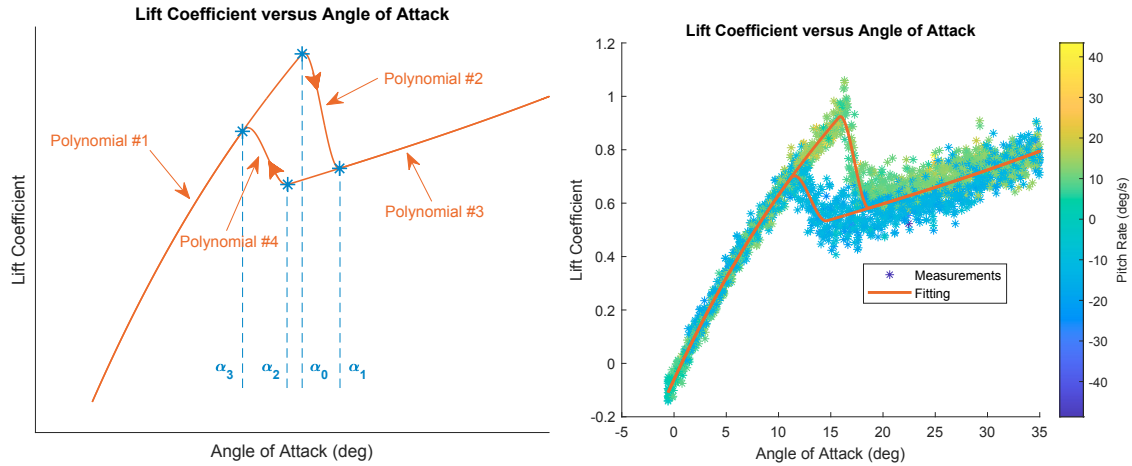
Revenons un instant sur les méthodes de commande utilisés dans nos travaux futurs. Du fait que la charge calculatoire de la méthode MPC (Model Predictive Control) soit relativement importante, il sera nécessaire d'évaluer d'autres méthodes de commande pour une implémentation en embarqué. Nous pensons notamment à la commande nommée « reference governor ». Dans un autre contexte, l'utilisation du contrôleur LQG pourrait être synthétisé dans un cadre stochastique. Nous pensons ici aux récents travaux de Panagiotis Tsiotras de Georgia Institute of Technology dans lesquels nous pourrions contribuer soit en proposant une étude de loi de commande sur une application d'un avion au décrochage ou bien intégrant dans le schéma de commande un estimateur invariant (IEKF ou IUKF).

10. <https://hal.archives-ouvertes.fr/FONISEN>

Sur les méthodes d'estimation sans modèle

Commençons par quelques remarques sur l'utilisation de l'approche multifractale pour la détection d'une cyber-intrusion. L'objectif de l'étude présentée à la section 2.3.4, consiste à mettre en évidence l'attaque injectée dans un réseau de communication à partir du spectre multifractal (ou signature) du signal à analyser. Nous pouvons ainsi construire une bibliothèque étiquetée de signatures à des fins d'apprentissage et de classification ultérieurs. Les résultats de cette étude montrent que l'utilisation de l'approche multifractale permet non seulement d'obtenir de bonnes performances en termes de faux-positif sur la détection de l'intusion pour des attaques de type MITM (Man In the Middle) mais aussi de réduire par 100 le temps d'apprentissage. Dans une tout autre application, nous envisageons d'utiliser cet outil de détection pour analyser la qualité d'observation de capteurs embarqués dans un contexte de flotte de drones. La déformation de la signature pourra servir de métrique pour identifier un ou plusieurs capteurs défaillants. Le travail portera donc sur la prise en main de l'outil, l'utilisation de celui-ci dans une application multi-information et le choix d'un algorithme d'apprentissage adapté. Bien évidemment, l'apprentissage pourra s'effectuer avec des outils de géométrie de l'information comme présenté dans la section précédente. Un projet de stage puis un co-encadrement de thèse est déjà en cours de montage avec Emmanuel Lochin et Brice Berthelot de l'INERIS (Institut National de l'Environnement industriel et des RISques). Mentionnons enfin, qu'une action de valorisation a été menée pour être au plus proche de l'attente des industriels dans la cyber-sécurité. Un projet R&T avec le CNES est envisagé.

Enfin, revenons un instant sur la commande sans modèle qui soulève aussi quelques problématiques de recherches intéressantes pour le futur. Tout d'abord, une piste d'amélioration pour pallier à la nécessité de trouver le bon réglage de la fenêtre d'intégration dans la commande MFC (section 5.3.3) serait de modifier la structure de l'estimateur en proposant un filtre adaptatif en fréquence comme celui proposé dans (Casiez et al. [2012]). Les auteurs utilisent un filtre passe-bas du premier ordre avec des fréquences de coupures qui réduisent les fluctuations et le retard en fonction de la variation rapide ou lente du signal. Par ailleurs, il est tout à fait légitime de se poser la question de savoir si l'architecture d'une commande MFC peut être appliquée à tous les systèmes étudiés dans ce manuscrit. La commande MFC est fortement dépendante de la qualité de l'estimateur et *a fortiori* des mesures, ce qui restreint son utilisation à des systèmes à minimum de phase. De ce fait, en l'état, il sera difficilement envisageable d'appliquer la MFC pour des systèmes à retard comme les systèmes flexibles (section 2.2.1.1) ou bien des systèmes intégrant des phénomènes d'hystérésis (décrochage dynamique). Ainsi, les futurs travaux en commande devront porter sur des lois spécifiques aux systèmes hybrides et aux systèmes sur-actionnés dont l'utilisation de différentes surfaces de contrôle permettra de commander les modes propres des ailes en flexion et en torsion. De nombreuses réflexions sur le thème des drones flexibles sont déjà en cours à travers un co-encadrement de thèse avec Laurent Burlion de l'université de Rutgers.



(a) Le modèle proposé pour le coefficient de portance. (b) Résultats de l'identification sur des données expérimentales.

FIGURE 5.14 – Résultats sur l'identification d'un modèle à ailes rigides au décrochage.

Sur la méthode d'analyse par Sum-of-Squares

Dans un tout autre registre, les développements entrepris sur l'estimation des régions de stabilité des systèmes non linéaires ont aussi fourni de premiers résultats prometteurs dont les perspectives d'amélioration restent nombreuses. Suite à nos travaux d'adaptation de la méthode d'analyse par Sum-of-Square (SoS) à une classe de système dit à basculement (en anglais, switching system), nous pouvons envisager de poursuivre les recherches sur l'analyse de modèles non linéaires plus complexes. Nous pensons aux travaux de thèse en cours de VINCENT GUIBERT sur l'identification d'un modèle aérodynamique à ailes rigides au décrochage présentés dans la [Conf 21]* ci-jointe et dans lequel il fait apparaître une forme hystérésis sur le coefficient de portance $CL(\alpha)$ (voir figure 5.14) ou bien aux futurs travaux en lien avec la thèse en cours de ROMAIN JAN sur l'identification d'un modèle aérodynamique à ailes flexibles au décrochage dans lequel de multiples formes hystérésis apparaissent en fonction de la déformation de la voilure. D'une part, il sera nécessaire de prendre en compte des saturations sur les actionneurs dans la recherche des régions de stabilité et d'autre part, les joints de coupures de la modélisation en polynôme par morceaux devront être déterminés de façon systématique ce qu'aucune technique d'optimisation ne permet de faire aujourd'hui du fait d'optimum locaux. Sur ce dernier point, une piste de recherche intéressante serait d'utiliser la technique d'estimation algébrique pour rechercher de manière numérique des ruptures. Enfin, un dernier point et non des moindres, consiste à réduire le temps de calcul de l'analyse par SoS. Pour donner un exemple, l'analyse effectuée sur 4 variables de décision nécessite près de 4h de calcul. Pour pallier ce problème, une piste de recherche consiste à fixer le degré de la fonction de Lyapunov *a priori* ou bien adopter un autre formalisme comme l'IQC (Integral Quadratic Constraint) (Prot et al. [2007]). Pour explorer ce dernier point, un projet de stage est en cours de montage avec Jean-Marc Biannic de l'ONERA.

Bibliographie

- Allen, Michael J and Lin, Victor (2007). Guidance and Control of an Autonomous Soaring Vehicle with Flight Test Results. *45th AIAA Aerospace Sciences Meeting and Exhibit*, 2007.
- Barczyk, M., Bonnabel, S., & Deschaud, J-E. (2015). Invariant EKF Design for Scan Matching-Aided Localization. *IEEE Tansaction on Control Systems Technology*, 23(6), 2440–2448.
- Barrau, A., & Bonnabel, S. (2015). Intrinsic filtering on Lie groups with applications to attitude estimation. *IEEE Tansaction on Automatic Control*, 60(2), 436–449.
- Bonnabel, S., Martin, P., & Rouchon, P. (2008). Symmetry-preserving observers. *IEEE Tansaction on Automatic Control*, 53(11), 2514–2526.
- Bonnabel, S. (2007). Left-invariant extended Kalman filter and attitude estimation. In *Proceedings of the 46th IEEE Conference on Decision and Control*, New Orleans (LA), USA, 12–14 December 2007 (pp. 1027–1032).
- Bonnabel, S., Martin, P., & Rouchon, P. (2009). Non-linear symmetry-preserving observers on Lie groups. *IEEE Tansaction on Automatic Control*, 54(7), 1709–1713.
- Bonnabel, S., Martin, P., & Salaün, E. (2009). Invariant Extended Kalman Filter : Theory and Application to a Velocity-Aided Attitude Estimation Problem. In *Proceedings of the 48th IEEE Conference on Decision and Control*, Shanghai, China, 16–18 December 2009 (pp. 1297–1304).
- Bonnin, V (2015). From Albatrosses to Long Range UAV Flight by Dynamic Soaring. *PhD Thesis*, ISAE, 2015.
- Brossard, M., Barrau, A., Bonnabel, S (2020). A Code for Unscented Kalman Filtering on Manifolds (UKF-M). In *Proceedings of International Conference on Robotics and Automation (ICRA)*, May 2020, Paris, France.
- Bulka, E. and Nahon, M. (2017). Autonomous control of agile fixed-wing UAVs performing aerobatic maneuvers. *International Conference on Unmanned Aircraft Systems*, Miami, US-FL, jun 2017,104–113.
- Bunge, Roberto A. and Kroo, Ilan M. (2018). Automatic Spin Recovery with Minimal Altitude Loss. *2018 AIAA Guidance, Navigation, and Control Conference*, Kissimmee, US-FL, 2018.
- Casiez, G., Roussel, N. and Vogel, D. (2012). 1€ Filter : A Simple Speed-based Low-pass Filter for Noisy Input in Interactive Systems. In *Proceedings of the ACM Conference on Human Factors in Computing Systems (CHI'12)*., Austin, Texas (May 5-12, 2012). New York : ACM Press, pp. 2527-2530.

- Cunis, Torbjørn and Condomines, Jean-Philippe and Burlion, Laurent (2020). Local stability analysis for large polynomial spline systems. *Automatica*, 113, doi : 108773 March 2020.
- Chakraborty, Abhijit and Seiler, Peter and Balas, Gary J. (2011). Nonlinear region of attraction analysis for flight control verification and validation. *Control Engineering Practice*, 19(4), 335–345.
- Choi, M. D. and Lam, T. Y. and Reznick, B. (1995). Sums of Squares of Real Polynomials. *Proceedings of Symposia in Pure Mathematics*, 58(2), 103–126.
- S. Diemer and S. Bonnabel, (2015). An invariant Linear Quadratic Gaussian controller for a simplified car. In *Proceedings of IEEE International Conference on Robotics and Automation (ICRA)*, 2015, pp. 448-453.
- Engelbrecht, Jacobus A. A. (2016). Automatic Flight Envelope Recovery for Large Transport Aircraft. *PhD thesis*, University of Stellenbosch, Matieland, ZA, 2016.
- Ellis, Matthew and Liu, Jinfeng and Christofides, Panagiotis D. (2017). Economic Model Predictive Control : Theory, Formulations and Chemical Process Applications. *Springer*, Basel, CH, 2017.
- Fliess M. and Join C. (2009). Model-free control and intelligent PID controllers : towards a possible trivialization of nonlinear control ?. *15th IFAC Symposium on System Identification*, (SYSID), 2009.
- Fliess M. and Join C. (2009). Model-free control. *International Journal of Control*, Taylor & Francis, 2228–2252, 2013.
- Jäschke, Johannes and Yang, Xue and Biegler, Lorenz T. (2014). Fast economic model predictive control based on NLP-sensitivities. *Journal of Process Control*, 24(8), 1260–1272.
- Johansson, Mikael and Rantzer, Anders (1998). Computation of piecewise quadratic Lyapunov functions for hybrid systems. *IEEE Transactions on Automatic Control*, 43(4), 555–559.
- Julier, S. J. (2002). The scaled unscented transformation. In *Proceedings of the 2002 American Control Conference*, Anchorage (AK), USA, 8–10 May 2002 (pp. 4555–4559).
- Kwatny, Harry G. and Dongmo, Jean-Etienne Temgoua and Chang, Bor-Chin and Bajpai, Gaurav and Yasar, Murat and Belcastro, Christine (2013). Nonlinear Analysis of Aircraft Loss of Control. *Journal of Guidance, Control, and Dynamics*, 36(1), 149–162.
- Nikola, G. (2018). Endurance improvement of mini UAVs through energy harvesting from atmospheric gusts. *PhD Thesis*, ISAE, 2018.
- McGee, Victor E. and Carleton, Willard T. (1970). Estimates for the Points of Intersection of Two Polynomial Regressions. *Journal of the American Statistical Association*, 65(331), 1109–1124.

- Motzkin, Theodore S.(1967). The arithmetic-geometric inequality. *Symposium on Inequalities*, Air Force Academy, US-CO, 205–224.
- Papachristodoulou, Antonis and Prajna, Stephen (2009). Robust Stability Analysis of Nonlinear Hybrid Systems. *IEEE Transactions on Automatic Control*, 54(5),1035–1041.
- Angeli, David and Amrit, Rishi and Rawlings, James B. (2012). On Average Performance and Stability of Economic Model Predictive Control. *IEEE Transactions on Automatic Control*, 57(7), 1615–1626.
- Parillo, & Pablo A. (2003). Semidefinite programming relaxations for semialgebraic problems. *Mathematical Programming, Series B*, 96(2), 293–320.
- Prot, Olivier Apkarian, Pierre Noll, Dominikus. (2008). A nonsmooth IQC method for robust synthesis. In *Proceedings of Conference on Decision and Control (CDC)*, May 2007, 824 - 829. 10.1109/CDC.2007.4434313.
- Robison, D. E.(1964). Estimates for the Points of Intersection of Two Polynomial Regressions. *Journal of the American Statistical Association*, 59(305), 214–224.
- Schuet, Stefan R. and Lombaerts, Thomas J. J. and Kaneshige, John and Shish, Kimberlee H. and Stepanyan, Vahram (2017). Stall Recovery Guidance Using Fast Model Predictive Control. *AIAA Guidance, Navigation, and Control Conference*, Grapevine, US-TX, 2017.
- Smeur, E. (2018). Incremental Control of Hybrid Micro Air Vehicles. *PhD Thesis*, <https://doi.org/10.4233/uuid:23c338a1-8b34-40a6-89e9-997adbda75>, 2018.
- Stéphane Jaffard, Bruno Lashermes, Patrice Abry (2006). Incremental Control of Hybrid Micro Air Vehicles. *PhD Thesis*, <https://doi.org/10.4233/uuid:23c338a1-8b34-40a6-89e9-997adbda75>, 2018.
- Slotine, Jean-Jacques E. and Li, Weiping (1991). Applied Nonlinear Control. *Prentice-Hall*, 1991.
- Sparks, D. W. and Moerder, D. D. (2002). Optimal aircraft control upset recovery with and without component failures. *Proceedings of the American Control Conference*, Anchorage, US-AK, 2002, 3644–3649.
- Stéphane Jaffard, Bruno Lashermes, Patrice Abry (2006). Wavelet leaders in multifractal analysis. *Wavelet Analysis and Applications*, Birkhauser Verlag, pp.219–264, 2006,

Copie de 5 articles

- **Conf 9** : J.P. Condomines, C. Seren, G. Hattenberger. « Invariant Unscented Kalman Filter with Application to Attitude Estimation », *56th IEEE Conference on Decision and Control (CDC)*, MELB., Australia, 2017.
- **Revue 3** : T. Cunis, J.P. Condomines, L. Burlion. « Dynamical Stability Analysis of Aircraft Flight in Deep-Stall », *AIAA Journal of Aircraft*, 2019.
- **Conf 21** : V. Guibert, J.P. Condomines, M. Brunot, M. Bronz. « Piecewise Polynomial Model Identification using Constrained Least Squares for UAS Stall », *SYSID, System Identification*, 2021.
- **Revue 1** : J.M.O. Barth, J.P. Condomines, M. Bronz, J.M. Moschetta, C. Join, M. Fliess. « Model-Free Control Algorithms For Micro Air Vehicles With Transitioning Flight Capabilities », *International Journal of Micro Air Vehicles*, 2020.
- **Revue 7** : R. Zhang, J.P. Condomines, E.Lochin. « A Multifractal Analysis and Machine Learning based Intrusion Detection System with Application in a UAS/RADAR system », *Drones*, MDPI, 2022.

Invariant Unscented Kalman Filter with application to attitude estimation

Jean-Philippe Condomines^a, Cédric Seren^b and Gautier Hattenberger^a

Abstract—This paper addresses the problem of nonlinear attitude estimation for mini-UAVs and proposes a novel formulation of the Unscented Kalman Filter (UKF), named Invariant UKF (IUKF), adapted to dynamical systems possessing symmetries. A first attempt for designing a symmetry-preserving observer based on an UKF-like technique has been proposed by the authors recently, leading to the development of the so-called π -IUKF estimation algorithm. The IUKF presented in this article relies on the same ideas as the usual UKF, but instead of using a linear correction term based on a linear output error, it uses a geometrically adapted correction term based on an invariant output error; similarly the gain matrix is not updated from linear error terms (in state and output), but from invariant ones. Therefore, its mathematical formulation differs from the one associated with former π -IUKF observer in not requiring the definition of a compatibility condition. From a practical point of view, the advantage of KF-like methods for designing any invariant state observer is their automatic tuning of the correction gains based on the computation of estimation error covariance matrices. Thus, this paper investigates a systematic approach to construct invariant filters derived from the unscented transform. The invariance properties, as well as the filtering performances, of the proposed IUKF are evaluated by post-processing real data gathered from experiments carried out on a quadrotor mini-UAV equipped with low-cost sensors. The results obtained validate our design.

I. INTRODUCTION

Many recent progresses in the miniaturization of electromechanical sensors have led to the design of small and cheap integrated navigation system hardwares (complete inertial measurement unit, Global Positioning System (GPS) module, etc.), which have, for their part, contributed to boost the market of mini-UAVs over the last decades significantly, making them more accessible to everyone. Nevertheless, this accessibility is frequently inconsistent with good measurement performances. For instance, the GPS modules commonly used in the *Paparazzi* autopilot (see <https://paparazziuav.org/>) deliver an absolute position with an average accuracy of 5m up to 10m under certain flight conditions. Therefore, a need for data fusion arises, especially when the final objective consists in developing robust and powerful advanced control strategies to increase the autonomy of mini-UAVs. So much so that full state (or estimated state) feedback designs (e.g., LQG/LTR syntheses) can provide full authority to efficiently control the flight of mini-UAVs in terms of stability and handling

^a Assistant-professors at ENAC, University of Toulouse, Toulouse, France
 ▶ jean-philippe.condomines@recherche.enac.fr
 ▶ gautier.hattenberger@enac.fr

^b Research scientist at ONERA, The French Aerospace Lab, Information Processing and Systems Department, Toulouse, France
 ▶ cedric.seren@onera.fr

qualities. To this aim, *nonlinear estimation* offers several well-proven algorithmic techniques which permit to recover an acceptable level of accuracy on some key flight parameters (anemometric angles, orientation/attitude, linear and angular speeds, position, etc.) when these latter are badly measured. An overview of nonlinear estimation methods can be found in the literature from many books or surveys (e.g., [12],[13]). Figure 1 attempts to propose a non exhaustive classification of these latter and positions the article’s topic in it (white terms in grey boxes). As they involve several theoretical principles, *Kalman-based invariant observers* can be qualified as hybrid filters. Although dynamical systems possessing symmetries have been already studied in control theory, few results on symmetry-preserving observers exist today. Invariant nonlinear estimation theory appears so as a young research domain whose first main contributions can be dated from the beginning of 2000s ([1]-[5], [7]-[10], [14], [16], [17]). At that time, research works led to construct symmetry-preserving observers whose correction gains were not tuned automatically, but determined to guarantee a local convergence of the estimated state around every trajectory. The choice of their associated numerical values can also be driven by more specific considerations (e.g., decoupled state estimation, perturbations rejection, etc.). Hence, such an approach appears as non-systematic to be reproduced for all dynamical systems and can sometimes require to tune an important number of variables when the model is too complex. Thereafter, researchers have tried to develop more generic procedures which facilitate the design of invariant observers, by performing an automatic tuning of the correction gains which occur in any filtering equation associated with nonlinear state observer.

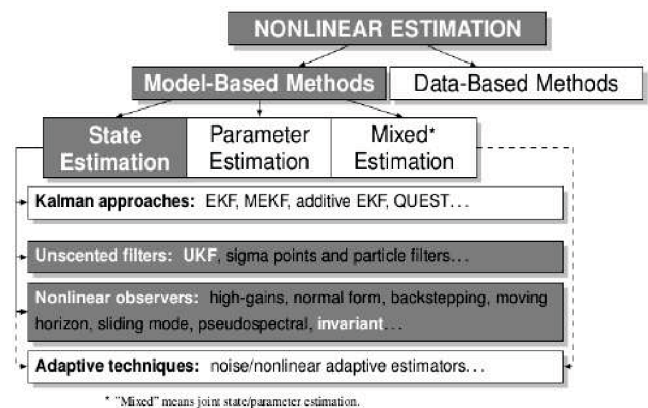


Fig. 1. Non exhaustive classification of existing nonlinear state estimation techniques and paper topic positioning.

Regarding the state of the art, there exist two techniques that allow an automatic tuning of these gains while preserving all invariant framework properties (e.g., larger convergence domain): the Invariant Extended Kalman Filter (IEKF - [4], [7]) and more recently the Invariant Particle Filter (IPF - [5]). For instance, the symmetry-preserving IEKF observer computes an optimal correction gain matrix such that the estimated state will be of minimum variance. This optimality must be considered here w.r.t. an invariant state error. Such as in the standard version of the EKF, the IEKF requires multiple linearization operations to derive an appropriate formulation enabling the computation of the correction gain matrix as in the EKF (see [7] for more details). In particular, it needs to linearize a system of nonlinear differential equations which govern the invariant state estimation error dynamics. From a computational point of view, it may sometimes be difficult to achieve this kind of calculation depending on system modeling complexity, especially when this complexity constrains any linearization to be performed numerically. Thus, to alleviate this potential numerical burden specific to the IEKF, the idea of using an UKF-like technique ([15], [18], [19]) to compute the correction gain matrix has emerged. The main contributions of this paper are therefore:

- to propose a novel and generic formulation of the UKF (in its square-root form) which preserves systems symmetries (in §II). This formulation relies on both notions of invariant state/output estimation errors that are used to calculate all predicted covariance terms. Like the IEKF, the resulting IUKF observer possesses invariant properties;
- to make explicit (in §III.A and §III.B) the system of differential equations that describes the proposed IUKF in the benchmarking case of an Attitude and Heading Reference System (AHRS);
- and finally to assess the IUKF on the basis of real flight data gathered from experiments performed on a quadrotor mini-UAV equipped with low-cost sensors (in §III.C).

II. THE INVARIANT UNSCENTED KALMAN FILTER

Inspired by the theory of continuous-time symmetry preserving observer [6] a novel and original UKF-based approach has been developed in [11] to address the approximation issue of the invariant EKF without requiring any linearization of the dynamical systems equations or compatibility condition such as proposed in the π -IUKF algorithm [9], [10]. The IUKF relies on the basic theoretical principles developed by Julier and Uhlmann at the beginning of 2000s (see [15]) which have been since widely applied to various nonlinear state estimation problems (cf. [18]).

Proposition 1: Considering a whole state space representation, the composite transformation $\phi_{\mathbf{g} \in \mathbf{G}} = (\psi_{\mathbf{g}}, \varphi_{\mathbf{g}}, \rho_{\mathbf{g}})$ and starting from initial values $\hat{\mathbf{x}}_0 = \mathbf{E}[\mathbf{x}_0]$, $\mathbf{P}_0^{\mathbf{xx}} = \mathbf{E}[\boldsymbol{\eta}(\mathbf{x}_0, \hat{\mathbf{x}}_0)\boldsymbol{\eta}^T(\mathbf{x}_0, \hat{\mathbf{x}}_0)]$ the two-steps procedure (prediction/correction) permit to design the following invariant nonlinear state observer in discrete time:

Step ① - Prediction:

(i) State ($\forall i \in \llbracket 0; 2n \rrbracket$):

$$\mathcal{X}_{k+1|k}^{(i)} = f(\mathcal{X}_{k|k}^{(i)}, \mathbf{u}_k) \Rightarrow \hat{\mathbf{x}}_{k+1|k} = \sum_{i=0}^{2n} W_m^{(i)} \mathcal{X}_{k+1|k}^{(i)}$$

(ii) Invariant state error covariance:

By posing: $\forall i \in \llbracket 0; 2n \rrbracket$, $\boldsymbol{\eta}_{k+1|k}^{(i)} = \boldsymbol{\eta}(\hat{\mathbf{x}}_{k+1|k}, \mathcal{X}_{k+1|k}^{(i)})$
And: $\boldsymbol{\Delta} = [\boldsymbol{\eta}_{k+1|k}^{(1)} \mid \boldsymbol{\eta}_{k+1|k}^{(2)} \mid \dots \mid \boldsymbol{\eta}_{k+1|k}^{(2n)}] \in \mathbb{R}^{n \times 2n}$

$$\mathbf{S}_{k+1|k}^{\mathbf{xx}} = \begin{cases} \textcircled{1} \text{qr}(W_{c,(1)}^{1/2} \cdot \boldsymbol{\Delta} \cdot \mathbf{V}_k^{1/2}) \\ \textcircled{2} \text{cholupdate}(\mathbf{S}_{k+1|k}^{\mathbf{xx}}, \boldsymbol{\eta}_{k+1|k}^{(0)}, W_{c,(0)}) \end{cases}$$

(iii) Output ($\forall i \in \llbracket 0; 2n \rrbracket$):

$$\hat{\mathbf{y}}_{k+1|k}^{(i)} = h(\mathcal{X}_{k+1|k}^{(i)}, \mathbf{u}_k) \Rightarrow \hat{\mathbf{y}}_{k+1|k} = \sum_{i=0}^{2n} W_m^{(i)} \hat{\mathbf{y}}_{k+1|k}^{(i)}$$

(iv) Invariant output error covariance:

By posing:

$$\forall i \in \llbracket 0; 2n \rrbracket, \mathbf{E}_{k+1|k}^{(i)} = \mathbf{E}(\mathcal{X}_{k+1|k}^{(i)}, \mathbf{l}_{\mathbf{u}_k}^{\mathcal{X}_{k+1|k}^{(i)}}, \hat{\mathbf{y}}_{k+1|k}^{(i)})$$

And: $\boldsymbol{\Lambda} = [\mathbf{E}_{k+1|k}^{(1)} \mid \mathbf{E}_{k+1|k}^{(2)} \mid \dots \mid \mathbf{E}_{k+1|k}^{(2n)}] \in \mathbb{R}^{p \times 2n}$

$$\mathbf{S}_{k+1|k}^{\mathbf{yy}} = \begin{cases} \textcircled{1} \text{qr}(W_{c,(1)}^{1/2} \cdot \boldsymbol{\Lambda} \cdot \mathbf{W}_k^{1/2}) \\ \textcircled{2} \text{cholupdate}(\mathbf{S}_{k+1|k}^{\mathbf{yy}}, \mathbf{E}_{k+1|k}^{(0)}, W_{c,(0)}) \end{cases}$$

(v) Invariant state/output error cross-covariance:

$$\mathbf{P}_{k+1|k}^{\mathbf{xy}} = \sum_{i=0}^{2n} W_{c,(i)} \boldsymbol{\eta}_{k+1|k}^{(i)} (\mathbf{E}_{k+1|k}^{(i)})^T$$

Step ② - Correction gain matrix computation:

$$\mathbf{K} = (\mathbf{P}_{k+1|k}^{\mathbf{xy}} / (\mathbf{S}_{k+1|k}^{\mathbf{yy}})^T) / \mathbf{S}_{k+1|k}^{\mathbf{yy}}$$

Step ③ - Correction (prediction updates):

(i) State:

By posing: $\hat{\mathbf{E}}_{k+1|k} = \mathbf{E}(\hat{\mathbf{x}}_{k+1|k}, \mathbf{l}_{\mathbf{u}_k}^{\hat{\mathbf{x}}_{k+1|k}}, \mathbf{z}_{k+1})$

And: $\forall i \in \llbracket 1; n \rrbracket$, $\bar{\mathbf{K}}_i[\mathbf{E}] = i^{\text{th}}$ row of \mathbf{K}

$$\hat{\mathbf{x}}_{k+1|k+1} = \hat{\mathbf{x}}_{k+1|k} + \sum_{i=1}^n \bar{\mathbf{K}}_i[\mathbf{E}] \cdot \hat{\mathbf{E}}_{k+1|k} \cdot \mathbf{w}_i(\hat{\mathbf{x}}_{k+1|k})$$

(ii) Invariant state error covariance:

$$\mathbf{S}_{k+1|k+1}^{\mathbf{xx}} = \text{cholupdate}(\mathbf{S}_{k+1|k}^{\mathbf{xx}}, \mathbf{K} \mathbf{S}_{k+1|k}^{\mathbf{yy}}, -1)$$

Previous matricial computations rely on both QR decomposition and rank 1 update to Cholesky factorization (cholupdate). Local transformations $(\psi_{\mathbf{g}}, \varphi_{\mathbf{g}}, \rho_{\mathbf{g}})$ are here defined as for a dynamical system preserving symmetries [6]. In this formulation, state, output and crossed error covariances are now defined from system modeling invariants. It is clear by transitivity that these matricial quantities are left unchanged by the composite transformation $\phi_{\mathbf{g} \in \mathbf{G}} = (\psi_{\mathbf{g}}, \varphi_{\mathbf{g}}, \rho_{\mathbf{g}})$. Unlike the Invariant Extended Kalman Filter (IEKF), the proposed invariant IUKF does not require a linearization of $\dot{\boldsymbol{\eta}}(\mathbf{x}_t, \hat{\mathbf{x}}_t)$ w.r.t $\boldsymbol{\eta}$ for its gain matrix computation step.

When any given permanent trajectory $t \mapsto (\mathbf{x}_p(t), \mathbf{u}_p(t))$ is followed (*i.e.*, such that $\forall t, \mathbf{I}_{\mathbf{u}_p}^{\mathbf{x}_p}(t) = \mathbf{I}$), 1st order approximation of the dynamical error $\boldsymbol{\eta}$ shows that if \mathbf{K} is also determined such that matrix $\partial\Upsilon(0, \bar{\mathbf{I}})/\partial\boldsymbol{\eta}$ is stable, then observer F will converge locally around $(\mathbf{x}_p(t), \mathbf{u}_p(t))$. Reuse of system modeling invariances within invariant observer design also guarantees that it will converge for any group action image $(\psi_{\mathbf{g}}(\mathbf{u}_p(t)), \varphi_{\mathbf{g}}(\mathbf{x}_p(t)))_{\mathbf{g} \in G}$. This property is remarkable especially for dynamical systems described by kinematics relationships whose dynamics is invariant by translation and rotation movements inside an invariant frame. By doing this, correction step procedure relies on the determination of the n additive gain which depend on system fundamental invariants and invariant innovation terms. Moreover, the invariant correction terms are projected on each component of the dynamical equations by considering the canonical basis of \mathbb{R}^n such as $\mathcal{B}(\hat{\mathbf{x}}_{k+1|k}) = \{\omega_i(\hat{\mathbf{x}}_{k+1|k})\}_{i \in \llbracket 1; n \rrbracket}$ vectors form an invariant frame for each $\hat{\mathbf{x}} \in \mathcal{X}$. Thus, the IUKF algorithm relies on a multiple parametrization defined by local transformation groups. Considering the transformation group $\phi_g = (\varphi_g, \psi_g, \rho_g)$ each inverse of sigma point can be defined as a local parameter of $(2n+1)$ invariant frame which project each sigma point on the neutral element e thought the local application φ_g .

III. BENCHMARK AND APPLICATION ON ATTITUDE ESTIMATION

A. Dynamic system modeling

This subsection details the generic modeling used to tackle and solve the issue of estimating some key flight variables (attitude-orientation, angle rates, etc.) of mini-UAVs fitted out with an Attitude and Heading Reference System (AHRS). UAVs dynamics representation corresponds here to a pure quaternional kinematics modeling (whose related quaternion will be denoted by \mathbf{q}), supplemented by additive state variables which represent low frequency sensors' imperfections (such as slowly varying biases denoted by a_s and b_s). Thereby, we consider:

$$\Sigma : \begin{cases} \dot{\mathbf{x}} = \begin{pmatrix} \dot{\mathbf{q}} = \mathbf{q} * (\boldsymbol{\omega}_m - \boldsymbol{\omega}_b)/2 \\ \dot{\boldsymbol{\omega}}_b = \mathbf{0} \\ \dot{a}_s = 0 \\ \dot{b}_s = 0 \end{pmatrix}, \\ \mathbf{y} = \begin{pmatrix} \mathbf{y}_A = a_s \mathbf{q}^{-1} * \mathbf{A} * \mathbf{q} \\ \mathbf{y}_B = b_s \mathbf{q}^{-1} * \mathbf{B} * \mathbf{q} \end{pmatrix} \end{cases}, \quad (1)$$

where $\boldsymbol{\omega}_m$ is seen as an imperfect and noisy, but known, measured input, like \mathbf{B} . Constant $\mathbf{A} = (0 \ 0 \ g)^T$ refers to the local Earth's gravity vector. Nonlinear state space representation of Eq. (1) can be described in a compact form such that $\dot{\mathbf{x}} = f(\mathbf{x}, \mathbf{u})$ and $\mathbf{y} = h(\mathbf{x}, \mathbf{u})$ where $\mathbf{u} = \boldsymbol{\omega}_m$, $\mathbf{x} = (\mathbf{q}^T \ \boldsymbol{\omega}_b^T \ a_s \ b_s)^T$ and $\mathbf{y} = (\mathbf{y}_A^T \ \mathbf{y}_B^T)^T$ are the input, state and output vectors respectively. The nonlinear state estimation problem makes use of 3 triaxial sensors which deliver a total of 9 scalar measurement signals: \blacktriangleright 3 *magnetometers* permit to obtain a local measurement of Earth's magnetic field, which is known constant and expressed in

the body-fixed frame such that vector $\mathbf{y}_B = \mathbf{q}^{-1} * \mathbf{B} * \mathbf{q}$ (where $\mathbf{B} = (B_x \ B_y \ B_z)^T$) can be considered as an output of the observation equations; \blacktriangleright 3 *gyroscopes* produce the measurements associated with the instantaneous angular rates gathered in $\boldsymbol{\omega}_m \in \mathbb{R}^3$ such that $\boldsymbol{\omega}_m = (\omega_{mx} \ \omega_{my} \ \omega_{mz})^T$; \blacktriangleright and 3 *accelerometers* provide the measured output signals corresponding to the specific acceleration, denoted by $\mathbf{a}_m \in \mathbb{R}^3$ with $\mathbf{a}_m = (a_{mx} \ a_{my} \ a_{mz})^T$. As no velocity and position information are available (no GPS, nor airspeed sensor), this AHRS is often qualified as *non-aided*.

B. IUKF estimator derivation

Let's consider the observer in [10] for the IUKF algorithm such that:

$$\begin{aligned} \dot{\hat{\mathbf{q}}} &= \frac{\hat{\mathbf{q}} * (\boldsymbol{\omega}_m - \hat{\boldsymbol{\omega}}_b)}{2} + \dots \\ &\quad \sum_{i=1}^3 (\bar{\mathbf{K}}_i^{1:3}[\mathbf{E}].\mathbf{E}_A + \bar{\mathbf{K}}_i^{4:6}[\mathbf{E}].\mathbf{E}_B) \mathbf{v}_i * \hat{\mathbf{q}} + \mathbf{C}_{\hat{\mathbf{q}}} \\ \dot{\hat{\boldsymbol{\omega}}}_b &= \hat{\mathbf{q}}^{-1} * \left(\sum_{i=4}^6 (\bar{\mathbf{K}}_i^{1:3}[\mathbf{E}].\mathbf{E}_A + \bar{\mathbf{K}}_i^{4:6}[\mathbf{E}].\mathbf{E}_B) \right) * \hat{\mathbf{q}} \\ \dot{\hat{a}}_s &= \hat{a}_s \cdot (\bar{\mathbf{K}}_7^{1:3}[\mathbf{E}].\mathbf{E}_A + \bar{\mathbf{K}}_7^{4:6}[\mathbf{E}].\mathbf{E}_B) \\ \dot{\hat{b}}_s &= \hat{b}_s \cdot (\bar{\mathbf{K}}_8^{1:3}[\mathbf{E}].\mathbf{E}_A + \bar{\mathbf{K}}_8^{4:6}[\mathbf{E}].\mathbf{E}_B) \end{aligned} \quad (2)$$

The invariant state estimation error dynamics $\dot{\boldsymbol{\eta}}(\mathbf{x}_t, \hat{\mathbf{x}}_t)$ is given by:

$$\begin{cases} \dot{\boldsymbol{\eta}} = \left(\sum_{i=1}^3 (\bar{\mathbf{K}}_i^{1:3}[\mathbf{E}].\mathbf{E}_A + \bar{\mathbf{K}}_i^{4:6}[\mathbf{E}].\mathbf{E}_B) \mathbf{v}_i \right) * \boldsymbol{\eta} - \frac{1}{2} \boldsymbol{\eta} * \boldsymbol{\beta} \\ \dot{\boldsymbol{\beta}} = (\boldsymbol{\eta}^{-1} * \mathbf{I}_{\mathbf{u}}^{\mathbf{x}} * \boldsymbol{\eta}) \times \boldsymbol{\beta} + \dots \\ \boldsymbol{\eta}^{-1} * \sum_{i=1}^3 (\bar{\mathbf{K}}_i^{1:3}[\mathbf{E}].\mathbf{E}_A + \bar{\mathbf{K}}_i^{4:6}[\mathbf{E}].\mathbf{E}_B) * \boldsymbol{\eta} \\ \dot{\boldsymbol{\alpha}} = -\boldsymbol{\alpha} \cdot (\bar{\mathbf{K}}_7^{1:3}[\mathbf{E}].\mathbf{E}_A + \bar{\mathbf{K}}_7^{4:6}[\mathbf{E}].\mathbf{E}_B) \\ \dot{\boldsymbol{\gamma}} = -\boldsymbol{\gamma} \cdot (\bar{\mathbf{K}}_8^{1:3}[\mathbf{E}].\mathbf{E}_A + \bar{\mathbf{K}}_8^{4:6}[\mathbf{E}].\mathbf{E}_B) \end{cases}$$

As it was mentioned, the reader can notice that the invariant state estimation error dynamics depends on system's trajectory $t \mapsto (\mathbf{x}_t, \mathbf{u}_t)$ through the invariant quantity $\mathbf{I}_{\mathbf{u}}^{\mathbf{x}}$ which is a major difference with most of nonlinear estimators. Unlike the Invariant Extended Kalman Filter (IEKF - see references [7]), the proposed IUKF does not require a linearization of $\dot{\boldsymbol{\eta}}(\mathbf{x}_t, \hat{\mathbf{x}}_t)$ w.r.t. $\boldsymbol{\eta}$ for its gain matrix computation step. This linearization can appear as a difficult operation in itself and especially for any practical implementation.

C. Experimental results

We evaluate the IUKF performances experimentally by post-processing a set of experimental data on the basis of both the dynamical modeling of Eq. (1) and the filtering equations of Eq. (2). Figure 2 displays a picture of the Parrot quadrotor mini-UAV under test and an image of the indoor flight performed to gather these real data. It also illustrates that this experiment has been made using an OptiTrack system which permits to have at disposal absolute references (see <http://www.optitrack.com/>).

As no specific autopilot hardware device has been designed for this experiment, it is noteworthy that data fusion

Fig. 3. Quaternion states estimation.

(a) Parrot quadrotor mini-UAV. (b) Indoor flight experiment.

Fig. 2. Experimental materials: Parrot quadrotor mini-UAV and OptiTrack device.

will merge low quality measurement signals delivered directly by the cheap MEMS sensors which equip any Parrot quadrotor. The interest of the following results relies less on the ability of the IUKF algorithm to estimate systems' states and outputs than on the practical verification of the theoretical properties asserted by the invariant observers framework when dealing with real data. To point out these latter, the results obtained with the IUKF algorithm have been systematically compared with the ones provided by a standard UKF approach. To lead a fair comparison, both techniques share identical setting parameters values *i.e.*, similar estimated process and measurement covariances values for matrices \mathbf{V} and \mathbf{W} . Figures 3 and 6 gather some estimation results due to a lack of space. Figure 3 shows the estimation results of the quaternion state components obtained by both UKF and IUKF algorithms. It is noticeable that both methods provide correct estimates w.r.t. the absolute

references plotted in solid red lines. The differences between the two algorithms appear when we consider the dispersion around the estimated state trajectory. Indeed, the lines plotted on figure 5, which correspond to the $\hat{\mathbf{q}}(t) \pm 3 \times \hat{\sigma}_{\mathbf{q}}(t)$ standard deviations around the mean estimated value, tend to prove that the IUKF estimation algorithm calculates more trustful quaternion estimates, or at least reduces the dispersion of these state estimates, due to the invariant framework used.

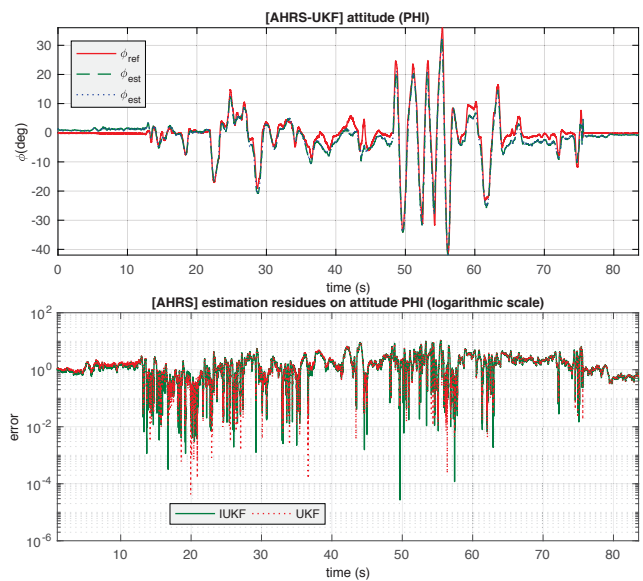


Fig. 4. Euler angles attitude estimation on ϕ and associated errors

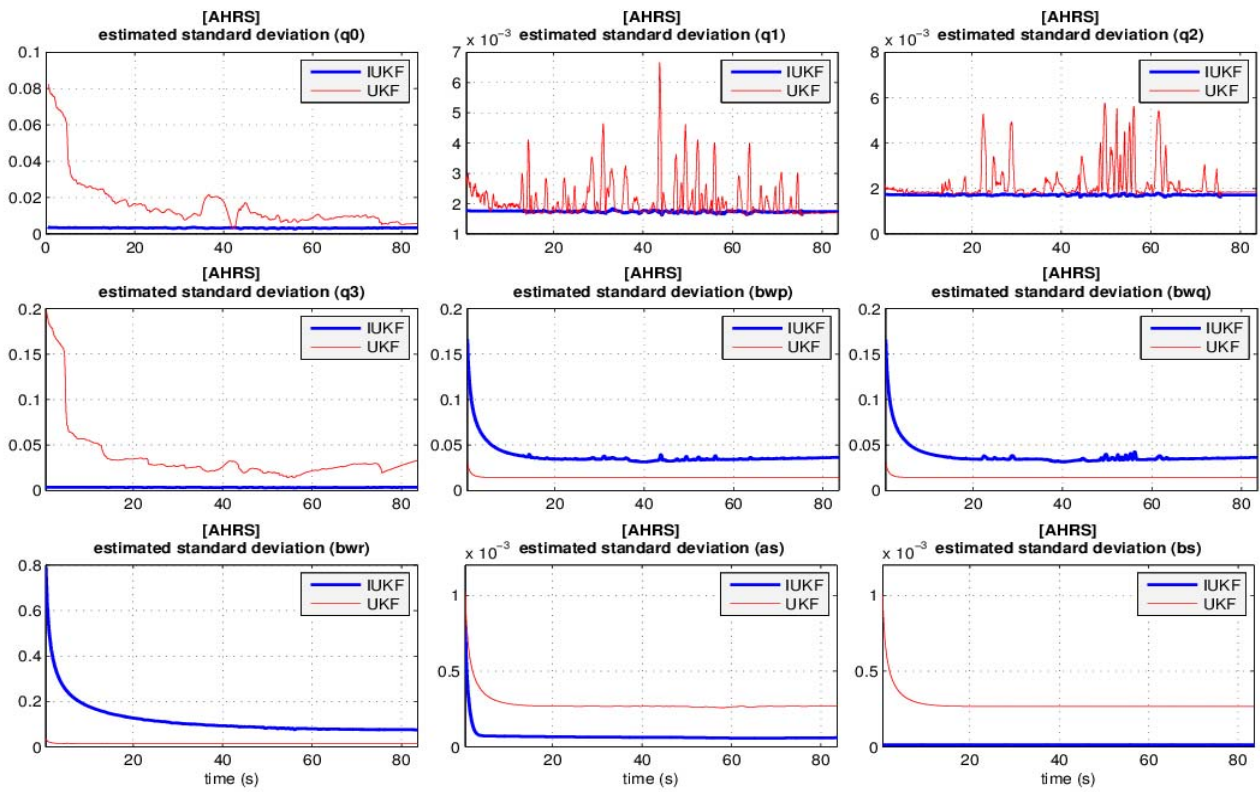


Fig. 5. Estimated theoretical standard deviations: comparison UKF/IUKF (state components).

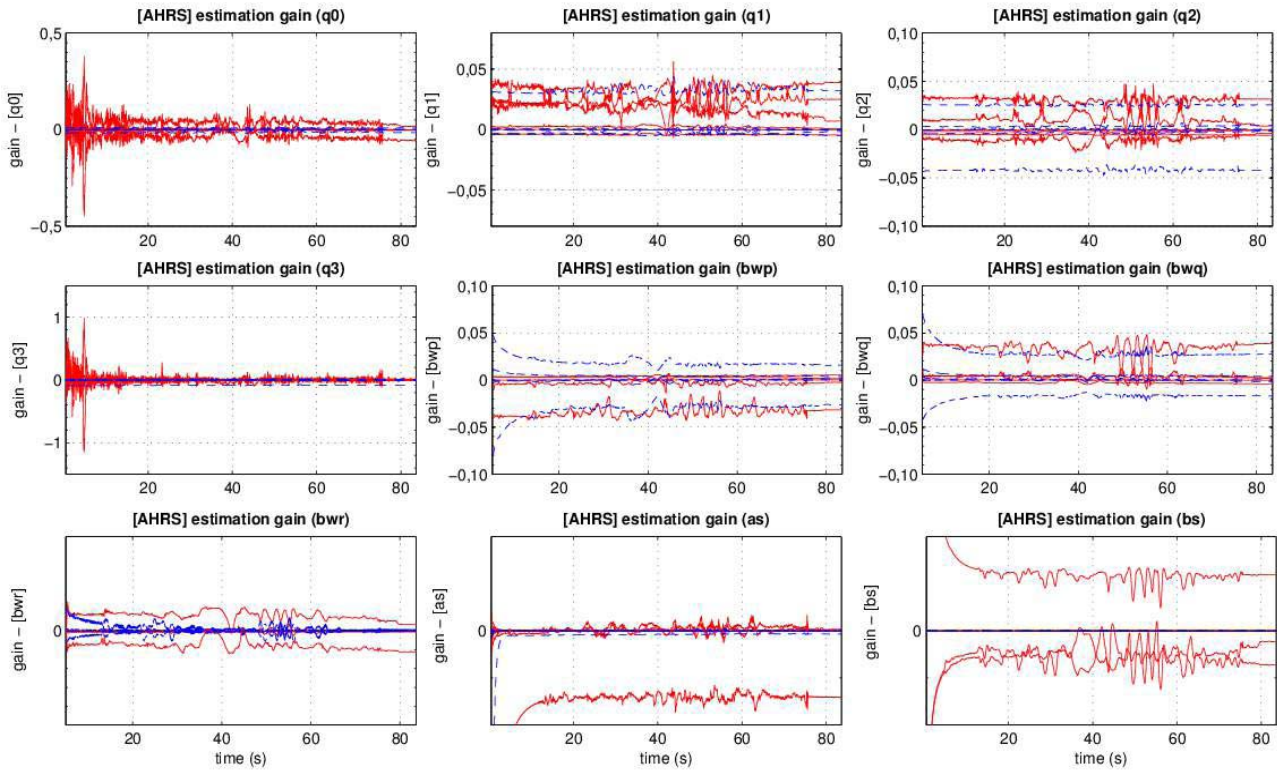


Fig. 6. Correction gains: comparison UKF (red) /IUKF (blue) (state components).

Based on these quaternion estimates, the instantaneous Euler attitude angles values, which describe at any time instant the orientation of the flying Parrot, have been deduced through time and compared with the absolute references determined by the OptiTrack system. It appears that both algorithms allow to reconstruct a suitable attitude estimation for control purposes. Due to a lack of space only the ϕ -axis estimation state error w.r.t. the absolute references is drawn in figure 4 using a logarithmic scale and show comparable results for both techniques. Expected differences brought by the invariant observer theory used to design our IUKF algorithm can be observed on Figures 5 and 6, which display, through time, both computed theoretical standard deviations and filters correction gains. By merging these results, it can be concluded that our proposed IUKF estimation technique is characterized by quasi-constant estimated standard deviations and correction gains w.r.t. any standard UKF estimation algorithm. Exploiting system's dynamics invariances in order to design nonlinear state estimation approaches allows to construct powerful nonlinear observers whose properties will be quasi-independent from the current followed trajectory. Therefore, state estimation uncertainties can be quantified by quasi-constant values through time (see for instance standard deviations on $\hat{\mathbf{q}}$).

This paves the way for designing less conservative, but robust, estimated state-feedback control laws in order to improve mini-UAVs flying and handling qualities. It is noteworthy that the reasoning made previously about the residual estimation uncertainties which impair $(\hat{\omega}_b, \hat{a}_s, \hat{b}_s)$ for both techniques is still valid when analyzing the results of Figure 5. Although it has not been demonstrated by any theoretical proof, we can notice that, when they are consistent with UKF-based results (*i.e.*, not for the state components related to gyrometer biases), the theoretical standard deviations computed by our proposed IUKF estimation technique minimize along the whole experiment the ones determined by the standard UKF methodology. This is especially remarkable for quaternion components estimates $\hat{\mathbf{q}} = (\hat{q}_0 \hat{q}_1 \hat{q}_2 \hat{q}_3)^T$. Similarly to the theoretical standard deviations computed by the IUKF observer, the correction gains (cf. Fig. 6) appear less sensitive to the non-stationary noises levels, so that we can conclude that the invariant framework offers a better high frequency perturbations rejection in terms of filtering capabilities. In the case of the IUKF estimator, these gains could be also approximated by constant values, after a given transient regime, rather than in the case of the standard UKF algorithm.

IV. CONCLUSION AND FUTURE PROSPECTS

This article has presented an innovative procedure to derive an invariant observer for nonlinear state estimation. This latter, named IUKF, combines both invariant observers theory and unscented filtering principles. The experimental results presented and gathered in §III-C have shown an equivalent capability of our proposed IUKF technique in comparison with an UKF method for nonlinear state estimation. These results have also permitted to check in realistic conditions

some invariance properties which characterize our designed observer. Among these latter, stability of estimated standard deviations, which characterize estimated state trajectory uncertainties, must be highlighted since it could facilitate new control strategies design with less conservatism.

Future works will investigate the possibility to use constant gain matrices, optimized offline by the IUKF, into a complementary observer. The benefit of this solution would be to take advantage of the computational simplicity of the complementary observer but with optimal correction terms provided by the IUKF.

REFERENCES

- [1] N. Aghannan and P. Rouchon, "On invariant asymptotic observers," in *Proc. of the 41st IEEE Conf. on Decision and Control*, vol. 2, pp. 1479-1484, 2002.
- [2] M. Barczyk, S. Bonnabel and J-E. Deschaud, "Invariant EKF design for scan matching-aided localization," *IEEE Trans. on Control Syst. Technology*, vol. 23, no. 6, pp. 2440-2448, 2015.
- [3] M. Barczyk and A. F. Lynch, "Invariant observer design for helicopter UAV aided inertial navigation system," *IEEE Trans. on Control Syst. Technology*, vol. 21, no. 3, pp. 791-806, 2013.
- [4] A. Barrau and S. Bonnabel, "Intrinsic filtering on Lie groups with applications to attitude estimation," *IEEE Trans. on Automat. Control*, vol. 60, no. 2, pp. 436-449, 2015.
- [5] A. Barrau and S. Bonnabel, "Invariant particle filtering with application to localization," in *Proc. of the 53rd IEEE Conf. on Decision and Control*, pp. 5599-5605, 2014.
- [6] S. Bonnabel, P. Martin and P. Rouchon, "Non-linear symmetry-preserving observers on Lie groups," *IEEE Trans. on Automat. Control*, vol. 54, no. 7, pp. 1709-1713, 2009.
- [7] S. Bonnabel, P. Martin and E. Salaun, "Invariant extended Kalman filter: theory and application to a velocity-aided attitude estimation problem," in *Proc. of the 48th IEEE Conf. on Decision and Control*, pp. 1297-1304, 2009.
- [8] S. Bonnabel, P. Martin and P. Rouchon, "Symmetry-preserving observers," *IEEE Trans. on Automat. Control*, vol. 53, no. 11, pp. 2514-2526, 2008.
- [9] J-P. Condomines, C. Seren and G. Hattenberger, "Pi-invariant unscented Kalman filter for sensor fusion," in *Proc. of the 53rd IEEE Conf. on Decision and Control*, pp. 1035-1040, 2014.
- [10] J-P. Condomines, C. Seren and G. Hattenberger, "Nonlinear state estimation using an invariant unscented Kalman filter," in *Proc. of the AIAA Guidance, Navigation and Control Conf.*, pp. 1-15, 2013.
- [11] J-P. Condomines, C. Seren and G. Hattenberger, *Optimal invariant observers theory for nonlinear state estimation*. Multisensor attitude estimation: fundamental concepts and applications, CRC Press, Taylor & Francis, pp. 391-408, 2017.
- [12] J. L. Crassidis, F. L. Markley and Y. Cheng, "Survey of nonlinear attitude estimation methods," *Journal of Guidance, Control and Dynamics*, vol. 30, no. 1, pp. 12-28, 2007.
- [13] J. L. Crassidis and J. L. Junkins, *Optimal estimation of dynamic systems*. Chapman & Hall, CRC Press, 2004.
- [14] S. Diemer and S. Bonnabel, "An invariant linear quadratic Gaussian controller for a simplified car," in *Proc. of the IEEE Conf. on Robotics and Automat.*, pp. 448-453, 2015.
- [15] S. J. Julier and J. K. Uhlmann, "Unscented filtering and nonlinear estimation," in *Proc. of the IEEE*, vol. 92, no. 3, pp. 401-422, 2004.
- [16] A. Khosravian, J. Trunpf, R. Mahony and C. Lageman, "Observers for invariant systems on Lie groups with biased input measurements and homogeneous outputs," *Automatica*, vol. 55, pp. 19-26, 2015.
- [17] P. Martin and E. Salaun, "Invariant observers for attitude and heading estimation from low-cost inertial and magnetic sensors," in *Proc. of the 46th IEEE Conf. on Decision and Control*, pp. 1039-1045, 2007.
- [18] S. Sarkka, "On unscented Kalman filtering for state estimation of continuous-time nonlinear systems," *IEEE Trans. on Automat. Control*, vol. 52, no. 9, pp. 1631-1641, 2007.
- [19] R. van der Merwe, and E. A. Wan, "The square-root unscented Kalman filter for state and parameter estimation," in *Proc. of the IEEE Int. Conf. on Acoustics, Speech and Signal Proc.*, pp. 3461-3464, 2001.



Dynamic Stability Analysis of Aircraft Flight in Deep Stall

Torbjørn Cunis*

ONERA–The French Aerospace Lab, 31055 Toulouse, France

Jean-Philippe Condomines†

ENAC, Université de Toulouse, 31055 Toulouse, France

Laurent Burlion‡

Rutgers University, Piscataway, New Jersey 08854

and

Anders la Cour-Harbo§

Aalborg University, 9220 Aalborg East, Denmark

<https://doi.org/10.2514/1.C035455>

Beyond aerodynamic stall, the analysis of aircraft flight requires models accurately representing nonlinearities and instabilities. Previous bifurcation analysis studies therefore had a priori knowledge of the aircraft dynamics including dynamic damping. Yet, unlike airliners, extensive wind-tunnel tests and high-fidelity models are rarely available for small unmanned aircraft. Instead, continuous fluid dynamic simulations may provide basic insights into the aerodynamics, however limited to static conditions. In this paper, bifurcation analysis is presented as a tool to discuss the effects of unidentified pitch-damping dynamics during deep-stall transition that allows development of a nonlinear pitch-damping model for a small unmanned aircraft. By preliminary study of the static case, the model is extended based on deep-stall flight data to predict dynamics and stability. As a result, the deep-stall modes of the extended model are investigated in full envelope.

Nomenclature

C_D	= aerodynamic drag coefficient, parallel to airstream, -
C_L	= aerodynamic lift coefficient, perpendicular to airstream, -
C_m	= aerodynamic coefficient moment body y_f axis, -
\mathbf{D}	= drag force, pointing toward negative air-path x_a axis, N
\mathbf{F}	= thrust force, pointing toward positive body x_f axis, N
k	= number of measurements
\mathbf{L}	= lift force, pointing toward negative air-path z_a axis, N
p, r	= roll and yaw rates, rad/s
q	= pitch rate, rad/s
V_A, \mathbf{V}_A	= aircraft speed and velocity relative to air ($V_A = \ \mathbf{V}_A\ _2$), m/s
\mathbf{X}^*, η^*	= state vector and elevator deflection at trim condition
x_a, y_a, z_a	= air-path axis system
x_f, y_f, z_f	= body axis system
x_g, y_g, z_g	= normal Earth-fixed axis system
α	= angle of attack, rad
α_0	= low angle-of-attack boundary ($\alpha_0 = 16.2949^\circ$)
γ_A	= flight-path angle relative to air, rad
η	= elevator deflection, which is negative if leading to positive pitch moment, rad
Θ	= pitch angle, rad
κ_{pr}, κ_q	= parameters of (linear) roll–yaw and pitch damping, -
κ_{qq}	= parameter of linear damping model, -

λ_{aq}	= parameter of model of induced angle of attack, -
ξ, ζ	= aileron and rudder deflections, which is negative if leading to positive moments, rad
Φ	= bank angle, rad
$(\cdot)^{\text{post}}$	= domain of high angle of attack
$(\cdot)^{\text{pre}}$	= domain of low angle of attack

I. Introduction

THE analysis of aircraft dynamics is nowadays retrieved from the discussion of aerodynamic models by means of systems theory, which is occasionally combined with high-fidelity Monte Carlo simulations. The underlying aerodynamic model is based on physical models of the vehicle dynamics that include a description of the causes of motion (the external forces experienced by the aircraft). In the context of the flight dynamics of aerial vehicles, these forces include aerodynamic loads, gravitational forces, and propulsion. The models are typically parametric and require an initial identification phase before operation [1]. Hence, they heavily rely on our a priori knowledge. The knowledge model needs to be as representative as possible for the aircraft physics, such that it can be used to simulate the aircraft dynamics.

A. Literature Review

In the normal flight regime, where the aerodynamic coefficients are fairly linear, and for small perturbations from the trim condition, linear analysis methods apply, such as the Nyquist stability criterion or Bode plots and margins [2]. For flights at high angles of attack (as in deep stall), beyond the bounds of the linear approximation, linear approaches fail [3]. With the aircraft dynamics being highly nonlinear and mostly unstable here [4], disparate methods have been applied for analysis: bifurcation analysis is rooted on mathematical continuation and the bifurcation theory to compute trim conditions, critical (bifurcation) points, and periodical orbits of the nonlinear aircraft dynamics [5–8]. Recoverable or safe sets are determined by means of reachability [9,10], control invariance [11], and regions of local attraction [12,13]. Modeling dynamic systems by means of state representations, whether linear or nonlinear, gives us access to a direct formulation of the underlying physics of the process [1].

An understanding of the aerodynamics of the aircraft is usually gained by performing tests on the aircraft or a scaled replica in a wind tunnel. Among the aircraft studied in a wind tunnel, including

Received 31 January 2019; revision received 13 September 2019; accepted for publication 16 September 2019; published online 26 November 2019. Copyright © 2019 by the American Institute of Aeronautics and Astronautics, Inc. All rights reserved. All requests for copying and permission to reprint should be submitted to CCC at www.copyright.com; employ the eISSN 1533-3868 to initiate your request. See also AIAA Rights and Permissions www.aiaa.org/randp.

*Currently University of Michigan, Ann Arbor, MI 48109; tcunis@umich.edu. Member AIAA.

†Assistant Professor, Drones Research Group; jean-philippe.condomines@enac.fr.

‡Assistant Professor, Department of Mechanical and Aerospace Engineering; laurent.burlion@rutgers.edu.

§Associate Professor, Department of Electronic Systems; alc@es.aau.dk.

almost every commercial type as well as many experimental designs, NASA's Generic Transport Model stands out for its extensively studied aerodynamics [14,15] and wide recognition in the literature [5,12,16–20]. Establishing a satisfactory model is rarely straightforward, and ensuring that it is sufficiently representative of every aspect of the operational behavior of the true vehicle can be extremely challenging. Today, constant improvements in experimental technology and processing power have enabled us to develop increasingly reliable and accurate forecasting knowledge models. Modern computer programs allow numerical derivation of aerodynamics based on the aircraft's geometry only: additionally, or alternatively, to classical wind-tunnel experiments. Computational Fluid Dynamics (CFD) simulates aerodynamic forces and moments acting on the body in a static condition (cf. Ref. [21]); CFD offers simulations of wide ranges of incidence angles and surface deflections, just as if placed in a real wind tunnel; but, although the injection of body rates is possible too, these computations are highly expensive. In a different approach, the AVL program takes advantage of an extended vortex lattice model to linearize the aerodynamics around a specified trim point [22]. AVL includes dynamic coefficients, but it is limited to linearized predictions. In any case, an advanced aerodynamics model demands significant investment of time and funding that should be carefully considered before a modeling approach is adopted by an unmanned aircraft development project with "low-cost" constraints.

B. Main Contributions

In this study, we aim to develop a nonlinear flight dynamics model in order to study the deep-stall transition behavior of an unmanned aircraft with an extended flight envelope. For this purpose, we present bifurcation analysis as a tool to discuss the effects of pitch damping, which has been unknown here, onto the stability and dynamics of the aircraft in deep stall. In previous work analyzing and discussing bifurcations of nonlinear aircraft models, knowledge of the dynamic behavior of the aircraft was considered a priori. Without this information, in the beginning of our study, we incorporate models of aerodynamic damping into the analysis while critically assessing the model response against observations from test flights. We further propose and evaluate different approaches for dynamic models.

We consider Cumulus One, which is a commercially developed small-size unmanned aircraft. It is designed to land in a stable near-vertical descent in deep stall in order to accommodate landing where most other fixed-wing aircraft cannot; therefore, its elevator is capable of exceptionally large deflection angles, and the wings are set in a dihedral manner to enhance lateral stability. For the purpose of deep-stall analysis and control, CFD simulations resulted in static data covering large incidence angles and surface deflections. These computations took approximately 3 h per configuration.[†] (Here, "configuration" means a static aircraft with the angle of attack, sideslip angle, and control surfaces fixed to selected values. An Intel Xeon E5 with 28 cores and 64 GB RAM was used.) Further simulations of the aircraft's unsteady dynamics would have resulted in additional computations of about 10 h per configuration and each value of the rotational speed.^{**} (Namely 1 s of simulation equates to roughly 5 h of computation; simulating the aircraft pitching up from -10° to $+70^\circ$ at a speed of 2 rad/s and back to -10° at -1 rad/s then takes around 2 s to be simulated. Faster rotation indeed reduces the simulation time, but initial trials indicate the need of smaller time steps here too.) Instead, Cumulus One has performed several experimental flights demonstrating the deep-stall descents, including flights with the elevator fixed at various large deflections. With the available full-envelope modeling data as well as in-flight measurements at high angles of attack, the Cumulus One provides an advantageous testbed for the derivation and discussion of nonlinear analysis approaches for low-cost aircraft. However, because the CFD data do not include dynamic behavior, the effects of body rates to dynamics and stability at high angles of attack need to be modeled separately. We therefore will

study the effect of longitudinal pitch damping during the transition into deep stall and subsequently extend the flight dynamics model in order to predict static and dynamic stabilities. The extended model then enables the assessment of deep-stall modes on the basis of real flight data gathered from experiments performed on the Cumulus One.

C. Outline

In the following section, we briefly introduce the Cumulus One aircraft as well as the flight data used in this study, we derive a longitudinal aerodynamic model of Cumulus One from well-known equations of motion, and we provide an algebraic representation of its aerodynamic coefficients by a smoothed piecewise polynomial interpolation of the discrete CFD data points. The subsequent sections are organized as follows: In Sec. III, we investigate the existence and stability of longitudinal trim conditions by a bifurcation analysis of the static model. By extension of the original model, we introduce in Sec. IV two different approaches to take into account pitch damping in terms of the pitch rate and each an unknown model parameter. We thus will be able to describe the dynamic behavior around trim conditions; in particular, we discuss the influence of the model parameters and find optimal values by differential parameter optimization. In Sec. V, finally, we study the developed model in a six-degree-of-freedom trim analysis investigating poststall and deep-stall flight.

II. Piecewise Aircraft Model

In this section, we present the aircraft that we study and provide the longitudinal equations of motions based on the aerodynamics. We further discuss different fitting methods for the aerodynamic coefficients in order to attain a closed functional expression of the equations of motion suitable for continuation analysis over the full flight envelope.

A. Cumulus One

The Cumulus One (Fig. 1) is a fully autonomous 1.65-m-wingspan unmanned aircraft carried by the Danish company Sky-Watch for agricultural mapping, surveillance, and reconnaissance [23]. Instead of landing gear, it is equipped with shock-absorbing foam at its belly and intended to land vertically descending by a deliberate deep-stall maneuver. In this maneuver, with steeper flight paths, the drag of the wings becomes the dominant component to counteract the gravitational force, leading to a stable trim condition; and the horizontal distance covered during the landing is minimized. For the purpose of stable deep-stall flight, the elevator is designed to exceed the usual range and reach deflections of up to -60° . In the flight experiments considered in this study, the transition to deep stall is initiated in level flight by a step in the elevator deflection. At the same time, the throttle is reduced to zero. The aircraft responds by pitching up, reduces forward velocity to near zero, and, as a consequence, stalls. In stall, the aircraft accelerates vertically downward and the pitch angle decreases rapidly, until the system settles in a stable deep-stall trim condition with a small, negative pitch angle. During test flights, the descent is aborted after several seconds by setting the flight configuration to takeoff mode, which is basically full throttle and an elevator setting for a gentle climb. The transition from deep stall to post-takeoff climb condition takes less than 2 s. The aircraft subsequently climbs to cruising altitude, ready for a new deep stall. This procedure has been repeated for various deep-stall elevator deflections.



Fig. 1 Digital rendering of Cumulus One ready for flight [23].

[†]Private communication with V. K. Dasam, Sky-Watch A/S, Støvring, Denmark, February 2018.

^{**}Private communication with V. K. Dasam, March 2018.

Table 1 Parameters of Cumulus One

Parameter	Variable	Value	Unit
Flight mass ^a	m	1.55	kg
Wing span	b	1.66	m
Mean chord	c_a	0.174	m
Wing area	S	0.277	m ²
Air density ^b	ρ	1.25	kg/m ³
Gravitational constant	g	9.80665	m/s ²

^aTotal mass at take-off, including payload.

^bDuring the flight experiment, air density has been $\rho = 1.156 \text{ kg/m}^3$.

Figure 2 shows pitch angle and elevator deflection during initiation, descent, and recovery of an example deep-stall descent maneuver. The parameters of the Cumulus One and its environment used in this study are given by Table 1.

B. Aerodynamic Modeling

Due to its dihedral wings, the Cumulus One is considered to be laterally stable. We therefore initially neglect the lateral dynamics for the analysis of stability and, consequently, assume the sideslip angle β to vanish. In deep-stall flight and transition, the aircraft is further unthrottled; i.e., the thrust force is zero ($F = 0$). We will refer to the international standard body axis system (x_f, y_f, z_f), air-path axis system (x_a, y_a, z_a), and Earth-fixed axis system (x_g, y_g, z_g), which are, respectively, defined by the aircraft’s fuselage, velocity with respect to air (V_A), and the ground [24]. Here, lift and drag forces are defined along the air-path axes and denoted L and D ; the angle of attack α , flight-path angle γ_A , and pitch angle Θ are given by rotations between the axis systems (Fig. 3). If not stated otherwise, all variables are in SI units, i.e., meters (m), meters per second (m/s), radians (rad), radians per second (rad/s), kilograms (kg), etc.; angles are, however, given in degrees where convenient.

C. Longitudinal Equations of Motion

The longitudinal equations of motion without thrust are given as nonlinear four-state ordinary differential equations [12,16,25]:

$$m\dot{V}_A = -\frac{1}{2}\rho V_A^2 S C_D(\alpha, \eta) - mg \sin \gamma_A \quad (1)$$

$$mV_A\dot{\gamma}_A = \frac{1}{2}\rho V_A^2 S C_L(\alpha, \eta) - mg \cos \gamma_A \quad (2)$$

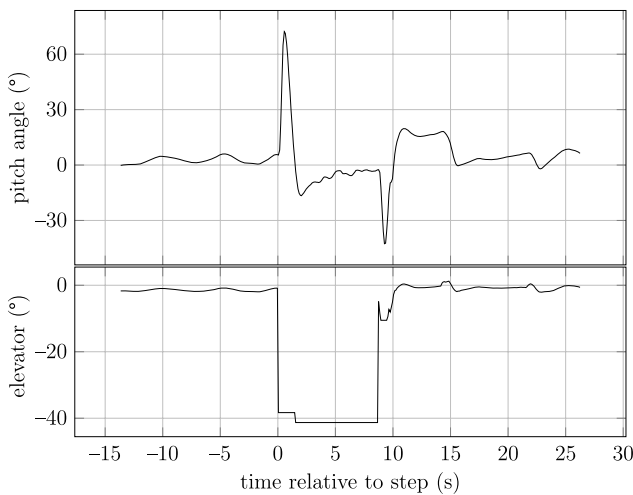


Fig. 2 Aborted deep-stall maneuver, initiated in level flight by a step in the elevator deflection command to $\eta_{t=0} \approx -38^\circ$, and then trimmed at $\eta_{t \geq 0} \approx -41^\circ$.

$$I_y \dot{q} = \frac{1}{2}\rho V_A^2 S c_a C_m(\alpha, \eta) \quad (3)$$

$$\dot{\Theta} = q \quad (4)$$

with the pitch angle

$$\Theta = \gamma_A + \alpha \quad (5)$$

and the air speed V_A as the norm of the velocity vector relative to air. Then, C_L , C_D , and C_m are dimensionless coefficients connected to the lift force, drag force, and pitching moment. The elevator deflection η is, by convention, negative when causing a positive pitching moment.

The aerodynamic coefficients of the body, wing, and surfaces of Cumulus One have been simulated at selected angles of attack and elevator deflections using static computational fluid dynamics and are given to

$$(\alpha_i, \eta_i, C_{L,i}, C_{D,i}, C_{m,i})_{1 \leq i \leq k} \subset \mathbb{R}^5 \quad (6)$$

where k denotes the number of combinations in α and η at which the CFD simulation was evaluated. Note that we do not further model the effects of the pitch rate q to aerodynamic coefficients due to a lack of dynamic data from CFD. Local stability is obtained by placing the center of gravity before the aerodynamic center [2,26]. It is well known that the pitch rate does not affect the trim conditions but, indeed, their stability; and we shall encounter this in the subsequent sections.

D. Polynomial Aerodynamic Coefficients

Polynomial models benefit from their infinite-differentiable nature, and have therefore been used to model full-envelope aerodynamic coefficients [12,16]. Fitting a polynomial function to discrete data points or measurements is straightforward and often provided by scientific computation software. We find optimal polynomials Γ of finite degrees for the CFD data in Eq. (6) by solving the functional minimization problem:

$$\Gamma_{\text{opt}} = \arg \min_{\Gamma} \sum_{i=0}^k w_i |\Gamma(\alpha_i) - C_{\odot,i}|^2 \quad (7)$$

where k is again the number of data points from CFD; C_{\odot} , and i are the simulated, aerodynamic coefficients at angle of attack α_i ; and $w_i > 0$ is a positive weight associated with the data. A solution to Eq. (7) can be obtained by least-squares optimization [27].

To prevent overfitting for the data points in the normal flight regime, where CFD simulations have been performed in steps in the angle of attack of 1° , we introduce the weights [28]

$$w_i = \begin{cases} 0.1 & \text{if } \alpha_i \leq 20^\circ; \\ 1 & \text{else} \end{cases}$$

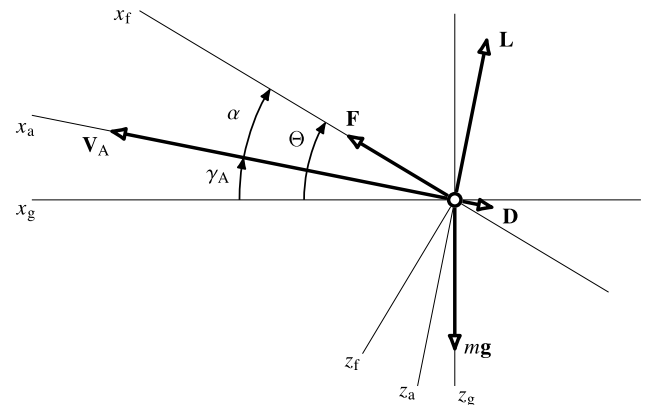


Fig. 3 Longitudinal axes with angles and vectors for $\beta = 0$.

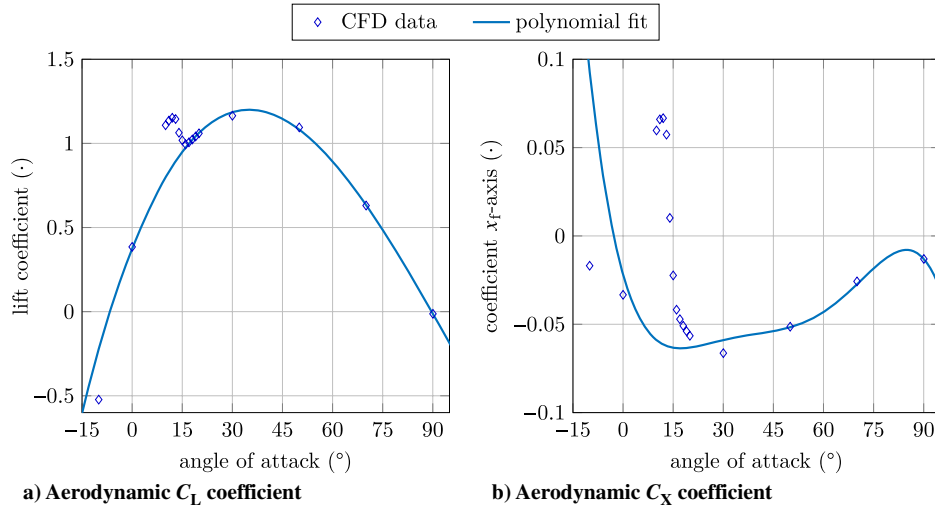


Fig. 4 Polynomial model of aerodynamic coefficients.

The resulting third-order polynomial model is shown in Fig. 4. While the polynomial roughly fits the CFD data for the lift coefficient (Fig. 4a), it fails to represent the aerodynamics in the body axis system, as demonstrated in Fig. 4b. An extensive discussion of polynomial aerodynamic models can be found in the work of Cunis et al. [29].

E. Piecewise Polynomial Aerodynamic Coefficients

To overcome the limits of polynomial models, Cunis et al. [29,30] proposed to fit polynomial segments piecewise, both for low and high angles of attack, as the aerodynamics are significantly altered by the stall of the wings. Here, a pair of polynomial functions virtually accounting for the dynamics before and after stall are obtained. The resulting model is continuous over the entire domain but not necessarily differentiable in its joint. Such piecewise optimal polynomial functions are obtained as a simultaneous solution to

$$\begin{aligned} (\Gamma_{\text{opt}}^{\text{pre}}, \Gamma_{\text{opt}}^{\text{post}}) = \arg \min_{\Gamma_{1,2}} \sum_{i \in \mathcal{I}_1} w_i |\Gamma_1(\alpha_i) - C_{\circ,i}|^2 \\ + \sum_{i \in \mathcal{I}_2} w_i |\Gamma_2(\alpha_i) - C_{\circ,i}|^2 \end{aligned} \quad (8)$$

where $\mathcal{I}_{1,2}$ are the indices of low and high angle-of-attack data, respectively, chosen a priori. The resulting piecewise model is given as

$$\Gamma_{\text{pw}}(\alpha, \dots) = \begin{cases} \Gamma_{\text{opt}}^{\text{pre}}(\alpha, \dots) & \text{if } \alpha \leq \alpha_0; \\ \Gamma_{\text{opt}}^{\text{post}}(\alpha, \dots) & \text{else} \end{cases} \quad (9)$$

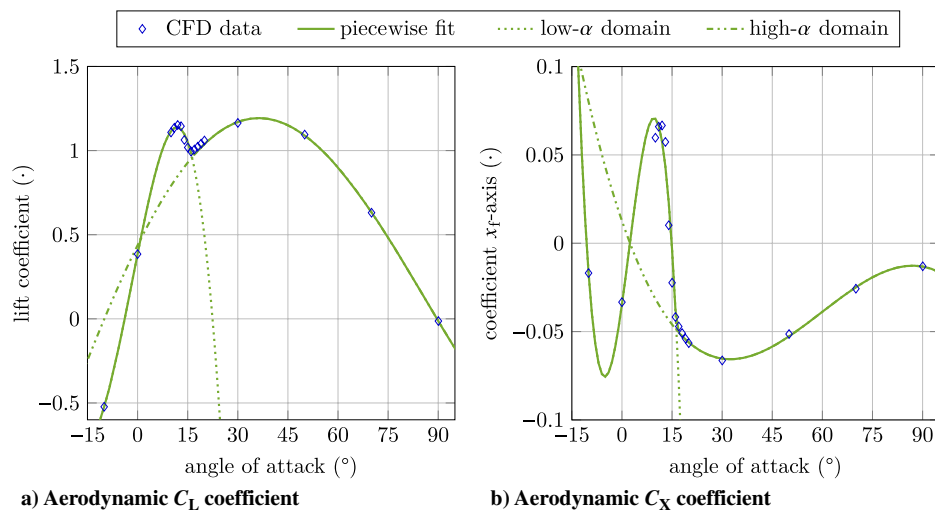


Fig. 5 Piecewise model of aerodynamic coefficients with polynomial segments.

with $\Gamma_{\text{opt}}^{\text{pre}}(\alpha_0, \cdot) \equiv \Gamma_{\text{opt}}^{\text{post}}(\alpha_0, \cdot)$, and α_0 is found as the joint of the C_X coefficient. The `pwfit` toolbox then ensures that all coefficient models are continuous in the same angle of attack α_0 [31].

Figure 5 shows the piecewise model and their polynomial segments. Defined as piecewise polynomials, we are able to account for the full-envelope characteristics of both the lift and drag coefficients, as well as the coefficients in body axes. The pitch-moment coefficient C_m is modeled likewise [32].

F. Blending Function for the Piecewise Model

Numerical tools, such as the Newton method, that use the local gradient fail at the discontinuity of the partial first derivative of Eq. (9) in α . Instead, we are blending the polynomial segments into each other using the Heaviside step function:

$$\begin{aligned} \Gamma_{\mathcal{H}}(\alpha, \dots) = \mathcal{H}(\alpha - \alpha_0) \Gamma_{\text{opt}}^{\text{pre}}(\alpha, \dots) \\ + (1 - \mathcal{H}(\alpha - \alpha_0)) \Gamma_{\text{opt}}^{\text{post}}(\alpha, \dots) \end{aligned} \quad (10)$$

A smooth, analytic approximation for $\mathcal{H}(\cdot)$ is found in the logistic function:

$$\mathcal{H}_\epsilon(t) = \frac{1}{1 + e^{-2t/\epsilon}} \quad (11)$$

which has $\mathcal{H}_\epsilon(0) = (1/2)$, $\mathcal{H}_\epsilon(t \rightarrow -\infty) = 0$, and $\mathcal{H}_\epsilon(t \rightarrow +\infty) = 1$ for $\epsilon > 0$. Naturally, it is desirable to have the logistic parameter ϵ as small as possible in order to increase steepness; on the other hand,

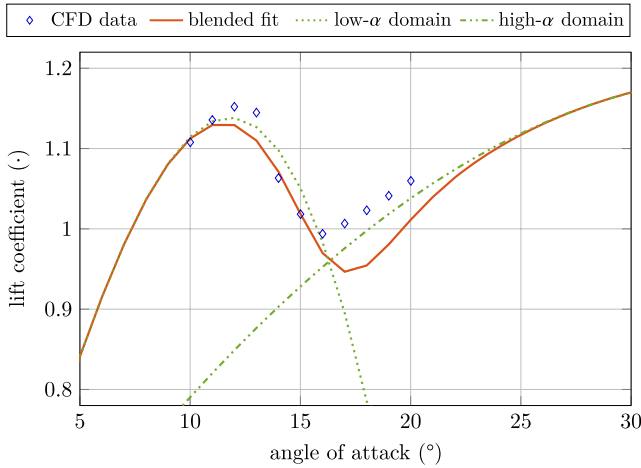


Fig. 6 Blended piecewise polynomial model of the aerodynamic lift coefficient for $\epsilon = \pi/36$.

we need ϵ to be sufficiently large to suit a numerical method. We then have that \mathcal{H}_ϵ underapproximates the Heaviside step by no more than $\delta > 0$ outside the interval $(-\tau; \tau)$ if, and only if,

$$\epsilon < \frac{2\tau}{\ln(\delta^{-1} - 1)}$$

Figure 6 shows the blended piecewise model around the joint α_0 . The polynomial segments are blended into each other by \mathcal{H}_ϵ with $\epsilon = \pi/36$.

III. Static Bifurcation Analysis

Aircraft trim conditions provide an initial insight into nonlinear aerodynamics. Unlike linear systems, nonlinear dynamics may exhibit multiple of those equilibria, and knowledge about their existence and stability is essential to any development of flight control laws. In this section, we conduct a preliminary study of longitudinal trim conditions without further assumption about damping. As a zero rate is imperative for trim, damping effects will affect stability but not the existence and the location of the trim conditions. The existence, branching, and stability of the equilibria are the domains of the continuation and bifurcation theory, which we are going to present first. We then discuss the longitudinal trim conditions and initial stability results before introducing damping models in the subsequent sections.

A. Theory of Bifurcation

The equations of motion of Sec. II are written as four-state ordinary differential equations:

$$\mathbf{f}(\mathbf{X}, \eta) = \begin{bmatrix} \dot{V}_A \\ \dot{\gamma}_A \\ \dot{q} \\ \dot{\Theta} - \dot{\gamma}_A \end{bmatrix} \quad (12)$$

with states $\mathbf{X}^T = [V_A \ \gamma_A \ q \ \alpha]$ and input η . The system is in an equilibrium or trim condition if, and only if, $\mathbf{f}(\mathbf{X}, \eta) = \mathbf{0}$. Here, Eq. (4) directly implies $q = 0$ as a necessary precondition for trim. The stability of an equilibrium (\mathbf{X}^*, η^*) in its close neighborhood is locally determined by the Jacobian matrix $\mathbf{J}^* = (\partial \mathbf{f} / \partial \mathbf{X})(\mathbf{X}^*, \eta^*)$; namely, (\mathbf{X}^*, η^*) is locally asymptotically stable if, and only if, all eigenvalues of \mathbf{J}^* have strictly negative real parts, and it is unstable otherwise [33]. If, for some parameter η^* , an eigenvalue of the Jacobian at the corresponding trim condition (\mathbf{X}^*, η^*) crosses zero and the trim condition changes stability, we have a critical (or bifurcation) point. Well-known bifurcations are the saddle node, pitchfork, and transcritical, as well as (for systems of second order or higher) Andronov–Hopf bifurcations; the latter are characterized by a family of periodic orbits emanating around the critical point [34].

With the elevator deflection as single parameter,^{††} the bifurcation analysis is a result of a continuation method, where the four equalities of $\mathbf{f}(\mathbf{X}, \eta^*) = \mathbf{0}$ are solved for small changes in η^* ; the stability of each trim condition is determined by its Jacobian \mathbf{J}^* , and we have the necessary condition $|\mathbf{J}^*| = 0$ for a bifurcation point [16]. The continuation and bifurcation of a given system can be computed using toolboxes such as the Continuation Core and Toolboxes (hereafter referred to as COCO) [35], MATCONT [36], or the Dynamical Systems Toolbox [37]. In this section, we analyze the trim conditions of longitudinal flight and their eigenvalues for the equations of motion of Sec. II. By comparison of the model with the flight experiment data and introduction of appropriate pitch damping models, we shall later extend the model to cover the dynamics of deep-stall transitioning flight.

B. Stability of Longitudinal Trim Conditions

The longitudinal trim conditions of unthrottled flight ($F = 0$) along the range of the elevator have been computed using COCO [38] for MATLAB and are shown in Fig. 7. For normal deflections (approximately $-3^\circ \leq \eta \leq 3^\circ$), the trim conditions resemble a stable, moderate descent with air speeds between 12 and 18 m/s and path inclination angles above -10° . With negative deflections, the angle of attack increases while the air speed decreases (which is a well-known behavior in aeronautics) until the additional lift decreases: the aircraft stalls (Fig. 7a). Yet, the branch of trim conditions is continued into a deep-stall descent of the almost leveled aircraft (Fig. 7b). At larger, positive deflections instead, the trim conditions indicate a steep nosedown dive. The regimes of unstable trim conditions in level flight, after stall, and in deep stall are marked by A, B, and C, respectively.

Classically, the longitudinal motion is divided into the short-period oscillation, involving the angle of attack and pitch rate, as well as the long-period phugoid oscillation of airspeed and the flight-path angle [2]. Consequently, we expect two pairs of complex-conjugated eigenvalues. Figure 8 illustrates the eigenvalues of Eq. (12) in the complex plane for the continuation of elevator deflections: The eigenvalues of the phugoid mode are distinguished by small real and imaginary parts, showing the characteristic underdamped and slow motion, whereas the short-period eigenvalues indicate the damped but fast oscillation. When one pair of eigenvalues enters the right half-plane, the longitudinal motion turns unstable and a Hopf bifurcation occurs.

IV. Analysis of Dynamic Models

With the pitch rate not being taken into account by the static CFD simulation, the aforementioned analysis has revealed that the model is insufficiently damped to be stable in deep-stall transition, whereas the flight experiments suggest stable equilibria here. Instead, we need to separately add damping effects to the aerodynamics. We will present two alternative models of pitch damping, with each depending on a single, unknown parameter; and we will discuss the stability and time responses for variations in these parameters. Finally, we obtain a quantitative model by optimization against the set of measured step responses.

A. Pitch Damping Models

Unsteady aerodynamics for stark changes of the aircraft's orientation relative to the airstream affect the damping of the aircraft. To describe the effects of a nonzero q to the pitch motion, we provide and compare the two models described in the following. The first model will consist of a simple linear damping term in the pitch-moment equation that constitutes a steady modeling approach. The second modeling approach takes into account the effective change of the angle of attack due to the rotation of the wings, and thus can be considered as quasi steady. To fully represent unsteady dynamics, one would need to include either the derivatives of the pitch rate and

^{††}The elevator deflection is chosen as continuation parameter, similar to previous studies [5, 18]; being a control input, this choice further allows a quick connection between the bifurcation analysis and in-flight measurements.

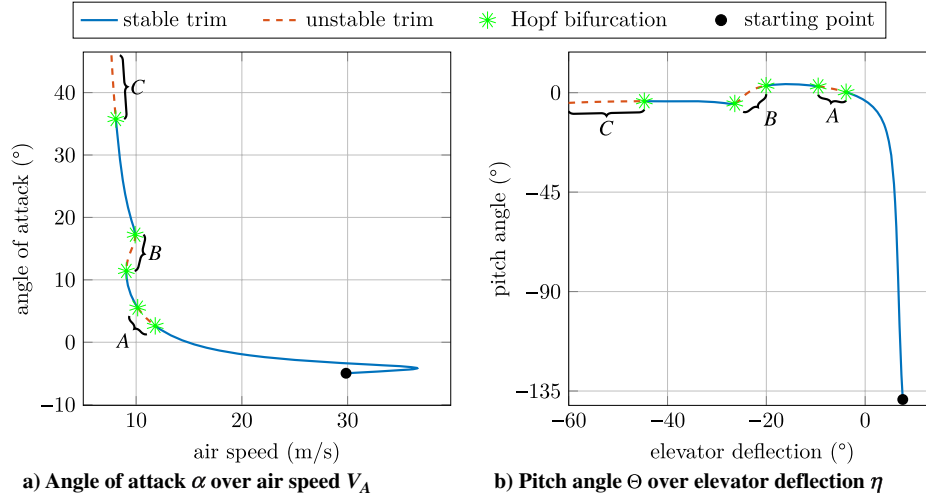


Fig. 7 Trim conditions of unthrottled longitudinal motion with the unstable regimes (A, B, C) of equilibria dashed and the starting point marked by a dot.

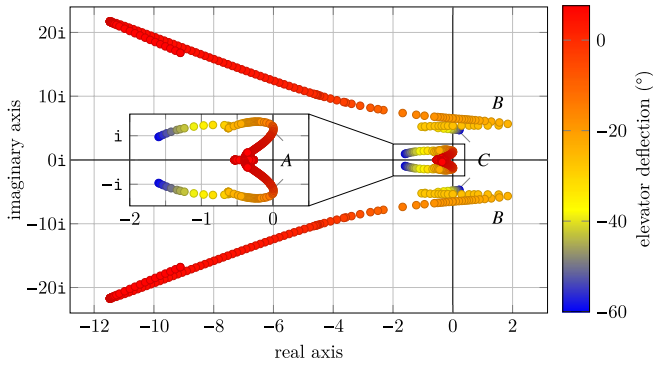


Fig. 8 Eigenvalues of longitudinal motion for varying elevator deflections; eigenvalues in the right half-plane (A, B, C) correspond to unstable trim conditions.

angle of attack or a sequence of their former values over time; this is left for future work. The models discussed here will be of the form $\dot{q} = g(X, \eta, \cdot)$ with a single, unknown parameter for each model.

1. Linear Damping Model

A simple model of the pitch damping effects is given by the extension of Eq. (3) with a damping term linear in q :

$$\dot{q} = \frac{1}{2} \rho V_A^2 S c_a I_y^{-1} C_m(\alpha, \eta) - \kappa_{\dot{q}q} q \quad (13)$$

where $\kappa_{\dot{q}q} > 0$ is the equivalent to linear dampers in classical mechanics.

2. Model of Induced Angle of Attack

More physically inspired, we can model the changes in the angle of attack induced by the nonzero pitch rate. Namely, the angle of attack and sideslip angle are calculated as [24]

$$\sin \alpha = \frac{w_A}{\sqrt{u_A^2 + w_A^2}}; \quad \sin \beta = \frac{v_A}{V_A} \quad (14)$$

where u_A , v_A , and w_A are the components of the air-path velocity vector in the body axis system. With the sideslip angle being neglected (i.e., the lateral component v_A is much smaller than V_A), Eq. (14) simplifies to

$$\sin \alpha = \frac{w_A}{V_A} \quad (15)$$

A nonzero pitch rate leads to a vertical motion of the wing as well as the horizontal tail, which is proportional to q :

$$\bar{V}_q \sim q \quad (16)$$

where the proportionality is positive if the aerodynamic center of the aircraft is located behind the aircraft's center of gravity. (That is, the aircraft is stable [26].) Introducing the induced angle of attack $\tilde{\alpha} = \alpha + \Delta\tilde{\alpha}$ and noting $\tilde{w}_A = w_A + \bar{V}_q$, we have

$$\sin \tilde{\alpha} = \frac{w_A}{V_A} + \frac{\bar{V}_q}{V_A} \quad (17)$$

Trigonometric identity yields

$$\sin(\alpha + \Delta\tilde{\alpha}) = \sin \alpha \cos \Delta\tilde{\alpha} + \cos \alpha \sin \Delta\tilde{\alpha}$$

and, with Eq. (15) and small changes $\Delta\tilde{\alpha}$, we conclude in

$$\Delta\tilde{\alpha} \approx \lambda' (\cos \alpha)^{-1} \frac{q}{V_A} \quad (18)$$

where λ' is the (unknown) constant of proportionality between \bar{V}_q and q . Using the notation of the normalized pitch rate $\hat{q} = q c_a / V_A$, insertion into Eq. (3) gives us

$$\dot{q} = \frac{1}{2} \rho V_A^2 S c_a I_y^{-1} C_m(\alpha + \lambda_{aq} (\cos \alpha)^{-1} \hat{q}, \eta) \quad (19)$$

with $\lambda_{aq} = \lambda' / c_a > 0$ for a stable aircraft. Here, for $\hat{q}, \eta = \text{const.}$, the curve of $C_m(\alpha, \cdot)$ is shifted to $C_m(\tilde{\alpha}, \cdot)$ by $\Delta\tilde{\alpha}$. With $C_m(\tilde{\alpha}, \cdot)$ monotonically decreasing in $\tilde{\alpha}$, a positive pitch rate decreases the pitch moment ($\alpha \leq \tilde{\alpha} \Rightarrow C_m(\alpha, \cdot) \geq C_m(\tilde{\alpha}, \cdot)$, and vice versa), effectively damping the motion. For an unstable aircraft where the wing's aerodynamic center is located before the center of gravity [26], $C_m(\tilde{\alpha}, \cdot)$ increases in $\tilde{\alpha}$; then, with $\lambda_{aq} < 0$, the pitch moment is again decreased by a positive pitch rate, resulting in a dissipative system.

B. Change of Stability Due to Pitch Damping

Both the linear damping model [Eq. (13)] and the model of the induced angle of attack [Eq. (19)] rely on the choice of suitable parameters $\kappa_{\dot{q}q}, \lambda_{aq} > 0$, which are not easily determined. We therefore provide an analysis of trim conditions, stability, and eigenvalues as well as dynamics system responses for variation of those parameters.

The change in $\kappa_{\dot{q}q}$ or λ_{aq} does not affect the existence or location of longitudinal trim conditions because $q = 0$ has been identified as a necessary precondition for trim. However, the occurrence of Hopf bifurcations (and thus the size of unstable regimes) alters for nonzero damping parameters: Fig. 9 shows the respective values of the damping parameters $\kappa_{\dot{q}q}$ and λ_{aq} for each of the two damping models, such that the trim condition for the elevator deflection η undergoes a Hopf bifurcation. As a result, the regimes of unstable trim conditions

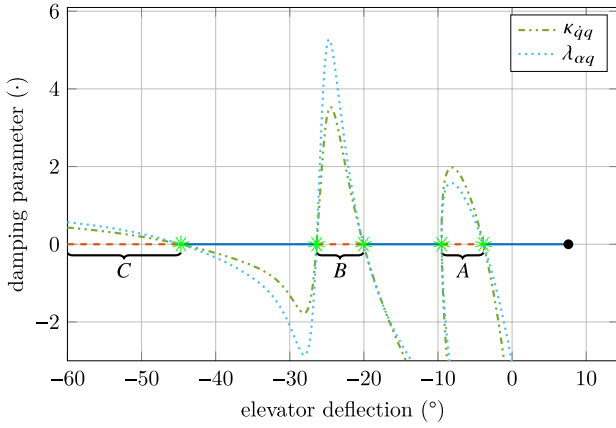


Fig. 9 Occurrences of Hopf bifurcations at elevator deflection η for continuation of the model parameters.

within the range of the elevator deflections shrink and eventually vanish for increasing values of the damping parameters. In regimes A and C, the damping models [Eqs. (13) and (19)] are similar in terms of Hopf bifurcations for increasing parameters $\kappa_{\dot{q}\dot{q}}$ and $\lambda_{\alpha q}$, respectively. Only, in regime B, larger values of $\lambda_{\alpha q}$ would be necessary to fully stabilize the dynamics with Eq. (19) in this regime. For negative damping, the unstable regimes are enlarged.

We shall discuss the effects of the damping coefficient for each of the unstable regimes:

1. *Instability in Level Flight*

In the undamped model ($\kappa_{\dot{q}\dot{q}} = \lambda_{\alpha q} = 0$), the eigenvalues of the phugoid mode enter the right half-plane in level flight and the trim

conditions are unstable for elevator deflections around $\eta = -8^\circ$ (marked with A in Figs. 7 and 8). From continuation of the Hopf bifurcations for the pitch damping coefficient in Fig. 9, we learn that this instability vanishes for damping coefficients of approximately $\kappa_{\dot{q}\dot{q}} \geq 2$ and $\lambda_{\alpha q} \geq 1.6$. Figure 10 shows step responses to elevator deflections from $\eta_{t < 0} = 0^\circ$ to $\eta_{t \geq 0} = -8^\circ$ and damping coefficients $\kappa_{\dot{q}\dot{q}}, \lambda_{\alpha q} \in [0; 5]$: with eigenvalues close to zero, both unstable and stable conditions respond slowly to the step input.

2. *Instability in Poststall*

At stall, flight dynamics often turn unstable, leading to various upset situations for conventional aircraft [5]. The Cumulus One model also has a regime of unstable trim conditions after stall (i.e., for elevator deflections around $\eta = -24^\circ$; Fig. 7, marked with B), that vanishes for pitch damping coefficients of approximately $\kappa_{\dot{q}\dot{q}} \geq 3.5$ and $\lambda_{\alpha q} \geq 5.3$ (Fig. 9). If the elevator is deflected to a value of this region, the system responds to this step with superposed oscillations that are smoothed for larger damping coefficients (Fig. 11; here, values of $\kappa_{\dot{q}\dot{q}}, \lambda_{\alpha q} \geq 5$ are sufficient for stability of the trim condition). Again, the unstable modes diverge slowly.

3. *Instability in Deep Stall*

The instability in deep stall is the first to vanish for the increasing pitch damping coefficient but is, in fact, pushed toward larger, infeasible elevator deflections (Fig. 9, marked with C). Yet, when unstable, an elevator step leads to an immediate divergence (see Fig. 12 for elevator deflection $\eta_{t \geq 0} = -50^\circ$ with $\kappa_{\dot{q}\dot{q}} = \lambda_{\alpha q} = 0$). Larger damping coefficients lead to a fast convergence in the deep-stall trim condition (Fig. 12 for $\kappa_{\dot{q}\dot{q}}, \lambda_{\alpha q} > 0$). Note that Cumulus One is known to be stable in deep stall from flight experiments.

In these regimes, the pitch damping of the original model seems insufficient to represent stable modes in deep stall. In addition to the

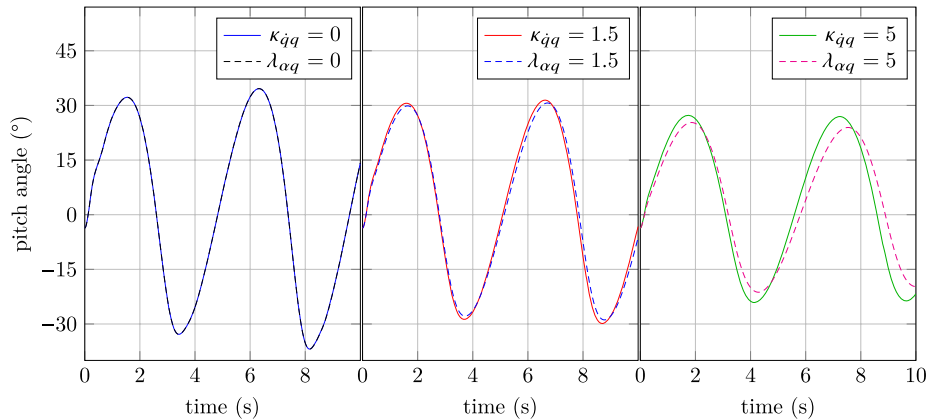


Fig. 10 Step responses for $\eta_{t \geq 0} = -8^\circ$ and increasing pitch damping coefficients.

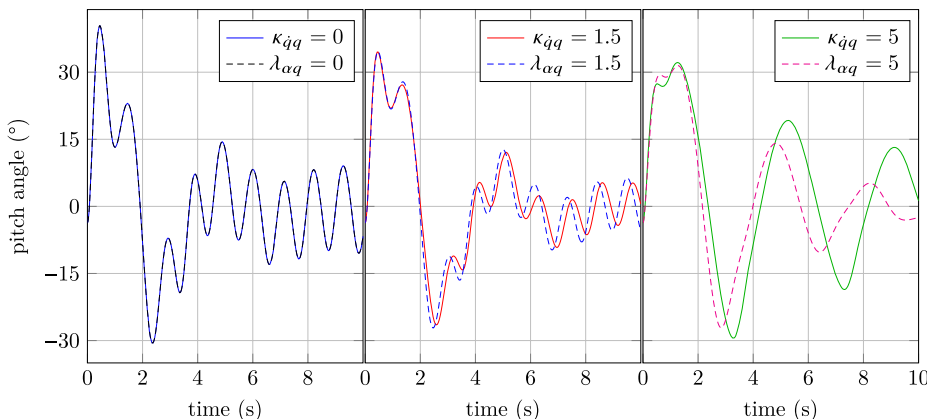


Fig. 11 Step responses for $\eta_{t \geq 0} = -24^\circ$ and increasing pitch damping coefficients.

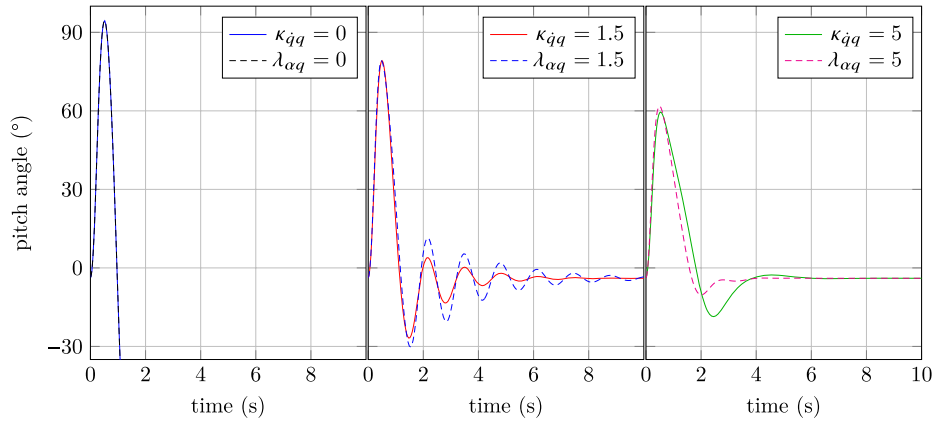


Fig. 12 Step responses for $\eta_{t \geq 0} = -50^\circ$ and increasing pitch damping coefficients.

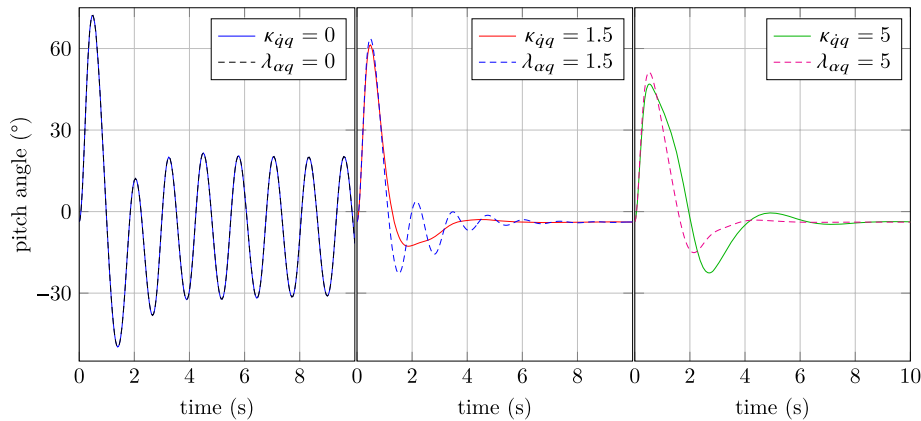


Fig. 13 Step responses for $\eta_{t \geq 0} = -38^\circ$ and increasing pitch damping coefficients.

trim conditions being unstable for large elevator deflections (regime *C* in Fig. 7), the undamped system does not represent the deep-stall transition behavior of the flight experiments, as illustrated by Fig. 13 for an elevator deflection of $\eta_{t \geq 0} = -38^\circ$ (a mathematically stable trim condition for $\kappa_{\dot{q}q} = \lambda_{\alpha q} = 0$); here, the aircraft state does not approach the equilibrium smoothly but rather yields an almost constant oscillation, which is unlike the case of a positive pitch damping coefficient, that converges rather slowly. In flight, we have experienced a smooth transition to deep stall for this elevator deflection.

Figure 14 now shows the location of eigenvalues for $\eta = -38^\circ$ and increasing pitch damping coefficients: For small values of $\kappa_{\dot{q}q}$ and $\lambda_{\alpha q}$, the pair of eigenvalues of the short-period oscillation is close to the imaginary axis, representing the underdamped dynamics

obtained in the previous figure. For larger values, this pair of eigenvalues moves deeper into the left half-plane, while the eigenvalues of the phugoid oscillation move toward the imaginary axis but do not come close. The imaginary parts of all four eigenvalues are marginally affected by the pitch damping coefficient.

C. Optimal Model Parameters

The static bifurcation analysis suggested the introduction of a pitch damping model; a further study of eigenvalues in this section has revealed the necessity of a sufficiently large damping parameter in order to ensure both static and dynamic stabilities of the deep-stall transition. However, neither provide an actual guess of the parameter; indeed, the pitch damping behavior is an unknown system property. A qualitative comparison of the model to the in-flight measurements can result in a rough estimate, but more accurate values are determined by optimization of the system output with respect to the recorded flight data. Different methods are commonly used for parameter estimation, with one of the most notable being the maximum-likelihood method [39]; but, without the covariance matrix of the measurements, we will rely instead on a simple differentially constrained optimization of the timewise \mathcal{L}_2 error norm in order to compare and evaluate the proposed damping models. Here, we are going to find optimal values for parameters of both pitch damping models and for each test flight dataset separately. The distribution of optimal parameters over the different (commanded) elevator deflections will then allow us to discriminate between the two proposed modeling approaches. As noted previously, this is not meant to be an identification of the real system; rather, it is an attempt to fit the model as close as possible (compare to Ref. [40] p. 29), and thus assess the proposed models. With the angle of attack and air speed not measured directly during flight, we use the recorded pitch angle during the initiation of the deep-stall maneuver as reference for the step response of the equations of motion to fit the damping parameter and the initial states for each step [39].

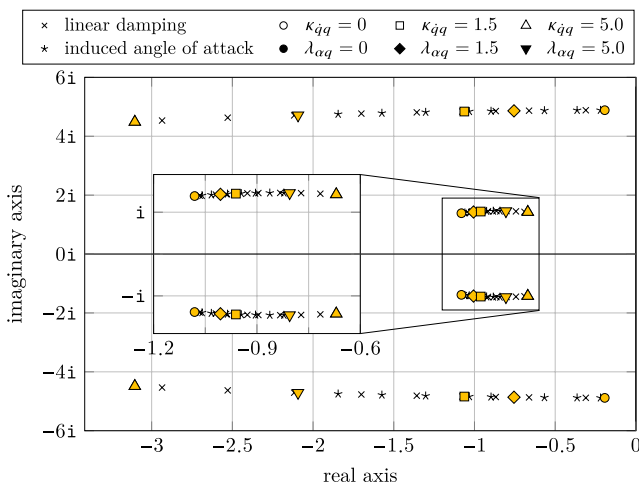


Fig. 14 Eigenvalues of longitudinal motion for $\eta = -38^\circ$ and varying pitch damping coefficients.

For optimal parameters of the pitch damping model, we solve the following differentially constrained, quadratic optimization problem:

$$I_{\text{opt}} = \min_{k_q, x_0, \delta_t} \int_0^T (\alpha(t) + \gamma_A(t) - \Theta_{\text{meas}}(t + \delta_t))^2 dt \quad (20)$$

$$\text{such that } \dot{\mathbf{x}}(t) = \mathbf{f}(\mathbf{x}(t), \eta_{t \geq 0}, k_q) \text{ for } 0 \leq t \leq T$$

where Θ_{meas} is the measured pitch angle in flight, and δ_t is the time difference between the recorded actuator command of the autopilot and the deflection of the elevator (time delay and actuator phase lag). The unknown parameter k_q (in lieu of parameters $\kappa_{\dot{q}q}$ and $\lambda_{\alpha q}$, of the linear damping model and the model of the induced angle of attack, respectively) is then subject to the optimization. Further free parameters are the initial state $\mathbf{x}(0) = \mathbf{x}_0$ as well as the time difference δ_t . Introducing discrete operators, a numerical solution to Eq. (20) is computed by MATLAB's `fmincon` function, solving for $\Xi \in \mathbb{R}^n \times \mathbb{R}^2$ and minimizing $I(t_i, \Xi) \in \mathbb{R}$, where

$$I(t_i, \Xi) = \sum_i (\alpha_i + \gamma_{\Lambda} i - \tilde{\Theta}(t_i + \delta_t))^2 \quad (21)$$

such that

$$\forall 1 \leq i \leq N \quad \frac{\Delta}{\Delta t} \mathbf{x}_i - \mathbf{f}(\mathbf{x}_{i-1}, \eta_{t \geq 0}, k_q) = 0 \quad (22)$$

with

$$\Xi^T = [\mathbf{x}_0 \quad \delta_t \quad k_q] \quad (23)$$

Here, the measured pitch angle has been cubically interpolated to $\tilde{\Theta}(\cdot)$ to yield continuity; the sequence $(\mathbf{x}_i, t_i)_{1 \leq i \leq N}$ is found using `ode45` with parameter k_q and $(t_i)_{i \in [1, N]} \subset [0, T]$. Table 2 presents the optimal values for $\kappa_{\dot{q}q}$ and $\lambda_{\alpha q}$, as well as for the time difference δ_t , of the linear damping model and the model of the induced angle of attack, respectively, using MATLAB's `active-set` algorithm and starting from $\kappa_0 = \lambda_0 = 5$ and $\delta_{t0} = 0$. A comparison of the in-flight measurement and optimal fits, both as sequences with respect to time t and their corresponding frequency spectra, is exemplarily shown in Fig. 15 for the first dataset.

Upon a large elevator deflection, one gets a stark response of the aircraft, yielding high angles of attack and pitch rates. If the pitch damping is not as simply linear as initially modeled but rather dependent on further parameters, we expect the optimal damping coefficient $\kappa_{\dot{q}q}$ of the linear model to be some function of the elevator deflection. Indeed, Table 2 clearly shows an increasing optimal linear coefficient as the elevator deflections decrease along the datasets. The optimal parameter of the model of the induced angle of attack, although slightly increasing, seems to be less dependent on the elevator deflection; however, this model is more sensitive to external

Table 2 Optimal pitch damping parameters, with dataset 10 marked as outlier of the linear damping model

Step	Dataset	Linear		Induced	
		$\kappa_{\dot{q}q}$	δ_t/s	$\lambda_{\alpha q}$	δ_t/s
$\eta_{t \geq 0} = -38^\circ$	1	1.24027	0.07914	1.58449	0.09756
	2	1.22823	0.06649	1.97405	0.05830
$\eta_{t \geq 0} = -41^\circ$	3	1.96633	0.04697	2.47311	0.04632
	4	1.74947	0.05418	1.67327	0.08602
$\eta_{t \geq 0} = -44^\circ$	5	2.09183	0.01937	2.87059	0.04486
	6	1.94578	0.07454	1.74974	0.09934
$\eta_{t \geq 0} = -47^\circ$	7	2.38401	0.03050	2.25481	0.08621
	8	2.17374	0.03221	2.77614	0.06609
$\eta_{t \geq 0} = -50^\circ$	9	2.23984	0.03321	2.41470	0.08421
	10	(3.55845)	0.02753	2.65245	0.10000
$\eta_{t \geq 0} = -53^\circ$	11	2.31744	0.04197	2.29133	0.08683
	12	2.22798	0.04316	2.29987	0.09294

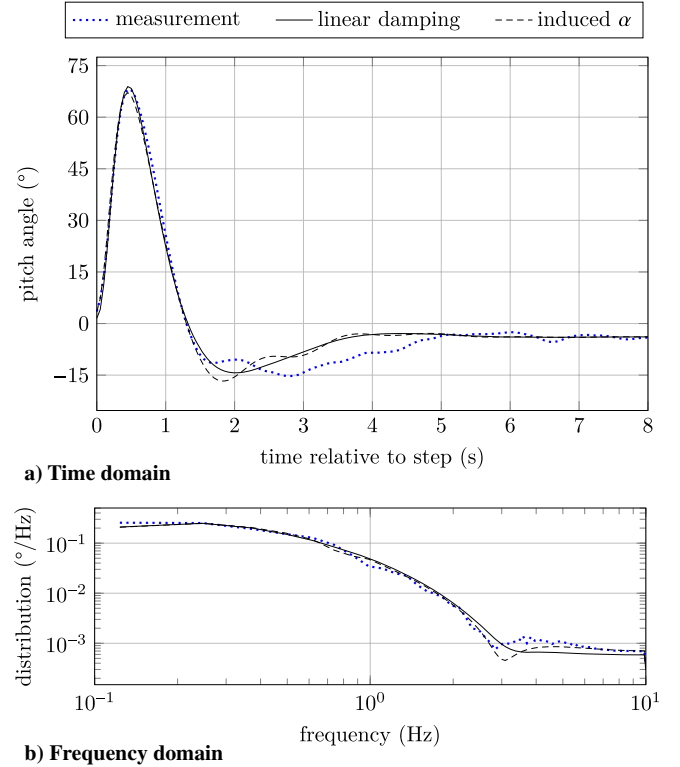


Fig. 15 Optimal model fit for dataset 1 ($\eta_{t \geq 0} = -38^\circ$; $\kappa_{\dot{q}q} = 1.24027$; $\lambda_{\alpha q} = 1.58449$).

parameters and shows a lot of variation within the dataset of equal steps in the deflection.

Removing the outlying dataset 10 for the linear damping model results in estimates for the pitch damping parameters as means of the optimal parameters with their 1σ -confidence intervals:

$$\hat{\kappa}_{\dot{q}q} = 1.96045 \pm 0.40234 \quad (24)$$

$$\hat{\lambda}_{\alpha q} = 2.25121 \pm 0.42714 \quad (25)$$

We are now going to investigate how the effectiveness of the models to capture the deep-stall transition dynamics changes if the optimal parameter values are changed for the averaged parameters. Figures 16 and 17 compare, for the linear damping model and the

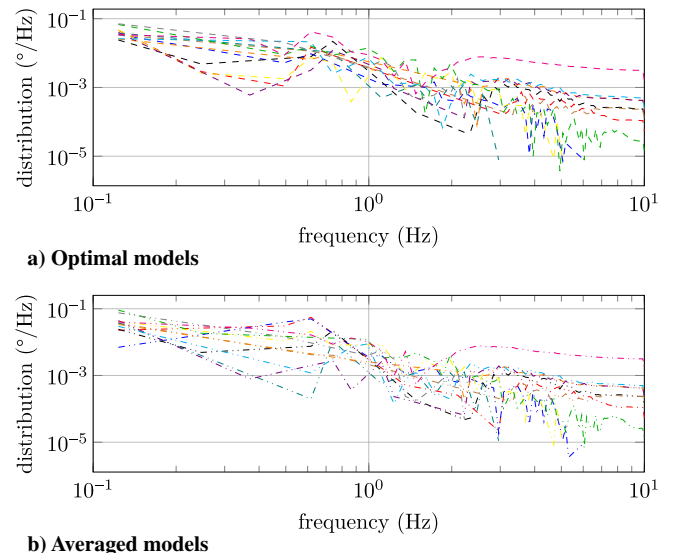


Fig. 16 Frequency spectra for the errors of optimal and averaged linear damping models.

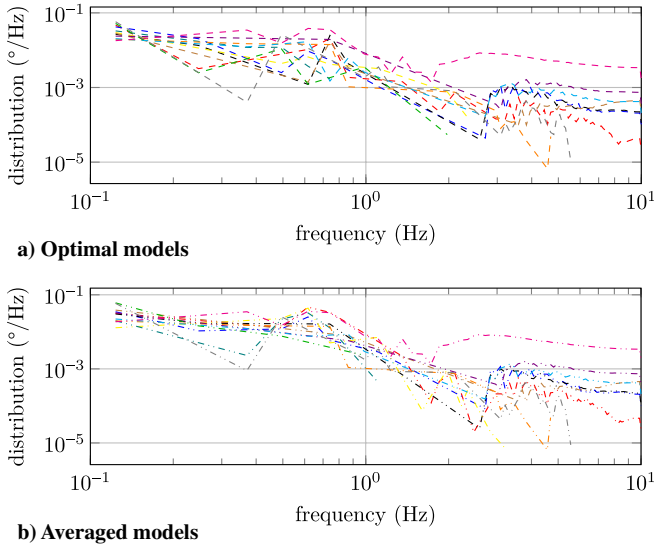


Fig. 17 Frequency spectra for the errors of optimal and averaged models of induced angle of attack.

model of induced angle of attack, respectively, the frequency spectra of the errors between optimal models from Table 2 and the respective datasets with the errors of the averaged models ($\hat{\kappa}_{\dot{q}q}$ and $\hat{\lambda}_{\dot{a}q}$). For the linear damping model, the errors are compatible, except for frequencies around approximately 0.6 Hz. The optimal model and averaged model of the induced angle of attack similarly show an increased disparity for frequencies in the range of approximately 0.6 to 0.75 Hz, although less so than for the linear damping. Neither the linear damping model or the model of induced angle of attack shows large disparities in the errors for higher frequencies (2 Hz and beyond), where wind gusts and turbulences disturb the flight.

The two kinds of pitch damping models that we proposed in this section (a constant gain on the pitch rate q , and a shifting of the pitch-moment coefficient by the normalized rate \hat{q}) have shown similar properties in terms of the stability and dynamics of the deep-stall transition as well as for the extraction of optimal parameters. Other approaches are reasonable, such as constant gain on the normalized rate or a pitch-moment derivative $C_m \hat{q} = (\partial C_m / \partial \hat{q})$, thus providing dependency on the air speed as well as the stability derivative $C_m \dot{\alpha} = (\partial C_m / \partial \alpha)$ contributing for the horizontal tail [41]. However, a further study of these is omitted here because the similar natures of the proposed models do not suggest additional insights and the obtained results satisfy our needs.

In the subsequent study of six-degree-of-freedom dynamics, we will therefore rely on the optimal linear model. The model of induced angle of attack, although more elaborate, does not provide a constructive method to incorporate damping of the lateral rotations.

V. Transition to Deep-Stall Flight

For conventional aircraft, aerodynamic stall of the wings almost inevitably leads to a departure of the vehicle. As a consequence, the aircraft often enters a spiral or oscillatory spin motion, which is fatal without appropriate recovery. An extensive study of poststall modes has been provided for the Generic Transport Model (GTM) in Ref. [5]. The GTM in particular is characterized by a “preference” to depart to the left rather than to the right when stalling due to its slightly asymmetric aerodynamics. Cumulus One, on the contrary, is supposed to enter a deep-stall descent mode that is both longitudinally and laterally stable. This stable transition to deep-stall flight can be evaluated in a six-degree-of-freedom bifurcation analysis. The CFD simulation was performed on a full-body assembly model of the aircraft, which was assumed to be symmetric by design; slight asymmetries in the obtained lateral aerodynamic coefficients might therefore be due to numerical inaccuracies.

^{††}Private communication with V. K. Dasam and J. Holst, Sky-Watch A/S, Støvring, Denmark, August 2019.

Here, we extend the longitudinal equations of motion of Eqs. (1–4) and (13) to eight differential equations for the states

$$\mathbf{X}_{6\text{dof}}^T = [u_A \ v_A \ w_A \ p \ q \ r \ \Phi \ \Theta] \quad (26)$$

with the components of air velocity $\mathbf{V}_A^T = [u_A \ v_A \ w_A]$ and angular rates $\boldsymbol{\omega}^T = [p \ q \ r]$, which are defined in body axes; bank and pitch angles, Φ and Θ , respectively, in earth-fixed axes; as well as inputs

$$\mathbf{U}_{6\text{dof}}^T = [\xi \ \eta \ \zeta] \quad (27)$$

The deflections of the elevator η , ailerons ξ , and rudder ζ are again negative when causing positive moments. (All variables as defined in the International Organization for Standardization’s ISO 1151-1 [24].)

The equations of motion are then given as

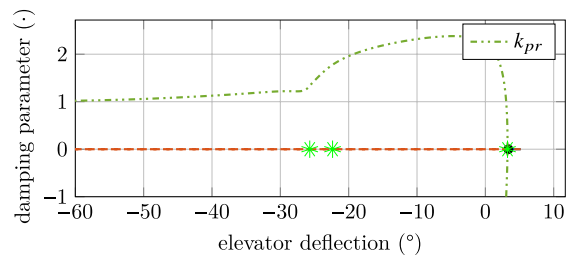
$$\dot{\mathbf{V}}_A = \frac{1}{2} \rho V_A^2 S m^{-1} \begin{bmatrix} C_X(\alpha, \beta, \xi, \eta, \zeta) \\ C_Y(\alpha, \beta, \xi, \eta, \zeta) \\ C_Z(\alpha, \beta, \xi, \eta, \zeta) \end{bmatrix} - g \begin{bmatrix} \sin \Phi \\ \sin \Phi \cos \Theta \\ \cos \Phi \cos \Theta \end{bmatrix} - \boldsymbol{\omega} \times \mathbf{V}_A \quad (28)$$

$$\mathbf{I} \dot{\boldsymbol{\omega}} = \frac{1}{2} \rho V_A^2 S \begin{bmatrix} bC_l(\alpha, \beta, \xi, \eta, \zeta) \\ c_a C_m(\alpha, \beta, \xi, \eta, \zeta) \\ bC_n(\alpha, \beta, \xi, \eta, \zeta) \end{bmatrix} - \boldsymbol{\omega} \times \mathbf{I} \boldsymbol{\omega} - \mathbf{K} \mathbf{I} \boldsymbol{\omega} \quad (29)$$

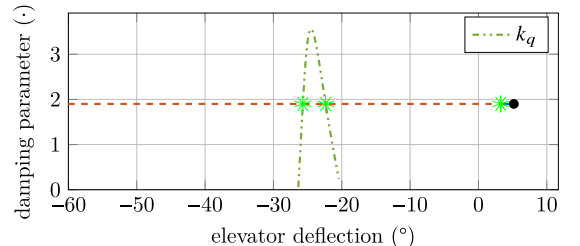
$$\begin{bmatrix} \dot{\Phi} \\ \dot{\Theta} \end{bmatrix} = \begin{bmatrix} 1 & \sin \Phi \tan \Theta & \cos \Phi \tan \Theta \\ 0 & \cos \Phi & -\sin \Phi \end{bmatrix} \boldsymbol{\omega} \quad (30)$$

where $\tan \alpha = w_A / u_A$, $\sin \beta = v_A / V_A$, and $V_A = \sqrt{u_A^2 + v_A^2 + w_A^2}$. The linear damping is modeled with the parameters $\mathbf{K} = \text{diag}(\kappa_{pr}, \kappa_q, \kappa_{pr})$. The aircraft’s heading and its rate of change are not considered here.

Note that, for this simple demonstration of a bifurcation analysis, we use a coupled roll–yaw damping parameter κ_{pr} because, without reliable flight data for an identification of the lateral damping, the observation of independent parameters κ_p, κ_r is infeasible. With the physical origins of roll and yaw damping differing considerable, additional tests to obtain separate lateral damping models in future use are strongly recommended. As for the longitudinal motion, stability of the aircraft depends on the choice of the damping parameters, and the underdamped system ($\kappa_{pr} = 0$) is in fact unstable for most parts of the normal flight range. A continuation of the



a) Roll–yaw damping for $\kappa_q = 1.96$



b) Pitch damping for $\kappa_{pr} = 0$

Fig. 18 Occurrences of Hopf bifurcations of the six-degree-of-freedom motion for continuation of the model parameters.

occurring Hopf bifurcations reveals this dependency (Fig. 18): The pitch motion exhibits a pair of Hopf bifurcations in the post-stall domain that was already encountered in the analysis of the longitudinal dynamics. For increasing pitch damping parameter κ_q , the Hopf bifurcation vanishes (note that the continuation of the pitch damping parameter has been set up around the optimal parameter; therefore, the longitudinal dynamics exhibit only a single pair). As for the longitudinal dynamics, the trim conditions between are unstable. A third Hopf bifurcation exists at a positive elevator deflection governing the overall stability. With increasing roll–yaw damping parameter κ_{pr} , this Hopf bifurcation moves toward a neutral elevator; but, from $\kappa_{pr} > 1$, a corresponding Hopf bifurcation appears for $\eta = -60^\circ$. If κ_{pr} is chosen sufficiently large, the pair of Hopf bifurcations also disappears. It should be noted, however, that roll damping in general does not have a stabilizing effect over the full envelope of bank angles. To maintain a stable system within the considered envelope, the damping parameters are chosen as

$$\mathbf{K} = \text{diag}(2.5, 1.96, 2.5) \quad (31)$$

With these damping parameters, we can then perform a six-degree-of-freedom bifurcation analysis starting from the elevator-neutral trim condition

$$\mathbf{X}_{6\text{dof}}^T = [14.09 \text{ m/s} \quad <0.01 \text{ m/s} \quad 0.12 \text{ m/s} \quad 0.01^\circ/\text{s} \quad <0.01^\circ/\text{s} \quad 0.17^\circ/\text{s} \quad <0.01^\circ \quad -3.64^\circ]$$

and

$$\mathbf{U}_{6\text{dof}}^T = [0.03^\circ \quad -0.00^\circ \quad 2.34^\circ]$$

Note that the roll–yaw rates are nonzero at trim due to a slightly positive bank angle.

The trim conditions of both longitudinal and lateral motions, as computed by COCO [38], are shown in Fig. 19. Due to a minor dependency of the aircraft’s lateral asymmetry, the bank angle at trim deviates from neutral for an increase in the angle of attack. On the other hand, the steep descent for positive elevator deflections involves increasing bank angles, and therefore constant change of the heading. The previously encountered Hopf bifurcations around stall bear a family of limit cycles, shown enlarged in the insets, that in fact mainly affects the longitudinal motion (compare Figs. 19a and 19b). A pair of saddle-node bifurcations (a single real eigenvalue crossing the imaginary axis) between -54° and -66° bank angles reveals a branch of unstable trim conditions for a constant angle of attack of approximately -3.2° . Figure 20 illustrates the deep-stall and steep descent modes encountered at each end of the bifurcation. Note that the aircraft is drawn scaled with respect to the horizontal plane but in equal time steps; both trajectories are depicted for 10 s. The steep descent, when compared to the deep-stall mode, establishes a significantly larger descent rate in a fast and tight downward helix. This circular trajectory must not be confused with a spiral motion, where the aircraft additionally exhibits rotations around its body axes. Instead, the turn is a result of lateral asymmetries of the

polynomial model. Our bifurcation analysis has not found any spin or spiral modes, although we would expect some; due to the stability of the aircraft in deep stall, the branches of such limit cycles involving the lateral axis are disconnected from the main branch of the

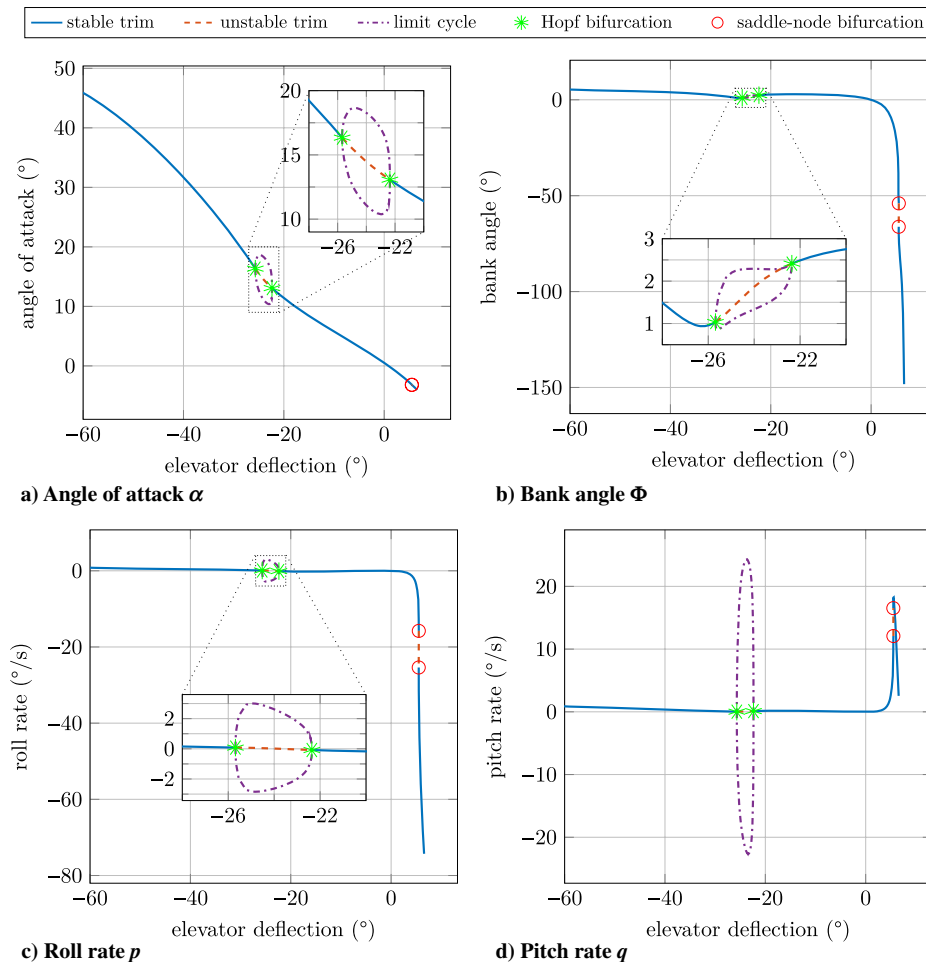
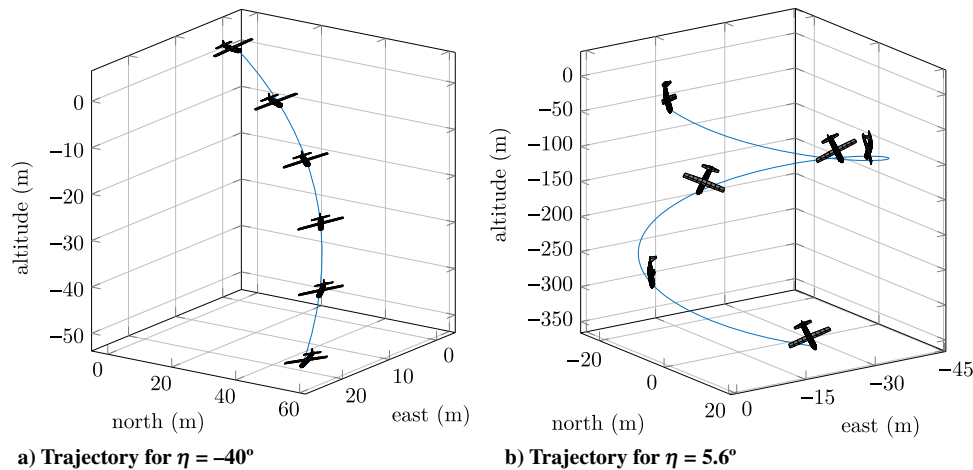


Fig. 19 Six-degree-of-freedom trim conditions for continuation of the elevator deflection η .



a) Trajectory for $\eta = -40^\circ$

b) Trajectory for $\eta = 5.6^\circ$

Fig. 20 Comparison of descent modes: a) deep-stall descent; and b) steep descent.

longitudinal trim conditions, and therefore difficult to find using continuation techniques. The analysis shows, however, that the Cumulus One aircraft does not depart at stall; it only develops a periodic orbit of longitudinal motion before settling to a stable deep-stall trim condition.

VI. Conclusions

In this paper, a nonlinear model of a small unmanned aircraft was developed in order to represent deep-stall transition dynamics from static CFD data. For this purpose, pitch-damping models were proposed, and the use of bifurcation analysis was demonstrated to discuss its effects when compared to the initially static model and flight experiments. Starting with a model of longitudinal equations of motion by a blended, piecewise polynomial fit of the aerodynamic coefficients from static CFD, a continuation analysis was able to predict trim conditions. However, we found the stability of deep-stall flight deduced from the model to be inconsistent with the flight experiments, and hence proposed alternative extensions to the initial model, with both including a single unknown damping parameter. Although larger parameters indeed led to the increased stability of both models, an isolated damping model could not be induced by the change of stability only. On the other hand, estimations could be provided for the coefficients by optimal model fitting, and thus provided a measure for the reliability of the proposed damping models. Both models seem to be simple and suitable for further analysis. An extensive six-degree-of-freedom bifurcation analysis was finally provided to investigate the extended model, and stability in the aircraft's different modes of poststall and deep-stall flights were discussed.

Acknowledgments

This work was funded by the AutoDescent project (HTF 56-2014-3) as well as by ONERA–The French Aerospace Lab. The authors remain grateful to Sky-Watch for the provision of test flight data and computational fluid dynamics simulations. Luminita C. Totu and Tobias Leth at Aalborg University further provided valuable discussions and feedback.

References

- [1] Klein, V., and Morelli, E. A., *Aircraft System Identification: Theory and Practice*, AIAA Education Series, AIAA, Reston, VA, 2006. <https://doi.org/10.1017/S0001924000087194>
- [2] Brockhaus, R., Alles, W., and Luckner, R., *Flugregelung*, 3rd ed., Springer, Berlin, 2011. <https://doi.org/10.1007/978-3-642-01443-7>
- [3] Chakraborty, A., Seiler, P., and Balas, G. J., "Susceptibility of F/A-18 Flight Controllers to the Falling-Leaf Mode: Linear Analysis," *Journal of Guidance, Control, and Dynamics*, Vol. 34, No. 1, 2011, pp. 57–72. <https://doi.org/10.2514/1.50674>
- [4] Chambers, J. R., and Grafton, S. B., "Aerodynamic Characteristics of Airplanes at High Angles of Attack," NASA Langley Research Center TM-74097, 1 Dec. 1977, <https://ntrs.nasa.gov/search.jsp?R=19780005068> [retrieved 2019].
- [5] Gill, S. J., Lowenberg, M. H., Neild, S. A., Krauskopf, B., Puyou, G., and Coetzee, E., "Upset Dynamics of an Airliner Model: A Nonlinear Bifurcation Analysis," *Journal of Aircraft*, Vol. 50, No. 6, 2013, pp. 1832–1842. <https://doi.org/10.2514/1.C032221>
- [6] Jahnke, C. C., "Application of Dynamical Systems Theory to Nonlinear Aircraft Dynamics," Ph.D. Thesis, California Inst. of Technology, Pasadena, CA, 1990, <http://resolver.caltech.edu/CaltechETD:etd-05092007-134504> [retrieved 2019].
- [7] Goman, M. G., Zagainov, G. I., and Khramtsovsky, A. V., "Application of Bifurcation Methods to Nonlinear Flight Dynamics Problems," *Progress in Aerospace Sciences*, Vol. 33, Nos. 9–10, 1997, pp. 539–586. [https://doi.org/10.1016/S0376-0421\(97\)00001-8](https://doi.org/10.1016/S0376-0421(97)00001-8)
- [8] Carroll, J. V., and Mehra, R. K., "Bifurcation Analysis of Nonlinear Aircraft Dynamics," *Journal of Guidance, Control, and Dynamics*, Vol. 5, No. 5, 1982, pp. 529–536. <https://doi.org/10.2514/3.56198>
- [9] Lombaerts, T. J. J., Schuet, S. R., Wheeler, K. R., Acosta, D. M., and Kaneshige, J. T., "Safe Maneuvering Envelope Estimation Based on a Physical Approach," *AIAA Guidance, Navigation, and Control Conference*, AIAA Paper 2013-4618, 2013. <https://doi.org/10.2514/6.2013-4618>
- [10] McDonough, K., and Kolmanovsky, I., "Fast Computable Recoverable Sets and Their Use for Aircraft Loss-of-Control Handling," *Journal of Guidance, Control, and Dynamics*, Vol. 40, No. 4, 2017, pp. 934–947. <https://doi.org/10.2514/1.G001747>
- [11] Lygeros, J., "On Reachability and Minimum Cost Optimal Control," *Automatica*, Vol. 40, No. 6, 2004, pp. 917–927. <https://doi.org/10.1016/j.automatica.2004.01.012>
- [12] Chakraborty, A., Seiler, P., and Balas, G. J., "Nonlinear Region of Attraction Analysis for Flight Control Verification and Validation," *Control Engineering Practice*, Vol. 19, No. 4, 2011, pp. 335–345. <https://doi.org/10.1016/j.conengprac.2010.12.001>
- [13] Chakraborty, A., Seiler, P., and Balas, G. J., "Susceptibility of F/A-18 Flight Controllers to the Falling-Leaf Mode: Nonlinear Analysis," *Journal of Guidance, Control, and Dynamics*, Vol. 34, No. 1, 2011, pp. 73–85. <https://doi.org/10.2514/1.50675>
- [14] Foster, J. V., Cunningham, K., Fremaux, C. M., Shah, G. H., and Stewart, E. C., "Dynamics Modeling and Simulation of Large Transport Airplanes in Upset Conditions," *AIAA Guidance, Navigation, and Control Conference and Exhibit*, AIAA Paper 2005-5933, 2005. <https://doi.org/10.2514/6.2005-5933>
- [15] Jordan, T. L., Foster, J. V., Bailey, R. M., and Belcastro, C. M., "AirSTAR: A UAV Platform for Flight Dynamics and Control System Testing," *AIAA Aerodynamics Measurement Technology and Ground Testing Conference*, AIAA Paper 2006-3307, 2006. <https://doi.org/10.2514/6.2006-3307>
- [16] Kwatny, H. G., Dongmo, J.-E. T., Chang, B.-C., Bajpai, G., Yasar, M., and Belcastro, C., "Nonlinear Analysis of Aircraft Loss of Control," *Journal of Guidance, Control, and Dynamics*, Vol. 36, No. 1, 2013, pp. 149–162. <https://doi.org/10.2514/1.56948>
- [17] McDonough, K., Kolmanovsky, I., and Atkins, E., "Recoverable Sets of Initial Conditions and Their Use for Aircraft Flight Planning After a

- Loss of Control Event," *AIAA Guidance, Navigation, and Control Conference*, AIAA Paper 2014-0786, 2014.
<https://doi.org/10.2514/6.2014-0786>
- [18] Engelbrecht, J. A. A., Pauck, S. J., and Peddle, I. K., "A Multi-Mode Upset Recovery Flight Control System for Large Transport Aircraft," *AIAA Guidance, Navigation, and Control Conference*, AIAA Paper 2013-5172, 2013.
<https://doi.org/10.2514/6.2013-5172>
- [19] Crespo, L. G., Kenny, S. P., Cox, D. E., and Murri, D. G., "Analysis of Control Strategies for Aircraft Flight Upset Recovery," *AIAA Guidance, Navigation, and Control Conference*, AIAA Paper 2012-5026, 2012.
<https://doi.org/10.2514/6.2012-5026>
- [20] Stepanyan, V., Krishnakumar, K., Kaneshige, J., and Acosta, D., "Stall Recovery Guidance Algorithms Based on Constrained Control Approaches," *AIAA Guidance, Navigation, and Control Conference*, AIAA Paper 2016-0878, 2016.
<https://doi.org/10.2514/6.2016-0878>
- [21] Kuzmin, D., A Guide to Numerical Methods for Transport Equations," Friedrich-Alexander Univ., Erlangen-Nürnberg, Germany, 2010, pp. 1–39, <https://www.mathematik.uni-dortmund.de/~kuzmin/Transport.pdf> [retrieved 17 May 2018].
- [22] Drela, M., and Youngren, H., *AVL 3.36 User Primer*, Massachusetts Inst. of Technology, Cambridge, MA, 2017, http://web.mit.edu/drela/Public/web/avl/avl_doc.txt [retrieved 17 May 2018].
- [23] "The Cumulus v1 UAV," Sky-Watch A/S, Støvring, Denmark, 2017, https://sky-watch.com/media/1121/sw_1pager_cumulus.pdf [retrieved 12 March 2018].
- [24] *Flight Dynamics—Concepts, Quantities and Symbols—Part 1: Aircraft Motion Relative to the Air*, 4th ed., International Organization for Standardization ISO 1151-1:1988, Geneva, Switzerland, 1988.
- [25] Chang, B.-C., Kwatny, H. G., Ballouz, E. R., and Hartmann, D. C., "Aircraft Trim Recovery from Highly Nonlinear Upset Conditions," *AIAA Guidance, Navigation, and Control Conference*, AIAA Paper 2016-0880, 2016.
<https://doi.org/10.2514/6.2016-0880>
- [26] Phillips, W. F., *Mechanics of Flight*, 2nd ed., Wiley, Hoboken, NJ, 2010.
- [27] Lawson, C. L., and Hanson, R. J., *Solving Least Squares Problems*, Classics in Applied Mathematics, Soc. for Industrial and Applied Mathematics, Philadelphia, PA, 1995.
<https://doi.org/10.1137/1.9781611971217>
- [28] Cunis, T., Leth, T., Totu, L. C., and la Cour-Harbo, A., "Identification of Thrust, Lift, and Drag for Deep-Stall Flight Data of a Fixed-Wing Unmanned Aircraft," *2018 International Conference on Unmanned Aircraft Systems*, IEEE Publ., Piscataway, NJ, 2018, pp. 531–538.
<https://doi.org/10.1109/ICUAS.2018.8453340>
- [29] Cunis, T., Burlion, L., and Condomines, J.-P., "Piece-Wise Identification and Analysis of the Aerodynamic Coefficients, Trim Conditions, and Safe Sets of the Generic Transport Model," *AIAA Guidance, Navigation, and Control Conference*, AIAA Paper 2018-1114, 2018.
<https://doi.org/10.2514/6.2018-1114>
- [30] Cunis, T., Burlion, L., and Condomines, J.-P., "Piecewise Polynomial Modeling for Control and Analysis of Aircraft Dynamics Beyond Stall," *Journal of Guidance, Control, and Dynamics*, Vol. 42, No. 4, 2019, pp. 949–957.
<https://doi.org/10.2514/1.G003618>
- [31] Cunis, T., "The pwpfit Toolbox for Polynomial and Piece-Wise Polynomial Data Fitting," *18th IFAC Symposium on System Identification*, Elsevier, Kidlington, UK, 2018, pp. 682–687.
<https://doi.org/10.1016/j.ifacol.2018.09.204>
- [32] Cunis, T., and la Cour-Harbo, A., "Piecewise Polynomial Model of the Aerodynamic Coefficients of the Cumulus One Unmanned Aircraft," Sky-Watch A/S TR hal-02280789, Støvring, Denmark, 2019, <https://hal-enac.archives-ouvertes.fr/hal-02280789> [retrieved 2019].
- [33] Slotine, J.-J. E., and Li, W., *Applied Nonlinear Control*, Prentice-Hall, Upper Saddle River, NJ, 1991.
- [34] Kuznetsov, Y. A., *Elements of Applied Bifurcation Theory*, 2nd ed., Vol. 112, Applied Mathematical Sciences, Springer, New York, 1998.
<https://doi.org/10.1007/978-1-4757-3978-7>
- [35] Dankowicz, H., and Schilder, F., *Recipes for Continuation*, *Computational Science and Engineering*, SIAM, Philadelphia, PA, 2013.
<https://doi.org/10.1137/1.9781611972573>
- [36] Dhooge, A., Govaerts, W., Kuznetsov, Y. A., Meijer, H. G. E., and Sautois, B., "New Features of the Software MatCont for Bifurcation Analysis of Dynamical Systems," *Mathematical and Computer Modelling of Dynamical Systems*, Vol. 14, No. 2, 2008, pp. 147–175.
<https://doi.org/10.1080/13873950701742754>
- [37] Coetzee, E., Krauskopf, B., and Lowenberg, M. H., "The Dynamical Systems Toolbox: Integrating AUTO into MATLAB," *16th US National Congress on Theoretical and Applied Mechanics*, Pennsylvania State Univ., University Park, PA, 2010.
- [38] Dankowicz, H., and Schilder, F., "Continuation Core and Toolboxes (COCO) [online database]," 2016, <https://sourceforge.net/projects/cocotools/> [retrieved 21 Nov. 2016].
- [39] Jategaonkar, R. V., *Flight Vehicle System Identification: A Time Domain Methodology*, 2nd ed., Progress in Astronautics and Aeronautics, AIAA, Reston, VA, 2006.
- [40] Graichen, K., "Feedforward Control Design for Finite-Time Transition Problems of Nonlinear Systems," Ph.D. Thesis, Univ. of Stuttgart, Stuttgart, Germany, 2006.
<https://doi.org/10.18419/opus-4093>
- [41] Nelson, R. C., *Flight Stability and Automatic Control*, 2nd ed., McGraw-Hill, Boston, MA, 1998.

Piecewise Polynomial Model Identification using Constrained Least Squares for UAS Stall

Vincent Guibert ^{*,**} Jean-Philippe Condomines ^{*}
Mathieu Brunot ^{**} Murat Bronz ^{*}

^{*} ENAC, Université de Toulouse, 31055 Toulouse, France
(e-mails: name.surname@enac.fr)

^{**} ONERA – The French Aerospace Lab, 31055 Toulouse, France
(e-mails: vincent.guibert-ext@onera.fr, mathieu.brunot@onera.fr)

Abstract: In this paper, we propose a new piecewise polynomial model (PwPM) for the modelling of an Unmanned Aircraft System (UAS) aerodynamic coefficients over a wide flight envelope, where they are characterized by nonlinear and hysteresis phenomena. An associated identification method using Constrained Least Squares (CLS) is then presented and successfully applied to experimental data obtained from wind tunnel measurements. The resulting fitting is finally compared with the similar piecewise models PWPFIT and AERODAS, showing a greater precision in its modelling, while maintaining their relative simplicity and computation performance.

Copyright © 2021 The Authors. This is an open access article under the CC BY-NC-ND license (<http://creativecommons.org/licenses/by-nc-nd/4.0>)

Keywords: Flight dynamics identification, Piecewise polynomial, Constrained least squares, Unmanned aircraft system, Stall modelling

1. INTRODUCTION

Accurate Unmanned Aircraft System (UAS) dynamics modelling is rarely straightforward and requires extensive experiments to ensure a sufficient representation of every aspect of the operational envelope of the aircraft. (Hoffer et al., 2014; Uhlig and Selig, 2017; Cunis et al., 2019)

Based on an identification phase using wind tunnel campaigns, Computational Fluid Dynamics (CFD) calculations or flight tests, a parametric model needs to be elaborated which is as representative as possible of the physical reality. This task is extremely challenging due to nonlinear and unsteady aerodynamic phenomena beyond the nominal flight envelope, as is the case during an upset situation (Saderla et al., 2018). For instance, at the stall angle of attack the flow around the wings detaches and goes from laminar to turbulent. This phenomenon creates a disparity between aerodynamic forces when flying in the so-called pre-stall (below the stall angle of attack) and post-stall (above this same angle of attack) domains. In addition, a stalled aircraft can still reach angles of attack below the previous value without re-attaching the air flow and only do so later at a new and lower angle of attack. This second nonlinear phenomenon is called aerodynamic hysteresis, and is of practical importance since it affects the behaviour of the aircraft and its possible recovery from stall and/or spin flight conditions.

Furthermore, with the ongoing certification and integration into civil airspace of UASs found in EU regulations (EU, May 2019), there is a clear need for reliable full-envelope models of UAS flight dynamics, and in particular during upset situations. Such models can be used for

the certification of an aircraft or a control law as well as for safety and automation operations, including flight-envelope protection and restoration (Ancel et al., 2017; Bertrand et al., 2017). Having a robust upset recovery controller leveraging accurate predictions of the vehicle dynamics can indeed provide an increased safety for a drone in critical situations where it experiences an in-flight anomaly, as well as for other users of the airspace, ground infrastructures and people.

Modelling the aerodynamic behaviour of an aircraft can be done in several ways. For instance, one can solve numerically the Navier-Stokes equations as in Keller et al. (2019), use semi-empirical models as in Leishman and Beddoes (1989) or the AERODAS model (Spera, 2008), or use fully data-driven models such as locally weighted projection regression (Farcy et al., 2020) or splines (Morelli et al., 2013). However, while splines present today a powerful yet complex tool for accurate and smooth interpolation (Tol et al., 2016), they are unsuitable for functional analysis of trim conditions and stable sets, as in Kwatny et al. (2013). Moreover, high-fidelity models often require hard to obtain data, such as the flow separation point, which is usually not available. More recently, research works (Cunis et al., 2019) have been conducted on piecewise polynomial models in order to provide a constructive method fit for system analysis due to their continuous and differentiable nature. However, those results do not represent completely a real-life upset situation, due to the authors' choice to focus on deep stall control and as such to consider neither the hysteresis phenomenon nor a higher count of pieces.

Motivated by all these reasons, this paper focuses on a new formulation for a piecewise polynomial model and

its identification in order to improve the accuracy of aerodynamic forces modelling for UASs, and in particular around the aerodynamic hysteresis. The contributions include: (i) the definition in Section 2 of a new Piecewise Polynomial Model (PwPM) for the lift coefficient ; (ii) the presentation of the identification problem, where the Least Square (LS) cost metric is introduced Section 3 ; (iii) a quick and efficient algebraic solution to this problem using Lagrange multipliers in Section 4, followed by a proposal for hyper-parameters optimisation. Finally, experimental results based on wind tunnel data are presented Section 5, with a comparison of PwPM's performance to that of the PWPFIT and AERODAS methods.

2. PIECEWISE POLYNOMIAL MODEL (PWPM)

As previously stated, this study was motivated by the desire to model the aerodynamic coefficients of a UAS during stall. Since stall behaviour is mainly represented by the lift coefficient, it is this particular example that will be presented here. Based on *a priori* knowledge in Leishman and Beddoes (1989) and the experimental data presented Section 5, the model should respect the five following items:

- (1) There should be two established domains respectively representing the pre-stall and post-stall dynamics.
- (2) Those domains are to be linked by two transitions for going back and forth between them.
- (3) No polynomial depends directly on the pitch rate $\dot{\alpha}$, although it can still be used to determine in which domain the drone is flying.
- (4) The model is to be continuous and continuously differentiable on the whole of its domain.
- (5) Each polynomial should be of the lowest degree possible to avoid over-fitting and maintain simplicity and computation performance.

As such, the following four-pieced polynomial model is proposed, where each polynomial is cubic in α and does not depend on $\dot{\alpha}$, as presented Fig. 1:

- A first polynomial, defining the pre-stall dynamics.
- A second polynomial, making the transition from the pre-stall domain at the stall angle of attack α_0 to the post-stall domain at α_1 .
- A third polynomial, modelling the stalled dynamics.
- A final (fourth) polynomial, linking back from the post-stall to the pre-stall dynamics between the separation angles of attack α_2 and α_3 .

In addition, in order to accommodate requirement 4 of the previous list, each two neighbouring polynomials (1 and 2 ; 1 and 4 ; 3 and 2 ; 3 and 4) are to respect same-value and tangency constraints at their separation. This proposed model leaves us with 16 polynomial coefficients to be identified under a set of 8 constraints.

3. MODEL IDENTIFICATION

Identifying the model is akin to the fitting problem below.

3.1 Problem description

Let there be a set of n measurements composed of q abscissae values $\mathbf{x}_1, \mathbf{x}_2, \dots, \mathbf{x}_q \in \mathbb{R}^n$ and a single ordinate

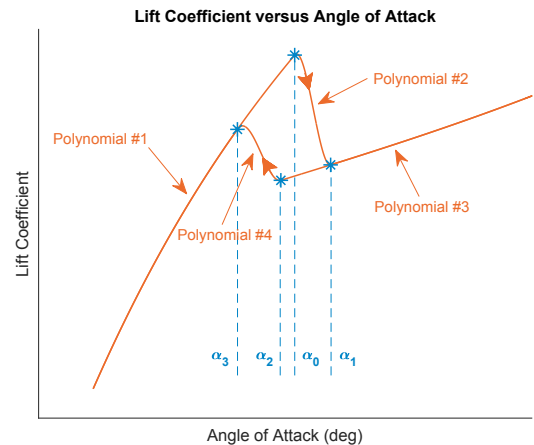


Fig. 1. The proposed model for the lift coefficient

value $\mathbf{z} \in \mathbb{R}^n$ defining a function $f : \mathbb{R} \times \mathbb{R} \times \dots \times \mathbb{R} \rightarrow \mathbb{R}$ to be identified.

$$\forall j \in \llbracket 1, n \rrbracket, \quad \mathbf{z}_j = f(\mathbf{x}_{1j}, \mathbf{x}_{2j}, \dots, \mathbf{x}_{qj}) \quad (1)$$

Let there be a model, defined beforehand as in Section 2, defining p polynomials, their respective degree with each of the abscissa parameters d_j^i (where this notation denotes the degree of the i^{th} polynomial with respect to the j^{th} parameter) and their associated domains in the abscissa space $\mathcal{P}_i \subset \mathbb{R}^q$. Those domains should form a partition of the abscissa space such that they are disjoint two by two and cover it completely.

$$\begin{cases} \mathcal{P}_i \cap \mathcal{P}_j = \emptyset & \forall i, j \in \llbracket 1, p \rrbracket, i \neq j \\ \bigcup_{i=1}^p \mathcal{P}_i = \mathbb{R}^q \end{cases} \quad (2)$$

In order to better represent the underlying data, the model also defines a set of m constraint functions c_j depending linearly in the polynomial coefficients to be respected by the fitted polynomials. Those constraints will be considered respected if they reach a desired value d_j .

$$\text{"The } j^{\text{th}} \text{ constraint is respected"} \Leftrightarrow c_j(\cdot) = d_j \quad (3)$$

This linearity condition was chosen to simplify the algebraic solution below. It can seem reducing but it allows for the definition of most common constraints, including all derivatives continuity (including regular continuity) and specific value at a given abscissa.

Let there finally be a cost function $J \in \mathbb{R}$ to be minimised, quantifying the quality of the fitting. In this paper, a weighted Least Square (LS) formulation will be used such that J can be written

$$J = \sum_{j=1}^n \frac{1}{2} \gamma_j \left[\mathbf{z}_j - \mathfrak{F}(\mathbf{x}_{1j}, \mathbf{x}_{2j}, \dots, \mathbf{x}_{qj}) \right]^2 \quad (4)$$

where $\mathfrak{F} : \mathbb{R} \times \mathbb{R} \times \dots \times \mathbb{R} \rightarrow \mathbb{R}$ is the fitted model prediction and the coefficients $\gamma_j \neq 0$ are non-zero weighting coefficients on each measurement. It is noted that this choice of a cost function could reduce the quality of the model in the case where the abscissae (angles of attack) are too noisy. The difference in precision with other forms such as the Total Least Squares (TLS) is however only marginal, making this simpler LS formulation more attractive.

3.2 Matrical formulation

Based on the piecewise polynomial shape of the model \mathfrak{F} , one can introduce a simplified expression for each of the polynomials through a vector of monomial products and that of the polynomial coefficients. The vector of monomial products for the i^{th} polynomial, $\mu_i : \mathbb{R} \times \mathbb{R} \times \dots \times \mathbb{R} \rightarrow \mathbb{R}^{\delta_i}$, returns all the possible combinations of monomials products according to the maximal degrees defined by the model,

$$\mu_i(x_1, x_2, \dots, x_q) = \begin{bmatrix} x_1^{d_1^i} \times x_2^{d_2^i} \times \dots \times x_{q-1}^{d_{q-1}^i} \times x_q^{d_q^i} \\ x_1^{d_1^i} \times x_2^{d_2^i} \times \dots \times x_{q-1}^{d_{q-1}^i-1} \times x_q^{d_q^i} \\ \vdots \\ x_1^{d_1^i} \times x_2^{d_2^i} \times \dots \times x_{q-1}^{d_{q-1}^i} \times x_q^0 \\ x_1^{d_1^i} \times x_2^{d_2^i} \times \dots \times x_{q-1}^{d_{q-1}^i-1} \times x_q^{d_q^i} \\ \vdots \\ x_1^0 \times x_2^0 \times \dots \times x_{q-1}^0 \times x_q^0 \end{bmatrix} \quad (5)$$

where $\delta_i = \prod_{j=1}^q (d_j^i + 1)$ is the dimension of this vector. It is noted here that the order in which the monomial products appear is arbitrary and does not matter as long as it remains the same throughout the problem. In addition, it is not required that all monomial products are used as long as the coefficients vector is amended in the same way.

By noting $\theta_i \in \mathbb{R}^{\delta_i}$ the vector of coefficients for that same polynomial, one can then write

$$\forall (x_1, x_2, \dots, x_q) \in \mathcal{P}_i, \quad \mathfrak{F}(x_1, x_2, \dots, x_q) = \langle \mu_i(x_1, x_2, \dots, x_q), \theta_i \rangle = \mu_i(x_1, x_2, \dots, x_q)^\top \theta_i \quad (6)$$

where the notation $\langle \cdot, \cdot \rangle$ denotes the inner product (here in the \mathbb{R}^{δ_i} space).

Using this simplified notation, one can then rewrite the cost function

$$J = \sum_{i=1}^p J_i, \quad (7)$$

$$J_i = \sum_{j=1}^{n_i} \frac{1}{2} \gamma_{ij} \left[z_{ij} - \mu_i(\mathbf{x}_{1,i_j}, \mathbf{x}_{2,i_j}, \dots, \mathbf{x}_{q,i_j})^\top \theta_i \right]^2$$

where J_i is the contribution of the i^{th} polynomial to the total cost, the vectors $\mathbf{z}_i, \mathbf{x}_{1,i}, \dots, \mathbf{x}_{q,i} \in \mathbb{R}^{n_i}$ are the restriction of their respective vectors to only the measurements whose abscissae lie in the domain \mathcal{P}_i , the vector $\gamma_i \in \mathbb{R}^{n_i}$ is the vector of weights for the measurements in this same domain and n_i is the number of those measurements. This can be further simplified using the matrical formulation

$$J_i = \frac{1}{2} (\mathbf{z}_i - \Phi_i \theta_i)^\top \Gamma_i (\mathbf{z}_i - \Phi_i \theta_i) \quad (8)$$

where $\Gamma_i = \text{diag}(\gamma_i) \in \mathbb{R}^{n_i \times n_i}$ is the weight matrix and $\Phi_i \in \mathbb{R}^{n_i \times \delta_i}$ is the matrix of monomial products for the i^{th} polynomial:

$$\Phi_i = \begin{bmatrix} \mu_i(\mathbf{x}_{1,i_1}, \dots, \mathbf{x}_{q,i_1})^\top \\ \mu_i(\mathbf{x}_{1,i_2}, \dots, \mathbf{x}_{q,i_2})^\top \\ \vdots \\ \mu_i(\mathbf{x}_{1,i_{n_i}}, \dots, \mathbf{x}_{q,i_{n_i}})^\top \end{bmatrix} \quad (9)$$

Finally, one can express the cost function in pure matrical formulation

$$J = \frac{1}{2} (\mathbf{z} - \Phi \theta)^\top \Gamma (\mathbf{z} - \Phi \theta) \quad (10)$$

with $\Phi \in \mathbb{R}^{n \times \delta}$ the matrix of monomial products for all measurements, $\theta \in \mathbb{R}^\delta$ the total vector of polynomial coefficients and $\Gamma \in \mathbb{R}^{n \times n}$ the total weight matrix. The total polynomial coefficients vector has dimension $\delta = \sum_{i=1}^p \delta_i$.

$$\Phi = \text{diag}(\Phi_1, \Phi_2, \dots, \Phi_p) \quad (11a)$$

$$\theta = [\theta_1^\top \theta_2^\top \dots \theta_p^\top]^\top \quad (11b)$$

$$\Gamma = \text{diag}(\Gamma_1, \Gamma_2, \dots, \Gamma_p) \quad (11c)$$

It can be noted that the row-wise order in which the measurements appear does not matter and there is therefore no need to sort the data prior to the fitting.

Moreover, based on the linearity with respect to θ of the constraint functions, one can write that

$$\forall j \in \llbracket 1, m \rrbracket, \quad \exists \mathbf{c}_j \in \mathbb{R}^\delta \mid c_j(\cdot) = \langle \mathbf{c}_j, \theta \rangle = \mathbf{c}_j^\top \theta \quad (12)$$

such that all the constraints can too be rewritten under the matrical formulation

$$\text{"All the constraints are respected"} \Leftrightarrow \mathbf{C} \theta = \mathbf{d} \quad (13)$$

where $\mathbf{C} \in \mathbb{R}^{m \times \delta}$ is a matrix deriving from those constraint vectors and $\mathbf{d} = [d_1 \ d_2 \ \dots \ d_m]^\top \in \mathbb{R}^m$ is the vector of the constraints desired values.

$$\mathbf{C} = [\mathbf{c}_1 \ \mathbf{c}_2 \ \dots \ \mathbf{c}_m]^\top \quad (14)$$

The problem at hand can then be entirely expressed under the simplified matrical form of the Constrained Least Squares (CLS) problem:

Problem 1. (Constrained Least Squares).

$$\text{Find } \theta^* = \arg \min_{\theta} \frac{1}{2} (\mathbf{z} - \Phi \theta)^\top \Gamma (\mathbf{z} - \Phi \theta) \quad \text{s.t. } \mathbf{C} \theta = \mathbf{d}$$

where θ^* is the constrained solution.

4. PROBLEM SOLUTION

4.1 Common solving methods

Several work have already been conducted on the CLS problem. Three methods in particular come to mind:

A first solution makes use of the simplification:

$$\theta^* = \arg \min_{\theta} \frac{1}{2} (\mathbf{z} - \Phi \theta)^\top \Gamma (\mathbf{z} - \Phi \theta) + \|\mathbf{d} - \mathbf{C} \theta\|_2^2 \quad (15)$$

This however suffers from a trade-off between a low value for the cost J and respecting the constraints. Depending on the data at hand, the obtained results can be unusable because the constraints are not respected.

To balance this issue, a weight constant $\omega \in \mathbb{R}^+$ has been proposed to put more weight on the constraint while retaining the simplicity of the previous formulation under the new form

$$\theta^* = \arg \min_{\theta} \frac{1}{2} (\mathbf{z} - \Phi \theta)^\top \Gamma (\mathbf{z} - \Phi \theta) + \omega \|\mathbf{d} - \mathbf{C} \theta\|_2^2 \quad (16)$$

such that when ω approaches $+\infty$, the constraint is perfectly respected (Golub and Van Loan, 2013).

Finally, the most common solution is to make use of iterative algorithms such as quadratic programming, as is used by MATLAB's "lsqlin" method (Coleman and Li, 1996). This method is more general, as it also authorizes inequality constraints, but it can have quite a long execution time and require high computation power and memory space.

4.2 Algebraic solution

An exact solution to Problem 1 can be found using the Lagrange multiplier method under the assumption that $\Delta = \Phi^T \Gamma \Phi \in \mathbb{R}^{\delta \times \delta}$ is invertible and so is $C \Delta^{-1} C^T \in \mathbb{R}^{m \times m}$. It arises from the KKT matrix equality

$$\begin{bmatrix} \Delta & C^T \\ C & 0 \end{bmatrix} \begin{bmatrix} \theta^* \\ \lambda^* \end{bmatrix} = \begin{bmatrix} \Phi^T \Gamma z \\ d \end{bmatrix} \quad (17)$$

where the solution for θ^* is then given by the 2×2 block matrix inversion formula:

$$\theta^* = \theta^\circ + P(d - C\theta^\circ) \quad (18)$$

where $\theta^\circ = \Delta^{-1} \Phi^T \Gamma z \in \mathbb{R}^\delta$ is the unconstrained solution and $P = \Delta^{-1} C^T (C \Delta^{-1} C^T)^{-1} \in \mathbb{R}^{\delta \times m}$ is a correction matrix. Several properties can be shown from this solution: 1) in the case where the unconstrained solution respects the constraints, the constrained solution is also the unconstrained one ($C\theta^\circ = d \implies \theta^* = \theta^\circ$), and 2) in any case the above result respects the constraints (by noting that $CP = I_m$).

It can also be noted that by construction the non-singularity conditions on Δ and $C \Delta^{-1} C^T$ can be simplified using the fact that Γ is diagonal with non-zero coefficients to the form

$$\text{"A solution exists"} \Leftrightarrow \begin{cases} \Phi \text{ has full column rank} \\ C \text{ has full row rank} \end{cases} \quad (19)$$

from which an additional condition can be derived: there must be at least as many coefficients than there are constraints ($m \leq \delta$). It might be worth noting that in the case $m = \delta$, the solution becomes $\theta^* = C^{-1}d$ which is the only value respecting the constraint.

4.3 Hyper-parameters optimisation

Although the solution from (18) always yields the optimal solution to the CLS problem, it requires the knowledge of both matrices Φ and C to compute. In the case where either the distribution of measurements in the various domains \mathcal{P}_i or the constraints c_j depend on a set of additional parameters $s \in \mathbb{R}^r$ another optimisation process must be devised.

Due to the impracticality of conducting a grid search over a high-dimensional grid, the solution we retained for this is the use of an iterative optimisation algorithm over the optimal cost

$$J^*(s) = J(\theta^*)|_s \quad (20)$$

where s is treated as a vector of hyper-parameters. This solution has the advantage of reducing the complexity of the iterative algorithm by only considering the r hyper-parameters for optimisation, ensuring higher chances of convergence and speed.

Several optimisation algorithm can be used but it was chosen in our case to use the first order adaptive gradient

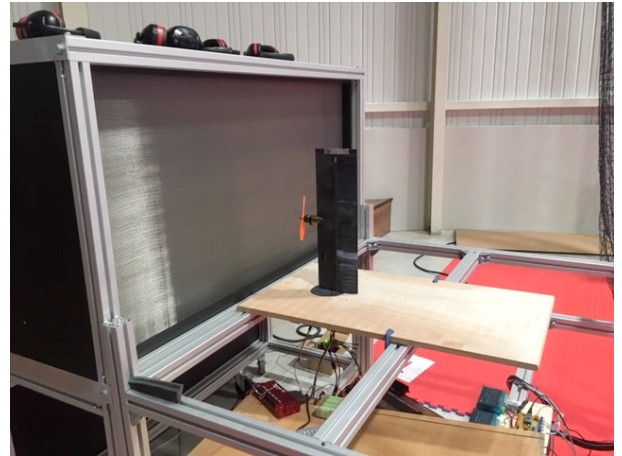


Fig. 2. The experimental setup used to gather data.

descent (AdaGrad) method (Duchi et al., 2011). This choice was motivated by the desire to improve on the basic gradient descent for stability and convergence speed while keeping a reduced complexity relative to Newton derivatives. Computing the Hessian is indeed a lengthy process and yielded no significant improvements in our tests on the problem at hand.

It should be noted however that any gradient-based method relies on the continuity of J^* . This is trivially guaranteed while no measurement changes domain due to their variation, assuming that conditions (19) are respected, but it should otherwise be ensured for each two neighbouring domains. In the case of the lift model defined Section 2, the hyper-parameters are the four separation angles of attack α_i , $i \in \llbracket 0, 3 \rrbracket$ described in Fig. 1. Continuity of the optimal cost function is ensured by the continuity constraints between each two neighbouring domains and the fact that the weights are kept constant throughout the study.

5. APPLICATION TO EXPERIMENTAL DATA

Following from the previously-defined model for the lift coefficient and identification process, the polynomial identification method will be applied to experimental data.

5.1 Experimental setup

Experimental data has been obtained as shown Fig. 2 from eight open wind tunnel experiments on a single aileron-less straight wing with NACA profile 0012, chord 0.15m and span 0.5m, placed perpendicular to the wind flow as to get no side slip. The flow straightening grid hides a set of 162 independent fans placed in a 9-by-18 configuration that were tasked with generating a constant and uniform wind velocity for the duration of each experiment, while the angle of attack of the wing was progressively increased from 0° to 35° at a speed of approximately $10^\circ/s$ and back to 0° at $12^\circ/s$. Two wind velocities of 7.5m/s and 10m/s were tested, with four experiments each, and the wind velocity was measured by a Pitot tube located ahead of the wing. Although it can be seen from Fig. 2 that the wing used was fitted with a propeller, it was free-moving during the experiments and only spun due to the incoming wind. The same experiment with a clean, propeller-less

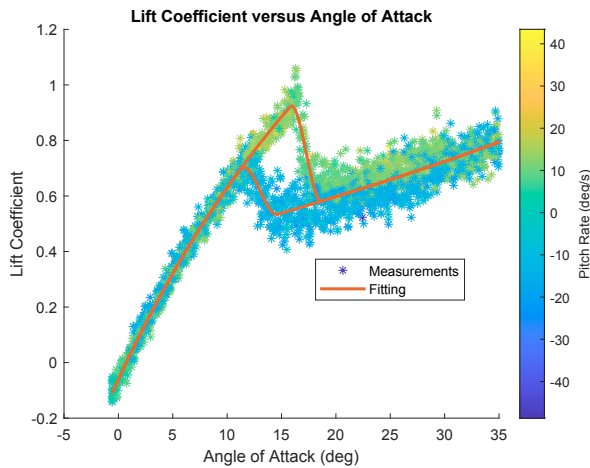


Fig. 3. The fitting results on the experimental data

wing yielded no significant change in the collected data and as such it was decided to keep it for this study.

5.2 Results

The resulting fitting is presented Fig. 3, where the hyper-parameters have been found to be $\alpha_0 = 15.77^\circ$, $\alpha_1 = 18.69^\circ$, $\alpha_2 = 14.65^\circ$ and $\alpha_3 = 11.13^\circ$.

Immediately, one can find that the model seems to accurately represent the lift on the whole of the domain considered. The total cost is $J = 1.08 \times 10^{-3}$, which represents in our case half of the Mean Squared Error (MSE) of the fitting with respect to the given data. In particular, the pre-stall model seems to accurately represent the lift of the wing up to the stall angle of 15.77° , with an MSE of only 8.08×10^{-4} . The fitting in the post-stall domain (third polynomial) is also accurately representing the lift coefficient of the wing but suffers from the noisier data given, with a higher MSE of 2.80×10^{-3} . This is due to unstationary effects of the turbulent flow that "pollute" our measurements. Finally, the fitting about the aerodynamic hysteresis interestingly gave good results, with once again an accurate representation of the lift. The MSEs on these domains were 5.42×10^{-3} for the polynomial going from the pre-stall to the post-stall domain and 2.98×10^{-3} going in the opposite direction.

A robustness analysis of the iterative optimisation process was conducted by running the algorithm a thousand times with randomized initial hyper-parameters (taken from the estimated best solution plus or minus 1.5° for the first two separations and $\pm 1.7^\circ$ for α_2 and α_3). It gave a convergence rate of 100% for a stop condition of $\forall j \in \llbracket 1, r \rrbracket, \|\Delta \mathbf{s}_j / \mathbf{s}_j\| < 10^{-4}$ (0.01 %). The maximum number of iterations was 518 for an average of 163.6, a median of 146.5 and a standard deviation of 87.18, showing the ability of the algorithm to quickly yield an accurate result.

5.3 Comparison with other methods

The results from Section 5.2 will finally be compared with two piecewise polynomial formulations: the PWPFIT method developed by the authors of Cunis et al. (2019) and the AERODAS model (Spera, 2008). However, since the

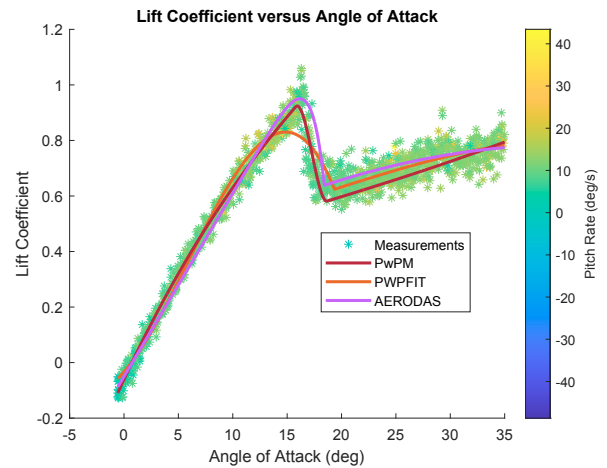


Fig. 4. Comparison of the fitting for the three models

authors of these papers chose not to consider the hysteresis phenomenon, only the measurements with a positive pitch rate will be used. The results of this comparison are presented Fig. 4.

Without even considering, as stated, the hysteresis, the PwPM method we propose here seems to be better at modelling the lift of the wing, and in particular in the transition from pre-stall to post-stall dynamics, where Fig. 4 shows that PWPFIT fails to account for the brusque variation in lift and AERODAS's simpler shape overshoots the measurements. In addition, both models are not differentiable at the separation between the pre-stall and post-stall curves, an issue that was addressed in part by the authors of Cunis et al. (2020) by adding a sigmoid blending term between the two polynomials. However, doing so loses the polynomial formulation. PwPM in turn seems to underestimate the lift in the post-stall domain, which can be explained by the fact that it takes into account some unrepresented data with negative pitch rates the other two don't.

The poorer performance of the PWPFIT and AERODAS models can be traced back to some choices by the authors. Indeed, they both consider the lift on the entire flight envelope up to $\alpha = 90^\circ$ of angle of attack to be composed of only two pieces, one for pre-stall flight and one for post-stall, which forces them to sacrifice some precision for the sake of simplicity of the model. As a result, the transition is unsurprisingly where the fitting is the poorest. In addition, the experiment featured is characteristic of the so-called leading edge stall where the air flow detaches abruptly due to the burst of a laminar separation "bubble" near the leading edge and the flow separation point moves backward toward the trailing edge. Such a behaviour is a lot less common in the literature than the trailing edge stall and one can assume that the authors of Cunis et al. (2019) and Spera (2008) developed their models with this second behaviour in mind, making it less effective on the dataset at hand. PwPM is however compatible as is with trailing edge stall behaviour and it is expected that it would still outperform its competitors on such a dataset.

Table 1 proposes a summary of the MSEs for each of the methods on the three domains considered, namely in the pre-stall ($\alpha < \alpha_0$), transition ($\alpha_0 < \alpha < \alpha_1$) and

Table 1. Mean Squared Errors comparison for the methods presented

Domain	PwPM	PWPFIT	AERODAS
pre-stall	8.29×10^{-4}	1.50×10^{-3}	1.47×10^{-3}
transition	5.42×10^{-3}	1.16×10^{-2}	1.69×10^{-2}
post-stall	2.67×10^{-3}	1.72×10^{-3}	1.97×10^{-3}
Whole domain	2.05×10^{-3}	2.42×10^{-3}	2.95×10^{-3}

post-stall ($\alpha > \alpha_1$) domains. Each of the three models considers a different value for α_1 but the value from PwPM was used here for continuity. As noted before, the two methods PWPFIT and AERODAS are better than PwPM on the post-stall domain. However, their overall precision is impacted by their worst fitting on the two other pieces, where their MSEs are significantly higher, and in particular on the transition domain.

6. CONCLUSION AND PERSPECTIVES

This paper proposed a new piecewise polynomial model (PwPM) for the modelling of the lift coefficients of a UAS as well as a Constrained Least Squares (CLS) method to identify it. The model was chosen specifically for a better modelling of the behaviour of the aircraft at stall when going from laminar to turbulent flow and vice-versa, including the aerodynamic hysteresis. Comparison with the PWPFIT two-pieced polynomial model and the AERODAS one showed that the PwPM approach outperformed both overall and particularly in the transition from pre-stall to post-stall dynamics, fulfilling its requirements. In addition, the proposed method for identification is able to quickly yield accurate results, even with noisy experimental data.

Further work will however be needed on the subject before upset recovery can be tackled. In particular, polynomial models for the other aerodynamic coefficients not presented here will have to be defined and identification on real flight data must be carried on. In addition a recursive adaptation of this algorithm must be defined before attempting flights in the post-stall domains in order to ensure airspace and ground safety.

ACKNOWLEDGEMENTS

This work was supported by the Defense Innovation Agency (AID) of the French Ministry of Defense (research project CONCORDE N° 2019 65 0090004707501).

REFERENCES

- Ancel, E., Capristan, F.M., Foster, J.V., and Condotta, R.C. (2017). Real-time risk assessment framework for unmanned aircraft system (uas) traffic management (utm). *17th AIAA Aviation Technology, Integration, and Operations Conference*, 3273, 3273.
- Bertrand, S., Raballand, N., Viguier, F., and Muller, F. (2017). Ground risk assessment for long-range inspection missions of railways by uavs. *2017 International Conference on Unmanned Aircraft Systems (ICUAS)*, 1343–1351.
- Coleman, T.F. and Li, Y. (1996). A Reflective Newton Method for Minimizing a Quadratic Function Subject to Bounds on Some of the Variables. *SIAM Journal on Optimization*, 6(4), 1040–1058.
- Cunis, T., Condomines, J.P., Burlion, L., and la Cour-Harbo, A. (2020). Dynamic stability analysis of aircraft flight in deep stall. *Journal of Aircraft*, 57(1), 143–155.
- Cunis, T., Burlion, L., and Condomines, J.P. (2019). Piecewise polynomial modeling for control and analysis of aircraft dynamics beyond stall. *Journal of Guidance, Control, and Dynamics*, 42(4), 949–957.
- Duchi, J., Hazan, E., and Singer, Y. (2011). Adaptive subgradient methods for online learning and stochastic optimization. *Journal of machine learning research*, 12(7), 39.
- EU (May 2019). Commission implementing regulation (eu) 2019/947 of 24 may 2019 on the rules and procedures for the operation of unmanned aircraft (text with eea relevance). *Official Journal of the European Union*, 2019.
- Farcy, D., Khrabrov, A.N., and Sidoryuk, M.E. (2020). Sensitivity of spin parameters to uncertainties of the aircraft aerodynamic model. *Journal of Aircraft*, 1–16.
- Golub, G.H. and Van Loan, C.F. (2013). *Matrix computations. xxi*. The Johns Hopkins University Press Baltimore.
- Hoffer, N.V., Coopmans, C., Jensen, A.M., and Chen, Y. (2014). A survey and categorization of small low-cost unmanned aerial vehicle system identification. *Journal of Intelligent & Robotic Systems*, 74(1-2), 129–145.
- Keller, D., Farcy, D., and Le Roy, J.F. (2019). Numerical Investigation of the Aerodynamic Behavior of a Generic Light Aircraft. In *AAAF AERO2019*. PARIS, France.
- Kwatny, H.G., Dongmo, J.E.T., Chang, B.C., Bajpai, G., Yasar, M., and Belcastro, C. (2013). Nonlinear analysis of aircraft loss of control. *Journal of Guidance, Control, and Dynamics*, 36(1), 149–162.
- Leishman, J.G. and Beddoes, T. (1989). A semi-empirical model for dynamic stall. *Journal of the American Helicopter society*, 34(3), 3–17.
- Morelli, E.A., Cunningham, K., and Hill, M.A. (2013). Global aerodynamic modeling for stall/upset recovery training using efficient piloted flight test techniques. In *AIAA Modeling and Simulation Technologies (MST) Conference*, 4976.
- Saderla, S., Kim, Y., and Ghosh, A. (2018). Online system identification of mini cropped delta uavs using flight test methods. *Aerospace Science and Technology*, 80, 337–353.
- Spera, D.A. (2008). Models of Lift and Drag Coefficients of Stalled and Unstalled Airfoils in Wind Turbines and Wind Tunnels. Technical Report NASA/CR-2008-215434, NASA – Jacobs Technology Inc.
- Tol, H., De Visser, C., Sun, L., van Kampen, E., and Chu, Q. (2016). Multivariate spline-based adaptive control of high-performance aircraft with aerodynamic uncertainties. *Journal of Guidance, Control, and Dynamics*, 39(4), 781–800.
- Uhlig, D.V. and Selig, M.S. (2017). Modeling micro air vehicle aerodynamics in unsteady high angle-of-attack flight. *Journal of Aircraft*, 54(3), 1064–1075.

Model-free control algorithms for micro air vehicles with transitioning flight capabilities

International Journal of Micro Air Vehicles

Volume 12: 1–22

© The Author(s) 2020

Article reuse guidelines:

sagepub.com/journals-permissions

DOI: 10.1177/1756829320914264

journals.sagepub.com/home/mav

Jacson MO Barth¹ , Jean-Philippe Condomines¹,
Murat Bronz¹, Jean-Marc Moschetta², Cédric Join^{3,4} and
Michel Fliess^{4,5}

Abstract

Micro air vehicles with transitioning flight capabilities, or simply hybrid micro air vehicles, combine the beneficial features of fixed-wing configurations, in terms of endurance, with vertical take-off and landing capabilities of rotorcrafts to perform five different flight phases during typical missions, such as vertical takeoff, transitioning flight, forward flight, hovering and vertical landing. This promising micro air vehicle class has a wider flight envelope than conventional micro air vehicles, which implies new challenges for both control community and aerodynamic designers. One of the major challenges of hybrid micro air vehicles is the fast variation of aerodynamic forces and moments during the transition flight phase which is difficult to model accurately. To overcome this problem, we propose a flight control architecture that estimates and counteracts in real-time these fast dynamics with an intelligent feedback controller. The proposed flight controller is designed to stabilize the hybrid micro air vehicle attitude as well as its velocity and position during all flight phases. By using model-free control algorithms, the proposed flight control architecture bypasses the need for a precise hybrid micro air vehicle model that is costly and time consuming to obtain. A comprehensive set of flight simulations covering the entire flight envelope of tailsitter micro air vehicles is presented. Finally, real-world flight tests were conducted to compare the model-free control performance to that of the Incremental Nonlinear Dynamic Inversion controller, which has been applied to a variety of aircraft providing effective flight performances.

Keywords

MAV with transitioning flight capabilities, hybrid MAVs, control system architecture, flight control, model-free control

Date received: 26 April 2019; Revised 6 December 2019; accepted: 13 February 2020

Introduction

Micro air vehicles (MAVs) with transitioning flight capabilities, or simply hybrid MAVs, operate over a wide flight envelope including different flight phases, such as vertical take-off, efficient forward flight, transitioning flights, hovering and vertical landing, see Figure 1. While this complete flight envelope enlarges the application range of MAVs, new aerodynamics optimization approaches must be developed to improve the MAV flight performance, considering the aerodynamics challenges of each flight domain. Furthermore, the autopilot system must ensure the stability and the tracking of trajectories for all these flight domains which results in a higher degree of challenge and complexity also for the guidance, navigation, and control

community. Different hybrid MAV configurations such as tilt-rotors¹ or tilt-wings,² quadplanes,³ and tilt-body or tailsitter⁴ can be found in literature.

¹ENAC, Université de Toulouse, Toulouse, France

²Department of Aerodynamics, Energetics and Propulsion, ISAE-Supaero, Toulouse, France

³CRAN, Université de Lorraine, Vandœuvre-lès-Nancy, France

⁴AL.I.E.N (ALgèbre pour Identification & Estimation Numérique), Vézelize, France

⁵LIX, École Polytechnique, Palaiseau, France

Corresponding author:

Jacson MO Barth, UAV Systems Group, ENAC, Université de Toulouse, France.

Email: jacson-miguel.olszanecki-barth@enac.fr



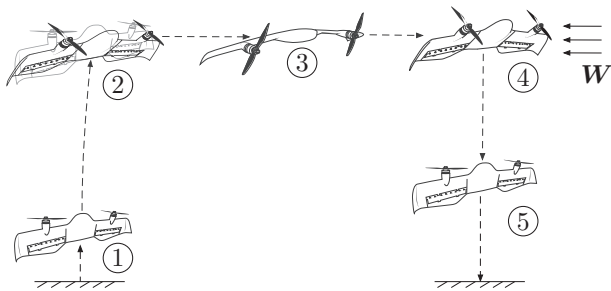


Figure 1. Typical flight phases of micro air vehicles with transitioning flight capabilities: 1 – Vertical take-off; 2 – Transition; 3 – Forward flight; 4 – Hover flight; 5 – Vertical landing. The vector W represents the wind disturbances.

These platforms have been designed in order to solve the aerodynamics and mechanical limitations of each of them, and the choice of the appropriated MAV configuration varies according to the imposed flight mission specifications, e.g., maximum payload, the desired endurance and range, etc. Generally, hybrid MAVs are designed and optimized to perform an efficient forward flight, since this flight phase represents most of its mission. Various studies have improved and assessed the aerodynamic properties of hybrid MAVs previously.^{5,6} A critical point is the design of flap effectiveness which needs to be optimized in order to create sufficient pitch moment ensuring the control authority during transitioning flights. We focus this research project in the design and control of tailsitter MAVs, and we investigate the performance of this peculiar MAV class for three reasons: (1) Tailsitters have a better endurance in forward flight when compared to other configurations of hybrid MAVs; (2) The simple transition mechanism of tailsitters facilitates the control design for its entire flight envelope, unlike to tiltrotors that need additional actuators to orient the propeller in order to perform transitioning flights; (3) The design of controllers requiring little prior knowledge of the dynamics of tailsitter MAVs remains an attractive, motivating and challenging topic that needs to be answered by the control community. Typically, the entire flight envelope of tailsitter MAVs can be analyzed in three distinct flight modes, namely, hovering flight, forward flight and transitioning flight. The stabilization of hovering and forward flights can be achieved using linearized models around an equilibrium point facilitating the implementation of classical linear control algorithms. On the other hand, transitioning flights present some peculiarities that include fast changing of aerodynamic forces and moments with wing behaviors partially stalled. Based on such aerodynamic effects, the identification of a reliable model that accurately represents the nonlinear

dynamics of a tailsitter MAV over its entire flight envelope remains an expensive, a time consuming and a difficult task. Because of these practical problems related to the characterization of a model for the design of model-based controllers, some research works considered the transition flight as an undesirable and transient flight phase. However, transitioning flights need to be continuously stabilized in order to ensure a smooth and safe flight, especially for flying missions in windy environments. Hybrid MAVs are often considered by the control community as a parameter varying system, e.g. the change of aerodynamic coefficients according to the hybrid MAV attitude orientation and the environmental wind conditions. Consequently, designing a control technique for autopilot systems that does not rely on prior knowledge of the hybrid MAV model becomes an intuitive, innovative and, from the point of view of the authors, an appropriate control methodology. Therefore, the development of such a controller that estimates the hybrid MAV dynamics and counteracts it, in real time, can be easily adaptable and implemented for different hybrid MAVs.

Literature review

Different control strategies have been designed for hybrid MAVs; we present some of them in the following with particular emphasis in the controllers developed for the tailsitter class. For practical reasons, classical linear controllers designed using PID techniques have been applied in the control of hybrid MAVs.^{7–11} Although simple to tune without the knowledge of the controlled system, PID controllers have insufficient robustness properties against wind disturbances. Autopilot systems designed from optimal control theory, have been researched.^{12,13} For instance, the linear quadratic regulator which was designed and applied for a tailsitter MAV previously modeled and identified from wind tunnel campaign.¹⁴ However, the performance of model-based controllers may differ primarily in the fidelity with which the plant is modeled and the accuracy of the identified model parameters. Hence, classical model-based control techniques seem to be neither optimal for hybrid MAVs nor easily transposable for a new platform. Gain scheduling methods employing different control algorithms with both linear¹⁵ and nonlinear approaches,¹⁶ have been developed to stabilize hybrid MAVs at different pitch angle orientations within the transitioning flight. Gain scheduling techniques allow easy understanding and simple implementation of the control gains that cover the entire flight envelope of hybrid MAVs. However, the principal disadvantage of this control method, found in literature,¹⁷ is the expensive computational

cost for operations in real time. In the same way, an attitude controller based on optimal control algorithms was proposed by Ritz and Andrea,¹⁸ different control solutions for a set of attitude errors were precomputed and stored in a lookup table. According to the current flight conditions and for each autopilot system update, the desired control gains are obtained by reading their predefined values in the table. Further analysis is needed to determine if this proposed control strategy can be effective and easily adaptable for different hybrid MAVs. Adaptive control techniques which account for uncertainties present in the hybrid MAV model were developed by some authors.^{19,20} However, instability problems with adaptive control methods can still exist with regard to unmodeled dynamics or inaccurate models used in the adaptation criterion of controller's gains. Different research topics applying nonlinear control techniques on hybrid MAVs, such as backstepping,^{19,21,22} NDI^{20,23,24} and INDI,²⁵ appears to be positively researched in literature. The INDI approach, which is a control that depends less on the model, was experimentally flight tested providing excellent performance against wind disturbances. This controller requires the identification of the system actuator behavior in order to estimate its control effectiveness. As the actuator's effectiveness varies according to the flight phase, e.g. hovering or forward flight, a gain scheduling method was implemented to fit the actuator effectiveness under the respective flight domain. Some theoretical research has analyzed the performance of nonlinear feedback control on axisymmetric aerial vehicles²⁶ proposing an extended control solution to a larger set of generic aerodynamic models²⁷ which could include hybrid MAVs. Additionally, a variety of nonlinear control strategies based on Lyapunov's stability concepts have been designed to hybrid MAVs.^{4,28}

Links with the model-free control algorithm

The literature presents some particular control algorithms that do not rely on modeling. For instance, the model-free control (MFC) approach proposed by Fliess and Join²⁹ has been successfully illustrated in different concrete case-studies varying from wastewater denitrification,³⁰ nanopositioning of piezoelectric systems³¹ up to inflammation resolution in biomedical applications,³² see also its references for additional case-study examples and supplementary information. Some research works based on MFC techniques have led to patents, such as Join et al.³³ and Abouaïssa et al.³⁴ This control approach has been applied in the aerospace field^{35,36} and, except for our previous work, it has never been applied on hybrid MAVs which is an additional motivation for the development of our

research project. The advantage of the control methodology proposed in this paper is the capability to estimate the hybrid MAV dynamics, without a prior knowledge of its parameters, only from its output and input-control signal measurements. Thus, the disturbances that may affect flight performances are measured and the MFC algorithms are able to estimate as well as counteract the undesirable dynamics in order to continuously stabilize the hybrid MAV for arbitrary attitude orientations covering its entire flight envelope.

Present work

The main contribution of our current work is to develop a fully autonomous MAV with transitioning flight capabilities that performs a given mission accurately. Depending upon the mission complexity and its requirements, the MAV should fly at low and high air speeds, respectively corresponding to hovering and forward flight phase. Based on these mission requirements, and the modeling issue presented in the previous section involving this particular MAV class, we present a part of our previous work that deals with:

- (i) comparison between a model-based controller and our MFC architecture during the transition flight in a disturbed environment;³⁷
- (ii) uncertain parameter analysis of fixed-wing MAVs in forward flight;³⁸
- (iii) full MFC architecture for position tracking, velocity control and attitude stabilization of a hybrid MAV during its entire flight envelope;³⁹

Our intention is to analyze our control architecture through additional flight simulations and real-world flight tests in order to investigate its operational behavior, its limits and the interaction between each MFC control block. The new contributions of this paper, with respect to our previous works, are:

- (i) initial condition analysis during hovering and transitioning flight phases in order to empirically determine a safe and stable boundary for distinguished initial conditions of attitudes and velocities;
- (ii) control performance analysis in the frequency domain during hovering and forward flights;
- (iii) study of MFC's adaptive properties for parametric variation illustrations during the forward-to-hover transition through flight simulations;
- (iv) real-world flight tests to compare the MFC attitude stabilization performance to that of the INDI controller in indoor flight conditions;

The paper is organised as follows: in the next section, we present the manufacturing process and the particular aerodynamics of the hybrid MAV prototype named DarkO. Then, we describe the hybrid MAV behavior from a mathematical formulation based on equations of motion. This is followed by a section in which the control strategy is detailed as well as the proposed control architecture. Flight simulations are presented then and real-world flight tests follow. Finally, the reader can find the conclusion and the future work.

Hybrid MAV prototype

Throughout the whole study, we have used the DarkO vehicle which is a tailsitter configuration consisting of two motors, positioned in front of the wing, and two exceptionally large double-flapped control surfaces. Mission definition of DarkO has been mainly optimized for forward flight with the capability of taking off and landing vertically. Therefore, it has not been particularly designed for hovering for long duration.

Manufacturing

The DarkO's frame is completely manufactured by the 3D printing method using Onyx material. Figure 2 shows the printed pieces that are assembled in order to build the whole frame. The shell structure for the wing and the fuselage halves are manufactured as 0.7 mm thick skins, and the spar is manufactured with the addition of unidirectional concentric carbon fibers embedded into Onyx material. This method ensures to have a sufficiently rigid airframe that supports aerodynamic forces and yet also flexible enough to absorb harsh impacts during landing and test flights.

Control surface design

A particular feature that is required by the tailsitter configuration is to generate excessive amount of pitching moment in order to transition mainly from forward flight phase to hovering flight phase. Therefore, DarkO frame's control surfaces have been designed as double-flap which has a passive mechanical constant ratio. Traditionally, multi-section flaps have been designed for lift enhancement; however, in our case the design objective is to generate as much positive pitching moment as possible without having a massive flow separation on the bottom surface of the airfoil. The advantage of using double-flap (δ_{II}) control surface with respect to using a single-flap (δ_I) control surface has been shown in Figure 3. Variation of the sectional lift C_l , drag C_d , and moment coefficients C_m at different flap deflection angles have been compared for the two different flap configurations. The analysis has been

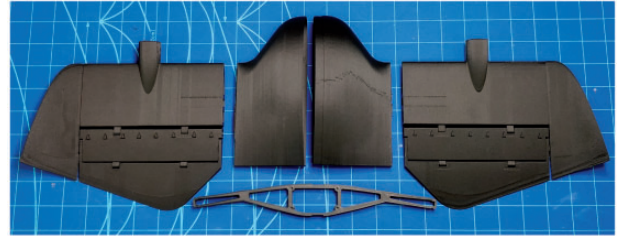


Figure 2. Printed parts of DarkO out of Onyx material.

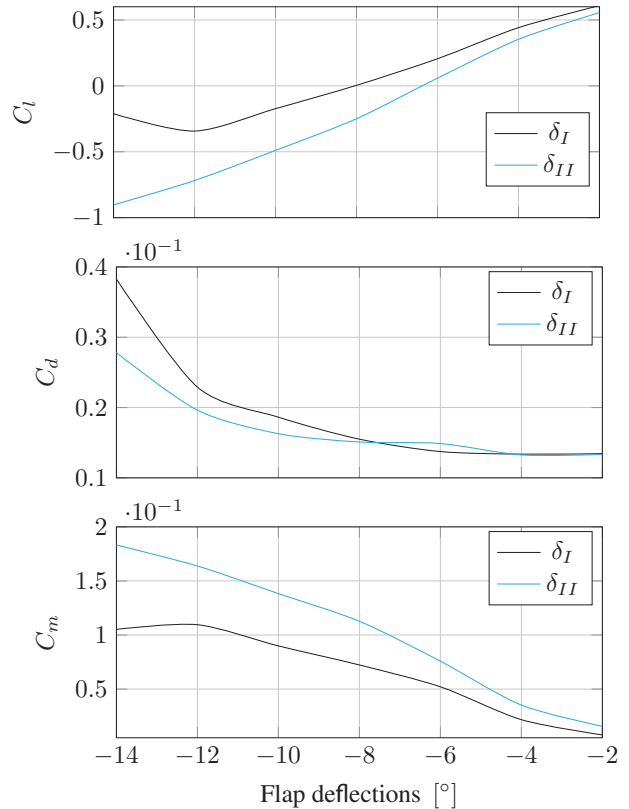


Figure 3. Variation of the sectional lift C_l , drag C_d , and moment coefficients C_m with respect to flap angles for different flap configurations: double-flap (δ_{II}) control surface and a single-flap (δ_I) control surface

done by using the open-source program XFOIL.⁴⁰ Reynolds number used during the analysis corresponds to the slipstream velocity seen by the blown portion of wing and is approximately 150k. The DarkO's motor mounts have an incidence angle of -6 degrees on DarkO's wings; therefore, the airfoil has been set to an angle of attack of $+6$ degrees and then the flap angle has been varied between -2 and -14 degrees (negative flap angle being upward). Particular attention should be given to the pitching moment C_m in the figure. We notice that double-flap (δ_{II}) control surface

can generate almost two times the pitching moment generated by the single-flap (δ_f) control surface. As a side effect, the double-flap control surface also works efficiently for lift generation; however, as we are trying to increase the pitching moment (in positive direction), the lift generation happens in negative direction. The vehicle requires the excessive amount of pitching moment only during transition phase, and the duration of this maneuver is very short; therefore, lift reduction caused while increasing the pitching moment has not been taken as an issue.

Simplified tailsitter MAV model

This section is divided into two parts. First, we present the mathematical formulation of aerodynamic forces and moments, and the aerodynamic assumptions used in the hybrid MAV model. Then, the equations of motion, based on Newton's second law, are introduced to describe the hybrid MAV behavior. The obtained hybrid MAV dynamics are used to establish a flight simulator in order to analyze the proposed control approach before real-world flight tests.

Formulation of aerodynamic forces and moments

We present an analytic continuous singularity-free formulation of aerodynamic forces $\mathbf{F}_{a_b} \in \mathbb{R}^3$ and moments $\mathbf{M}_{a_b} \in \mathbb{R}^3$ acting in a wing over a complete 360° angle of attack, based on previous work proposed by Lustosa et al.⁴¹ The wing with a surface S , is immersed in an incompressible and inviscid airflow with air density ρ . The free-stream velocity is composed by the linear element $\mathbf{v}_\infty \in \mathbb{R}^3$ and the angular component defined by $\boldsymbol{\omega}_\infty \in \mathbb{R}^3$ which, in the absence of wind, is equal to the hybrid MAV angular velocity $\boldsymbol{\omega}_b \in \mathbb{R}^3$. This formulation of aerodynamic forces and moments is given by

$$\begin{pmatrix} \mathbf{F}_{a_b} \\ \mathbf{M}_{a_b} \end{pmatrix} = -\frac{1}{2}\rho S\eta C\Phi(\boldsymbol{\eta}_b)C\boldsymbol{\eta}_b \quad (1)$$

where

$$\eta = \sqrt{v_\infty^2 + \mu c^2 \omega_\infty^2}, \quad \text{with } \mu \in \mathbb{R} > 0 \quad (2)$$

and

$$\boldsymbol{\eta}_b = \begin{pmatrix} \mathbf{v}_\infty \\ \boldsymbol{\omega}_\infty \end{pmatrix} \quad (3)$$

The vector $\boldsymbol{\eta}_b$ describes the linear and angular free-stream velocities in the body coordinate frame. The matrix C denotes the reference wing parameters in an extended representation

$$C = \begin{pmatrix} I_{3 \times 3} & 0_{3 \times 3} \\ 0_{3 \times 3} & \begin{bmatrix} b & 0 & 0 \\ 0 & c & 0 \\ 0 & 0 & b \end{bmatrix} \end{pmatrix} \quad (4)$$

where b and c are, respectively, the wingspan and the mean chord. Finally, the matrix $\Phi \in \mathbb{R}^{6 \times 6}$, which is subdivided into four matrices $\Phi^{(i)} \in \mathbb{R}^{3 \times 3}$, shows the interaction between aerodynamic forces and moments with linear and angular free-stream velocities

$$\Phi = \begin{pmatrix} \Phi^{(fv)} & \Phi^{(fw)} \\ \Phi^{(mv)} & \Phi^{(mw)} \end{pmatrix} \quad (5)$$

The Φ parameters are deduced from thin airfoil theory; we refer the interested reader to Lustosa⁴² for further information. Nonetheless, we mention that

$$\Phi_0^{(fv)} = \begin{pmatrix} C_{d0} & 0 & 0 \\ 0 & C_{y0} & 0 \\ 0 & 0 & 2\pi + C_{d0} \end{pmatrix} \quad (6)$$

$$\Phi^{(f\omega)} = \begin{pmatrix} 0 & 0 & 0 \\ 0 & 0 & b^{-1}\Delta r C_{y0} \\ 0 & -c^{-1}\Delta r(2\pi + C_{d0}) & 0 \end{pmatrix} \quad (7)$$

$$\Phi_0^{(mv)} = \begin{pmatrix} 0 & 0 & 0 \\ 0 & 0 & -c^{-1}\Delta r(2\pi + C_{d0}) \\ 0 & b^{-1}\Delta r C_{y0} & 0 \end{pmatrix} \quad (8)$$

$$\Phi^{(m\omega)} = \frac{1}{2} \begin{pmatrix} C_{lp} & C_{lq} & C_{lr} \\ C_{mp} & C_{mq} & C_{mr} \\ C_{np} & C_{nq} & C_{nr} \end{pmatrix} \quad (9)$$

with C_{d0} the minimal drag coefficient and C_{y0} the minimal side force coefficient. The parameter Δr represents the distance between the center of gravity location and the aerodynamic center (neutral point). The negative values of Δr , according to the defined coordinate system, imply a positive static margin of the hybrid MAV. Finally, C_l , C_m and C_n are the aerodynamic moment coefficients which depend on the angular hybrid MAV velocities (p , q , r). The lift curve slope corresponding to 2π , in equations (6), (7) and (8), was deduced from the thin airfoil theory in 2D.

In this work, we evaluate the lift curve slope in 3D considering the wing aspect ratio (AR). According to Diederich's formula, we consider

$$\Phi_0^{(fv)}(:, 3) = \begin{pmatrix} 0 \\ 0 \\ \frac{\pi AR}{1 + \sqrt{1 + (\frac{AR}{2})^2}} + C_{d0} \end{pmatrix} \quad (10)$$

$$\Phi_0^{(f\omega)}(:, 2) = \begin{pmatrix} 0 \\ 0 \\ -c^{-1} \Delta r \left(\frac{\pi AR}{1 + \sqrt{1 + (\frac{AR}{2})^2}} + C_{d0} \right) \end{pmatrix} \quad (11)$$

$$\Phi_0^{(mv)}(:, 3) = \begin{pmatrix} 0 \\ -c^{-1} \Delta r \left(\frac{\pi AR}{1 + \sqrt{1 + (\frac{AR}{2})^2}} + C_{d0} \right) \\ 0 \end{pmatrix} \quad (12)$$

where

$$AR = \frac{b^2}{S} \quad (13)$$

Finally, the flap deflections are modeled as varying cambered airfoils and the aerodynamic forces and moments created by these deflections are approximated by the following equations

$$\Phi_0^{(fv)}(\delta_i) = \Phi_0^{(fv)}(I - [\xi_f]_{\times} \delta_i) \quad (14)$$

$$\Phi_0^{(mv)}(\delta_i) = \Phi_0^{(mv)}(I - [\xi_m]_{\times} \delta_i) \quad (15)$$

the flap deflection effectiveness is represented by two skew-symmetric matrices, $[\xi_f]_{\times}$ for the force effectiveness and $[\xi_m]_{\times}$ for the moment effectiveness, given by

$$[\xi_f]_{\times} = \begin{bmatrix} 0 & -\xi_f & \xi_f \\ \xi_f & 0 & -\xi_f \\ -\xi_f & \xi_f & 0 \end{bmatrix}$$

$$[\xi_m]_{\times} = \begin{bmatrix} 0 & -\xi_m & \xi_m \\ \xi_m & 0 & -\xi_m \\ -\xi_m & \xi_m & 0 \end{bmatrix}$$

Equations of motion

The hybrid MAV model is divided into four rigid bodies (two propellers and two wings composing the fuselage) with constant mass (m), represented by 10 states $\mathbf{x} = (\mathbf{v}_b, \boldsymbol{\omega}_b, \mathbf{q})$, where $\mathbf{v}_b \in \mathbb{R}^3$ is the vehicle's linear velocity, $\boldsymbol{\omega}_b \in \mathbb{R}^3$ is the vehicle's angular velocity equals to $[p \ q \ r]^T$ both expressed in the body coordinate frame and $\mathbf{q} \in \mathbb{R}^4$ is the quaternion formulation. The system is controlled via four control-inputs, $\mathbf{u} = (\omega_l, \omega_r, \delta_l, \delta_r)$, respectively, the left and right propeller rotation speeds and the left and right flap deflections, which are represented in Figure 4.

In order to compute the forces and moments caused by the wing-propeller interaction, we define two segments. Each segment is composed of one wing j and one propeller k . Thus, the sum of aerodynamic forces acting on the wing j with the thrust \mathbf{T}_k generated by the propeller rotation ω_k and the total moment described in the body coordinate frame, are given by

$$\mathbf{F}_b = \sum_{j,k=1}^2 (\mathbf{F}_{a_{bj}} + \mathbf{T}_k) \quad (16)$$

$$\mathbf{M}_b = \sum_{j,k=1}^2 (\mathbf{M}_{a_{bj}} + \boldsymbol{\tau}_{b_k} + \mathbf{p}_p \times \mathbf{T}_k + \mathbf{p}_a \times \mathbf{F}_{a_{bj}}) \quad (17)$$

The vector $\mathbf{p}_p = [p_{p_x} \ p_{p_y} \ p_{p_z}]^T$ defines the distance between the propeller k with the hybrid MAV center of mass. Both propellers are positioned symmetrically with respect to the hybrid MAV center of mass. The distance between the aerodynamic center and the center of mass is represented by the vector $\mathbf{p}_a = [p_{a_x} \ p_{a_y} \ p_{a_z}]^T$. The internal torque of the propeller $\boldsymbol{\tau}_{b_k}$ that is a

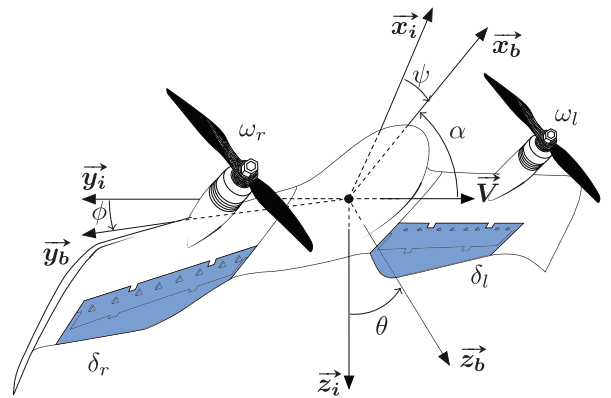


Figure 4. Illustration of the used coordinate frames, angles and actuators. The inertial coordinate frame is represented by $\mathcal{R}_i = \{\vec{x}_i, \vec{y}_i, \vec{z}_i\}$ and the body coordinate frame by $\mathcal{R}_b = \{\vec{x}_b, \vec{y}_b, \vec{z}_b\}$.

function of the vehicle's angular velocity (pqr), and the thrust force T_k , are defined by

$$T_k = k_f \omega_k^2 \vec{x}_b, \quad k_f \in \mathbb{R} > 0 \quad (18)$$

$$\tau_{b_k} = N_{b_k} - J_p(p + \omega_j) \begin{pmatrix} 0 \\ r \\ -q \end{pmatrix} \quad (19)$$

where

$$N_{b_k} = -\text{sign}(\omega_k) k_m \omega_k^2 \vec{x}_b, \quad k_m \in \mathbb{R} > 0 \quad (20)$$

with k_f and k_m the propeller force and moment coefficients and N_{b_k} the propeller moment. Equation (19) describes the gyroscopic interaction between the propellers and the fuselage with J_p equals to the propeller inertia. The vehicle's equations of motion are given by equation (21).

$$\begin{cases} m\dot{\mathbf{v}} &= R^T \mathbf{F}_b(\mathbf{x}, \mathbf{u}, \mathbf{W}) + m\mathbf{g} \\ J\dot{\boldsymbol{\omega}}_b &= \mathbf{M}_b(\mathbf{x}, \mathbf{u}, \mathbf{W}) - [\boldsymbol{\omega}_b]_{\times} J \boldsymbol{\omega}_b \\ \dot{\mathbf{q}} &= \frac{1}{2} \mathbf{q} \otimes \boldsymbol{\omega}_b \\ \dot{\mathbf{p}} &= \mathbf{v} \end{cases} \quad (21)$$

The gravitational acceleration vector is equals to $\mathbf{g} = g\vec{z}_i$ and $\mathbf{W} \in \mathbb{R}^3$ is the wind disturbance vector. The rotation matrix R , namely the Direction Cosines Matrix (DCM, Note: The DCM can be defined with quaternion formulation.), represents the MAV rotation in three dimensions as a mathematical formulation. We assume that the hybrid MAV inertia matrix J is diagonal and it equals to $J = \text{diag}[J_{xx} J_{yy} J_{zz}]$. The position vector in the inertial coordinate frame is represented by $\mathbf{p} = [x \ y \ z]^T$. The highly maneuverable nature of the vehicle calls for a global numerically stable formulation of attitude and justifies the use of quaternions. The symbol \otimes in the previous equation corresponds to the quaternion product. Supplementary Appendix A presents the tailsitter MAV parameters used in this work.

Control strategy

The proposed control strategy is based on MFC algorithms with no information about the tailsitter MAV parameters (e.g. mass, inertia, aerodynamics coefficients, etc.). This controller can be implemented on multiple-input multiple-output systems by assuming an approximate decoupling between the dynamics of the controlled system. This major assumption has been verified by different practical experiments.⁴³

Therefore, for simplicity reasons, we present the MFC algorithms for single-input single-output systems. We use a prior knowledge of sign-convention between control-input influence in the MAV states based on simple flight mechanics equations to develop the correct block interactions in the proposed control architecture. In terms of tuning model-based control approaches, the model given in the previous section is only used to simulate the tailsitter MAV dynamics and not for control design.

MFC principles

As introduced by Fliess and Join,²⁹ an unknown finite-dimensional system with a single control-input (u) and a single output (y) can be described by the following input/output relation in a differential equation formulation

$$\mathbb{E}(y, \dot{y}, \dots, y^{(a)}, u, \dot{u}, \dots, u^{(b)}) = 0 \quad (22)$$

where \mathbb{E} is a polynomial function with real unknown coefficients. We can also describe

$$y^{(v)} = \mathbb{E}(t, y, \dot{y}, \dots, y^{(v-1)}, y^{(v+1)}, \dots, y^{(a)}, u, \dot{u}, \dots, u^{(b)}) \quad (23)$$

with $0 < v \leq a$ and $\frac{\partial \mathbb{E}}{\partial y^{(v)}} \neq 0$. These unknown dynamics can be modeled by a purely numerical equation, so-called *Ultra-Local Model*

$$y_m^{(v)} = F_y + \lambda \cdot u \quad (24)$$

In equation (24), v is the order of the derivative of y_m , $\lambda \in \mathbb{R}$ is a non-physical constant parameter. Moreover, the exploitation of this numerical model requires the knowledge of F_y . This quantity represents the real dynamics of the model as well as the different disturbances which could damage the performance of the output-system. Thus, an accurate estimation of F_y , defined as \hat{F}_y , is crucial and plays an important role in the MFC control performance. Different works in literature proved that the use of a first-order *Ultra-Local Model* ($v=1$) is enough to stabilize unknown dynamics. However, if the unknown dynamics present second-order behavior with small friction coefficients, the use of a first-order *Ultra-Local Model* would be insufficient to stabilize poorly damped dynamics.²⁹ In light of this, we propose to develop MFC algorithms with a second-order *Ultra-Local Model* ($v=2$)

$$\ddot{y}_m = F_y + \lambda \cdot u \quad (25)$$

The first step to obtain an estimation of the system dynamics, is to apply the *Laplace Transform* in equation (25), considering F_y as a constant piece-wise function. According to elementary operational calculus we transform equations (25) to (26)

$$s^2 Y_m(s) - sy_m(0) - \dot{y}_m(0) = \frac{F_y}{s} + \lambda U(s) \quad (26)$$

where $Y_m(s)$ and $U(s)$ correspond to the *Laplace transforms* of y_m and u . By differentiating twice the previous equation, we can remove the initial conditions $y_m(0)$ and $\dot{y}_m(0)$

$$2Y_m(s) + 4s \frac{dY_m(s)}{ds} + s^2 \frac{d^2 Y_m(s)}{ds^2} = \frac{2F_y}{s^3} + \lambda \frac{d^2 U(s)}{ds^2} \quad (27)$$

However, the variable s in the time domain corresponds to a derivative term with respect to time, which is sensitive to noise corruptions and could amplify the noise measurement in the output of \hat{F}_y . In order to reduce noise in the output estimation, we replace these derivative terms by integral functions ($\frac{1}{s}$) who have robust properties against noise. Thus, multiplying both sides of equation (27) by s^{-3} , we obtain

$$\frac{2Y_m(s)}{s^3} + \frac{4}{s^2} \frac{dY_m(s)}{ds} + \frac{1}{s} \frac{d^2 Y_m(s)}{ds^2} = \frac{2F_y}{s^6} + \frac{\lambda}{s^3} \frac{d^2 U(s)}{ds^2} \quad (28)$$

Equation (28) can be transferred back to the time domain employing elementary calculus and *Cauchy's formula* to reduce multiple integrals in a simple one

$$\begin{aligned} \hat{F}_y(t) = & \frac{5!}{2T^5} \int_{t-T}^t [(T-\sigma)^2 - 4\sigma(T-\sigma) + \sigma^2] y_m(\sigma) \\ & - \left[\frac{\lambda}{2} \sigma^2 (T-\sigma)^2 u(\sigma) \right] d\sigma \end{aligned} \quad (29)$$

From measurements of $y_m(t)$ and $u(t)$ obtained in the last T seconds, the unmodeled dynamics of y and the disturbances are estimated by $\hat{F}_y(t)$ which is updated for each interval of integration $[t-T, t]$. This interval corresponds to the integration window of a receding horizon strategy which results in a trade-off. The idea is to choose small integration windows to calculate the estimation within an acceptable short delay but large enough in order to preserve the low-pass filter properties, whose noise attenuation of $y_m(t)$. Based on such estimator, it is possible to design a robust controller that estimates the system dynamics on-line by a

piece-wise function $\hat{F}_y(t)$ periodically updated for each measure of $y_m(t)$ and $u(t)$. According to Figure 5, the MFC closed-loop command is given by

$$u(t) = \underbrace{-\frac{\hat{F}_y(t)}{\lambda}}_{\text{Nonlinear Cancellation}} + \underbrace{\frac{\ddot{y}_{sp}(t) + u_{\mathcal{K}}(t)}{\lambda}}_{\text{Closed-loop tracking}} \quad (30)$$

where $\xi_y(t) = y_m(t) - y_{sp}(t)$ represents the tracking error and $u(t)$ is the closed-loop command of a feedback controller $\mathcal{K}(\xi_y(t))$, usually defined as a proportional (P), proportional-derivative (PD) or even so as proportional-integral-derivative (PID) gains. In this paper, the feedback controller was composed of proportional K_p and derivative K_d gains. We recognize in equation (30) the typical mathematical expression of a nominal control in the flatness-based in which the nonlinear terms $\hat{F}_y(t)$ is added with a closed-loop tracking of a reference trajectory $t \rightarrow y_{sp}(t)$. The error dynamic can be deduced from the combination of equation (30) with equation (25)

$$\ddot{y}_m(t) - \ddot{y}_{sp}(t) = \overbrace{F_y(t) - \hat{F}_y(t)}^{\xi_{F_y}} + K_p \xi_y(t) + K_d \dot{\xi}_y(t) \quad (31)$$

$$\ddot{\xi}_y(t) = \xi_{F_y} + K_p \xi_y(t) + K_d \dot{\xi}_y(t) \quad (32)$$

$$\ddot{\xi}_y(t) - K_d \dot{\xi}_y(t) - K_p \xi_y(t) = \xi_{F_y} \quad (33)$$

Note that, if the error (ξ_{F_y}) between the estimator and the true dynamics is approximately zero during $[t-T, t]$, a simple proportional-derivative controller will be enough to ensure the error convergence to zero because an integration effect is implicitly involved in the MFC algorithm.

MFC design

The MFC closed-loop allows the design of both tracking and regulation performance with distinguished

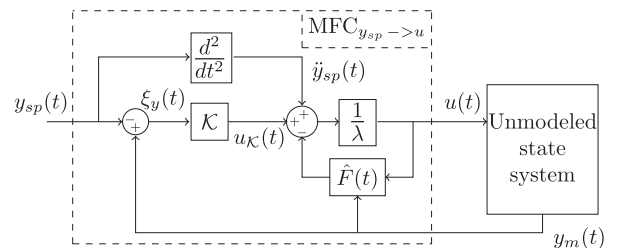


Figure 5. Overview of the model-free control schema.

Table 1. MFC parameters used in the simulations.

States	T_i	λ_i	Kp_i	Kd_i
x	5	25	-0.1225	-0.7
y	10	25	-0.04	-0.4
z	5	20	-0.25	-1
v_{xb}	2	10	-16	-8
v_{yb}	2	70	-7.84	-5.6
v_{zb}	5	2350	-4.6225	-4.3
ϕ	5	300	-4	-4
θ	5	450	-16	-8
ψ	3	1.15	-0.16	-0.8

parameters that can be tuned with little prior knowledge of the system. The following points describe the design methodology used in this work to obtain the MFC parameters presented in Table 1.

1. The proportional-derivative gains (K_p and K_d) have been easily tuned according to classical root locus method. In practice, the MFC estimator provides an accurate estimation of the system ($\xi_{F_y} \approx 0$). Thus, the error dynamics of the closed-loop system can be approximated by a double integrator (33), which can be tuned by pole location approach. In this perspective, we define double real closed-loop poles at $-s_d$, which results the following characteristic polynomial

$$(s + s_d)^2 = s^2 + 2s_d s + s_d^2 \quad (34)$$

The feedback controller with these proportional-derivative gains can be identified by neglecting the initial conditions in the Laplace transform of equation (33)

$$\frac{U_{\mathcal{K}}(s)}{\xi_y(s)} = s^2 - K_d s - K_p \quad (35)$$

Therefore, we obtain the following from equations (34) and (35)

$$K_p = -s_d^2 \quad \text{with} \quad s_d > 0 \quad (36)$$

$$K_d = -2s_d \quad \text{with} \quad s_d > 0 \quad (37)$$

2. The integration window (T) could be defined with prior information about the noise present in the measured signal (y_m). The choice of the integration window implies some expertise according to a trade-off between fast estimations and effective noise

attenuation. For instance, due to the integrator in equation (29) with low-pass filter features, a large integration window provides an effective noise attenuation, but slow estimations with a direct impact on the control-loop responsiveness. On the other hand, small integration windows result in fast estimations with the constraint of estimating noises. In this context, oscillations could be observed in the closed-loop system with high frequency commands (u), which is known as ‘chattering’. In this work, we use an invariant observer⁴⁴ that smooths the measured signals, allowing the set of small integration windows to estimate the fast dynamics of the DarkO tailsitter MAV while suppressing the oscillations generated by the noises in the closed-loop system.

3. Finally, the constant coefficient (λ) is used to scale the amplitude between the command (u) and the dynamics of (\ddot{y}_m). This parameter can be represented as the control effectiveness of the nominal system. Nonetheless, if this parameter is poorly defined or if the actual control effectiveness of the system changes on within a bounded domain, the estimator (\hat{F}_y) is able to compensate this bounded discrepancy ensuring the closed-loop stability. A nominal setting of λ can be achieved by calculating the ratio between the command saturation and the maximum allowable value of (\ddot{y}_m).

From a practical point of view, the proposed MFC design allows a time-saving approach to stabilize complex dynamic systems. The fact that, the closed-loop system can be approximated by the dynamics of a double integrator system simplifies the control design process of proportional-derivative gains.

Control architecture

Figure 6 shows the main ideas of our control architecture. The block *Trajectory generator* is composed of a state flow algorithm that defines constantly the desired positions (x_{sp} , y_{sp} , z_{sp}) in the inertial coordinate system. These references are taken into account by the *Position control* block and are compared with the respective measures (x_m , y_m , z_m) creating three errors that are minimized by the MFC algorithms in the *Position control* block. These three MFC algorithms in charge of the position tracking, also compute the desired velocity in their respective axes. These reference values which are defined in the inertial coordinate frame are transformed to the body coordinate frame as well as the velocities measurements. Thus, the velocity control $MFC_{v_{xb}}$ computes the required thrust T_d to reach this desired velocity along \vec{x}_b , the block $MFC_{v_{zb}}$ assures the velocity control along \vec{z}_b and determine the necessary pitch angle θ_{sp} to reach this desired velocity $v_{zb_{sp}}$. Both blocks control their

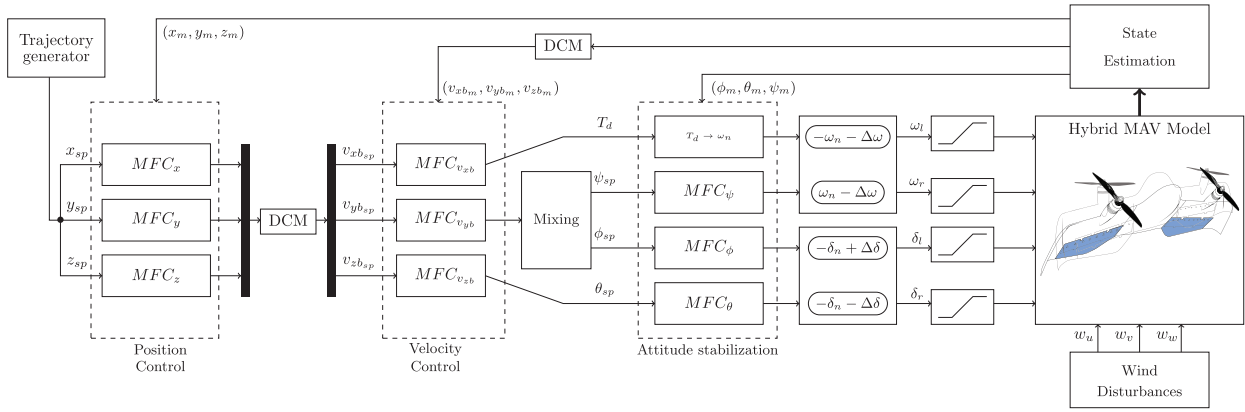


Figure 6. Cascaded MFC architecture designed for tailsitter MAVs. Position control blocks send desired velocities for the velocity control blocks that compute the necessary thrust value as well as the references for attitude stabilization control loop. Based on these desired values, propeller speeds (ω_l , ω_r) and flap deflections (δ_l , δ_r) are defined. MAV: micro air vehicle; DCM: Direction Cosines Matrix.

respective velocities and define the desired thrust and pitch angle for the entire flight envelope, i.e. hover, transition and forward flight. However, the velocity control along \vec{y}_b is designed depending on the current hybrid MAV flight phase. Therefore, in hover flight, the block $MFC_{v_{yb}}$ defines the desired yaw angle ψ_{sp} and the block MFC_{ψ} controls its dynamics through differential-thrust commands creating moments around \vec{z}_b in order to reach the desired velocity along \vec{y}_b . In forward flight, this lateral velocity is reached from roll rotations around \vec{x}_b . These rotations orient the lift force and the hybrid MAV can perform left-right turns with, respectively, negative and positive roll angles ϕ . The propeller speeds (ω_l , ω_r) are defined by the sum of nominal propeller rotation ω_n with a differential propeller speed $\Delta\omega$ which is in charge of the yaw control. The negative sign of ω_n for the left-propeller ω_l is due to the counter-rotation sense. And the flap-deflections (δ_l , δ_r), which are in convention negative for pitch-up, are composed by the sum of symmetrical flap deflection δ_n with anti-symmetrical flap deflections $\Delta\delta$ that are respectively the control-input for the pitch angle θ and for the roll angle ϕ .

Flight simulation results

A comprehensive set of flight simulations, discretized at 500 Hz, were performed from MATLAB/Simulink using the tailsitter MAV model described in the ‘Simplified tailsitter MAV model’ section that is controlled by the proposed MFC architecture, see Figure 6. Our flight simulator is based on the DarkO tailsitter MAV dynamics with sensor measurements corrupted by Gaussian white noises, whose standard deviations can be found in literature.⁴⁵ The MFC parameters, i.e. λ_i , T_i , Kp_i and Kd_i , were tuned for the entire flight envelope of the DarkO with constant

values for all flight simulations. In order to evaluate our control algorithm, we have introduced external perturbations such as wind disturbances during these flights. The results provide a straightforward way to validate the methodological principles presented in this article as well as to evaluate the designed MFC parameters, and to establish a conclusion regarding MFC benefits in both theoretical and practical contexts. The flight simulations are presented in a series of case studies in order to analyze separately each flight domain of the DarkO, such as hovering, transitioning and forward flights.

Hovering flight

In hovering flight, we analyze the velocity and attitude controller’s ability to recover the MAV from different unstable initial condition points. Also, we present an average frequency content of yaw and pitch angle signals using the Fast Fourier Transform (FFT) algorithm over the entire time that the signals were acquired. In addition, we present two position tracking missions in hovering flight, and we verify the interaction between the position, velocity and attitude control blocks.

Initial condition analysis. The initial conditions for pitch angle and for forward speed during the hovering flight (θ_{ic} and $V_{x_{ic}}$), follow a normal distribution law according to equations (38) and (39).

$$\theta_{ic} \sim \mathcal{N}\left(\frac{\pi}{2}, \left(\frac{\pi}{6}\right)^2\right) \quad (38)$$

$$V_{x_{ic}} \sim \mathcal{N}\left(0, \left(\frac{5}{3}\right)^2\right) \quad (39)$$

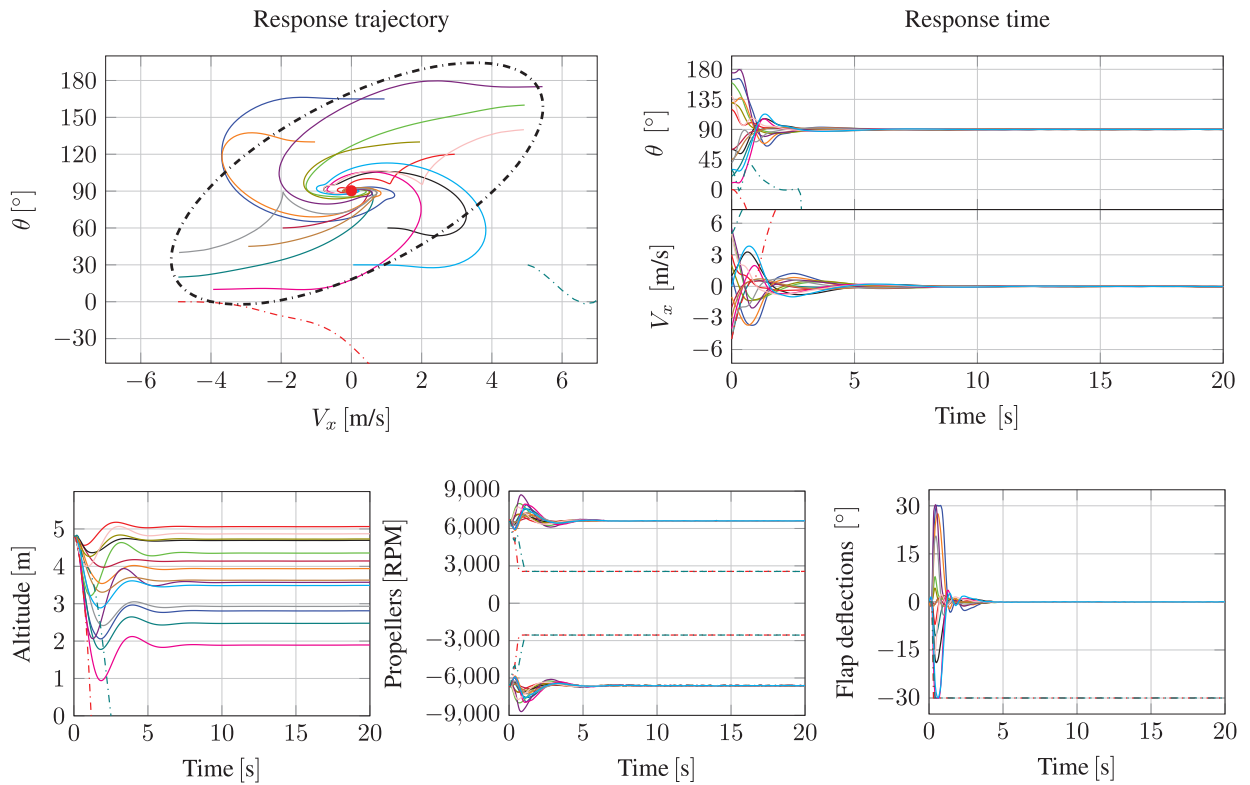


Figure 7. Initial pitch angle and forward speed condition analysis during hovering flight phase without wind disturbances. Forward speed setpoint equals to 0 m/s, the MFC architecture computes the pitch angle setpoint equals to 90° in order to reach the stationary flight.

The stability boundary presented in Figure 7, was empirically defined by evaluating all recovery trajectories from initial conditions to the desired setpoint. The desired setpoint corresponds to a stationary flight in the vertical position, respectively, 0 m/s for the forward speed and 90° for the pitch angle. Basically, three classes of trajectories were distinguished during these simulations. The first one combines trajectories with initial pitching angles larger than 90° with positive initial conditions for forward speeds. Likewise, trajectories with initial pitching angles smaller than 90° and negative initial conditions for forward speeds are also included in this class. The peculiarity of these trajectories is that, both converge directly to the desired equilibrium setpoint with small oscillations in the response time. This can be explained by the fact that, for initial pitching angles larger than 90° , the thrust vector is already well-oriented and it can be increased in order to decelerate the initial positive forward speeds. This thrust vector is increased from increments of the propeller rotations, which improves the flap effectiveness creating a powerful pitch moment that can easily align the attitude of the hybrid MAV in the right direction, towards the attitude setpoint. The same reasoning can be done for initial pitching angles smaller than 90° with

negative forward speeds. In this initial flight condition and orientation, the controller generates the thrust vector in order to increase the forward speed resulting in an effective pitch moment which also steer the hybrid MAV towards the setpoint. The second class of trajectories is composed by all initial pitching angles smaller than 90° with positive initial forward speeds and by all initial pitching angles larger than 90° with negative initial forward speeds. These trajectories diverge at the beginning of the simulation. The thrust vector, in these flight orientations, is unable to generate an opposing force to decelerate the initial forward speed to zero. The only force opposing to the movement is the drag force. By increasing the pitch angle, in this case the angle of attack, the hybrid MAV generates more drag and can reach the forward speed setpoint. For extreme cases, within the stability boundary, we can observe flap saturation which justifies the shape of the concerned trajectories with overshoots and undershoots. By analyzing the altitude results, we can mention that the position control is not activated. However, we can observe that the altitude is stabilized at given values according to the velocity control block which cancels the vertical velocity component. The MFC can theoretically ensure a

stable flight for all initial points inside the boundary, with more or less oscillations, according to the initial conditions. Otherwise, the hybrid MAV performs an unstable flight, as shown by the two particular initial points outside the stability boundary corresponding to the third class of trajectories in this simulation.

FFT analysis. This analysis focuses on the MFC tuning problem. Usually, the flight controller parameters are adjusted according to a setpoint trajectory and with trim points in a respective flight condition. However, hybrid MAV covers different flight domains which would imply a variety of setpoint trajectories with different frequencies. Thus, we analyze the entire bandwidth of frequencies corresponding to the yaw and the pitch angle during the hovering flight. And, we compare its setpoint trajectory spectrum with its measured spectrum in order to evaluate the designed MFC parameters. We excite the attitude dynamics adequately in order to capture the important frequencies by varying the velocity setpoint along the $y_b - axis$ and the velocity setpoint along the $z_b - axis$. According to Figure 6, the block MFC_{v_y} generates, in hovering flight, the setpoint to the yaw angle ψ_{sp} and the block MFC_{v_z} the setpoint to the pitch angle θ_{sp} . Figure 8 shows the comparison between the desired yaw angle and its respective measured signal in both time and frequency domains. High precision tracking for frequencies up to 4 rad/s is observed which means that the controller is able to track, with high precision, yaw setpoint variations up to 285 degrees per second ($^\circ/s$). Furthermore,

the tuned yaw control parameters present a reasonable trade-off to track low and high frequencies that compose its bandwidth. The results of the pitch angle presented in Figure 9, shows an effective tracking over its entire frequency spectrum. In addition, for high frequencies, the controller filters the references providing a smooth pitch output, but with an offset between the signals creating a small error.

Hovering flight missions. The main objective of the first flight simulation in hovering mode, see Figure 10, is the study of wind influence in the position tracking, for the following desired positions

$$\begin{aligned} x_{sp} &= 0, \forall t \\ y_{sp} &= 0, \forall t \\ z_{sp} &= \begin{cases} 10, & t \in [0; 155]s \\ 0, & t > 155s \end{cases} \end{aligned}$$

During this flight mode (**#Flight 1**), the hybrid MAV is more susceptible to aerodynamics disturbances. We can explain this by the fact that, in the vertical position, the wind gust along the $x_i - axis$, respectively along the $z_b - axis$, is in contact with the total reference wing area generating a considerable drag force. Also, the hybrid MAV is not able to compensate this force in the vertical position. That is why, the transition is performed and the drag force created by the wind can be compensated by the thrust in order to ensure the position tracking. The thrust used to reject this

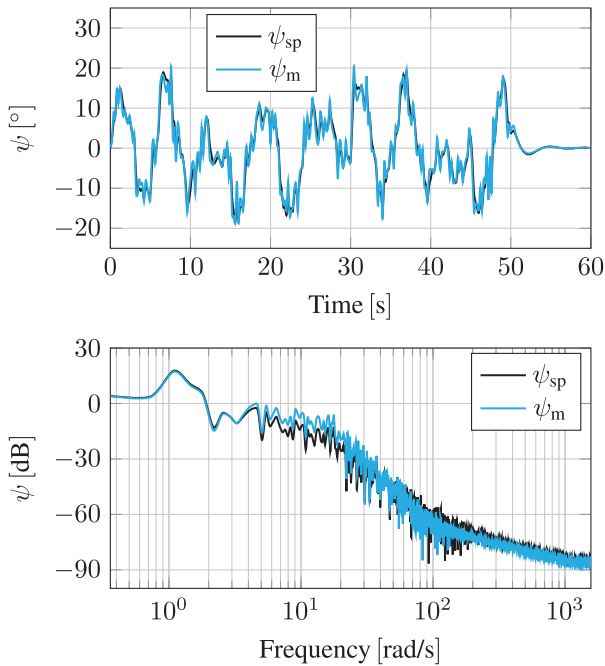


Figure 8. Frequency analysis of the yaw angle in hover flight.

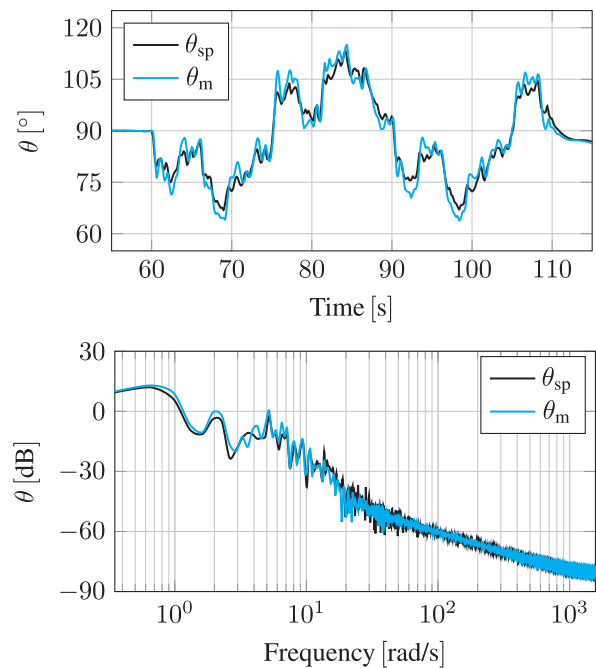


Figure 9. Frequency analysis of the pitch angle in hover flight.

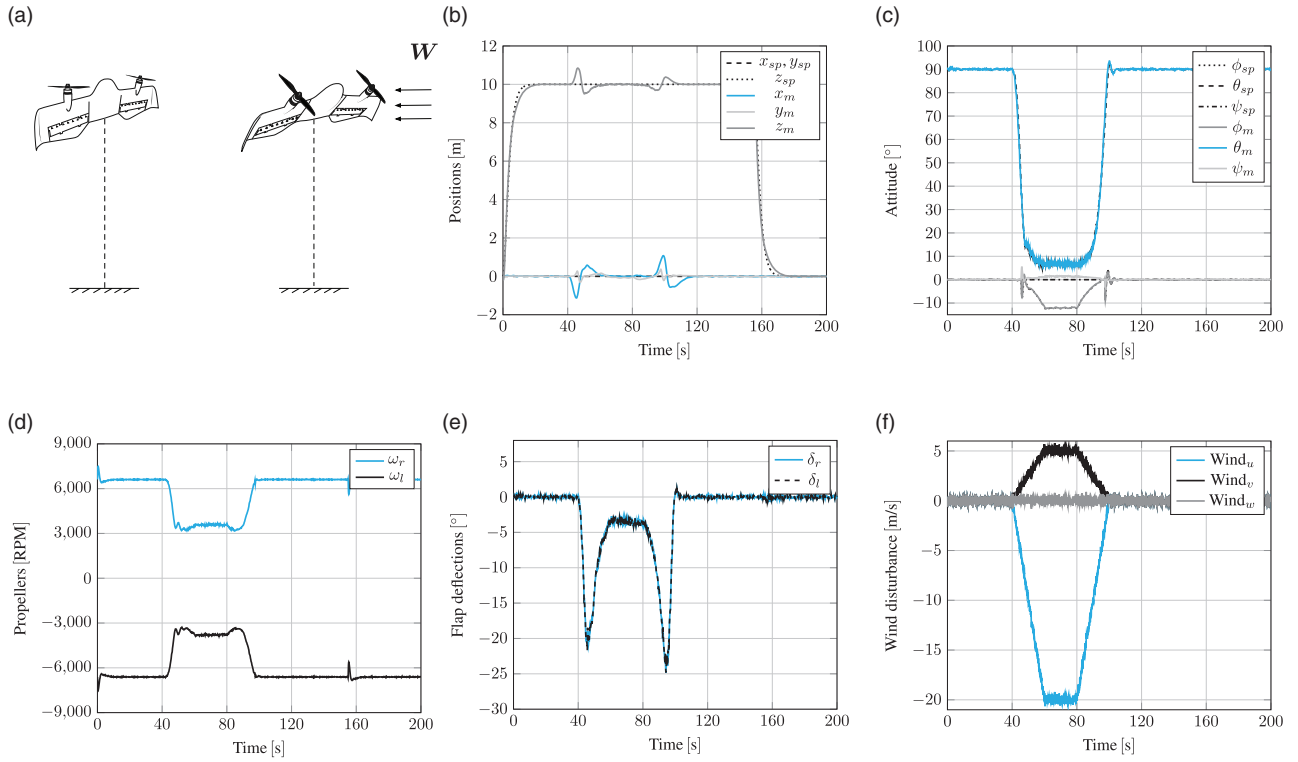


Figure 10. (#Flight 1) – Vertical take-off and transition flight to assure position tracking during high crosswind. On the top, from left to right: simulation illustration, positions in the inertial coordinate frame and attitude. On the bottom: propeller speeds ($\omega_l < 0$ and $\omega_r > 0$) due to counter-rotation sense, flap deflections (δ_l and δ_r) convention negative for pitch-up, and wind disturbance.

perturbation can be seen in Figure 10(d). And the wind from east with a magnitude of 5 m/s, see Figure 10(f), also produces a side force in the y_b – axis. This force is compensated by orienting the lift force with a symmetrical rotation around the x_b – axis, corresponding to the negative roll angle described in Figure 10(c).

In the second flight simulation, we impose a circular setpoint path (**#Flight 2**) in order to validate the interaction between all control blocks in the proposed control architecture. The following equations define the desired trajectories (x_{sp} , y_{sp} , z_{sp})

$$x_{sp} = \begin{cases} 0, & t < 30s \\ x_c + r \cos\left(\frac{2\pi}{40}t\right), & t \in [30; 130]s \\ 1, & t > 130s \end{cases}$$

$$y_{sp} = \begin{cases} 0, & t < 30s \\ y_c + r \sin\left(\frac{2\pi}{40}t\right), & t \in [30; 130]s \\ 5, & t > 130s \end{cases}$$

$$z_{sp} = \begin{cases} 10, & t \in [0; 155]s \\ 0, & t > 155s \end{cases}$$

where x_c and y_c correspond to the center of the circle and r is its radius. This maneuver requires the hybrid MAV to fly along a circular trajectory while constantly pointing its nose towards the exact center of the circle. Accurate position, velocity and especially yaw angle control are needed to accurately follow the desired flight plan with the desired attitude. Figure 11 shows the simulation results.

Remark (Conclusion hovering flight phase). *In hovering flight simulations, the MFC architecture has shown the capability to recover the tailsitter MAV from a large range of initial conditions for both pitch angle and forward speed, thereby validating the interactions between attitude and velocity control blocks. The disturbances that deteriorate the controlled output signal, are estimated and annulled by the controller providing robust disturbance rejections in order to track a desired position. For strong wind disturbances, the tailsitter MAV performs a smooth transitioning flight ensuring position tracking. Indeed, the FFT analysis validated the designed MFC parameters for a wide attitude frequency spectrum.*

Transitioning flight

The transitioning flight simulations were examined in two parts. In the first one, similar to the hovering flight,

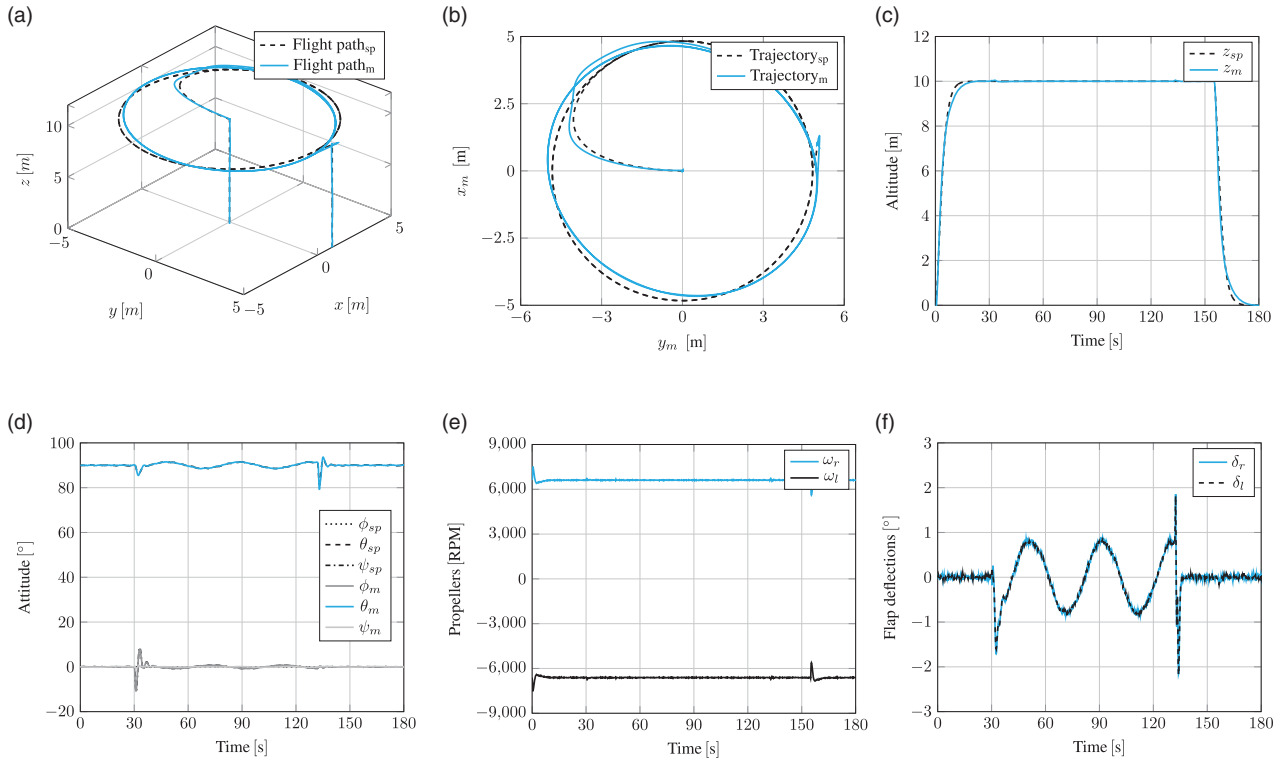


Figure 11. (#Flight 2) – Circular position tracking in hover flight mode. On the top, from left to right: the 3D flight path, North and East positions and altitude. On the bottom: attitude, propeller speeds and flap deflections.

we analyze the velocity and attitude controller’s ability to recover the MAV from different unstable initial conditions to the desired stable setpoint. The second case study presents variations of nominal hybrid UAV parameters in flight at different pitch angles in order to evaluate the MFC adaptive properties during the forward-to-hover transition.

Initial condition analysis. In this case study, we define a forward speed setpoint of 5 m/s and the MFC architecture computes a pitch angle setpoint of around 45° . The desired forward speed setpoint was chosen to prove, by flight simulations without predefined gains or gain scheduling methods, that the proposed control architecture is able to stabilize the tailsitter MAV in a critical flight domain corresponding to stall region where the aircraft flies at low forward speed and high angle of attack. The initial conditions during the transitioning flight analysis (θ_{ic} and $V_{x_{ic}}$), are defined from a normal distribution law given by the following equations (40) and (41).

$$\theta_{ic} \sim \mathcal{N}\left(\frac{\pi}{4}, 30^2\right) \quad (40)$$

$$V_{x_{ic}} \sim \mathcal{N}(5, 2^2) \quad (41)$$

The empirically defined stability boundary, for initial conditions in transitioning flight, is presented in Figure 12. The three classes of trajectories discussed in the hovering flight analysis, can be also observed in this case study. These trajectories have a slower convergence time with respect to the trajectories in hovering flight domain. Flap saturation affects the response time, but the main reason for the slower convergence time, in the transitioning flight domain, is the difficulty to decelerate the tailsitter MAV which depends on only of the drag force. For these initial conditions, the tailsitter MAV was not controlled in position allowing a supplementary degree of freedom to recover the stable attitude setpoint. During the transitional regime, that corresponds to the trajectory from the initial conditions to the setpoints, the tailsitter MAV loses altitude because the initial condition for both pitch angle and forward speed precludes the production of lift force and the thrust orientation is not adequate to compensate the weight of the tailsitter MAV. Thus, fast attitude stabilization is crucial to steer the thrust and bring the tailsitter MAV back to safe flight conditions.

Parameter-varying analysis. In this analysis, we evaluate the altitude tracking and the attitude stabilization, more precisely, the pitch angle stabilization by imposing variations of mass and inertia at different points in

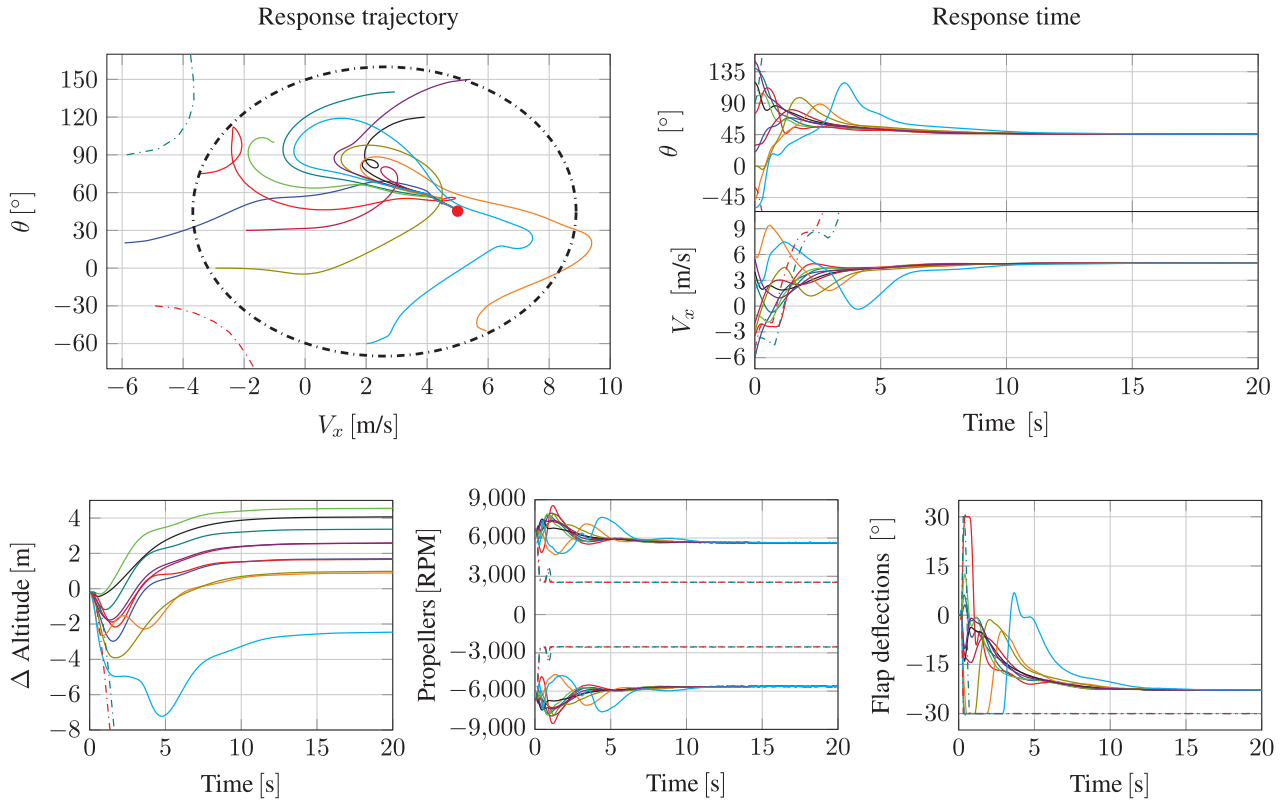


Figure 12. Initial pitch angle and forward speed condition analysis during the transitioning flight phase without wind disturbances. Forward speed setpoint equals to 5 m/s, the MFC architecture computes the pitch angle setpoint approximately equals to 45°.

the pitch angle trajectory during the forward-to-hover transition. For each point in which the variations occur, we compute the standard deviation between the altitude setpoint and its measurement. Figure 13 shows a typical pitch angle response time for the forward-to-hover transition with the nominal DarkO parameters. The altitude behavior and its standard deviation values computed for different mass and inertia values are also presented. We impose a maximum mass and inertia variation of around 45% of the nominal DarkO parameters. This study concludes that, the DarkO is less robust to variations of mass and inertia when it occurs between 20° and 40° of pitch angle. However, the impact of mass and inertia variations on altitude tracking remains very low with a maximum standard deviation of 0.3 m. The proposed control approach is able to stabilize the forward-to-hover flight transition with little prior knowledge of the tailsitter MAV. By using the estimator (\hat{F}) in the closed loop, any impact on the tailsitter MAV dynamics caused by parametric variations are estimated and immediately compensated in order to reach the altitude setpoint trajectory previously imposed.

Remark ((Conclusion transitioning flight phase)).
Fast changing of aerodynamic forces and moments

present in this critical flight domain have been countered by the proposed control architecture. The tailsitter MAV is stabilized in a critical attitude setpoint from different initial conditions. Further, the parameter-varying analysis highlighted the promising adaptive properties of the proposed control technique.

Forward flight

The last phase of flight studied corresponds to the forward flight. Given that, the MFC parameters are tuned for the entire flight envelope without any type of gain scheduled and the hybrid MAV dynamics change between the flight phases, we compute the FFT to the roll and the pitch angles in order to compare the frequency control performance with the previous results in hovering flight. In addition to this analysis, we present a full flight simulation exploring all hybrid MAV flight phases, with a major focus on forward flight, in which the hybrid MAV performs a position tracking.

FFT analysis. In forward flight, the roll setpoint ϕ_{sp} is generated from the velocity control block along the $y_b - axis$. This velocity is excited in order to create different setpoint values and frequencies to the roll angle. The roll tracking results in both time and frequency

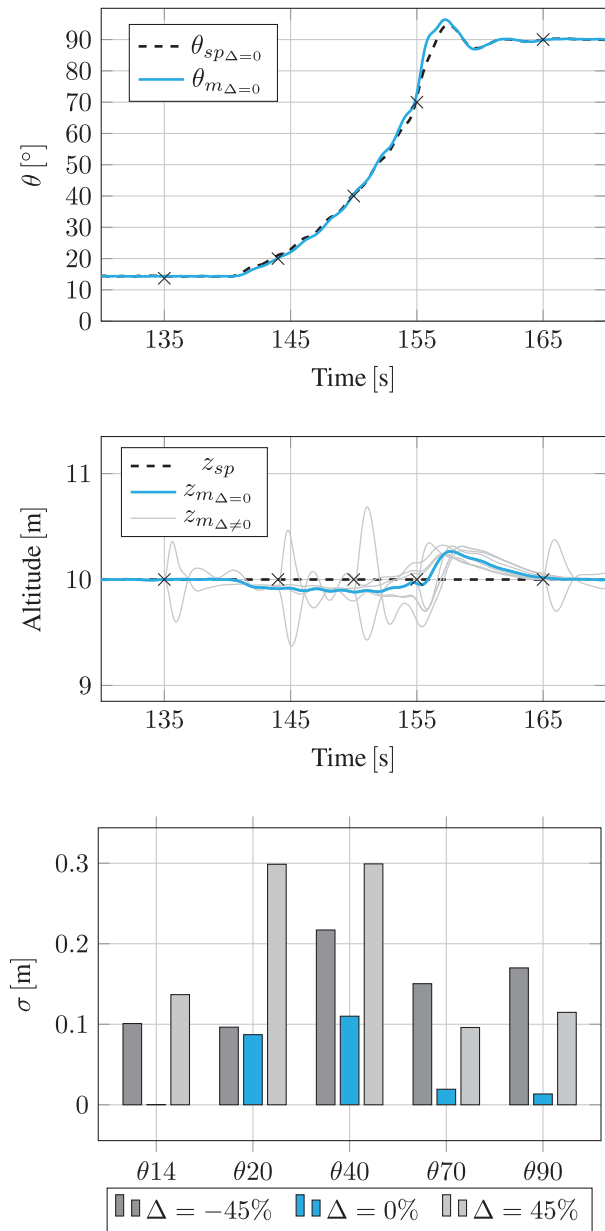


Figure 13. Parameter variation analysis for different points in the forward-to-hover transition. The black crosses in altitude and pitch angle trajectories indicate the points in which the parameters were changed. Δ represents the variation of nominal mass and inertia in percentage. The standard deviation between the altitude setpoint and its measurements is denoted by σ .

domains are presented in Figure 14. The proposed controller provides a high quality tracking up to 3 rad/s which is equal to 170 ($^{\circ}$ /s). An offset between the roll setpoint trajectory and the roll measurement is observed at high frequencies. However, in this frequency range, the signals are almost negligible, given their respective attenuation in decibels.

Pitch angle results are presented in Figure 15. We quantify a maximum pitch tracking error of 1.58 ($^{\circ}$) for

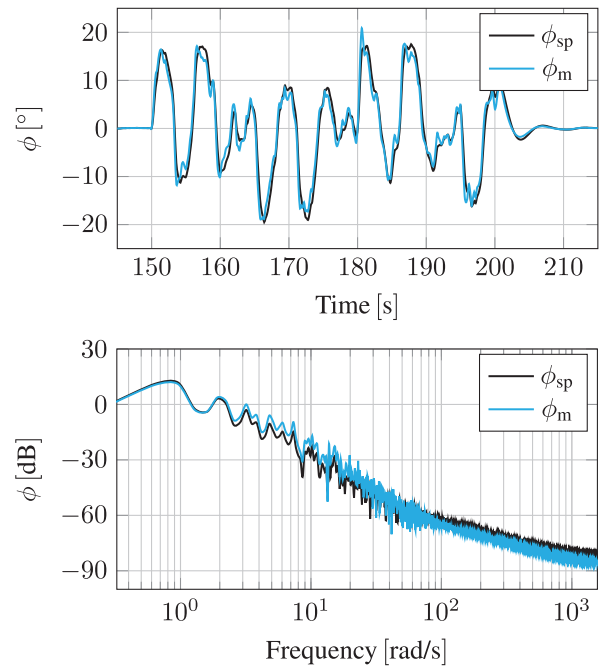


Figure 14. Frequency analysis of the roll angle in forward flight.

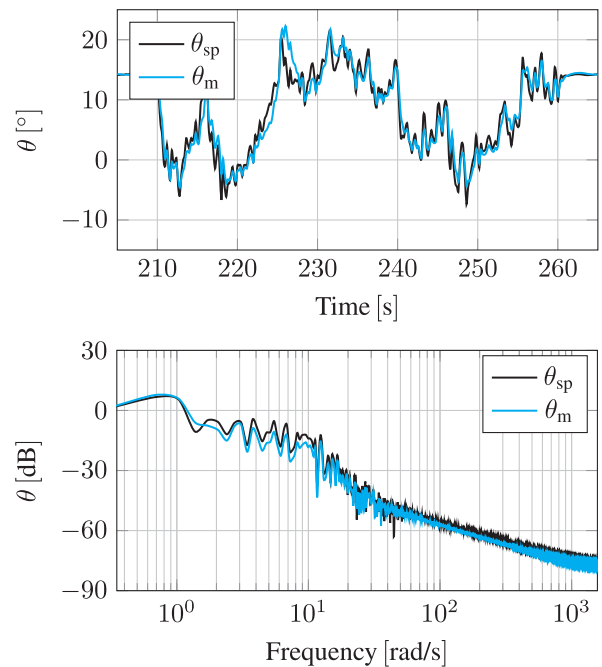


Figure 15. Frequency analysis of the pitch angle in forward flight.

pitch angle setpoints varying between 1 and 10 rad/s, which represent 57 and 573 ($^{\circ}$ /s). Overall, the FFT analysis revealed, in hovering and forward flight, the promising performance of MFC for altitude tracking. Further, this analysis shows that the MFC parameters were well-adjusted considering the trade-off between

the quality of attitude stabilization with delays and noises in the control loop.

Forward flight mission. A complete flight mission (#Flight 3) is presented in Figure 16 in which we evaluate all hybrid MAV flight capabilities through a vertical take-off from 0 to 10 m of altitude followed by the hover-to-forward transition with a position tracking in the xy – plane and an altitude change in forward flight. Then, the forward-to-hover transition is performed with a position tracking in hovering flight. The flight simulation ends with a vertical landing. The complete 3D flight path is presented in Figure 16(a). The controller assures the position tracking during the entire mission. As we can see in Figure 16(b), the altitude presents small oscillations at 45 and 165 s of simulation which is acceptable for this MAV class. These oscillations are due to the fast variations of aerodynamics forces and moments that occur during the transition flight phases where the pitch angle changes resulting in significant variations in the angle of attack, see Figure 16(d). In the same figure, between 45 and 90 s of simulation, we can see the roll dynamics to reach the desired east position in forward flight. Similarly, between 180 and 215 s of simulation, the yaw behavior to reach the east position in hovering flight.

Figure 16(c) presents the velocities in the body coordinate system and the actuator dynamics, respectively, the propeller rotations and the flap deflections are shown in Figure 16(e) and (f).

Remark ((Conclusion forward flight)). *We confirm in this subsection that, the proposed MFC architecture also ensures the position tracking, velocity control and attitude stabilization in forward flight. With the FFT analysis, we show the attitude control performance for a large range of frequencies. Furthermore, we validate the interactions between each control block independently of the hybrid MAV attitude orientation that covers its entire flight envelope.*

Flight tests

In this section, we present real-world flight tests to compare the MFC attitude stabilization performance to that of the INDI controller in indoor flight conditions. For more details about the INDI, we refer the interested reader to literature.^{25,46} Both controllers were tested using the Paparazzi Open Source Autopilot System.⁴⁷ The methodology used during the flight tests to define the DarkO's attitude setpoints are based on four steps. First, with an RC transmitter, the security pilot imposes slow yaw setpoints generating lateral motions in the system. Then, slow pitch

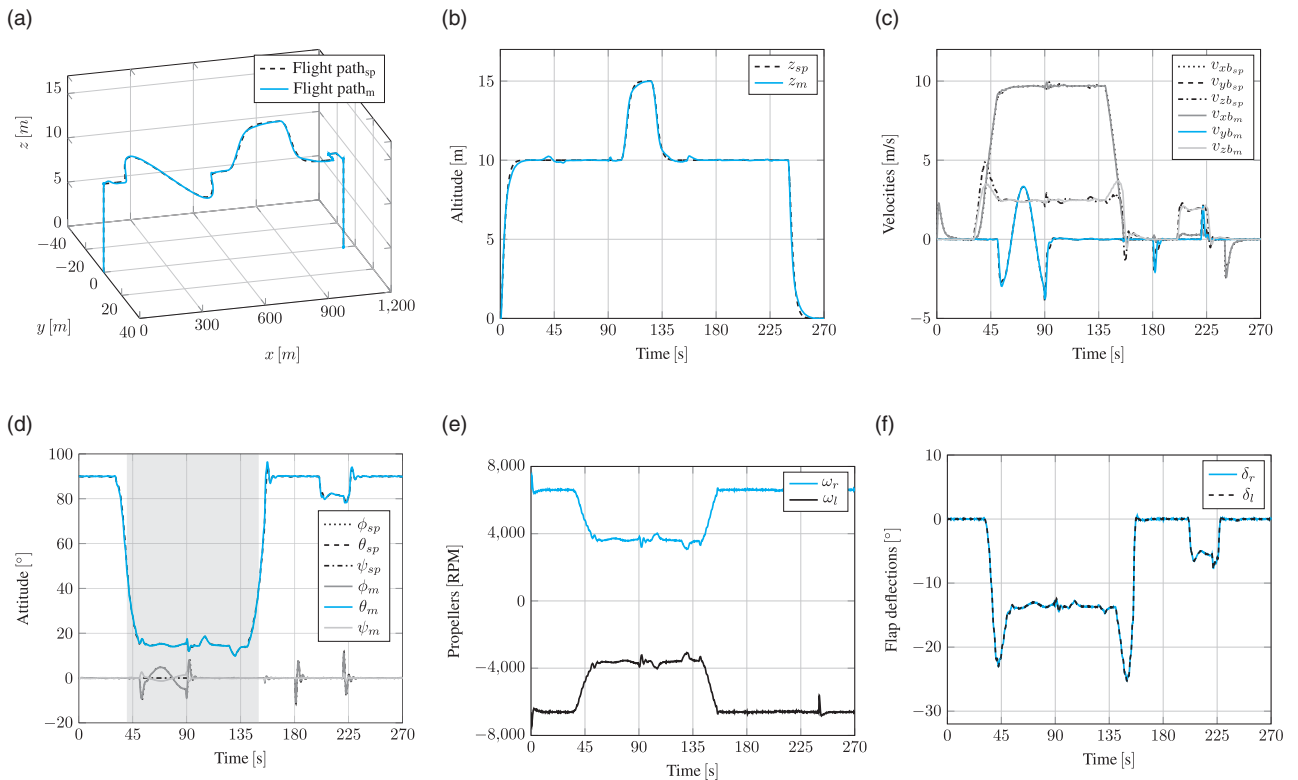


Figure 16. (#Flight 3) – Entire flight envelope simulation in relatively calm flight conditions. On the top, from left to right: the 3D flight path, altitude and velocities in the body coordinate system. On the bottom: attitude, propeller speeds and flap deflections.

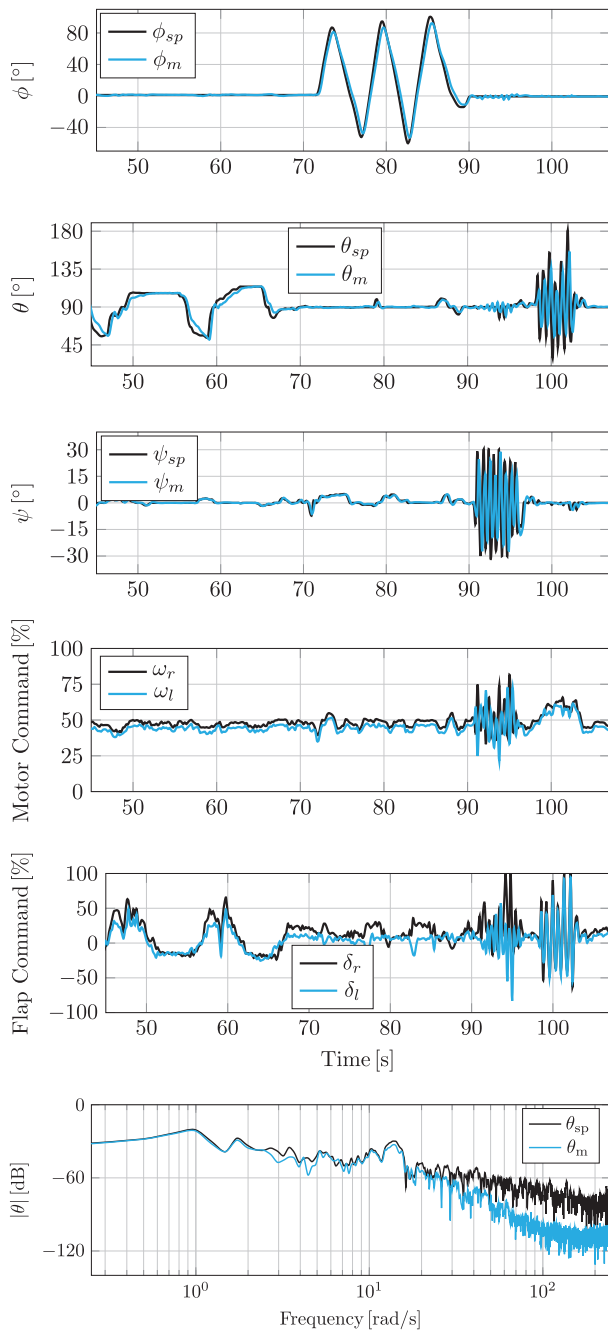


Figure 17. MFC attitude stabilization – nominal DarkO.

setpoints generate forward and backward movements according to positive and negative pitch setpoints, respectively. Then, slow roll setpoints which define the heading of the system. Finally, the pilot imposes fast yaw and pitch setpoints to evaluate the response of the system for high frequency attitude setpoints. Two flight test cases were conducted in indoor environment comparing MFC to INDI controllers. In the first case, both controllers stabilize the DarkO in its nominal configuration, i.e. wings and control surfaces are

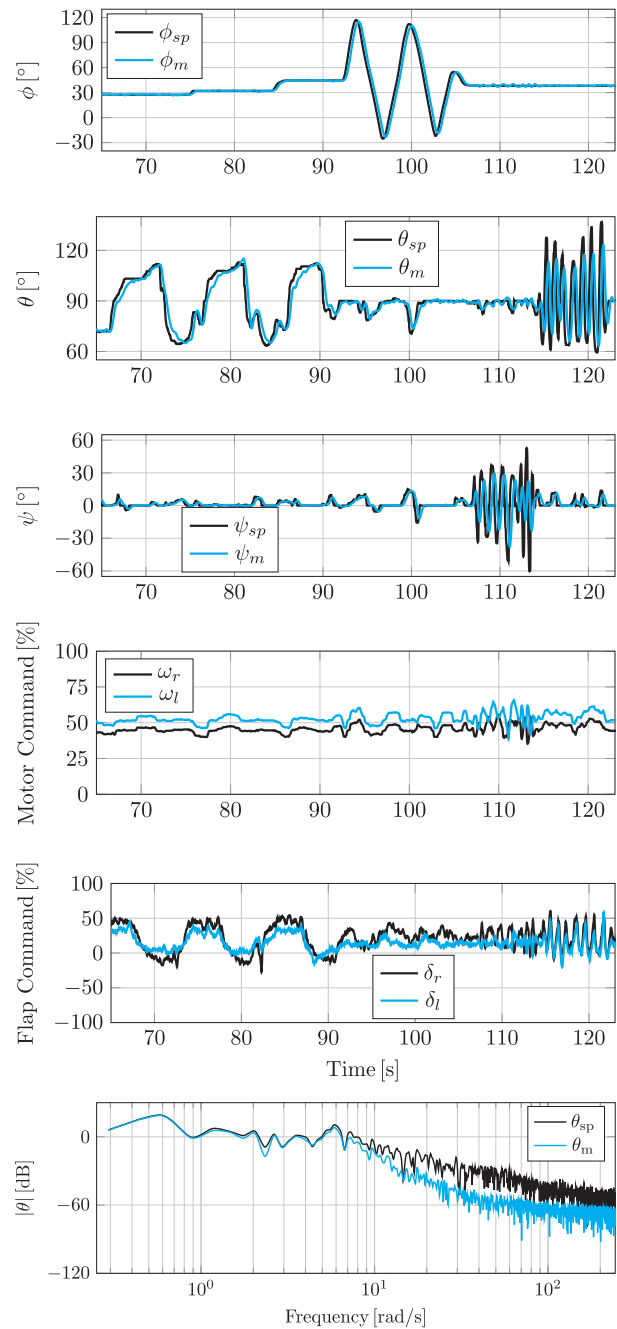


Figure 18. INDI attitude stabilization – nominal DarkO.

attached correctly. In the second case, the wingtips and half of the control surface are removed, and additionally the propulsion system has been modified by using a different set of propellers. The nominal components of the DarkO were changed to evaluate the adaptive properties of both controllers. The attitude stabilization results performed by MFC and INDI with the nominal DarkO, are presented in the Figures 17 and 18, respectively. Figures 19 and 20 show the MFC and INDI attitude stabilization performances

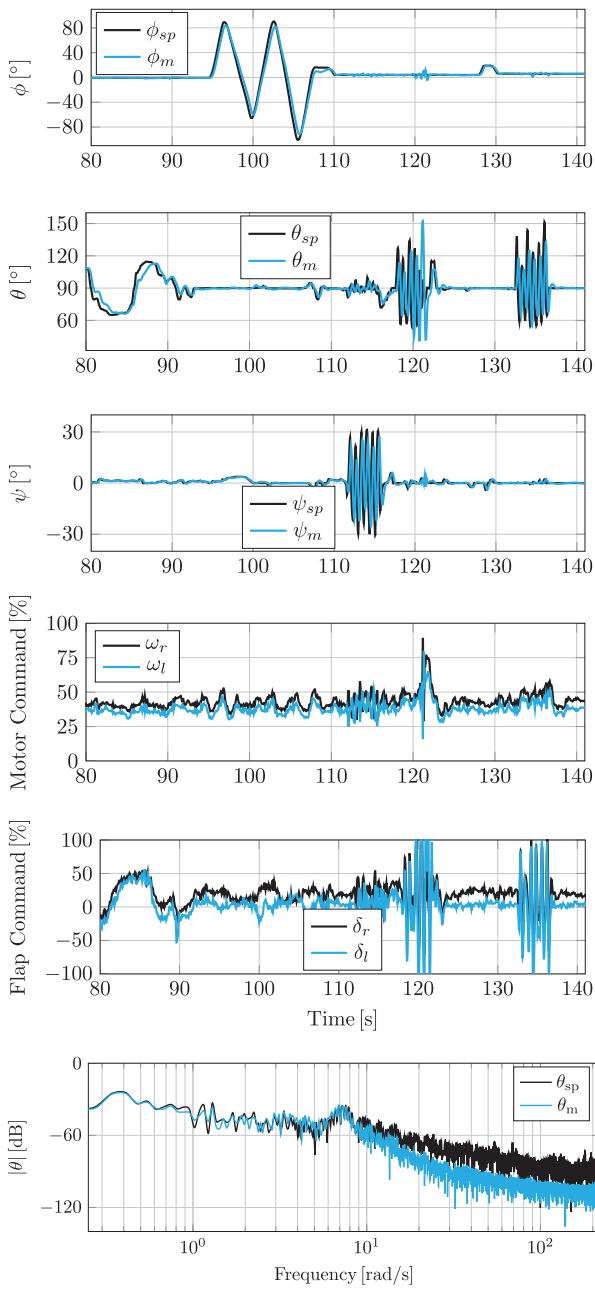


Figure 19. MFC attitude stabilization – modified DarkO.

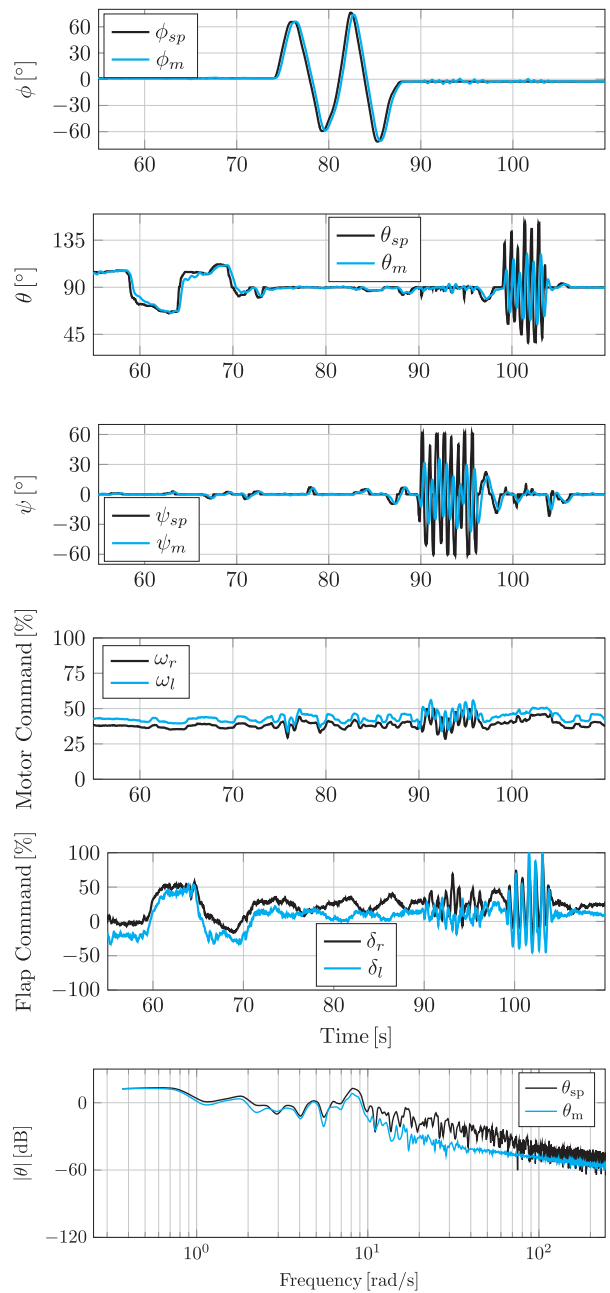


Figure 20. INDI attitude stabilization – modified DarkO.

for the modified DarkO configuration, see Figure 21. It is difficult to analyze graphically each controller in the time domain, because of their different setpoint trajectories. For this reason, we investigated their control performance in the frequency domain by calculating the FFT of the pitch angle, which is the dynamics most affected by a loss of control surface effectiveness. We observe a better tracking performance with a larger frequency spectrum for the MFC (20 rad/s) when compared to that of the INDI (7 rad/s) for the nominal

flight test. Both controllers stabilized the modified DarkO, showing their adaptive control properties. The present study concludes that MFC and INDI provide satisfactory performance for hovering and transitioning flight domains in indoor flight conditions. These results suggested a more in-depth analysis to evaluate the performance of both controllers for the entire flight envelope of the DarkO, in particular during forward flights in outdoor environment.

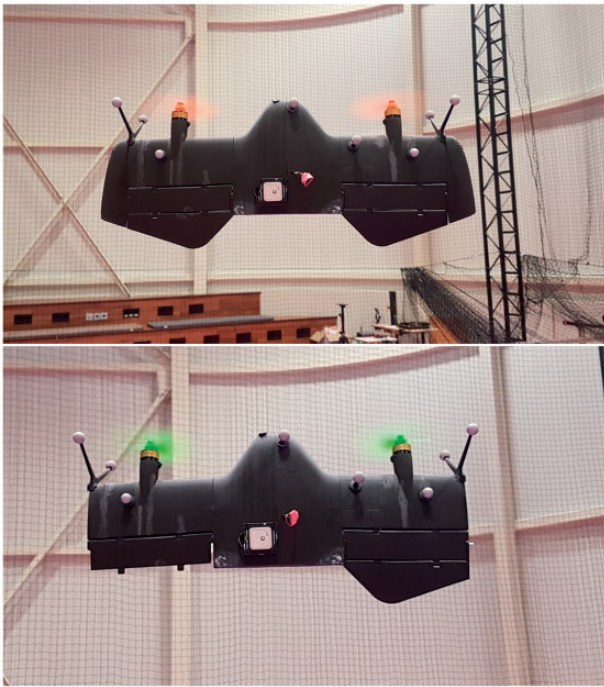


Figure 21. Tailsitter MAV configurations used during flight tests. At the top, DarkO with nominal wings, control surfaces and two-blade propellers. At the bottom, DarkO has been modified by removing its wingtips, half of its control surface and three-blade propellers were used.

Table 2. DarkO MAV parameters.

Parameters	Values	SI units
Mass (m)	0.492	(kg)
Mean chord (c)	0.13	(m)
Wingspan (b)	0.55	(m)
Wing area (S)	0.0743	(m ²)
J_{xx}	0.0070	(kg m ²)
J_{yy}	0.0028	(kg m ²)
J_{zz}	0.0061	(kg m ²)
J_p	5.1116e-06	(kg m ²)
k_f	5.13e-6	(kg m)
k_m	2.64e-7	(kg m ²)
C_{d0}	0.025	No units
C_{y0}	0.1	No units
C_{l_p}	0.2792	No units
C_{l_q}	0.0	No units
C_{l_r}	0.1145	No units
C_{m_p}	0.0	No units
C_{m_q}	1.2715	No units
C_{m_r}	0.0	No units
C_{n_p}	0.081	No units
C_{n_q}	0.0	No units
C_{n_r}	0.0039	No units
p_{p_x}	0.065	m
p_{p_y}	0.155	m

(continued)

Table 2. Continued

Parameters	Values	SI units
p_{p_z}	0.0	m
p_{a_x}	0.0	m
p_{a_y}	0.155	m
p_{a_z}	0.0	m
ξ_f	0.85	No units
ξ_m	0.55	No units

Discussion and conclusion

The main objective of this study is to show the easy implementation of the MFC algorithm to different hybrid MAV platforms. We have presented the development of a full control architecture based on MFC techniques, applied to MAV with transitioning flight capabilities. Numerical flight simulations were performed in order to validate the interactions between each control block for different flight domains covering the entire tailsitter MAV flight envelope. Attitude control loop performance was examined in frequency domain during the hovering and the forward flight. The FFT results demonstrated high tracking performance for most of the attitude bandwidth. As a critical point, during forward-to-hover transition, we have investigated the adaptive properties of the controller by varying the parameters of the tailsitter MAV during flight. MFC algorithms estimated and rejected the variations of 45% of the nominal parameters providing a stable transitioning flight. The velocity control performance has also been investigated simultaneously with the attitude control block in hovering and transitioning flights for different unstable initial conditions. Both control blocks are able to stabilize the tailsitter MAV from a variety of initial pitch angles and initial forward-speeds recovering the MAV to stable equilibrium points. The proposed control approach provides high performance position tracking, velocity control and attitude stabilization without gain scheduling method and by using only little prior knowledge of the tailsitter MAV. Furthermore, the MFC attitude stabilization performance, its real time estimation and its adaptive properties have been validated in real-world flight conditions. In addition, comparative indoor flight tests between MFC and INDI have been conducted. However, it has been realized that in order to come to a conclusion between the performance of the two controllers, additional flight experiments have to be performed. In particular, during the forward flight phase at outdoor environment so that the disturbance rejection properties of each control approach can be compared and evaluated properly.

Future work will include additional flight tests with different MAV configurations with a wide variety of design parameters. We would also like to investigate if a proof of stability can be established, analyzing the adaptation properties of the MFC estimator in the closed-loop system.

DarkO MAV parameters

The DarkO hybrid MAV's parameters used in this paper for all flight simulations, are presented in Table 2.


Declaration of conflicting interests

The author(s) declared no potential conflicts of interest with respect to the research, authorship, and/or publication of this article.

Funding

The author(s) received no financial support for the research, authorship, and/or publication of this article.

ORCID iD

Jacson MO Barth  <https://orcid.org/0000-0001-7132-2929>




References

- Santos MA, Cardoso DN, Rego BS, et al. A discrete robust adaptive control of a tilt-rotor UAV for an enlarged flight envelope. In: *IEEE 56th annual conference on decision and control (CDC)*, Melbourne, Australia, 12–15 December 2017. pp.5208–5214.
- Hartmann P, Meyer C and Moormann D. Unified velocity control and flight state transition of unmanned tilt-wing aircraft. *J Guid Control Dyn* 2017; 40: 1348–1359.
- Gu H, Lyu X, Li Z, et al. Development and experimental verification of a hybrid vertical take-off and landing (VTOL) unmanned aerial vehicle (UAV). In: *International conference on unmanned aircraft systems (ICUAS)*, Miami, FL, USA, 13–16 June 2017, pp. 160–169.
- Flores A, Montes de Oca A and Flores G. A simple controller for the transition maneuver of a tail-sitter drone. In: *IEEE conference on decision and control (CDC)*, Miami Beach, FL, USA, 17–19 December 2018, pp. 4277–4281.
- Chinwicharnam K, Gomez Ariza D, Moschetta J-M, et al. Aerodynamic characteristics of a low aspect ratio wing and propeller interaction for a tilt-body MAV. *Int J Micro Air Veh* 2013; 5: 245–260.
- Bronz M, Smeur EJJ, de Marina HG, et al. Development of a fixed-wing mini UAV with transitioning flight capability. In: *35th AIAA applied aerodynamics conference, AIAA AVIATION forum*, Denver, CO, USA, 6 July 2017.
- Argyle ME, Beard RW and Morris S. The vertical bat tailsitter: dynamic model and control architecture. In: *American control conference (ACC)*, Washington, DC, USA, 7 June 2013, pp.806–811.
- Forshaw JL, Lappas VJ and Briggs P. Transitional control architecture and methodology for a twin rotor tail-sitter. *J Guid Control Dyn* 2014; 37: 1289–1298.
- Matsumoto T, Kita K, Suzuki R, et al. A hovering control strategy for a tail-sitter Vtol UAV that increases stability against large disturbance. In: *IEEE international conference on robotics and automation (ICRA)*, Anchorage, AK, USA, May 2010, pp. 54–59.
- Bilodeau P-R and Wong F. Modeling and control of a hovering mini tail-sitter. *Int J Micro Air Veh* 2010; 2: 211–220.
- Hochstenbach M, Notteboom C, Theys B, et al. Design and control of an unmanned aerial vehicle for autonomous parcel delivery with transition from vertical take-off to forward flight – VertiKUL, a quadcopter tailsitter. *Int J Micro Air Veh* 2015; 7: 395–405.
- Casau P, Cabecinhas D and Silvestre C. Autonomous transition flight for a vertical take-off and landing aircraft. In: *IEEE conference on decision and control and European control conference (CDC-ECC)*, Orlando, FL, USA, December, 2011, pp. 3974–3979.
- Park S, Bae J, Kim Y, et al. Fault tolerant flight control system for the tilt-rotor UAV. *J Franklin Instit* 2013; 350: 2535–2559.
- Lustosa LR, Defay F and Moschetta J-M. Longitudinal study of a tilt-body vehicle: modeling, control and stability analysis. In: *International conference on unmanned aircraft systems (ICUAS)*, Denver, Colorado, USA, 9–12 June 2015, pp. 816–824.
- Kita K, Konno A and Uchiyama M. Transition between level flight and hovering of a tail-sitter vertical takeoff and landing aerial robot. *Adv Rob* 2012; 24: 763–781.
- Silva NBF, Fontes JVC, Inoue RS, et al. Dynamic inversion and gain-scheduling control for an autonomous aerial vehicle with multiple flight stages. *J Control Autom Elec Syst* 2018; 29: 328–339.
- Saeed AS, Younes AB, Cai C, et al. A survey of hybrid unmanned aerial vehicles. *Progr Aerosp Sci* 2018; 98: 91–105.
- Ritz R and D'Andrea R. A global controller for flying wing tailsitter vehicles. In: *IEEE international conference on robotics and automation (ICRA)*, Singapore, 29 May–3 June 2017 pp. 2731–2738.
- Knoebel NB and McLain TW. Adaptive quaternion control of a miniature tailsitter UAV. In: *American control conference*, Seattle, WA, USA, June 2008 (ACC), pp.2340–2345.
- Jung Y and Shim DH. Development and application of controller for transition flight of tail-sitter UAV. *J Intell Rob Syst* 2011; 65: 137–152.
- Wang W, Zhu J and Kuang M. Design, modelling and hovering control of a tail-sitter with single thrust-vectored propeller. In: *International conference on intelligent robots and systems (IROS)*, Vancouver, BC, Canada, 24–28 September 2017, pp. 5971–5976.
- Hajiloo A and Rodrigues L. Modeling and backstepping control of under-actuated spherical UAV. In: *IEEE conference on control technology and applications (CCTA)*,

- Kohala Coast, Hawai'i, USA, 27–30 August 2017, pp. 2069–2074.
23. Fang X, Lin Q, Wang Y, et al. Control strategy design for the transitional mode of tiltrotor UAV. In: *10th IEEE international conference on industrial informatics (INDIN)*, Beijing, China, July 2012, pp. 248–253.
 24. Li Z, Zhou W, Liu H, et al. Nonlinear robust flight mode transition control for tail-sitter aircraft. *IEEE Access* 2018; 6: 65909–65921.
 25. Smeur EJJ, Bronz M and de Croon GCHE. Incremental control and guidance of hybrid aircraft applied to a tail-sitter unmanned air vehicle. *J Guid Control Dyn* 2019; 43: 1–14.
 26. Pucci D, Hamel T, Morin P, et al. Nonlinear feedback control of axisymmetric aerial vehicles. *Automatica* 2015; 53: 72–78.
 27. Pucci D, Hamel T, Morin P, et al. Nonlinear control of aerial vehicles subjected to aerodynamic forces. In: *IEEE conference on decision and control (CDC)*, Florence, Italy, 10–13 December 2013, pp.4839–4846.
 28. Wang W, Zhu J, Kuang M, et al. Adaptive attitude control for a tail-sitter UAV with single thrust-vectoring propeller. In: *IEEE international conference on robotics and automation (ICRA)*, Brisbane, Australia, 21–25 May 2018, pp. 6581–6586.
 29. Fliess M and Join C. Model-free control. *Int J Control* 2013; 86: 2228–2252.
 30. Join C, Bernier J, Mottelet S, et al. A simple and efficient feedback control strategy for wastewater denitrification. In: *20th world IFAC congress*, Toulouse, France, 9–14 July 2017 (Vol. 50, No. 1) pp. 7657–7662.
 31. Rodriguez-Fortun JM, Rotella F, Alfonso J, et al. Model-free control of a 3-DOF piezoelectric nanopositioning platform. In: *52nd IEEE conference on decision and control*, Florence, Italy, 10–13 December 2013, pp. 342–347.
 32. Bara O, Fliess M, Join C, et al. Toward a model-free feedback control synthesis for treating acute inflammation. *J Theor Biol* 2018; 448: 26–37.
 33. Join C, Robert G and Fliess M. Model-free based water level control for hydroelectric power plants. In: *IFAC conference on control methodologies and technologies for energy efficiency*, Vilamoura, Portugal, 29–31 March 2010 (Vol. 43, No. 1) pp. 134–139.
 34. Abouaïssa H, Fliess M and Join C. Fast parametric estimation for macroscopic traffic flow model. In: *17th IFAC world congress*, Seoul, South Korea, 6–11 July 2008, pp. 13040–13045.
 35. Chand AN, Kawanishi M and Narikiyo T. Non-linear model-free control of flapping wing flying robot using iPID. In: *IEEE international conference on robotics and automation (ICRA)*, Stockholm, Sweden, 16–20 May 2016, pp. 2930–2937.
 36. Al Younes Y, Drak A, Noura H, et al. Robust model-free control applied to a quadrotor UAV. *J Intell Rob Syst* 2016; 84: 37–52.
 37. Barth JMO, Condomines J-P, Bronz M, et al. Fixed-wing UAV with transitioning flight capabilities: model-based or model-free control approach? A preliminary study. In: *International conference on unmanned aircraft systems (ICUAS)*, Dallas, TX, USA, USA, 12–15 June 2018, pp. 1157–1164.
 38. Barth JMO, Condomines J-P, Moschetta J-M, et al. Model-free control approach for fixed-wing UAVs with uncertain parameters analysis. In: *23rd international conference on methods and models in automation and robotics (MMAR)*, Miedzyzdroje, Poland, 27–30 August 2018, pp. 527–532.
 39. Barth JMO, Condomines J-P, Moschetta J-M, et al. Full model-free control architecture for hybrid UAVs. In: *American control conference (ACC)*, Philadelphia, USA, 10–12 July 2019. Unpublished.
 40. Drela M. XFOIL: an analysis and design system for low reynolds number airfoils. In: *Conference on low Reynolds number airfoil aerodynamics*, University of Notre Dame, 5–7 June 1989.
 41. Lustosa LR, Defay F and Moschetta J-M. Global singularity-free aerodynamic model for algorithmic flight control of tail sitters. *AIAA J Guid Control Dyn* 2019; 42: 303–316.
 42. Lustosa LR. *The Phi-theory approach to flight control design of hybrid vehicles*. Ph.D. dissertation, Institut Supérieur de l'Aéronautique et de l'Espace, École Doctorale Aéronautique-Astronautique, Toulouse, France, ch. 2., 2017.
 43. Lafont F, Balmat J-F, Pessel N, et al. A model-free control strategy for an experimental greenhouse with an application to fault accommodation. *Comput Electron Agric* 2015; 110: 139–149.
 44. Martin P and Salaun E. Design and implementation of a low-cost observer-based attitude and heading reference system. *Control Eng Pract* 2010; 18: 712–722.
 45. Chahl JS, Jain LC, Mizutani A, et al. *Innovations in intelligent machines-1*. Berlin Heidelberg: Springer-Verlag, 2007, pp.181.
 46. Smeur EJJ, de Croon GCHE and Chu Q. Cascaded incremental nonlinear dynamic inversion control for MAV disturbance rejection. *Control Eng Pract* 2018; 73: 79–90.
 47. Hattenberger G, Bronz M and Gorraz M. Using the paparazzi UAV system for scientific research. In: *International micro air vehicle conference and competition (IMAV)*, Delft, Netherlands, 12–15 August 2014, pp. 247–252.

Article

A Multifractal Analysis and Machine Learning Based Intrusion Detection System with an Application in a UAS/RADAR System

Ruohao Zhang , Jean-Philippe Condomines  and Emmanuel Lochin 

ENAC, 7, Avenue Edouard Belin, CEDEX 4, 31055 Toulouse, France; jean-philippe.condomines@enac.fr (J.-P.C.); emmanuel.lochin@enac.fr (E.L.)

* Correspondence: ruohao.zhang@enac.fr

Abstract: The rapid development of Internet of Things (IoT) technology, together with mobile network technology, has created a never-before-seen world of interconnection, evoking research on how to make it vaster, faster, and safer. To support the ongoing fight against the malicious misuse of networks, in this paper we propose a novel algorithm called AMDES (unmanned aerial system multifractal analysis intrusion detection system) for spoofing attack detection. This novel algorithm is based on both wavelet leader multifractal analysis (WLM) and machine learning (ML) principles. In earlier research on unmanned aerial systems (UAS), intrusion detection systems (IDS) based on multifractal (MF) spectral analysis have been used to provide accurate MF spectrum estimations of network traffic. Such an estimation is then used to detect and characterize flooding anomalies that can be observed in an unmanned aerial vehicle (UAV) network. However, the previous contributions have lacked the consideration of other types of network intrusions commonly observed in UAS networks, such as the man in the middle attack (MITM). In this work, this promising methodology has been accommodated to detect a spoofing attack within a UAS. This methodology highlights a robust approach in terms of false positive performance in detecting intrusions in a UAS location reporting system.

Keywords: network intrusion detection system; wavelet leader multifractal analysis; spoofing; machine learning; long-short term memory



Citation: Ruohao, Z.; Condomines, J.-P.; Lochin, E. A Multifractal Analysis and Machine Learning Based Intrusion Detection System with an Application in a UAS/RADAR System. *Drones* **2022**, *6*, 21. <https://doi.org/10.3390/drones6010021>

Academic Editor: Vishal Sharma

Received: 10 December 2021

Accepted: 6 January 2022

Published: 12 January 2022

Publisher's Note: MDPI stays neutral with regard to jurisdictional claims in published maps and institutional affiliations.



Copyright: © 2022 by the authors. Licensee MDPI, Basel, Switzerland. This article is an open access article distributed under the terms and conditions of the Creative Commons Attribution (CC BY) license (<https://creativecommons.org/licenses/by/4.0/>).

1. Introduction

The "information age" has provided infinite possibilities of interconnecting various devices. Nowadays, networks have extended to every corner of our lives, thanks to their accessibility and versatility. Network technologies that used to be mission-specific and platform-restricted are now becoming more open and free of charge for general, day-to-day applications. However, the rapid growth of networks also creates bubbles, especially from the Internet of Everything (IoE) perspective. By adopting off-the-shelf components and off-the-git software, the development of IoE has greatly accelerated, with network security continuing to be a critical factor. Securing a network is considered just as challenging as constructing the network itself. Network attacks with similar characteristics can be targeted to various networks of markedly different physical entities. Among the different kinds of network attacks, the denial of service (DoS) flooding attacks and MITM/spoofing attacks are both commonly found in network systems, such as UAS and RADAR systems. These attacks have brought various challenges to the network developer and administrators. Recently, studies on UAS IDS dedicated to flooding anomalies [1] have been conducted. This type of attack severely disrupts the normal operation of a network by injecting an enormous amount of traffic into the network, paralyzing the entire system. While it has been demonstrated that an accurate model-based IDS dedicated to DoS attacks can perform adequately, such attacks are detectable by MF analysis [2,3] with better performance.

Spoofing is another more elaborate form of attack that targets specific data packets within specific system communications. This malicious intrusion aims to disrupt the normal operation of a system by altering crucial information transmitted between subsystems. In a complex system such as a UAS, once the network security is compromised, the condition in which to generate either type of attack is reached.

Additionally, in recent years, the number and diversity of applications involving UAS have grown rapidly. Swarms of UAVs are gaining popularity in commercial applications, such as drone light shows. Despite their magnificent and striking appearance, the related security issues are concerning. In critical situations where a cyber-attack is introduced into a wireless drone network, the physical UAS can be threatened, which can cause the whole swarm to crash. This concern has led to increased interest from the network community to design anomaly detection systems (ADS) or IDS for this specific situation. Furthermore, operations within an agglomeration, fully autonomous operations, and out-of-sight UAV operations are currently subject to strict regulations such as [4] for the European Union (EU) and [5] in the United States. In addition, there is the General Data Protection Regulation (GDPR) in the EU [6]. Further regulations exist for UAV categorization, certification, and integration into civil airspaces, such as the road maps in the EU [7] and the relevant regulations reviewed in [8]. We can conclude that there is a clear need for a reliable communication network for UAS with robust measures implemented to counter network intrusions and better protect the physical system of the UAS and the confidentiality of the data being transmitted through the UAANET. Thus, it is imperative to ensure the safe and healthy development of the future UAS, in compliance with the current and prospective regulations.

Motivated by the practical problems encountered with UAS network security, we aimed to further develop the potential of the IDS methodology that we proposed in [1], a methodology that takes advantage of the randomly varying nature of network statistics to detect network intrusions, by accomplishing it with a ML classification algorithm. In this article, we propose using the improved methodology to detect spoofing attacks for UAS location reporting systems. Guided by both WLM and ML principles, this new algorithm theoretically has a robust approach in terms of false positives in order to determine intrusions in a location reporting system.

As a preliminary result of this paper, the newly designed algorithm has been successfully applied to some relevant practical problems, such as a low intensity MITM attack in RADAR traces. Results are provided to illustrate the performance and potential of this algorithm.

The rest of the paper is structured as follows. The presentation in Section II of the methodology explains the general framework of the proposed IDS system. In addition, the theoretical background involved is clarified. Section III examines the application and simulation of the proposed methodology, detailing the specific simulation environment, data treatment and dataset generation from realistic RADAR traces obtained from a real Air Traffic Management (ATM) RADAR network system. In Section IV, we present the results and discuss the performance of this methodology based on the results. In Section V, we present a state-of-the-art summary of current research prior to the Conclusion, to allow the reader to better evaluate our proposal against existing works; and finally, in Section VI, we conclude and present proposals for the future development of the project.

2. The Proposed Intrusion Detection Methodology

2.1. IDS Framework

To take into account a modern type of intrusion which is particularly covert, such as an MITM attack within a location report and control packets, the research efforts have been shifted from network statistics to the payloads of network packets (e.g., the geo-position packets). The IDS methodology is based on a two-step process (as shown in Figure 1). In general, the IDS framework works starting by collecting information from the network by means of network sensors that are running capturing devices (either distributed or

centralized sensors depending on the topology of the network). The collected data are then properly treated within the pre-treatment step to better expose the features of interest. This stage of processing is unique to each problem. In the demonstration shown in Section 3, the particular pre-treatment step was achieved by a moving sample window and an algorithm used to calculate the moving Euclidean distance of each aircraft. Then the first stage of IDS (step 1) is dedicated to traffic characterization. Its objective is to obtain a specific signature of the signal we seek to analyze. The next stage (step 2) is the automatic classification of the signatures via a neural network model, the objective being to provide a binary trigger to either alert the administrator or start countering mechanisms, such as an IPS.

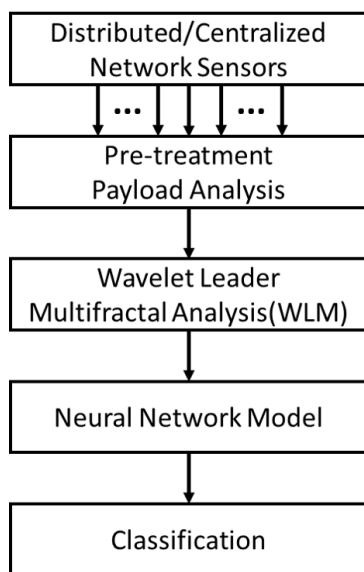


Figure 1. General framework of the proposed IDS system.

2.2. Wavelet Leader Multifractal Analysis

In our previous research, the WLM analysis for a UAV network was introduced [1]. Here we demonstrate the advantageous capability of the tool at capturing different density levels of singularities of the signal at different time scales and statistical moments of analysis. We show that this method can be efficient against flooding attacks within the UAS wireless network. Network signals of the same system, during different times of day and time scales, should share similar MF characteristics; for example, when zooming in and out of different time scales, in a time series, the distribution of local Höder exponent h should exhibit similar patterns.

MF analysis is essentially a mathematical term used for measuring or estimating the function of MF spectrum $D(h)$ of a certain time series. Instead of trying to describe the process by one constant scaling exponent (Fractal dimension D), the intention of the MF analysis is to provide a way to describe the distribution of the local Höder exponents.

For a random process $f(t)$, at each point t_i , its local Höder exponent can be given as $h_f(t_i)$. Then its iso-Höder set with respect to different values of h can be expressed as:

$$I_f(h) = \{t_i | h_f(t_i) = h\}. \tag{1}$$

Thus, the MF spectrum of such process can be defined as the Hausdorff (or fractal) dimension of the iso-Höder set:

$$D_f(h) = \dim_H I_f(h). \tag{2}$$

The direct numerical determination by computing the MF spectrum is impractical because it requires the calculation of the local Höder exponent at each point. Hence, the MF

formalism is introduced, and describes the MF spectrum by the Hurst dimension $H(q)$ when analyzing the signal at different scales q . The MF spectrum $D(h)$ is related to the Hurst dimension $H(q)$ through a Legendre transformation, as described in [9]:

$$D_f(h) = \min_{q \neq 0} (d + qh - H(q)), \quad (3)$$

where d is the dimension of the signal.

The wavelet leader (WL) coefficient is one of many multi-resolution quantities that can be used to estimate the MF spectrum $D_f(h)$. This is achieved thanks to the multi-resolution properties of the structure function $\zeta^L(q)$ of the WL coefficient. This allows the accurate approximation of $D_f(h)$ by replacing $H(q)$ with $\zeta^L(q)$. The MF spectrum estimated by the WL structure function provides a tight upper bound of the actual MF spectrum:

$$D_f(h) \leq D^L(h) = \min_{q \neq 0} (d + qh - \zeta^L(q)). \quad (4)$$

For simplicity, throughout the rest of the paper, the estimated MF spectrum $D^L(h)$ is denoted as $D(h)$ as the MF spectrum signature of the signal.

WLM analysis is frequently used to quantify the variability of any time series we wish to characterize: we focus here on the geo-position information of aerial vehicles. This method was first introduced by Dr. Herwig Wendt to analyze dynamical turbulence data (see [3,9–12] for details), and has the advantage of capturing the complexity of traffic for different time scales and different moments of analysis. This analysis then returns a numerical signature used to find the difference between legitimate traffic and traffic that contains an attack. Comparing this to the more traditional discrete wavelet method, this method not only shares the same advantageous performance boost, because they both rely on orthogonal wavelet decomposition and benefit from fast decomposition algorithms, but it also correctly estimates the MF spectrum at negative moments.

However, it is noted that when defining a fractal or self-similar system, it is necessary to verify the existence of the most significant scale which dominates the random process. Instead, for other types of random systems which only exhibit fractal behaviors in some individual ranges, the multifractal spectrum is a powerful tool for analyzing and characterizing the processes.

In this case, it is important to verify the similarity and patterns that emerge from the collected test samples of normal and abnormal data, as shown in Figure 5. It is quite apparent that even though it is not strictly proven that the moving traces acquired in this chapter are multifractal, the MF signature is still capable of distinguishing the differences.

The WLM (currently revised as the wavelet p-leader and bootstrap based multifractal analysis (PLBMF)) MATLAB toolbox, designed by Wendt et al., provides a simple and straightforward solution for estimating the MF spectrum by calculating the scaling function with the wavelet leader coefficient at given moments and then estimating the MF spectrum. It returns multiple attributes, which show different aspects of the multifractality of the analyzed signal, such as the set of structure functions S , the scaling exponent $\zeta^L(q)$, the scope of local Höder exponents, and the estimated MF spectrum $D^L(h)$.

2.3. Machine Learning Signature Classification

The next step after signature acquisition is to compare the signatures of the normal traffic to that of the traffic containing malicious intrusion, and then to observe the patterns that emerge from the different intensities of attack.

When considering the applicable methods, we first investigated the possibility of applying analytical methods, such as the curve matching algorithm proposed in [13], which is similar to our previous approach [1]. However, this was found to be inefficient. Such a method can be effectively applied to detecting a DoS attack due to the fact that this attack can significantly deviate the signature of the signal from that of the normal ones, thereby making it apparent in the similarity score. In addition, in the literature [14–19], we found

that machine learning classification outperforms the analytical method. More sophisticated neural networks have also been proposed to directly address the IDS problem as a whole, such as the one proposed in [20].

For the purpose of this research—to demonstrate the possibility of achieving an automatic alert when an intrusion is detected within the system—we first considered supervised learning, such that a binary trigger can be obtained from the classification. We selected the long short term memory (LSTM) network as the classification method, as it is simple and relatively easy to implement with good results for time series classification. Nevertheless, it is also possible to apply other classification methods, such as the support vector machine (SVM) or the convolution neural network (CNN) and treat the signatures as 2D images.

LSTM is a modified recurrent neural network (RNN), frequently used for time series, voice, and text classification. In comparison to the more conventional feed-forward neural network structures, such as CNN, RNN allows the modification of its internal states based on the output of the previous state, thereby forming a feedback structure. Classic RNN structures suffer from a gradient vanishing problem. To solve this, recent research has widely suggested using LSTM cells, as they can retain memory for an arbitrary duration and potentially solve this problem.

As shown in Figure 2, a typical LSTM neural unit consists of a cell, an input gate, an output gate, and a forget gate. This structure allows the network to preserve information from the previous state (past) with a weight. The cell state (c) is constantly updated by the gates according to the input state (X) and the hidden state (h). First, the forget gate (F) decides to what extent the information in the cell state will be preserved. Next, the input gate (I) decides which individual values in the cell state are to be updated, along with the levels of modification. Finally, the output gate (O) makes a filtered copy of the cell state to pass to the next state.

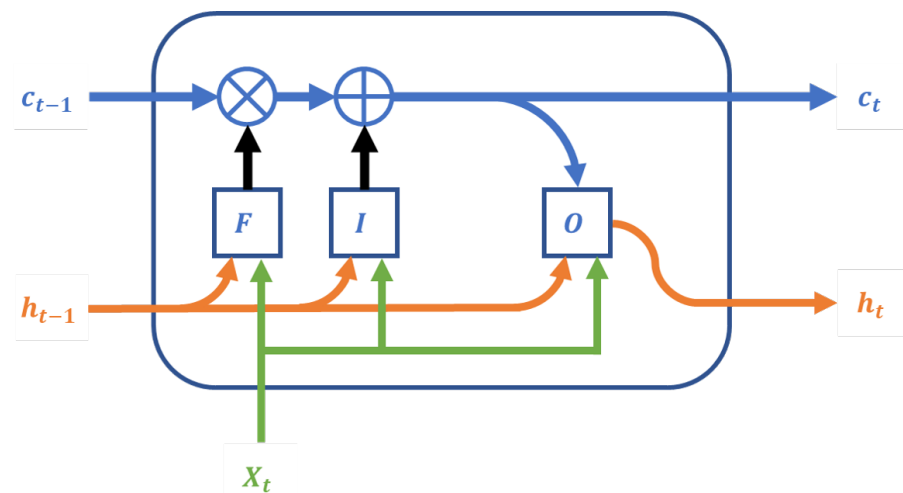


Figure 2. A simplified LSTM unit.

The particular LSTM network we made has a bidirectional LSTM (BiLSTM) network structure, typically used for sequence and time series classification. A BiLSTM basically duplicates and stacks an additional LSTM layer alongside the original LSTM layer and makes it run in the opposite direction (backward), which allows the network to preserve information from the next state, as shown in Figure 3. This method of implementation increases the network's ability to understand the context of the signal. A BiLSTM will generally outperform a regular unidirectional LSTM of similar complexity in tasks such as classification and forecasting, as illustrated in [21–24]. Our proposed model consists of a 1D sequence input layer, a BiLSTM layer of 500 hidden units, a fully connected layer, and a softmax layer.

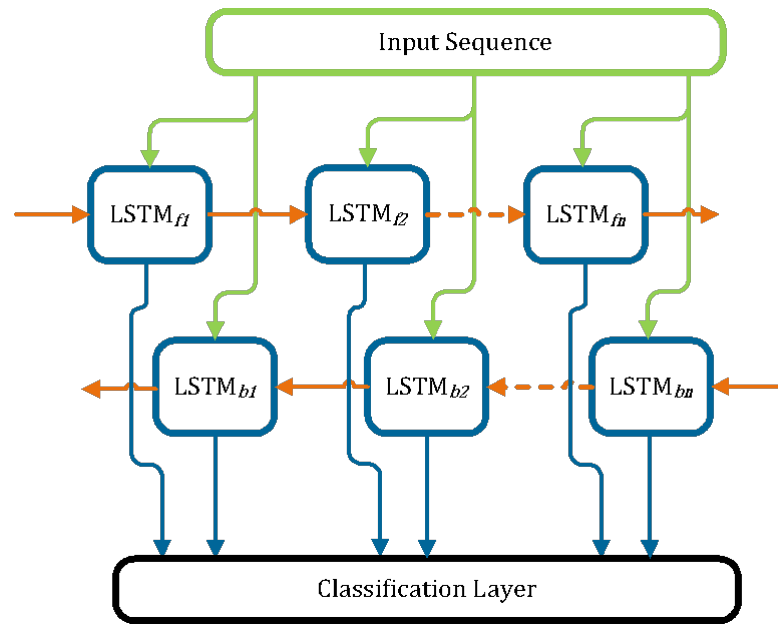


Figure 3. Typical architecture of a Bi-LSTM.

3. Application to Experimental Data

3.1. UAS Mobility Simulation

To demonstrate the feasibility of such a methodology, in the absence of a physically operating UAS, we have designed a test bench based on pre-recorded RADAR network recordings. Instead of applying random walk mobility models that have been employed in other research, we considered the mission profiles and mobility patterns of modern aircraft to be more suitable representations of a complex UAS. Thus, we considered that the RADAR recordings are viable representations of what a UAS ground control station would observe in a UAS network for the following reasons:

- **Payload** Each UAV would report its geographical position at a certain time period either for displaying or back-feeding purposes to allow its back-end control and path planning.
- **Mobility** The individual UAVs can join and leave the network at random times. The RADAR traces capture this behavior approximately by observing aircraft entering and exiting the scope of the RADAR.
- **Infrastructure** A UAS, like any other modern complex system, relies heavily on modern infrastructures, such as ports, stations, and check points, which closely resemble what is available in an existing civil aviation system.
- **Mobile patterns** The movement patterns of planes are similar to those of a drone system in an operational condition.

3.2. Pre-Treatment Euclidean Distance

Before the actual test, the individual recordings were processed to calculate the Euclidean distance: The output array consists of the moving distance that each UAV has traveled between each consecutive recording. Within the original recordings, each UAV position is defined using polar coordinates, such as:

$[\theta_{i,t}, \rho_{i,t}]$ where

$$\left(\begin{array}{l} i \in \mathbb{R}^+ \triangleq \text{“The aircraft’ identification number TN”} \\ t \in \mathbb{R}^+ \triangleq \text{“Time of Day index ToD”}. \end{array} \right) \quad (5)$$

We then define a function $F_{eucd} : \mathbb{R} \rightarrow \mathbb{R}^+$ is detailed thereafter:

$$F_{eucd}([\theta_{i,t}, \rho_{i,t}], [\theta_{i,t+t_{INT}}, \rho_{i,t+t_{INT}}]) = \sqrt{\rho_{i,t}^2 + \rho_{i,t+t_{INT}}^2 - 2\rho_{i,t}\rho_{i,t+t_{INT}} \cos(\theta_{i,t} - \theta_{i,t+t_{INT}})} \quad (6)$$

where $t_{INT} \in \mathbb{R}^+$ is the reporting interval of each individual UAV.

The pseudo-code of Euclidean distance array calculation from UAV positions is detailed in Algorithm 1.

Algorithm 1 Euclidean distance from UAV position.

Require: Recording loaded as a table TBL

Output: New table containing an array of Euclidean distance

- 1: TN_{uniq} = Find unique values in field $TBL.TN$
 - 2: Create an empty table TBL_{new}
 - 3: **for** $ii = 1, \dots, \text{Length of } TN_{uniq}$ **do**
 - 4: | rows of TBL to TBL_{temp}
| where $TBL.TN = LB_{uniq}(ii)$
 - 5: | **for** $i3 = 1, \dots, \text{Length of } TBL_{temp}-1$ **do**
 - 6: | | Create an empty table TBL_{eu}
 - 7: | | $TBL_{eu}.Eucl = \text{run } F_{eucd}$ at index $i3$
 - 8: | | $TBL_{eu}.Tod = TBL_{temp}.Tod(i3)$
 - 9: | **end for**
 - 10: | Parsing table TBL_{eu} with $t_{INT} \leq 10s$
 - 11: | Append TBL_{new} with TBL_{eu}
 - 12: **end for**
 - 13: Sort TBL_{new} with property $TBL_{new}.Tod$
-

As shown in Algorithm 1, each recording file was loaded as a table (TBL) with fields, such as position in θ and ρ , packet destination (DST), flight number (TN), and time of day (ToD). The purpose of Algorithm 1 is to obtain a new table to record the calculated travel distance of each UAV. We achieved this by calculating the Euclidean distance of each UAV between two consecutive records and saving this information in a field $Eucl$ of a new table TBL_{new} . The ToD of the latter record was used as the time stamp.

We iterated F_{eucd} according to Algorithm 1 for each recording file, obtaining the Δ_t —the list of random aircrafts' travel distances recorded at time t . This process better compresses the data and better exposes the abnormal moving patterns induced by the intruders.

3.3. Test Environment

Instead of focusing on variations in the network traffic, in this study, we only partially took into account the payload of the network, such as the coordinates and time. We excluded the physical effects of the network, such as propagation delay, network congestion, and packet loss, as considered in [1].

In this test, we considered the link between the drone and the GCS to be compromised and the malicious user to be initiating an MITM attack by intercepting packets from UAVs, changing the coordinates, and transmitting the forged packets to their original destination. Such an attack is particularly interesting because it is silent and trivial. Network traffic is not significantly modified, and the normal operation for the network itself remains mostly unaltered. We needed to exploit the internal pattern within the payload of each packet instead of the statistics of the network. The received packets on the receiver side were all stored and processed in a.csv file, with each row containing one polar coordinate record of a UAV's position, time of scan, flight number, and frame number.

In this test, we considered $t_{INT} \in \mathbb{R}^+$ to be a random time variable close to the physical period of the RADAR which indicates the time interval of the radar scanning through the same aircraft twice.

Note that, in this particular case, only $t_{INT} \leq 10$ s was taken into account as one trajectory: It is possible for the network to lose packets or for the aircraft to leave and re-join the network at different times of day and at different points of exit and re-entry. There are also cases where after an aircraft has left the network for a long period of time; the flight number TN is reassigned to a new aircraft entering the scope. Hence, it is important to filter the RADAR recordings to avoid taking into account the erroneous traces of aircraft flashing from one point to another in the RADAR's scope due to inaccurate recordings. The 10 s time window was selected to eliminate records that share the same TN but are actually missing more than two frames.

3.4. Datasets

The simulation environment was constructed based on the RADAR records. In total, 31 RADAR records were processed, which corresponded to one month of data. Each original recording contained around 800,000 samples. Each original recording was then used to generate 36 versions of traces with different levels of attack. The simulated attacks were conducted by randomly selecting a number of aircraft with the specific TN , then altering the recorded trajectories by a random amount between 0 and 10%. Each original or modified recording was then scanned by a moving window with a length of 100,000 samples, and the moving step was 10,000 samples. The process of dataset generation is illustrated in Figure 4.

The windowed samples, which contained TNs belonging to the selected attack list, were set to label 1, indicating that they were attacked records, and those that did not contain such TNs were labeled as 0, accordingly, indicating that they no attack took place.

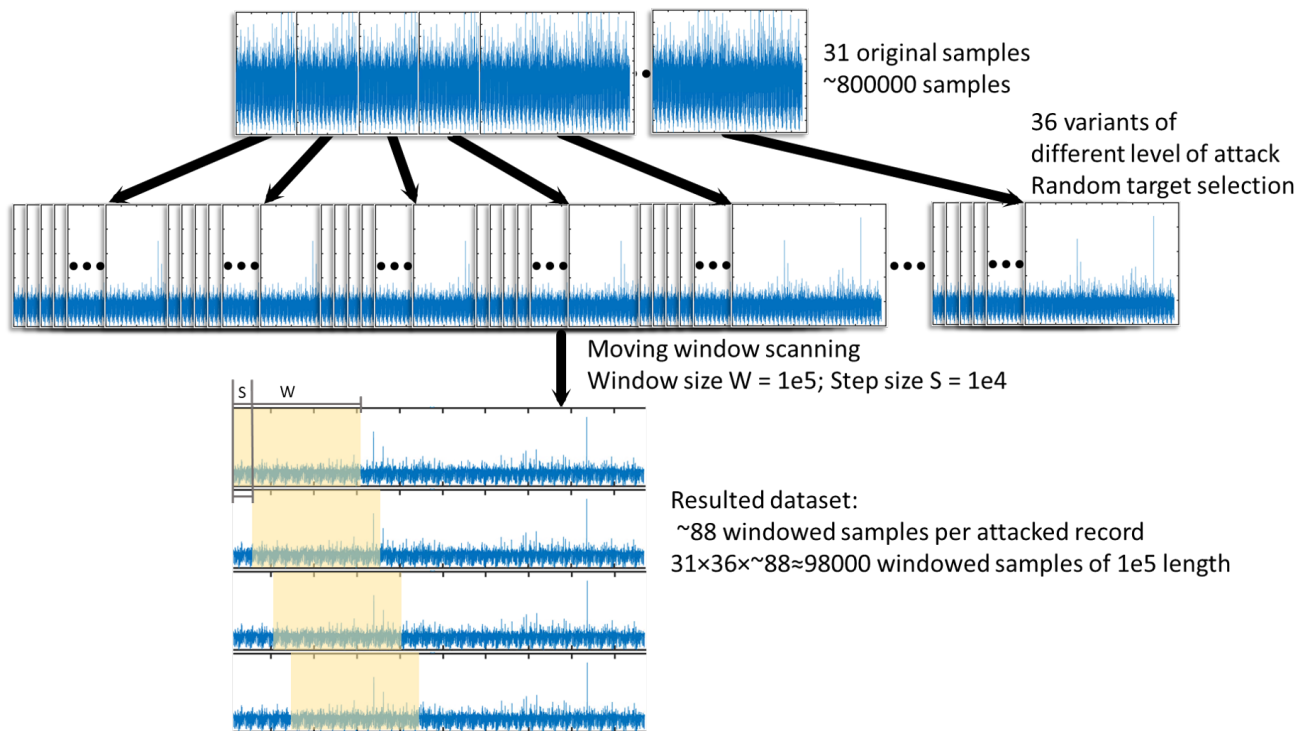


Figure 4. The process of dataset generation.

To avoid significantly out-weighting the normal set with the attacked set, a number of traces with a miniature attack (1 A/C, 1–10%) were also generated for the training set and considered as normal records. Due to the limited number of recordings available, the number of samples for a normal recording was around 25,000. To finally balance the

dataset, the normal samples were padded by duplicating the normal dataset by a factor of 3, thereby creating a normal set of around 75,000 samples. The exact distribution of the datasets is given in Table 1.

For verification purposes, the dataset generation process was replicated to generate a performance verification set, excluding the consideration of balancing.

Table 1. Distribution of samples in the dataset.

	Training Set	Verification Set
Normal	76,263	25,420
Abnormal	88,195	88,196

4. Results

4.1. WLM Signatures

We show two sets of sample MF spectrum signatures $D(h)$ obtained from the WLM toolbox, as discussed in Section III. As shown in Figure 5, during our test, we found that the signatures of the Euclidean distance records Δ_t of attacked traffic deviated from the normal ones. For the normal signal, the level of multifractality is relatively consistent, as shown by the span of h , which mostly ranges between 0.6 and 1, as shown on the left-hand side of Figure 5. The span of h is much wider, however, ranging between 0.3 and 1 in the sampled abnormal signal, as shown on the right-hand side of Figure 5. The MF spectrum $D(h)$ also shows different trends, as the curves appear to be mirrored. Some twisting patterns are also visible. Such twists are observed in the extreme cases where a high-intensity attack with large modifications is present in the signal. This kind of attack will disrupt the originally monotonic descending behavior of the Hurst dimension $H(q)$, making it become non-monotonic, thereby creating the twist in the estimated MF spectrum.

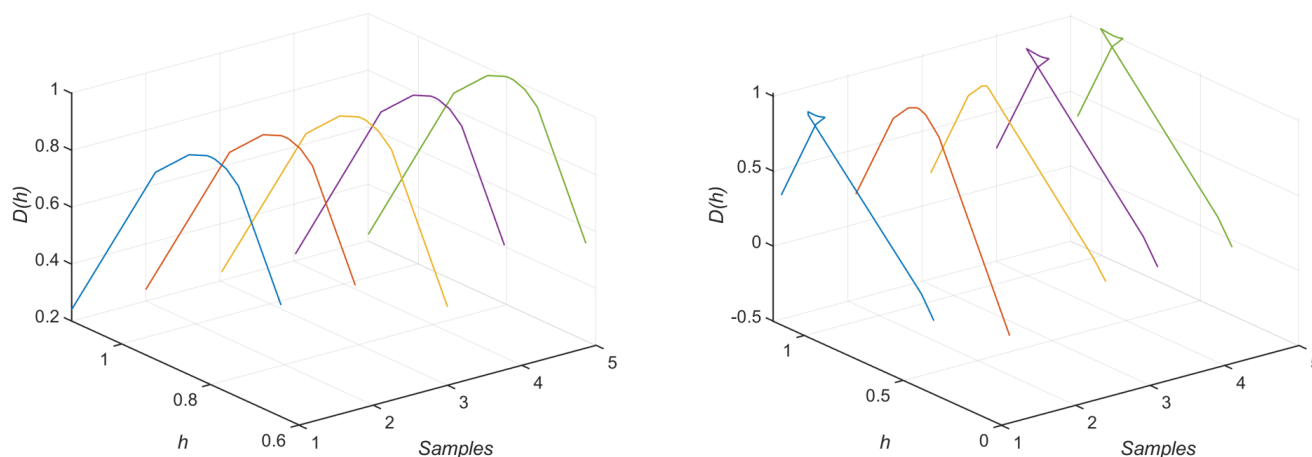


Figure 5. WLM $D(h)$ signatures of: (left) normal traces, (right) abnormal traces.

The signatures, though containing visually distinguishable features, are extremely difficult to identify by applying the curve matching algorithm mentioned in [1,13], because it is almost impossible to set a correct detection threshold without significantly sacrificing the accuracy or the false positive rate, particularly in cases where the attack level is low enough. In addition, the twisting behavior exhibited in the abnormal signatures is not correctly taken into account by the curve matching algorithm, hence our motivation for applying more advanced classification methods, such as the LSTM.

4.2. Machine Learning Classification

To apply a machine learning classifier to our problem, we first had to train with the training dataset. Since the training set was relatively balanced, it did not provide a significantly biased classification result.

The performance of the methodology was firstly measured by the following evaluation matrices:

- **True positive (TP):** attacked record that returned 1 from our IDS;
- **True Negative (TN):** non-attacked record that returned 0 from our IDS;
- **False positive (FP):** non-attacked record that returned 1 from our IDS;
- **False Negative (FN):** attacked record that returned 0 from our IDS;

The matrices are typically compiled as one matrix, called a confusion matrix. From this, the detection accuracy (ACC) is defined:

$$\text{Accuracy} = \frac{\text{TP} + \text{TN}}{\text{TP} + \text{TN} + \text{FP} + \text{FN}} \quad (7)$$

The verification performance is shown in Figure 6.

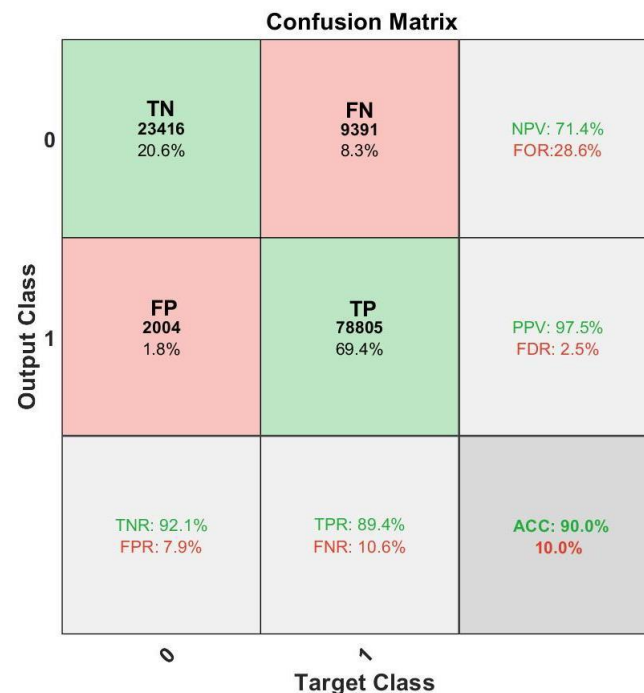


Figure 6. Confusion matrix of the performance verification with LSTM.

The IDS performance was also measured against attacks with different intensities (dictated by the number of A/C attacked). This is represented by an accuracy vs. inaccuracy matrix in percentages, as shown in Figure 7.

As for Figure 6, the main confusion matrix is plotted in red vs. green boxes, where the number of samples and overall probability of samples falling into particular categories are shown. The additional performance indexes are provided in the corresponding gray boxes.

- True positive rate (TPR), positive predictive value (PPV);
- False negative rate (FNR), false discovery rate (FDR);
- True negative rate (TNR), negative predictive value (NPV);
- False positive rate (FPR), false omission rate (FOR);

The overall accuracy was around 90.0%, whereas the relative FP and FN rates were 7.9% and 8.3%, respectively. Due to the way in which the modification levels are generated,

600 aircraft of different TN were presented on average. The attack intensity is mostly dependent on the number of A/C attacked. It is apparent in Figure 7 that with a higher intensity of attack, it was extremely easy to distinguish the malicious recordings from the normal ones. In the scenarios where only a small number of A/C were spoofed, the proposed methodology struggled to provide a valid classification. When there were zero A/C attacked, as shown on the far left of Figure 7 (which means the input samples contained no TN which appeared on the attack list), the method was able to return a good accuracy regarding true negatives.

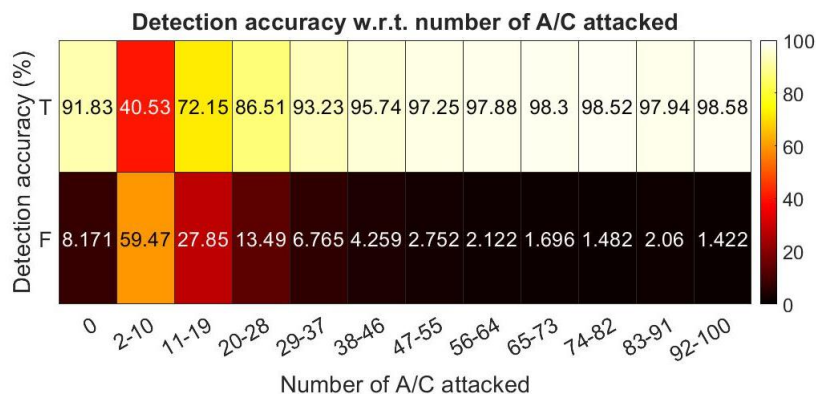


Figure 7. Verification with LSTM at different intensities.

Aside from the LSTM classification mentioned above, to better establish a performance baseline and demonstrate the advantages of LSTM, the experiment was replicated with another commonly used ML classification algorithm: SVM.

The IDS performance was also measured against attacks with different intensities (dictated by the number of A/C attacked). This is represented by an accuracy vs. inaccuracy matrix in percentages, as shown in Figure 8.

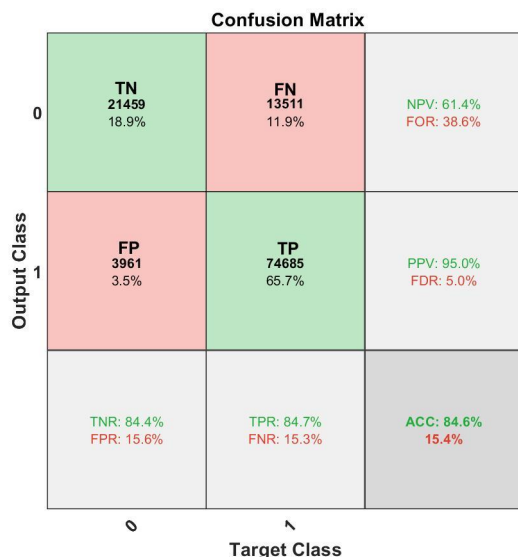


Figure 8. Confusion matrix of the performance verification with SVM.

As shown in Figures 8 and 9, the performance demonstrated here with SVM was slightly worse compared to the ones obtained with LSTM, although it should be noted that the performance matrices are dependent on the design and optimization of the ML schemes. With proper design, the performances of the two classification tools can be improved. Thus, the purpose of bringing SVM classification into the picture was to provide a better empirical perspective into the possible performance with an IDS of a similar methodology.

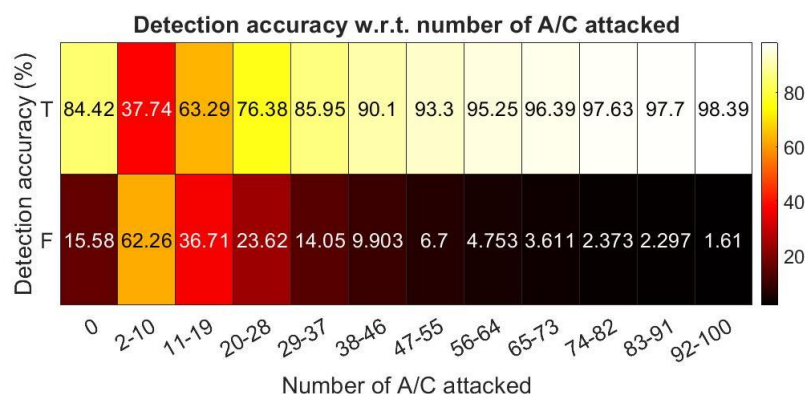


Figure 9. Verification with SVM at different intensities.

5. Related Work

The surge in the growth of network attached devices has led to an urgent need for IDS and IPS advancements. In recent years, IDS has become a hot topic in the network community. Due to the complex nature of networks and their related security concerns, various research fields, including statistics, cybernetics, optimization, and machine learning, are all working to find ways to thwart intrusions from inside various networks. Here we provide a comprehensive state-of-the-art summary of the different research recently published on these related topics.

In [25], Asharf et al. provides a thorough and recent review of the state-of-the-art of IoT-related IDS. The authors provide a comprehensive introduction to the structures of current IoT systems. The challenges and corresponding IDS research are presented.

In [26], a global overview of multiple research areas and application domains regarding general anomaly detection is presented by Chandola et al. The authors provide a well categorized review of different anomaly detection technologies and their fields of application. We note that the anomaly detection methods in the field of biology vastly differ from those in the field of telecommunications, although the underlying principles are interlinked and the template the authors provide is thought provoking. Among the fundamental methods, deep learning and neural networks dedicated to intrusion detection received considerable attention in recent years in terms of the various models and performance evaluations.

In [27], Aldweesh et al. reviewed the recent advancements in deep learning-based IDS. The authors provide a clear overview of a variety of deep learning-based IDS of differing taxonomies. Their article is an excellent guide for popular deep learning algorithms for IDS.

In [14], Shi et al. propose an interesting approach for network traffic classification. The authors employ the traditional wavelet coefficients-based multifractal energy spectrum teamed with a neural network based on a multi-layer perceptron neural network. This is structurally similar to our approach but with a different target. They were able to confirm the accurate classification of three networking application classes (Http, Streaming, P2P).

In [28], the authors demonstrate a powerful intrusion detection and prevention system (IDPS) based on distributed sensors and a software-defined network (SDN), called BroFlow. The proposed BroFlow system was simulated in a virtual network and showed excellent performance against DoS attacks. The proposed methodology is of great interest to us, as we plan to adopt a similar structure in our future research to achieve an automatic IPS based on SDR driven by our IDS. Besides this, rich literature can be found regarding IDS designs based purely on machine learning principles. For instance, in [15], Gwon et al. provide a clear implementation of an LSTM-based IDS design with feature embedding. The model was tested against the UNSW-NB15 dataset. A performance comparison against other methods is provided.

In [16], Kasongo et al. proposes using a deep LSTM (DLSTM) network-based classifier to solve classic IDS problems proposed in public datasets, such as the NSL-KDD intrusion

detection dataset. The advantageous performance of a DLSTM in comparison with several other traditional neural network models is presented.

In [19], X. Zhou et al. propose a novel approach to solving the industrial big data anomaly detection problem by applying a variational LSTM (VLSTM) framework, which incorporates an LSTM based encoder–decoder structure with a variational reparameterization module and an estimation module. This is particularly interesting because the purpose of the compression network is to extract interesting features from a raw data input, and the hidden variables are used to fulfill the estimation and classification purposes. The VLSTM framework allows for the extraction of a variety of features, and thus allows for the detection of various types of anomalies.

Some propose to use another recurrent neural network model, such as the Gated Recurrent Unit (GRU), to solve IDS problems, as they are easier to train and do not require memory units.

In [17,18], the authors demonstrate a novel IDS based on a GRU recurrent neural network and present its superior performance over the more traditionally used LSTM network.

In [29], Amouri et al. propose using distributed network sensors and supervised learning methods to construct an IDS within a Wireless Sensor Network (WSN) and a mobile ad-hoc network (Mannet), which has improved accuracy. Within the literature, contributions were also found regarding rule-based IDS methods, which assisted us with envisioning the overall structure of our IDS design.

In [30], the authors provide an insightful overview of IDS design in general and also demonstrate an advanced pattern matching technique and its application in the Snort IDS framework. It is also worth noting that a number of articles were found to be inspiring for the future improvement of our IDS design.

In [31], Zhang et al. present an interesting implementation of two deep learning networks consisting of a teacher–student network structure, which shows promising perspectives for implementation in a mobile environment. The proposed network is relatively lightweight, allowing it to be integrated into a low-power platform, such as a UAV, while being able to perform accurate traffic image classification.

In [32], Shafique et al. provide a new insight into a new type of network intrusion, called ranking attack, which mostly targets the IoT devices employing IPv6. The authors provide an in-depth discussion on the attack, along with a method of IDS with good accuracy.

In [20], A. Abdelkefi. propose a complete approach for network traffic anomaly detection and root-cause analysis called SENATUS. SENATUS also takes advantage of the traffic statistics which require the minimum amount of knowledge of the packets. The method was successfully applied to practical problems such as DoS/DDoS attacks with good accuracy.

To the best of our knowledge, our proposed method is unique in solving an MITM problem in a wireless network that exhibits mobile properties. Our contribution differentiates itself from the methods proposed in [16,18–20,31] and others reviewed in [25–27]. Our method eliminates the use of a deep neural network, which is advantageous in terms of scalability, interpretability, and computational overheads.

6. Conclusions and Perspectives

In this paper, we proposed an innovative approach to achieve network spoofing attack detection. We proposed this new methodology with an improvement over our previously designed IDS: incorporating neural network classification. We designed a test bench and demonstrated the preliminary performance results, showing the effectiveness of this new design. As shown in Section IV, this new design permits us to achieve high detection accuracy while keeping a low false positive rate. Compared to the literature in Section V, it is noted that our proposed method targets a very specific type of intrusion, which is commonly observed in mobile networks, such as the UAS network. Our method's positive overall performance enables us to further investigate it and its implementation possibilities.

As a next step, we are looking to achieve increased performance by fine-tuning the WLM toolbox for better feature extraction and by applying different neural network models to lower the computational costs further and achieve lower latency. In addition, we plan to apply training and working performance comparisons between it and other existing IDS. Beyond that, we propose to optimize the WLM toolbox for the mobile communication network environment. Finally, we plan to implement this system within a working UAS, to further investigate research possibilities of embedded IDS in a drone swarm.

Author Contributions: Conceptualization, R.Z. and J.-P.C.; methodology, R.Z.; software, R.Z.; validation, R.Z., J.-P.C., and E.L.; writing—original draft preparation, R.Z.; writing—review and editing, R.Z.; visualization, R.Z.; supervision, J.-P.C. and E.L.; project administration, J.-P.C. and E.L. All authors have read and agreed to the published version of the manuscript.

Funding: This research received no external funding.

Institutional Review Board Statement: Not applicable.

Informed Consent Statement: Not applicable.

Data Availability Statement: Not applicable.

Conflicts of Interest: The authors declare no conflict of interest.

References

1. Condomines, J.-P.; Zhang, R.; Larrieu, N. Network Intrusion Detection System for UAV Ad-hoc Communication from methodology design to real test validation. *Ad Hoc Netw.* **2018**. Available online: <https://www.sciencedirect.com/science/article/abs/pii/S1570870518306541> (accessed on 9 December 2021).
2. Barry, R.L.; Kinsner, W. Multifractal characterization for classification of network traffic. In Proceedings of the Canadian Conference on Electrical and Computer Engineering 2004 (IEEE Cat. No.04CH37513), Niagara Falls, ON, Canada, 2–5 May 2004; Volume 3, pp. 1453–1457. <http://doi.org/10.1109/CCECE.2004.1349677>.
3. Fontugne, R.; Abry, P.; Fukuda, K.; Veitch, D.; Cho, K.; Borgnat, P.; Wendt, H. Scaling in Internet Traffic: A 14 Year and 3 Day Longitudinal Study, with Multiscale Analyses and Random Projections. *IEEE/ACM Trans. Netw.* **2017**, *25*, 2152–2165.
4. EU. Commission Implementing Regulation (EU) 2019/947 of 24 May 2019 on the rules and procedures for the operation of unmanned aircraft (Text with EEA relevance) C/2019/3824. *Off. J. Eur. Union* **2019**, 45–71. Available online: <https://eur-lex.europa.eu/legal-content/EN/TXT/?uri=CELEX%3A32019R0947> (accessed on 9 December 2021).
5. FAA. Small Unmanned Aircraft Systems (UAS) REGULATIONS (Part 107). Small Unmanned Aircraft Systems (UAS) Regulations (Part 107) vert Federal Aviation Administration. 2020. Available online: <https://www.faa.gov/newsroom/small-unmanned-aircraft-systems-uas-regulations-part-107> (accessed on 9 December 2021).
6. EU. Regulation (EU) 2016/679 of the European Parliament and of the Council of 27 April 2016 on the protection of natural persons with regard to the processing of personal data and on the free movement of such data, and repealing Directive 95/46/EC (General Data Protection Regulation) (Text with EEA relevance). *Off. J. Eur. Union* **2016**, 1–71. Available online: <https://eur-lex.europa.eu/eli/reg/2016/679/oj> (accessed on 9 December 2021).
7. EU. Commission Implementing Regulation (EU) 2021/664 of 22 April 2021 on a regulatory framework for the U-space (Text with EEA relevance) C/2021/2671. *Off. J. Eur. Union* **2021**, 161–183. Available online: <https://eur-lex.europa.eu/legal-content/EN/ALL/?uri=CELEX%3A32021R0664> (accessed on 9 December 2021).
8. Stöcker, C.; Bennett, R.; Nex, F.; Gerke, M.; Zevenbergen, J. Review of the Current State of UAV Regulations. *Remote. Sens.* **2017**, *9*, 459.
9. Wendt, H. Contributions of Wavelet Leaders and Bootstrap to Multifractal Analysis: Images, Estimation Performance. Dependence Structure and Vanishing Moments. Confidence Intervals and Hypothesis Tests. 2008. Available online: <https://www.semanticscholar.org/paper/Contributions-of-Wavelet-Leaders-and-Bootstrap-to-Wendt/35c37137b8b51bd302967e0af861ce99347932a2> (accessed on 9 December 2021).
10. Wendt, H.; Abry, P.; Jaffard, S. Bootstrap for Empirical Multifractal Analysis. *IEEE Signal Process. Mag.* **2007**, *24*, 38–48.
11. Wendt, H.; Abry, P. Multifractality Tests Using Bootstrapped Wavelet Leaders. *IEEE Trans. Signal Process.* **2007**, *55*, 4811–4820.
12. Wendt, H.; Roux, S.G.; Jaffard, S.; Abry, P. Wavelet Leaders and Bootstrap for Multifractal Analysis of Images. *Signal Process.* **2009**, *89*, 1100–1114.
13. Grim, A.; O'Connor, T.; Olver, P.; Shakiban, C.; Slechta, R.; Thompson, R. Automatic Reassembly of Three-Dimensional Jigsaw Puzzles. *Int. J. Image Graph.* **2016**, *16*, 1650009.
14. Shi, H.; Liang, G.; Wang, H. A novel traffic identification approach based on multifractal analysis and combined neural network. *Ann. Telecommun. Ann. Télécommun.* **2014**, *69*, 155–169.
15. Gwon, H.; Lee, C.; Keum, R.; Choi, H. Network Intrusion Detection based on LSTM and Feature Embedding. *arXiv* **2019**, arXiv:1911.11552.

16. Kasongo, S.M.; Sun, Y. A Deep Long Short-Term Memory Based Classifier for Wireless Intrusion Detection System. 2020; pp. 98–103. Available online: <https://www.sciencedirect.com/science/article/pii/S2405959519301699> (accessed on 9 December 2021).
17. Chen, Z.; Zhang, W.; Xie, Z.; Xu, X.; Chen, D. Recurrent Neural Networks for Automatic Replay Spoofing Attack Detection. In Proceedings of the 2018 IEEE International Conference on Acoustics, Speech and Signal Processing (ICASSP), Calgary, AB, Canada, 15–20 April 2018; pp. 2052–2056.
18. Xu, C.; Shen, J.; Du, X.; Zhang, F. An Intrusion Detection System Using a Deep Neural Network with Gated Recurrent Units. *IEEE Access* **2018**, *6*, 48697–48707.
19. Zhou, X.; Hu, Y.; Liang, W.; Ma, J.; Jin, Q. Variational LSTM Enhanced Anomaly Detection for Industrial Big Data. *IEEE Trans. Ind. Inform.* **2021**, *17*, 3469–3477.
20. Abdelkefi, A.; Jiang, Y.; Sharma, S. SENATUS: An Approach to Joint Traffic Anomaly Detection and Root Cause Analysis. In Proceedings of the 2018 2nd Cyber Security in Networking Conference (CSNet), Paris, France, 24–26 October 2018.
21. Siami-Namini, S.; Tavakoli, N.; Namin, A.S. The Performance of LSTM and BiLSTM in Forecasting Time Series. In Proceedings of the 2019 IEEE International Conference on Big Data (Big Data), Los Angeles, CA, USA, 9–12 December 2019; pp. 3285–3292.
22. Graves, A.; Fernández, S.; Schmidhuber, J. Bidirectional LSTM Networks for Improved Phoneme Classification and Recognition. In Proceedings of the Artificial Neural Networks: Formal Models and Their Applications—ICANN 2005, Warsaw, Poland, 11–15 September 2005; pp. 799–804.
23. Graves, A.; Schmidhuber, J. Framewise phoneme classification with bidirectional LSTM networks. In Proceedings of the 2005 IEEE International Joint Conference on Neural Networks, Montreal, QC, Canada 31 July–4 August 2005; Volume 4, pp. 2047–2052.
24. Graves, A.; Schmidhuber, J. Framewise phoneme classification with bidirectional LSTM and other neural network architectures. *Neural Netw.* **2005**, *18*, 602–610.
25. Asharf, J.; Moustafa, N.; Khurshid, H.; Debie, E.; Haider, W.; Wahab, A. A Review of Intrusion Detection Systems Using Machine and Deep Learning in Internet of Things: Challenges, Solutions and Future Directions. *Electronics* **2020**, *9*, 1177.
26. Chandola, V.; Banerjee, A.; Kumar, V. Anomaly detection: A survey. *ACM Comput. Surv. (CSUR)* **2009**, *41*, 15.
27. Aldweesh, A.; Derhab, A.; Emam, A.Z. Deep learning approaches for anomaly-based intrusion detection systems: A survey, taxonomy, and open issues. *Knowl.-Based Syst.* **2020**, *189*, 105124.
28. Lopez, M.A.; Mattos, D.M.F.; Duarte, O.C.M.B. An elastic intrusion detection system for software networks. *Ann. Telecommun.* **2016**, *71*, 595–605.
29. Amouri, A.; Morgera, S.D.; Bencherif, M.A.; Manthena, R. A Cross-Layer, Anomaly-Based IDS for WSN and MANET. *Sensors* **2018**, *18*, 651.
30. Abbes, T.; Bouhoula, A.; Rusinowitch, M. On the fly pattern matching for intrusion detection with Snort. *Ann. Télécommun.* **2004**, *59*, 1045–1071.
31. Zhang, J.; Wang, W.; Lu, C.; Wang, J.; Sangaiah, A.K. Lightweight deep network for traffic sign classification. *Ann. Telecommun.* **2020**, *75*, 369–379.
32. Shafique, U.; Khan, A.; Rehman, A.; Bashir, F.; Alam, M. Detection of rank attack in routing protocol for Low Power and Lossy Networks. *Ann. Telecommun.* **2018**, *73*, 429–438,